TECHNISCHE UNIVERSITÄT MÜNCHEN

Max-Planck-Institut für Plasmaphysik

Finite beta effects on turbulent transport in tokamak plasmas

Tobias HEIN

Vollständiger Abdruck der von der Fakultät für Physik der Technischen Universität München zur Erlangung des akademischen Grades eines

Doktors der Naturwissenschaften

genehmigten Dissertation.

Vorsitzender: Univ.-Prof. Dr. R. Gross

Prüfer der Dissertation:

1. Hon.-Prof. Dr. S. Günter
2. Univ.-Prof. Dr. S. Paul

Die Dissertation wurde am 31.01.2011 bei der Technischen Universität München eingereicht und durch die Fakultät für Physik am 29.06.2011 angenommen.

TECHNISCHE UNIVERSITÄT MÜNCHEN

Max-Planck-Institut für Plasmaphysik

Finite beta effects on turbulent transport in tokamak plasmas

Tobias HEIN

January 2011

Das Wesen der Dinge hat die Angewohnheit, sich zu verbergen.

Heraklit

Contents

Chapter 1

Introduction

The requirement of an economically and ecologically viable energy source is one of the main challenges mankind is facing. This statement was broadly underlined in a study on the future of worlds economy by Meadows, et al. already in 1972 [1], on behalf of the Club of Rome, right before the 1973 oil crisis put the public attention on this topic. The main outcome of the report was that in case of further exponential growth of worlds population, food and industrial production, exploitation of natural resources, and environmental pollution, as it is suggested by extrapolation of statistical data, the absolute limits to growth will be reached within the next 100 years and a collapse will occur. However, by fulfilling all the necessary requirements even in the presence of a higher energy demand than at present, the state of a sustainable society can be reached. Nevertheless, since the publication of this study the initial position did not change significantly, as it was shown for instance in the 30-year update of this report [2]. Therefore, it remains essential that an enduring state is strongly associated with a clean and (relatively) cheap energy source, which may be nuclear fusion.

1.1 Fusion energy and magnetic confinement

The vital impact of energy provided by the Sun on the daily life of humankind has been known for a long time and resulted in astonishing cultural achievements like the Neolithic and Bronze Age monuments in Stonehenge (England) or the Pyramide of the Sun in Teotihuacán (Mexico). In contrast, the physics mechanism of the power generation has been largely obscure until the late 30s of the last century. At this time, the increased knowledge in nuclear physics and quantum mechanics led to the star model by Weizsäcker [3] and Bethe [4], which was able to explain the enormous energy production by nuclear fusion. The basic principle can be illustrated in Fig. 1.1, where the average binding energy per nucleon is shown as a function of its mass. The binding energy shows a maximum for medium-weight nuclei around ^{56}Fe, while the fusion of light nuclei or the fission of heavy nuclei increases the binding energy. These mechanisms lead to a net gain of energy of the order of mega electron-volts (MeV) per event, roughly six orders of magnitude higher than in chemical processes like combustion. From this figure it is also clear that the energy release per reaction is much higher in the case of fusion compared to fission. For that reason, the former was particularly interesting as a giant energy source, and mankind started to use it as a weapon. Beyond that the peaceful application of fusion energy

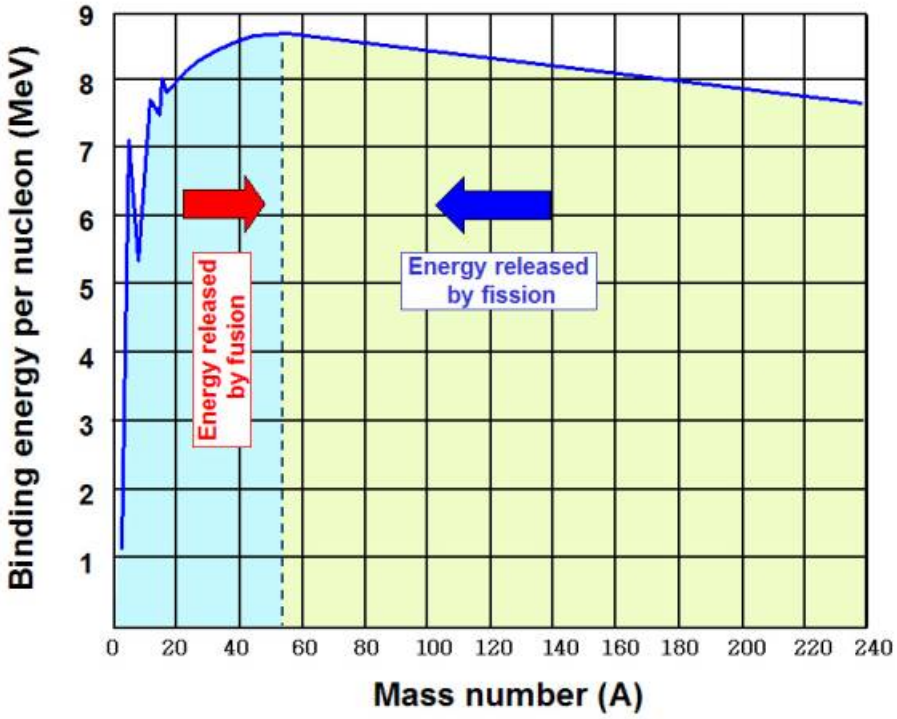

Figure 1.1: Binding energy of nuclei as a function of the mass (Source: http://www4.nau.edu).

is extremely attractive, mainly for three reasons. Firstly, nuclear fusion is inherently safe since no critical mass of fuel is needed for energy production. Secondly, the fuel is extremely abundant, making a long term use possible. Thirdly, and probably most important, the fusion reaction is environmentally benign since no long life radioactive waste and practically no greenhouse gases are produced. It became clear very soon that the fusion reaction providing the major amount of the power production on the Sun, namely the proton-proton reaction, which requires high pressures, is hardly applicable for energy production on Earth. Therefore, a reaction with a much higher cross-section and therefore higher reaction rate, namely the deuterium-tritium fusion reaction,

$$ {}^{2}_{1}\mathrm{H} + {}^{3}_{1}\mathrm{H} \rightarrow {}^{4}_{2}\mathrm{He} + {}^{1}_{0}\mathrm{n} + 17.6\mathrm{MeV}, \tag{1.1} $$

is favored instead. Both ${}^{2}_{1}\mathrm{H}$ and ${}^{3}_{1}\mathrm{H}$ can be extracted from seawater in very large amounts, the former directly and the latter via lithium, from which tritium can be obtained by nuclear activation using neutrons. While the reaction in Eq. (1.1) can be achieved rather easily for a few reactions, it is extremely difficult to realize it on a large scale with a positive energy balance needed for energy production, for both fundamental scientific and technological barriers.

In that respect, one of the most important issues is the question of confinement. The concept of magnetic confinement turned out to be the most promising. This is directly connected with the state of matter of the fuel at the high velocities provided by high temperatures required to overcome the Coulomb repulsion, namely the plasma state in which the burning material builds up a quasi–neutral gas consisting of deuterium and

tritium with the electrons entirely stripped off. The positively charged protons need to come very closely together (approximately 10^{-15} m) in order to experience the attractive nuclear force and agglomerate, releasing a huge amount of energy. Therefore, a kinetic energy of the order of 10 keV in a thermal plasma, or correspondingly a temperature of about 100 million degrees, is required in order to obtain fusion reactions with an acceptable rate. For this reason, the burning plasma needs to be kept away from the walls of the vacuum chamber because they would be destroyed very soon. Moreover, the plasma would be cooled and polluted. Magnetic fields are the best candidate for a confinement preventing the contact with the surrounding material. The charged particle motion in the presence of a magnetic field is described by the Lorentz force. Along a homogeneous magnetic field of straight field lines, the motion is restricted to a gyration perpendicular to the field lines while the motion parallel to the field lines remains unconstrained. For this reason, early linear fusion devices used magnetic field inhomogeneities in order to create a mirror force reflecting most of the charged particles at both ends. This is the concept of a 'magnetic bottle'. It turned out quite soon that a too large fraction of the fast particles was not reflected and led to unsatisfactorily high losses.

An alternative approach is to connect both ends and by this to form a toroidal device, thereby avoiding those losses. This attempt was firstly applied in Russia under the acronym 'tokamak' standing for 'toroidal chamber with magnetic coils' and turned out to be the most successful up to now. The main benefits in comparison to other magnetic confinement concepts like the 'reversed field pinch' are better energy confinement properties, with an acceptable magnetohydrodynamical stability. The basic principle is shown in

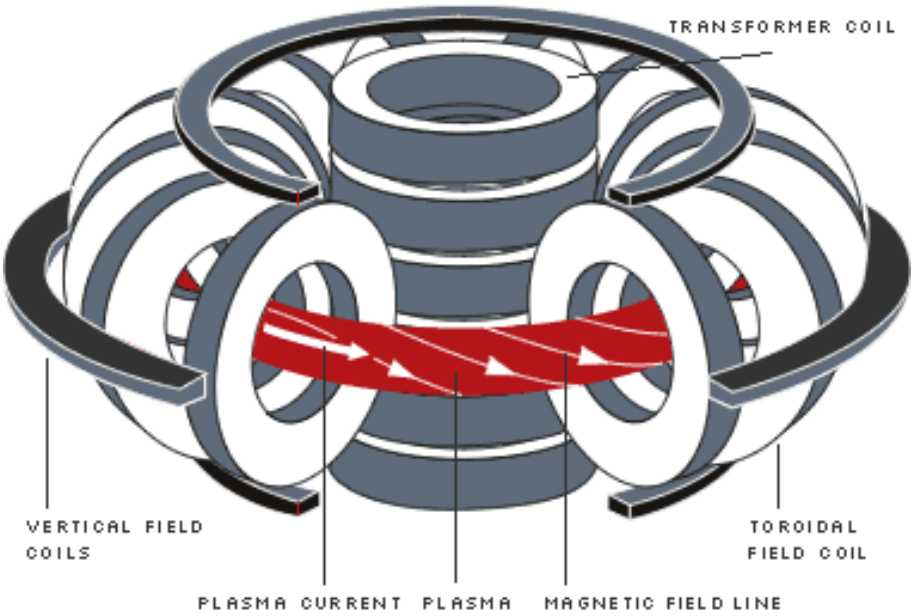

Figure 1.2: Basic concept of the tokamak (Source: http://www.ipp.mpg.de).

Fig. 1.2. The toroidal magnetic field is generated using toroidal field coils with a poloidal current. However, with a purely toroidal magnetic field, the magnetic field curvature and gradient result in a vertical drift which is in opposite directions for ions and electrons, as it is shown in Fig. 1.3. The resulting electric field causes an outward E×B drift of

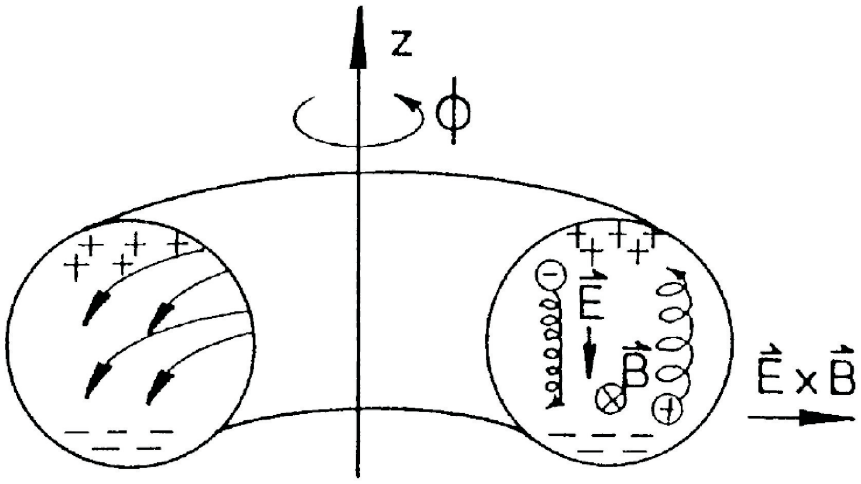

Figure 1.3: Vertical drifts and associated E×B drift in a toroidal field (Source: Script of IPP summer university of plasma physics 08).

the whole plasma, and therefore such a simple magnetic configuration will not confine the particles. The charge separation can be avoided by a poloidal magnetic field component, which is produced by a toroidal current. However, the latter reduces the magnetohydrodynamical stability, and is the main limitation of the tokamak concept since the toroidal current is produced by magnetic induction, along the transformer principle. According to the Maxwell–Faraday equation, the loop voltage is associated with a magnetic flux, which has to be varied in time and has to be provided from outside. In present day tokamaks the normal operation is inductive leading to an operation of tokamaks only in a pulsed regime, with typical pulse durations of the order of a few seconds. In the last decades, lots of work has been done in order to find non–inductive operational scenarios. These can be realized by current drive due to tangential neutral beam injection heating, lower hybrid or electron cyclotron current drive. Also, in the last years important progress has been made in order to reach and maintain high values of a self–generated toroidal plasma current, the so–called bootstrap current, and fully non–inductive scenarios can be realized [5, 6]. Stellerators, on the other side, are very promising in terms of long pulse operation since they do not need a plasma current. The very complicated field coil geometry, as it can be seen from Fig. 1.4, ensures the magnetic confinement. The main drawback of present day stellerators is the fact that they show energy confinement times of roughly one order of magnitude lower than in tokamaks of comparable vessel volume. Moreover, the research in terms of plasma behavior as well as engineering developments are still lagging behind compared to tokamaks, such that the latter ones will be the working–horse for the next decades in order to realize a viable energy source.

A figure of merit for the advances in confinement is the so–called Lawson criterion [7], which gives a lower boundary for the 'triple–product', namely density times temperature times energy confinement time, for a deuterium-tritium plasma to reach the 'break–even' point, where the amount of the total power P_{fus} generated by the fusion reactions in the plasma is equal to the total loss power of energy, P_{loss}, such that $Q = P_{\mathrm{fus}}/P_{\mathrm{loss}} = 1$ and the same amount of energy is generated from the fusion reactions as the applied energy

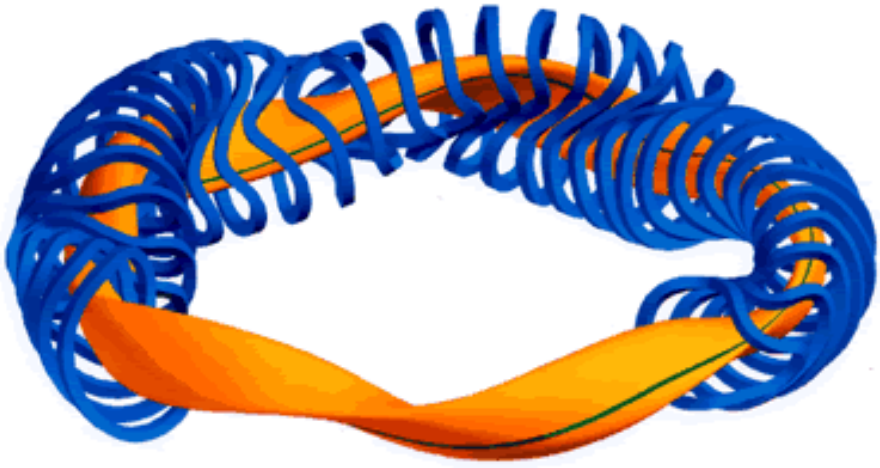

Figure 1.4: Coil and plasma geometry of the optimized stellerator (Source: http://www.ipp.mpg.de).

in order to heat the plasma and to compensate for energy losses. For the D-T reaction, it reads

$$n_e T \tau_E \geq 10^{21} \mathrm{keVs/m^3}, \tag{1.2}$$

where the energy confinement time τ_E is given by the fraction of the total stored energy W_{int} in the plasma divided by the total loss power. The challenge for plasma physicists is to obtain all three values needed for the Lawson–criterion at the same time, namely pressures of the order of several atm and energy confinement times of the order of a few seconds. The triple–product is shown in Fig. 1.5. Here and in the following, temperatures are measured in terms of energy, $k_B T \to T$. It is clear that in the last decades enormous progress has been made, but there is still a step to take in order to reach the goal of an economically viable energy source. One important milestone will be the International Thermonuclear Experimental Reactor (ITER) [8], a tokamak which is designed to overcome 'break–even' by reaching $Q = 10$ and to explore the plasma behavior under those conditions in order to build a power plant in the next future.

1.2 Charged particle trajectories and transport

In order to get a better understanding of the confinement in a tokamak, it is instructive to discuss the trajectory of a single charged particle. For typical operational parameters of present day devices, namely magnetic fields ∼3 T and temperatures of ∼3 keV, the particles are forced to a gyration around magnetic field lines with cyclotron angular frequencies $\Omega_{c,\sigma} = Z_\sigma e B/(mc)$, where σ denotes the species. For deuterium ions, $\Omega_{c,i} \simeq 2.9 \cdot 10^8$ rad/s and for electrons, $\Omega_{c,e} \simeq 5.3 \cdot 10^{11}$ rad/s. Thermal velocities are given by $v_{th,\sigma} = \sqrt{T_\sigma/m_\sigma}$, for deuterium ions $v_{th,i} \simeq 5.4 \cdot 10^5$ m/s, and for electrons $v_{th,e} \simeq 3.2 \cdot 10^7$ m/s. These correspond to average Larmor radii $\rho_{L,\sigma} = v_{th,\sigma}/\Omega_{c,\sigma}$ of about 0.19 mm for deuterium ions and 61 μm for electrons. Thus, they are much smaller than the characteristic variation length of the equilibrium parameters in the core, which are of the order of the tokamaks

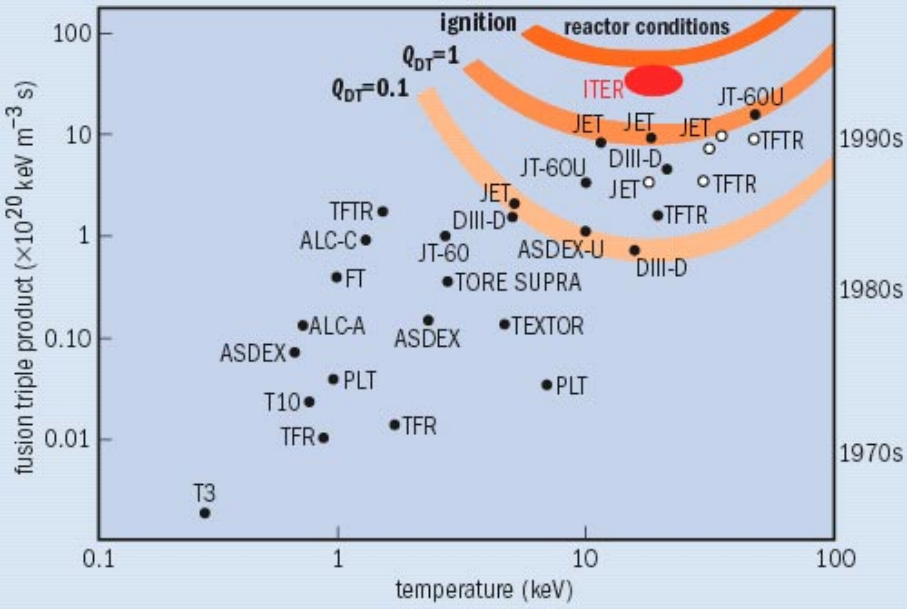

Figure 1.5: Fusion triple product as a function of temperature measured in keV (Source: http://images.iop.org).

minor radius and therefore a∼1 m. Under these conditions, the trajectory of a particle can be decomposed into its fast gyration, the slower motion of the center of gyration called guiding–center (GC) of the order of 10^6 s^{-1}, and the even slower drift frequencies of the GC across the magnetic field of the order of 10^3 s^{-1}. Following [9], a systematic perturbation series of the Lorentz force with electric and magnetic fields slowly varying compared to the gyration frequency in the sense that $1 \gg \delta \sim \rho_{\mathrm{L}}|\nabla B|/B, (\Omega_{\mathrm{c}}B)^{-1}dB/dt$ in combination with a very small electric field can be made in order to determine the equation of motion. If not specified otherwise, a gradient ∇ refers to the radial derivative of a quantity throughout this thesis. The perturbation series reads

$$\delta\frac{d^2\mathbf{x}}{dt^2} = \frac{e}{m}\mathbf{E} + \frac{Z_\sigma e}{mc}\frac{d\mathbf{x}}{dt}\times\mathbf{B}. \tag{1.3}$$

The particle trajectory $\mathbf{x}(t)$ is then given by

$$\mathbf{x}(t) = \mathbf{x}_0(t) + \delta\mathbf{x}_1(f(t),t) + \delta^2\mathbf{x}_2(f(t),t) + ..., \tag{1.4}$$

where $\mathbf{x}_0(t)$ denotes the GC motion independent of the gyration with the gyration phase $f(t)$, which is included in $\mathbf{x}_{1,2,..}(f(t),t)$. After a lengthy calculation one arrives at the following expressions:

$$\begin{aligned}
\mathbf{v}_{0,\perp} &= c\frac{\mathbf{E}\times\mathbf{B}}{B^2} \\
\mathbf{v}_{1,\perp} &= \frac{1}{\Omega_{\mathrm{c},\sigma}B}\mathbf{B}\times\frac{d\mathbf{v}_0}{dt} + \frac{\mu_{\mathrm{B},\sigma}}{m\Omega_{\mathrm{c},\sigma}}\mathbf{b}\times\nabla B \\
\frac{dv_{0,||}}{dt} &= Z_\sigma e E_{||} - \mu_{\mathrm{B},\sigma}\mathbf{b}\cdot\nabla B(\mathbf{x}_0)
\end{aligned} \tag{1.5}$$

Here, $\mathbf{b} = \mathbf{B}/B$, and $\mu_{\mathrm{B},\sigma} = m_\sigma v_{\perp,\sigma}^2/(2B)$ is the magnetic moment connected with the fast gyro–motion and therefore temporally nearly constant, an adiabatic invariant. The zero–order velocity is the E×B velocity, while the first–order velocity is given by the inertial drift consisting of the curvature and the polarization drift, and the ∇B drift. The parallel motion is given by the parallel electrostatic force and the so–called mirror force due to parallel inhomogeneities in the magnetic field. The latter one provides a special implication to the trajectories of charged particles in a tokamak: in case of large μ_{B} corresponding to large perpendicular velocities, particles can change their parallel direction depending on the actual direction of the magnetic field and its gradient, as it can be seen from the last expression in Eq. (1.5). This leads to trapping of particles and to the so–called banana orbits in the poloidal projection of the trajectory, and can be seen in Fig. 1.6.

Particles with small perpendicular energy do not change direction and are therefore passing, which means that they move around the full torus. In this sense, a useful parameter is the pitch angle defined as $\theta_{\mathrm{p}} = \arctan(v_\perp/v_{||})$. From the energy conservation and the adiabatic invariance of μ_{B} it can be concluded that in a simple, large aspect ratio R/a geometry, for pitch angles satisfying $\tan^2(\theta_{\mathrm{p}}) > R/(2r)$, where R and r are the major and the local minor radius of the tokamak, respectively, particles have a too small parallel velocity and are therefore trapped. Here, a the plasma minor radius, defined by $r_{\mathrm{edge}} = a$. Accordingly, the trapped fraction is given by $f_{\mathrm{t}} = \sqrt{2r/R}$, and the passing particle fraction by $(1 - f_{\mathrm{t}})$. For typical values in present day tokamaks at mid–radius, $r/R = 0.17$, and approximately 58% of the particles are trapped.

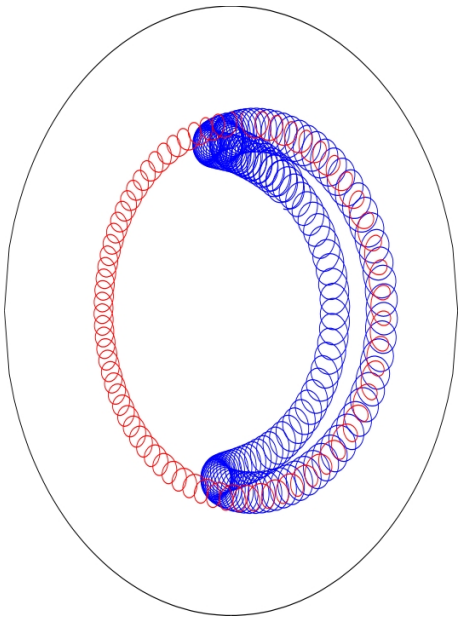

Figure 1.6: Schematic view of charged particle orbits in a tokamak poloidal cross section (Source: http://iter.rma.ac.be).

Apart from the drifts included in the GC trajectory, given by Eq. (1.5), magnetized tokamak plasmas exhibit an additional fluid drift resulting from the interplay between spatial inhomogeneities of temperature and density and the finiteness of the Larmor radius. The former are generally in radial direction since on a flux tube, which is characterized by

the current $\mathbf{j}$ and field lines of $\mathbf{B}$ (and therefore at constant minor radius), the pressure gradient is zero in the MHD approximation. This behavior can be seen from the stationary MHD equation of motion $\nabla p = \mathbf{j} \times \mathbf{B}$, in which flows have been neglected. Due to this interplay, the diamagnetic drift arises and can be illustrated as follows. Suppose the particle distribution to be a Maxwellian to zeroth order, i.e.

$$F_{\mathrm{M}}(\mathbf{x}_0, E) = \frac{n(\mathbf{x}_0)}{(2\pi T(\mathbf{x}_0))^{3/2}} \exp(-E/T(\mathbf{x}_0)), \tag{1.6}$$

where E is the particle energy and n and T depend on the GC position. Then, expansion to first order in Larmor radius leads to

$$F_{\mathrm{L1}} = \left[1 + \rho_{\mathrm{L}}(\mathbf{x}_0) \left(\frac{d \ln\, n(\mathbf{x}_0)}{dr} + \frac{dT}{dr} \frac{\partial}{\partial T(\mathbf{x}_0)} \right) \right] F_{\mathrm{M}}(r, E). \tag{1.7}$$

With this at hand, the average diamagnetic drift is given by

$$\mathbf{v}_{*,\sigma} \simeq \frac{1}{n(\mathbf{x}_0)} \int d^3 v F_{\mathrm{L1}} \mathbf{v} = -\frac{\nabla p(\mathbf{x}_0)}{n(\mathbf{x}_0)} \times \frac{\mathbf{b}}{Z_\sigma e B}, \tag{1.8}$$

where $p(\mathbf{x}_0) = n(\mathbf{x}_0) T(\mathbf{x}_0)$.

At this point it is instructive to summarize the different kind of drifts. They can be all written in the general form

$$\mathbf{v}_{\mathrm{drift}} = \frac{\mathbf{F} \times \mathbf{b}}{Z_\sigma e B}, \tag{1.9}$$

where $\mathbf{F}$ is the corresponding force, for instance the electric force $Z_\sigma e E$, the ∇B force $-m_\sigma \mu_\sigma$ or the pressure gradient force $-\nabla p / n$. The latter two forces do not depend on the charge, and therefore the corresponding drifts are in opposite direction for ions and electrons, while the electric force is charge dependent leading to the charge independent E×B drift. These properties are summarized in Fig. 1.7.

As already discussed, transport in the direction parallel to the magnetic field lines is very efficient and thus the density and temperature are nearly constant on a flux surface. What causes the quality of confinement is the radial transport of particles, (angular) momentum and energy. This can be directly seen from Eq. (1.2). The achievable densities depend on the transport of particles, while the temperature and the energy confinement time are up to the transport of energy. Those parameters are influenced by the transport of (angular) momentum, since this affects the transport of both particles and heat.

Cross–field transport describes the displacement of particles away from their original magnetic field line determining their trajectory. The basic classical transport mechanism is given by Coulomb collisions, causing a radial displacement of the size of the gyration radius ρ_{L}. A random–walk model leads to particle and thermal diffusivities of $D, \chi \sim \rho_{\mathrm{L}}^2 \nu$ with the collision frequency ν of particles of the same species. This leads to an estimate for the energy confinement time of $\tau_{\mathrm{E}} \sim a^2/\chi$, which is of the order of several minutes (a=0.5 m). Such a long energy confinement time is in clear disagreement with the experimental findings of $\tau_{\mathrm{E}} \lesssim 1$ s in present day tokamaks. Even when magnetic field inhomogeneities are taken into account in the neoclassical transport, the confinement is usually overestimated. There, the fact that particle GCs are not longer attached to magnetic field lines, but drift across them, is included. The toroidal geometry and the occurrence of banana orbits leads to larger displacement scales and thus to diffusion coefficients of about one order

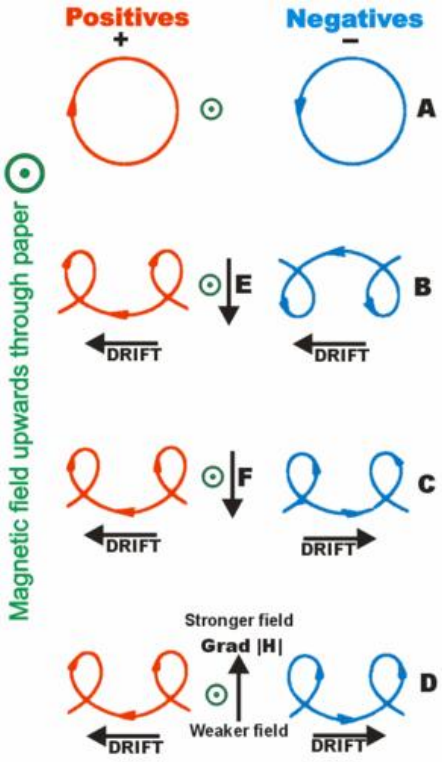

Figure 1.7: Schematic view of drifts of charged particles in a magnetic field (Source: http://www.plasma-universe.com/Charged_particle_drift).

of magnitude higher. While under certain conditions, like transport barriers with a very narrow radial extension, the level of the ion heat transport indeed can be attributed to these mechanisms and is therefore rather low, the transport level over the whole minor radius is undervalued by approximately one order of magnitude for ions and two orders of magnitude for electrons, see for instance [10].

Radial transport has to be ascribed to an 'anomalous', non–neoclassical, nature, as it has been reported for instance in [11] and references therein. Today, it is widely accepted that turbulence produced by small scale instabilities, which have a typical size of the order of the Larmor radius and is therefore called 'microturbulence', is responsible for large particle and thermal transport. These instabilities are fed by large gradients of temperature and density unavoidably connected with the concept of a tokamak (remember that the required central temperature of ∼100 million degrees drops to a few hundred degrees at the plasma edge within approximately one meter of distance). The most relevant and prominent examples for this kind of small scale turbulence are the ion temperature gradient (ITG) mode and the trapped electron mode (TEM), which will be discussed in detail in Chapter 3.

1.3 The plasma beta

The most important parameter characterizing the economical efficiency of a tokamak plasma is the plasma beta, defined as the ratio of kinetic to magnetic pressure,

$$\beta = \frac{8\pi\langle p\rangle}{B_{\mathrm{T}}^2}, \tag{1.10}$$

where $\langle p\rangle$ is the volume average kinetic pressure and B_{T} the toroidal magnetic field. Loosely speaking, this quantity determines the ratio of how much energy one can get out of fusion reactions in a tokamak compared to how much has to be provided for confinement.

A high value of β therefore has beneficial effects, namely the fusion reaction power is proportional to β^2. In terms of long discharge durations the bootstrap fraction, which is proportional to β, has a big influence. This fraction describes the amount of toroidal plasma current responsible for the poloidal magnetic field and generated within the plasma itself compared to the one induced by the transformer. This so–called bootstrap current is associated with the existence of trapped (banana) particles in toroidal magnetic confinement systems. These trapped particles must be able to complete their (banana) orbits, so a requirement for the existence of the bootstrap current is that the collision frequency is less than the banana bounce frequency. The difference in particle density on banana orbits crossing a given radial position then leads to a net toroidal current at this position.

For these reasons it is clear that operational scenarios with preferably high values of β are extremely attractive, but some limitations exist. The main one is related to large scale magnetohydrodynamic (MHD) modes which are very deleterious to the plasma confinement. This implies an upper limit to β. The most prominent limit is the Troyon limit [12], which was calculated from simulations on the onset of MHD ballooning modes, and reads

$$\beta_{\max}[\%] \approx 2.8\frac{I_{\mathrm{p}}[MA]}{a[m]B_{\mathrm{T}}[T]}, \tag{1.11}$$

where I_{p} the plasma current. This implies a β–limit of a few percent. The parameter

$$\beta_{\mathrm{N}} = \frac{\beta}{I_{\mathrm{p}}/(aB_{\mathrm{T}})} \tag{1.12}$$

is regularly used today to quantify a dimensionless form of the plasma pressure reached by operational scenarios.

The basic idea behind ballooning modes, a kind of interchange mode with a mode structure highly elongated along a magnetic field line, is the following: at the inner side of the torus, the curvature of the magnetic field acts stabilizing, while on the outer side it is destabilizing. In case of high pressure gradients, included in the parameter $\alpha_{\mathrm{MHD}} = -(8\pi q^2 R/B^2)\nabla p$ and therefore connected with a finite value of β, modes tend to balloon in the region of destabilizing curvature. The potential destabilizing energy available from the pressure gradient may exceed the energy needed for field line bending, which is higher the stronger the magnetic shear is, such that an unstable mode is driven. This kind of mode is essentially a destabilized Alfvén mode and, as such, of electromagnetic type. From Fig. 1.8 it is seen that at low values of $\alpha = \alpha_{\mathrm{MHD}}$ and high magnetic shear a stable region exists. A second stability region is located at very low magnetic shear.

Even below this β–limit, kinetic ballooning modes (KBMs) can occur with a strong decrease of confinement. They are the analogon to MHD ballooning modes, but calculated

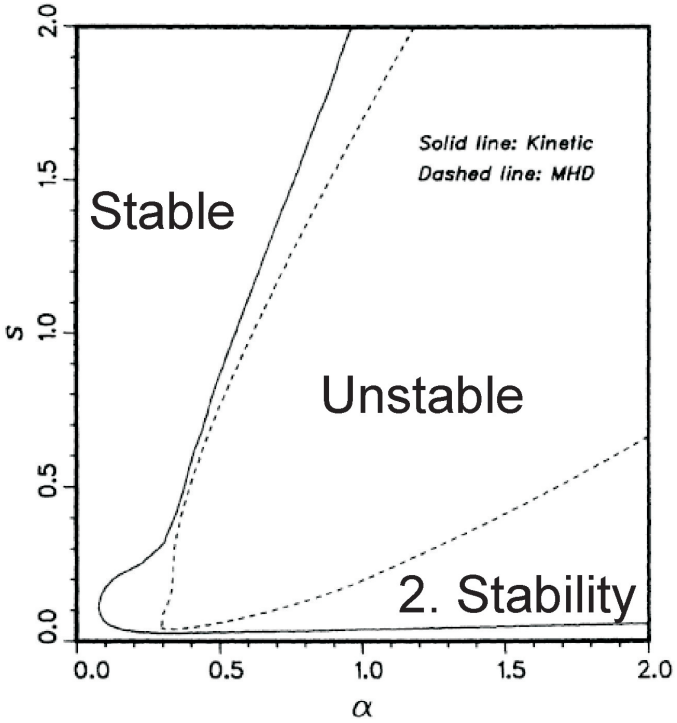

Figure 1.8: Stability diagram for ballooning modes (modified from [13]).

within a kinetic approach, which leads to modifications due to the treatment of finite Larmor radius effects and kinetic resonances [14, 13]. The main outcome of this approach is that KBMs are unstable within the second stability region of MHD ballooning modes as it can be seen in Fig. 1.8 [13]. Moreover, it is found that for magnetic shear values in the range 0.3-1.5, typical for tokamak plasmas at mid–radius, KBMs exhibit a slightly smaller α for the onset as compared to MHD ballooning modes. In a more recent publication [15], it has been found that the unstable behavior of KBMs at high α is connected with parallel magnetic field fluctuations, which increase the linear growth rate, but leave the onset of KBMs approximately constant. Another work dedicated to the problem of kinetic ballooning stability of internal transport barriers (ITBs) in tokamaks showed that in case of small shear $s \ll 1$, where the magnetohydrodynamic ballooning mode is known to be stable, the kinetic ballooning mode is stable only if the pressure gradient exceeds a threshold of α_{MHD} of the order of one [16]. It has to be noted that the effect of E×B shearing was not included in the latter study.

Also changes in magnetic topology due to magnetic reconnection at finite values of β_{e} which may be smaller than the threshold for KBMs, lead to so–called micro–tearing modes (MTMs) with short wavelength and high poloidal wave numbers. They form small scale magnetic islands due to magnetic perturbations. MTMs are driven unstable by a large electron temperature gradient, which exceeds the stabilization due to field line bending forces in a sufficient collisional plasma. They are not to be confused with neoclassical tearing modes (NTMs), which are destabilized and maintained by the loss of the bootstrap–current in (large scale) magnetic islands due to the vanishing pressure gradient therein, and connected with resonant surfaces at low poloidal to toroidal wave number ratio (usually

2/1 and 3/2).

Lastly, also electrostatic modes like ion temperature gradient (ITG) [17] or trapped electron modes (TEM) [18], typical for tokamak operation at low β, are modified due to finite values of β. These two kind of instabilities are driven by temperature and density gradients in the plasma, and will be the subject of Chapter 3.

1.4 Content of thesis

This thesis is structured as follows. In Chapter 2, the electromagnetic gyrokinetic set of equations, which provide the most appropriate model in order to describe microturbulent modes in tokamak plasmas, are introduced and the numerical solution with GYRO [19] is discussed. In Chapter 3, the physics mechanisms generating ITG and TEM instabilities are highlighted. In addition, a simple fluid model originating from conservation laws is derived in order to shed light on the properties of core plasma turbulence and the interplay of these two most common modes for tokamak operation. The impact of electromagnetic effects in conditions of ITG and TEM microinstabilities with respect to various transport channels will be discussed in the following. Chapter 4 includes electromagnetic investigations on the transport of electrons, from both analytical (gyrokinetic) calculations highlighting the main physics mechanism, and numerical simulations. In Chapter 5, the transport of impurities is discussed. To this purpose an analytical electromagnetic fluid model is used in order to interpret the numerical results. Chapter 6 deals with electromagnetic momentum transport. The main emphasis is put on the influence of the self–consistent mode structure. In Chapter 7, the electromagnetic transport of energy is considered and a particular comparison with experimental data is performed. Finally, Chapter 8 draws the main conclusions and gives an outlook.

Chapter 2

Gyrokinetic model and numerical solution with GYRO

In this Chapter, the most general approach for the description of electromagnetic low frequency modes in tokamak plasmas, namely the gyrokinetic Vlasov–Maxwell set of equations, is presented. Furthermore, its solution via the gyrokinetic simulation code GYRO [19, 20], which has been utilized in the framework of the present thesis, is briefly reviewed.

2.1 Gyrokinetic equation

In plasma theory, a kinetic problem can in principle be set up, in which the exact microscopic description is applied. That means to write down Newton's law, $\mathbf{F} = m\mathbf{a}$, for about 10^{20} individual particles and solving for all 10^{20} interacting trajectories. This, however, can not be realized even by the most advanced present day computers. Also, such a system is known to exhibit chaotic behavior, and the exact solution is extremely sensitive to the initial conditions, which are practically unknown from the experimental point of view. Microscopic theory moves to kinetic theory by the application of probabilistic concepts. Since one is not interested in all the microscopic particle data, one considers statistical ensembles of systems. This leads to the introduction of a distribution function, which defines the number of particles per unit volume in phase space. Then, kinetic equations can be found by averaging the microscopic information in the exact theory. While the particle locations are lost, the detailed knowledge of particle motion is required. In this sense, kinetic theory is still microscopic. The aim of this section is the derivation of a kinetic model for microturbulence in the plasma. It turns out that the gyrokinetic model, which is introduced below, is the most practical approach in order to describe low frequency plasma turbulence, which leads to the anomalous transport.

2.1.1 The idea

Microturbulent modes in magnetized plasmas have $\omega \sim 10^5$Hz, which is much slower than the basic plasma oscillation frequency $\omega_{\mathrm{p,e}} = \sqrt{4\pi n_{\mathrm{e}} e^2/m_{\mathrm{e}}}$ of several hundreds of GHz, and also slower than compressional Alfvén oscillations with $\omega = k_\perp v_{\mathrm{A}} \sim 100$ MHz. Moreover, also the gyration frequency of ions and electrons within a tokamak plasma is much higher. In the sense of a statistical description, where the detailed knowledge of the parti-

cle position in the gyro orbit is not needed, these fast timescales are averaged out by the assumption that the particle motion is given by its gyrocenter movement, while the charge, which is interacting with the fields, is distributed on the ring of the gyration. This, in turn, implies a modification of the trajectory due to 'ring'–averaged fields with respect to the guiding center trajectory determined by fixed fields. The averaging procedure implies the suppression of the gyro–angle, leading to a five dimensional (three in configuration space and two in velocity space) instead of a six dimensional treatment. Therefore, gyrokinetic theory is well suited for numerical investigations of microturbulence since the computational costs are significantly lowered as compared to the 'full' kinetic problem, while all the physics of interest is retained.

Gyrokinetic theory was originally developed in the 1960's as an extension to guiding center theory [21] to include finite gyroradius effects, which have to be necessarily kept due to the fact that density fluctuation spectra found peaks in the perpendicular wavenumber spectra at $k_\perp \rho_\mathrm{s} \sim 0.2 - 0.5$ [22, 23], on low frequency, short perpendicular wavelength electrostatic fluctuations in general geometry [24, 25]. In 1978, Catto [26] developed an important approach for the derivation of the gyrokinetic equation by first transforming the particle coordinate to those of the guiding center (GC) in the Vlasov equation (or collisionless Boltzmann equation) before performing the gyrophase averaging. This result then triggered a more consistent development of the linear theory [27, 28] and an early formulation of nonlinear gyrokinetic theory [29]. In the early 1980's, two important advances in GC theory were developed. First, Boozer [30] developed particle drift motion in magnetic coordinates which greatly simplifies the analysis of orbits in complex geometry and second, Littlejohn [31] introduced guiding center theory based on action variational and Lie perturbation methods [32] in order to obtain phase space conserving equations following the Liouville theorem. This was soon followed by an extension of the method to gyrokinetic theory [33]. In the late 80's, Hahm [34], Brizard [35] and co–workers extended the methodology to general magnetic geometries. A comprehensive recent review on the rigorous perturbation approach using action variational principles can be found in [36]. This includes the most general approach for the derivation of the gyrokinetic equation.

2.1.2 The system of equations

The modern derivation of the (collisionless) gyrokinetic equation consists of an initial formulation, which sets up a least action principle in phase space, and then two steps which are ultimately regarded as coordinate transformations. Here, we sketch a derivation following the Goal Oriented Training in Theory (GOTiT) lecture series course about gyrokinetic theory by B. D. Scott at the Max Planck Institut für Plasmaphysik (IPP) in 2008 (see http://www.ipp.mpg.de/˜bds/lectures/gotit).

Firstly, the derivation of the guiding center Lagragian of Littlejohn [37] is outlined. Starting point is the general Lagrangian for a particle of charge e and mass m in an electromagnetic field, with potentials ϕ and $\mathbf{A}$. It reads

$$L = m\frac{|\dot{\mathbf{x}}|^2}{2} + \frac{e}{c}\mathbf{A}\cdot\mathbf{x} - e\phi. \tag{2.1}$$

The canonical momentum $\mathbf{p}$ for the coordinate variable $\mathbf{q} = \mathbf{x}$ is given by

$$\mathbf{p} = \frac{\partial L}{\partial \dot{\mathbf{x}}} = \frac{e}{c}\mathbf{A} + m\dot{\mathbf{x}}. \tag{2.2}$$

Then, the Hamiltonian is given by

$$H = \mathbf{p}\cdot\dot{\mathbf{q}} - L = \frac{1}{2m}|\mathbf{p} - \frac{e}{c}\mathbf{A}|^2 + e\phi \tag{2.3}$$

in the $\{\mathbf{p},\mathbf{q}\}$ representation. The least action principle states that the action γ, which is given by the integral over time along the particle trajectory of the Lagrangian in Eq. (2.1), can be used in order to find the equations of motion through the variation

$$\delta\gamma = \delta\int dtL = 0. \tag{2.4}$$

In order to perform this step, it is useful to convert the Lagragian given by Eq. (2.1) into a phase space Lagrangian over the extended six dimensional space $\{\mathbf{p},\mathbf{q}\}$ by absorbing the factor of dt into L. The resulting differential form, which will be called the differential one–form,

$$d\gamma = \mathbf{p}\cdot\mathbf{dq} - Hdt, \tag{2.5}$$

can be expressed in symplectic representation for the phase space $\{\mathbf{x},\mathbf{v}=\dot{\mathbf{x}}\}$, namely

$$d\gamma = \left(\frac{e}{c}\mathbf{A} + m\mathbf{v}\right)\cdot\mathbf{dx} - Hdt \quad \text{with} \quad H = m\frac{v^2}{2} + e\phi. \tag{2.6}$$

Then, in a non–relativistic treatment, where the time is considered as an independent variable, Eq. (2.6) can be rewritten in terms of covariant coordinates z^a, $d\gamma = \gamma_{\mathrm{a}}dz^{\mathrm{a}} - Hdt$, such that the least action principle leads to Euler–Lagrange equations for $a,b\in\{1,...,6\}$

$$\left(\gamma_{\mathrm{b,a}} - \gamma_{\mathrm{a,b}}\right)\frac{dz^{\mathrm{b}}}{dt} = H_{,\mathrm{a}} + \frac{\partial\gamma_{\mathrm{a}}}{\partial t}, \tag{2.7}$$

where $\gamma_{\mathrm{b,a}} - \gamma_{\mathrm{a,b}}$ is called the symplectic structure with for instance $\gamma_{\mathrm{b,a}} \equiv \partial\gamma_{\mathrm{b}}/\partial z^a$, and includes the summation over repeated indices. This allows for the derivation of the equations of motion, which read

$$\frac{d\mathbf{x}}{dt} = \mathbf{v} \quad \text{and} \quad m\frac{d\mathbf{v}}{dt} = e\left(\mathbf{E} + \frac{1}{c}\mathbf{F}\cdot\mathbf{v}\right), \tag{2.8}$$

where $\mathbf{E} = -\partial\mathbf{A}/(c\partial t) - \nabla\phi$ and $\mathbf{F} = \nabla\mathbf{A} - (\nabla\mathbf{A})^T$. The latter represents the Lorentz force, since

$$\begin{aligned}\left[\nabla\mathbf{A} - (\nabla\mathbf{A})^T\right]\cdot\mathbf{v} &= (\partial_{\mathrm{i}}A_{\mathrm{j}} - \partial_{\mathrm{j}}A_{\mathrm{i}})v_{\mathrm{j}}\\ &= (\delta_{\mathrm{il}}\delta_{\mathrm{jm}} - \delta_{\mathrm{im}}\delta_{\mathrm{jl}})\partial_{\mathrm{l}}A_{\mathrm{m}}v_{\mathrm{j}}\\ &= \epsilon_{\mathrm{ijk}}\epsilon_{\mathrm{klm}}v_{\mathrm{j}}\partial_{\mathrm{l}}A_{\mathrm{m}}\\ &= \mathbf{v}\times\nabla\times\mathbf{A} \equiv \mathbf{v}\times\mathbf{B},\end{aligned} \tag{2.9}$$

where δ denotes the Kronecker delta and ϵ is the total antisymmetric (Levi–Civita) tensor.

Transformation to guiding center coordinates

Now, the change to GC coordinates $\{\mathbf{R}, U, \mu, \theta\}$ is straightforward. Using $\mathbf{x} = \mathbf{R} + \boldsymbol{\rho}$ and $\mathbf{v} = U\mathbf{b} + \dot{\boldsymbol{\rho}}$, where $\boldsymbol{\rho}$ includes the particle gyroradius and $\mathbf{b} = \mathbf{B}/B$, the fundamental one–form, Eq. (2.6), can be evaluated at the GC position $\mathbf{R}$ to order ρ/L_{B} (L_{B} being the magnetic field length scale). With

$$d\gamma = \left(\frac{e}{c}\mathbf{A} + \frac{e}{c}\boldsymbol{\rho}\nabla\mathbf{A} + mU\mathbf{b} + m\frac{\Omega_{\mathrm{c}}}{B}\boldsymbol{\rho}\times\mathbf{B}\right)\cdot(\mathbf{dR} + \mathbf{d}\boldsymbol{\rho}) - \left(m\frac{U^2}{2} + \mu B\right)dt, \quad (2.10)$$

where μ is the magnetic moment and the electrostatic potential ϕ is absent since it does not enter the equilibrium, a gauge transformation $\gamma \to \gamma + dS$ with $S = -(e/c)\boldsymbol{\rho}\cdot\mathbf{A} - (e/(2c))\boldsymbol{\rho}\cdot\nabla\mathbf{A}\cdot\boldsymbol{\rho}$ can be used to eliminate the θ dependence in first and second order in $\boldsymbol{\rho}$ and find the guiding center one form of Littlejohn [37]. The latter reads

$$d\gamma(\mathbf{R}, U, \mu, \theta) = \frac{e}{c}\mathbf{A}^*\cdot\mathbf{dR} + \frac{mc}{e}\mu d\theta - H_0 dt, \quad (2.11)$$

where

$$\begin{aligned}
H_0 &= m\frac{U^2}{2} + \mu B \\
\mathbf{A}^* &= \mathbf{A} + \frac{mc}{e}U\mathbf{b} \\
\mathbf{F}^* &= \nabla\mathbf{A}^* - (\nabla\mathbf{A}^*)^T \\
\mathbf{B}^* &= \nabla\times\mathbf{A}^* \\
B_\parallel^* &= \mathbf{b}\cdot\mathbf{B}^* = B + \frac{mc}{e}U\mathbf{b}\cdot\nabla\times\mathbf{b} \\
\mathbf{b}^* &= \frac{\mathbf{B}^*}{B_\parallel^*}
\end{aligned} \quad (2.12)$$

From the corresponding Euler–Lagrange equations, it can be derived that $\dot{\theta} = \Omega_{\mathrm{c}}$ and $\dot{\mu} = 0$ (adiabatic invariance). Moreover, the GC drift dynamics, as it was introduced in Chapter 1, is retained. Electric and magnetic field disturbances, which arise self consistently with the motion of the charged particles gyrocenters, are accounted for in these perturbed dynamical equations. Again, it is important to note that the background is expected to have no electric field, since any background electric field would lead to strong acceleration of particles, leading to huge charge separations and therefore electric fields on very short timescales. This, however, would violate the basic assumptions of gyrokinetics, namely $\rho/L_{\mathrm{B}} \ll 1$ and $1/(\Omega_{\mathrm{c}}t) \ll 1$, implying only small spatial and temporal fluctuations of the fields ϕ and $\mathbf{A}$. In conclusion, this step separates the fast gyromotion from the much slower GC motion in the background magnetic field, as it can be seen from the one–form, Eq. (2.11). It has to be mentioned that using Eq. (2.11) the drift–kinetic equation can be obtained.

Transformation to gyro–center coordinates

The second step includes a Lie transformation [32] taking the guiding centers to the corresponding gyrocenters including time–dependent field fluctuations, and expresses the field disturbances in terms of gyrophase averaged quantities. It is important to note that Lie

perturbation theory can be used to generate equations of motion that are gyrophase independent to any desired order in a smallness factor ϵ, for instance for spatial expansion $\epsilon_{\rm B} = \rho/L_{\rm B}$. In this formalism, the particle dynamics transforms simply under coordinate change, included in the Lie transformation at each order of the expansion, since a one–form transforms covariantly. The gauge freedom attributed to the one–form formalism leads to the elimination of the gyrophase dependence.

The Lie transform is a near identity transformation, defined by

$$T = \exp\left(\epsilon\mathcal{L}\right) \tag{2.13}$$

with its inverse

$$T^{-1} = \exp\left(-\epsilon\mathcal{L}\right), \tag{2.14}$$

where $\mathcal{L}$ is the Lie derivative of order n (not to be confused with the Lagrangian), defined by its influence on a scalar $\mathcal{L}_{\rm n} f = g^a_{\rm n}\partial f/\partial z^{\rm a} = g^a_{\rm n} f_{,{\rm a}}$ and on a one–form $\mathcal{L}_{\rm n}\gamma = g^{\rm b}_{\rm n}(\gamma_{{\rm a},{\rm b}} - \gamma_{{\rm b},{\rm a}})dz^{\rm a}$. It is crucial to note that the actual choice of the generating functions g^a is completely arbitrary. This means that one is free to chose a convenient member of the family of Lie transformations in order to maximize the simplicity of the gyrokinetic equation. While this attribute is extremely helpful, the actual choice affects, however, the derivation of the polarization equations for ϕ and $\mathbf{A}$, since for these the back transformation, Eq. (2.14) has to be applied. This can lead to an increase of complexity in the derivation of the field equations.

The Lie transform action on a scalar is defined by $F = T^{-1}f$ and on a one–form by $\Gamma = T^{-1}\gamma + dS$ (gauge freedom through adding dS), and it is manifestly covariant, such that $\Gamma = \Gamma_{\rm a} dZ^{\rm a}$ and $\gamma = \gamma_{\rm a} dz^{\rm a}$. Furthermore, it is important to note that coordinates and distribution functions are transformed together in a consistent way. Then, at each order of the transformation, gauge freedom in addition to the Lie derivative leads to

$$\begin{aligned} d\Gamma_0 &= d\gamma_0 + dS_0 \\ d\Gamma_1 &= d\gamma_1 - \mathcal{L}_1 d\gamma_0 + dS_1 \\ d\Gamma_2 &= d\gamma_2 - \mathcal{L}_1 d\gamma_1 + \left(\frac{1}{2}\mathcal{L}_1^2 - \mathcal{L}_2\right) d\gamma_0 + dS_2. \end{aligned} \tag{2.15}$$

By adjusting the gauge functions dS_0, dS_1 and dS_2 appropriately, the one forms $d\Gamma_0$, $d\Gamma_1$ and $d\Gamma_2$ will be independent of the gyro–angle. The freedom of choosing the generating functions g^a in the Lie derivatives is used to move the field dependences, which themselves depend on time, to the Hamiltonian H, where already time dependences occur. Thus, all time dependences will be stored in H at each order of the expansion. The lengthy calculations are given in the mentioned lecture notes. Here, only the important results are outlined.

Using appropriate gauge and generating functions up to first order in the expansion, see Eq. (2.15), the perturbed one–form Γ_1 has the desired result

$$d\Gamma_1 = -e\langle\phi - \frac{U}{c}A_\parallel\rangle dt. \tag{2.16}$$

The brackets $\langle ...\rangle$ denote the gyro–averaging over θ. This implies a dynamical equation for S_1, which results in the fact that the gauge function S_1 is simply a gyroaverage, defined by

$$S_1 = \frac{1}{\Omega_{\rm c}}\int d\theta e\tilde{\psi}, \tag{2.17}$$

where $\tilde{\psi} = \psi - \langle\psi\rangle$ and $\psi = \phi - (\mathbf{U}/c)\cdot\mathbf{A}$ is the generalized potential. Then, to this order in the expansion, one gets

$$d\Gamma_{(0+1)} = \frac{e}{c}\mathbf{A}^*\cdot\mathbf{dR} + \frac{mc}{e}\mu d\theta - H_{(0+1)}dt, \tag{2.18}$$

where

$$H_{(0+1)} = m\frac{U^2}{2} + \mu B + e\langle\psi\rangle, \tag{2.19}$$

where quantities with index $(0+1)$ contain both zeroth and first order contributions. In particular,

$$\begin{aligned} H_0 &= m\frac{U^2}{2} + \mu B \\ H_1 &= e\langle\psi\rangle. \end{aligned} \tag{2.20}$$

All the changes compared to the guiding center one form, Eq. (2.11) are included in $H_{(0+1)}$. This, in turn, implies that the Euler–Lagrange equations remain the same as for the GC motion, such that

$$\dot{\mathbf{R}} = \mathbf{b}^*\left(\frac{1}{m}\frac{\partial H}{\partial U}\right) - \frac{c}{eBB^*_\parallel}\mathbf{F}\cdot\nabla H_{(0+1)} \tag{2.21}$$

and

$$\dot{U} = -\frac{1}{m}\mathbf{b}^*\cdot\nabla H_{(0+1)}. \tag{2.22}$$

Also the results for gyromotion, namely $\dot{\theta} = \Omega_c$ and the adiabatic invariance of the magnetic moment, $\dot{\mu} = 0$, are recovered.

These are the equations of motion for individual gyrocenters. For the distribution function f, Eqn. (2.21) and (2.22) can be used in order to re–express phase space conservation of the distribution,

$$\frac{df}{dt} = \frac{\partial f}{\partial t} + \dot{\mathbf{R}}\cdot\nabla f + \dot{U}\frac{df}{dU} = 0 \tag{2.23}$$

in the form

$$\frac{\partial f}{\partial t} - \frac{c}{eBB^*_\parallel}\mathbf{F}\cdot\nabla H_{(0+1)}\nabla f - \left[\left(\mathbf{b}^*\cdot\nabla H_{(0+1)}\right)\left(\frac{1}{m}\frac{df}{dU}\right)\left(\frac{1}{m}\frac{dH_{(0+1)}}{dU}\right)\left(\mathbf{b}^*\cdot\nabla f\right)\right] = 0. \tag{2.24}$$

The form of this Eq. (2.24) is interesting. Due to the antisymmetry of $\mathbf{F}$ and of the combination of the last set of terms, each combination of pairs of derivatives appears in the form of a Poisson bracket, such that the gyrokinetic Eq. (2.24) can be written in the simple form

$$\frac{\partial f}{\partial t} + \left\{H_{(0+1)}, f\right\} = 0 \tag{2.25}$$

with

$$\left\{H_{(0+1)}, f\right\} = \nabla H_{(0+1)}\cdot\frac{c\mathbf{F}}{cBB^*_\parallel}\cdot\nabla f + \mathbf{b}^*\cdot\left(\frac{\partial H_{(0+1)}}{\partial p_\parallel}\nabla f - \frac{\partial f}{\partial p_\parallel}\nabla H_{(0+1)}\right), \tag{2.26}$$

where $p_\parallel = mU$ is used. This shows that the Hamiltonian structure for the gyrocenter motion is preserved. The form of the Poisson bracket is more complicated than the usual

one in Hamiltonian theory by involving $\mathbf{F}$ under the low frequency drift ordering. Moreover, since $H_{(0+1)}$ itself depends on f through the fields ϕ and $A_\parallel$, the gyrokinetic Eq. (2.25) is nonlinear. The phase space volume element is given by $B_\parallel^*$.

The usual particle drifts defined in Chapter 1 appear in the gyrokinetic equation under different terms. The E×B and ∇B drifts enter through the $-c\mathbf{F}\cdot\nabla H/(eBB_\parallel^*)$. The curvature drift involving $\nabla\times\mathbf{b}$ enters through the correction to the magnetic unit vector, $\mathbf{b}^*-\mathbf{b}$. Motion parallel to the unperturbed magnetic field is included in the terms involving $\mathbf{b}^*\cdot\nabla$ and $\partial/\partial U$, in particular the magnetic trapping arises from $\mathbf{b}^*\cdot\nabla H$, while the motion parallel to the perturbed magnetic field lines enters through the part of $-c\mathbf{F}\cdot\nabla H/(eBB_\parallel^*)$ due to $A_\parallel$.

While the form of the gyrokinetic Eq. (2.25) with Eq. (2.26) is already the final one, the restriction to the zeroth and first order in the Lie transformation has the disadvantage of not providing a closed energy theorem (energy conservation) and no quasineutrality, which is given by the role of polarization not introduced yet. Thus, it is necessary to go to the second order of the Lie transform formalism. It has to be mentioned that the choices made at first order have consequences at second order. Especially the choice of S_1, which was arbitrary up to first order, will enter the generalized potential to second order.

Polarization, induction and conservation properties

Here, the most general and elegant way in order to derive the gyrokinetic polarization, induction and energy conservation is briefly outlined. This is done by using gyrokinetic field theory [38], where the Lagrangian for a single particle p is given in the GC coordinates

$$L_\mathrm{p}=\left(\frac{e}{c}\mathbf{A}+p_\parallel\mathbf{b}\right)\cdot\dot{\mathbf{R}}+\frac{mc}{e}\mu\dot{\theta}-H \tag{2.27}$$

with

$$H=m\frac{U^2}{2}+\mu B+e\Phi\quad\text{and}\quad mU=p_\parallel-\frac{e}{c}J_0A_\parallel \tag{2.28}$$

using $J_0=J_0(k_\perp\rho)$ from the gyro–averaging, where the gyro–average operation $\langle Q(\mathbf{R})\rangle=J_0(Q(\mathbf{x}))$ is defined by

$$\frac{1}{2\pi}\int d\theta\exp\left[\boldsymbol{\rho}\cdot\nabla\right]=\frac{1}{2\pi}\int d\theta\exp\left[ik_\perp\rho\cos\theta\right]=J_0\left(k_\perp\rho\right). \tag{2.29}$$

With this notation, the gyroaveraged and screened electrostatic potential is given by

$$e\Phi=eJ_0\phi-\frac{e^2}{2B}\frac{\partial}{\partial\mu}\left[J_0(\phi^2)-(J_0\phi)^2\right]. \tag{2.30}$$

In the total Lagrangian, the magnetic field energy is also included,

$$L=\sum_\sigma\int d^3vL_\mathrm{p}f-\int dV\frac{B_\perp^2}{8\pi}, \tag{2.31}$$

where $\sum_\sigma$ denotes the summation over all particles and the velocity space integral is given by

$$\int d^3v=2\pi m^{-2}\int dp_\parallel\int B_\parallel^*d\mu. \tag{2.32}$$

Then, according to the least action principle, the variation of Eq. (2.31) with respect to ϕ gives the gyrokinetic polarization equation (Poisson law), which reads

$$\sum_\sigma \int d^3v \left[eJ_0 f + (J_0 \mathcal{M} J_0 - J_0 \mathcal{M}\phi)\right] = 0, \tag{2.33}$$

where $\mathcal{M} = -(e^2/B)(\partial f/\partial\mu)$ is the polarisability. For the induction (Ampère's law) one varies with respect to $A_\parallel$, finding

$$\nabla_\perp^2 A_\parallel = -\frac{4\pi}{c} \sum_\sigma \int d^3v e J_0 (Uf). \tag{2.34}$$

Here, it is important to note that the right hand side of this equation contains $A_\parallel$ as well due to $mU = p_\parallel - (e/c)J_0 A_\parallel$.

With this at hand, it is also easy to derive the electromagnetic energy conservation. The Noether theorem states that energy is preserved for the system having a symmetry in time, that is a transformation $t \to t + \delta t$ does not change the equations of motion and the field equations. The energy conservation is proven by using

$$\mathcal{E} = \sum_\sigma \int d\Lambda H f - \int dV \frac{B_\perp^2}{8\pi}, \tag{2.35}$$

where Λ is the full phase space volume. With (derivation details see reference to the GOTiT course given above)

$$\frac{\partial \mathcal{E}}{\partial t} = \sum_\sigma \int d\Lambda H \frac{\partial f}{\partial t} = -\sum_\sigma \int d\Lambda H \{H, f\} = -\sum_\sigma \int d\Lambda \frac{1}{2} \{H^2, f\} = 0, \tag{2.36}$$

it is clear that energy is conserved. The result of Eq. (2.36) was obtained using $\int d\Lambda \{H, f\} = 0$ and $\{H, g(f)\} = \{H, f\}\, \partial g/\partial f$.

With these relations and keeping Eq. (2.25) in mind, the particle and entropy conservations are easy to prove. The former is simply given by setting $g(f) = f$ and the latter by $g(f) = -Tf \log f$ such that $\partial g/\partial f = -T(1 + \log f)$. It is important to note that, while the proof of the latter two works for each species separately, the conservation of energy is applicable across species and requires the fields as well. This usually leads to the definition of free (thermal) energy $\mathcal{E}_\mathrm{F} = \sum_\sigma d\Lambda H_0 f$, where $H_0 = mU^2/2 + \mu B$, E×B energy $\mathcal{E}_{\mathrm{E}\times\mathrm{B}} = \sum_\sigma d\Lambda e\Phi f$ and magnetic energy $\mathcal{E}_\mathrm{M} = \sum_\sigma dV B_\perp^2/(8\pi)$. The transfer of energy between these three channels is an important measure for the turbulence properties.

In conclusion, the appropriate use of the Lie transform technique (and the gauge freedom) up to the second order enables the derivation of the gyrokinetic equation together with the polarization (Poisson) and induction (Ampère) equation, and a consistent conservation of particles, entropy and energy. Thus, it is convenient to stop at this order of the expansion, also because the consistency with the lower order pieces is guaranteed.

2.1.3 Linearization

The fully nonlinear gyrokinetic Eq. (2.25) is transformed to the linear case, being helpful for analytical calculations. To this purpose, the total distribution function f is split into an

equilibrium part F_{M}, which is assumed to be a Maxwellian independent of time, and a time dependent perturbed part δf, where the δ is a formal parameter in order to characterize the disturbance as small. It can be easily shown that the linearized equation follows

$$\frac{\partial \delta f}{\partial t} + \{\delta f, H_0\} = -\{F_{\mathrm{M}}, H_1\}, \tag{2.37}$$

where the definition of the zeroth and first order Hamiltonian, Eq. (2.20), was used. It is noteworthy that the zeroth order implies F_{M} to be time independent, such that the latter indeed describes a proper equilibrium. It is also instructive to write this equation also in a different set of coordinates, namely $\mathbf{X} = (\mathbf{R}, H_0 = \epsilon, \mu, \theta)$ with $\epsilon = E/T_{\mathrm{e}}$. Then, the usual evolution equation for the non–adiabatic part of δf,

$$h = \delta f - \frac{H_1}{T}\frac{\partial F_{\mathrm{M}}}{\partial \epsilon}, \tag{2.38}$$

is derived. It reads

$$\frac{\partial h}{\partial t} + (v_{\parallel}\mathbf{b} + \mathbf{v}_{\mathrm{d}})\nabla h = \left[\frac{c\mathbf{b}}{eB} \times \nabla F_{\mathrm{M}} \cdot \nabla - \frac{\partial F_{\mathrm{M}}}{\partial \epsilon}\frac{\partial}{\partial t}\right] H_1, \tag{2.39}$$

where the linearized drift velocity

$$\mathbf{v}_{\mathrm{d}} = -\frac{c\mathbf{b}}{eB} \times \left(m v_{\parallel}^2 (\mathbf{b} \cdot \nabla)\mathbf{b} + \mu \nabla B\right) \tag{2.40}$$

comprising both the curvature and the ∇B drifts, is introduced. Consistent conservation laws for the linearized system can be still derived.

The physical interpretation of Eq. (2.39) is the following. It describes the linear evolution of the nonadiabatic component of the distribution of 'rings', which represent the gyrating particles. This evolution is subject to physics processes, namely the 'rings' experience streaming in the parallel direction ($v_{\parallel}\mathbf{b}$) and drifts perpendicular to the (equilibrium) magnetic field ($\mathbf{v}_{\mathrm{d}}$), represented by the left hand side of the equation. Note again that here no background electric field is assumed to be present, and the fluctuating E×B drift is left out due to the linearization. The right hand side introduces the effect of collisionless work done on the 'rings' by gyro–averaged (fluctuating) electromagnetic fields in H_1, and can be seen as the wave–'ring' interaction.

2.2 Numerical solution with GYRO

Before the numerical solution of the nonlinear gyrokinetic set of equations, Eqn. (2.25), (2.33) and (2.34), is discussed, it is instructive to introduce a few basic concepts helping to understand the definitions made in GYRO [20, 19], which is the simulation code used throughout this thesis. The discussion is close to that in [39].

In order to fulfill the boundary conditions, a plasma perturbation in a torus must be a superposition of elementary perturbations of the form

$$f(r, \theta, \phi) = \bar{f}(r) \exp\left[i(m\theta - n\phi)\right], \tag{2.41}$$

where θ is the poloidal and ϕ the toroidal angle. The phase angle can be written as $m\theta - n\phi = k_\theta r\theta + k_\phi R\phi$ with $k_\theta = m/r$ and $k_\phi = -n/R$. The magnetic field is written as $\mathbf{B} = B_\theta \mathbf{e}_\theta + B_\phi \mathbf{e}_\phi$. Introducing the safety factor as

$$q(r) = \frac{\Delta\phi}{\Delta\theta} = \frac{B_\phi r}{B_\theta R}, \tag{2.42}$$

where $\Delta\phi$ and $\Delta\theta$ represent changes in ϕ and θ an the translation along a field line, respectively, the parallel wavenumber is given by

$$k_\parallel = \frac{\mathbf{k}\cdot\mathbf{B}}{B} = \frac{[m - nq(r)]}{Rq}, \tag{2.43}$$

where $B_\theta \ll B_\phi$ such that $B \approx B_\phi$ has been assumed. Since modes are generally most unstable around rational surfaces (at which $q(r) = m/n$ is a rational number), and $q(r)$ usually is a monotonically growing function of r, instabilities tend to be localized and exhibit a small $k_\parallel$. Taylor expansion around a rational surface at r_0 gives

$$k_\parallel = -\frac{n}{qR}\frac{dq}{dr}(r - r_0) = -n\frac{s}{rR}(r - r_0) \tag{2.44}$$

with the magnetic shear

$$s \equiv \frac{r}{q}\frac{dq}{dr}. \tag{2.45}$$

For a tokamak core, typically, s is small at the magnetic axis and otherwise of order 1. It can, however, become large at the edge, but this region is not considered in the framework of the present thesis. Another quantity of interest is the distance between neighboring rational surfaces since it can be used to define a radial length. If $q(r_0) = m/n$ and $q(r_0 + \Delta r) = (m+1)/n$, then

$$\Delta r = \left(n\frac{dq}{dr}\right)^{-1}. \tag{2.46}$$

2.2.1 Flux surface geometry

The explanation of the flux surface geometry and the code discretization used by GYRO follows the users manual (https://fusion.gat.com/theory/Gyrodoc). A more detailed and comprehensive description explanation of the gyrokinetic simulation code can be found there. Here, only the essential points are briefly discussed. In order to solve the gyrokinetic set of equations, Eqn. (2.25),(2.33) and (2.34), it is useful to introduce a right–handed, field–aligned coordinate system (ψ, θ, α) together with the Clebsch representation [40] for the magnetic field

$$\mathbf{B} = \nabla\alpha \times \nabla\psi \quad \text{such that} \quad \mathbf{B}\cdot\nabla\alpha = \mathbf{B}\cdot\nabla\psi = 0. \tag{2.47}$$

The angle α is written in terms of the toroidal angle ϕ as

$$\alpha \equiv \phi + \nu(\psi, \theta), \tag{2.48}$$

where ψ is the poloidal flux divided by 2π representing the radial coordinate, and θ is the poloidal angle. The Jacobian is given by

$$\mathcal{J}_\psi = \frac{1}{\nabla\psi \times \nabla\theta \cdot \nabla\alpha} = \frac{1}{\nabla\psi \times \nabla\theta \cdot \nabla\phi}. \tag{2.49}$$

Then, the magnetic field is written in those coordinates as

$$\mathbf{B} = \nabla\phi \times \nabla\psi + \frac{\partial\nu}{\partial\theta}\nabla\theta \times \nabla\psi. \tag{2.50}$$

The safety factor is written as a function of the poloidal flux,

$$q(\psi) \equiv \frac{1}{2\pi}\int_0^{2\pi} \frac{\mathbf{B}\cdot\nabla\phi}{\mathbf{B}\cdot\nabla\theta} d\theta = -\frac{1}{2\pi}\int_0^{2\pi}\left(-\frac{\partial\nu}{\partial\theta}\right) d\theta. \tag{2.51}$$

The toroidal flux is defined by

$$\Psi_\mathrm{t} \equiv \int\int_{\mathrm{S_t}} \mathbf{B}\cdot d\mathbf{S} = \frac{1}{2\pi}\int\int\int_{\mathrm{V_t}} \mathbf{B}\cdot\nabla\phi dV, \tag{2.52}$$

and the poloidal flux is written as

$$\Psi_\mathrm{p} \equiv \int\int_{\mathrm{S_p}} \mathbf{B}\cdot d\mathbf{S} = \frac{1}{2\pi}\int\int\int_{\mathrm{V_p}} \mathbf{B}\cdot\nabla\theta dV. \tag{2.53}$$

Using these two definitions, $q = d\Psi_\mathrm{t}/d\Psi_\mathrm{p}$. The effective minor radius r is defined as the half width of the flux surface elevation, the effective major radius R as the average of the major radius at the inner and outer side of the flux surface, and the effective magnetic field strength, B_unit, as

$$B_\mathrm{unit} \equiv \frac{1}{2\pi r}\frac{d\Psi_\mathrm{t}}{dr}. \tag{2.54}$$

The Miller flux surface model shape [41] in (R, Z) coordinates, where Z is the centroid elevation, is generalized and given by

$$\begin{aligned} R(r,\theta) &= R(r) + r\cos(\theta + \arcsin\delta\sin\theta), \\ Z(r,\theta) &= Z(r) + \kappa(r) r\sin(\theta + \zeta\sin 2\theta), \end{aligned} \tag{2.55}$$

where κ is the elongation, δ the triangularity and ζ is the squareness. In order to calculate the shape functions for the flux surface at r according to this model, ten parameters are required, namely

$$\left\{R, \frac{dR}{dr}, Z, \frac{dZ}{dr}, \kappa, s_\kappa, \delta, s_\delta, \zeta, s_\zeta\right\}. \tag{2.56}$$

However, within this thesis the squareness has been set to be zero. Thus, only eight parameters are required to model the flux surface shape. The required radial derivatives of elongation and triangularity are given by $s_\kappa \equiv (r/\kappa)(\partial\kappa/\partial r)$ and $s_\delta \equiv r(\partial\delta/\partial r)$.

As an example, the large aspect ratio limit of the general geometry is given. Considering a shifted circular (Shafranov) flux–surface shape,

$$\begin{aligned} R(r,\theta) &= R + \Delta(r) + r\cos\theta \\ Z(r,\theta) &= r\sin\theta, \end{aligned} \tag{2.57}$$

with the Shafranov shift $\Delta(r) = wr^2/(2R)$ with w being a constant, the shape functions are given in a Taylor series in the small parameter r/R to first order by

$$\begin{aligned}
|\nabla r| &\sim 1 - w\frac{r}{R}\cos\theta, \\
\frac{B_{\rm t}(r,\theta)}{B_{\rm unit}(r)} &\sim 1 - \frac{r}{R}\cos\theta, \\
\frac{B_{\rm p}(r,\theta)}{B_{\rm unit}(r)} &\sim \frac{r}{qR}\left[1 - (w+1)\frac{r}{R}\cos\theta\right], \\
\frac{B(r,\theta)}{B_{\rm unit}(r)} &\sim 1 - \frac{r}{R}\cos\theta, \\
gsin(r,\theta) &\sim \sin\theta\left[1 - \frac{r}{R}\cos\theta\right], \\
gcos_1(\theta) &\sim \cos\theta - \frac{r}{R}\left[\cos^2\theta - \frac{1}{q^2}\right], \\
\Theta(r,\theta) &\sim s\theta - q^2 R\beta^*\sin\theta + \Theta_1\frac{r}{R}, \\
G_{\rm q}(r,\theta) &\sim 1 + (w-1)\frac{r}{R}\cos\theta, \\
G_\theta(r,\theta) &\sim 1 + w\frac{r}{R}\cos\theta
\end{aligned} \tag{2.58}$$

Here, Θ_1 is the function

$$\Theta_1 = (1-2w)s\theta\sin\theta + \sin\theta\left[(3w-1)s - 2(1+w) + \frac{1}{2}(w-3)q^2R\beta^*\cos\theta\right]. \tag{2.59}$$

The first four relations in Eq. (2.58) characterize the flux surface shape directly while the last five relations enter the perpendicular drifts and the flux surface average, for instance

$$\mathbf{v}_{\rm d}\cdot\nabla_\perp = -k_\theta G_{\rm q}\left(\frac{v_\parallel^2 + \mu B}{\Omega_{{\rm c},\sigma}R}\right)(gcos_1 + \Theta gsin)\,. \tag{2.60}$$

Here, $k_\theta = i(q/r)\frac{\partial}{\partial\alpha}$ has been introduced. From the shape functions it is instructive to introduce the popular $s-\alpha$ equilibrium model [42]. This means to take the limit $r/R \to 0$ in all the expressions above, and $B/B_{\rm unit} = 1$. Then the pressure parameter β^* is included in

$$\alpha_{\rm MHD} \equiv q^2R\beta^* = -q^2R\frac{8\pi}{B_{\rm unit}^2}\frac{dp}{dr} > 0. \tag{2.61}$$

In this equilibrium, which is clearly not an exact Grad–Shafranov equilibrium, the perpendicular ∇B and curvature drifts are combined in the drift frequency

$$\omega_{\rm d,k} = \omega_{\rm D,k}\left[\left(v_\parallel^2 + v_\perp^2/2\right)/v_{{\rm th},\sigma}^2\right]\left[\cos\theta + (s\theta - \alpha_{\rm MHD}\sin\theta)\sin\theta\right], \tag{2.62}$$

where $\omega_{\rm D,k} = k_{\rm y}\rho_{\rm s}c_{\rm s}/R$. It has to be noted that the subscript 'MHD' is often left out. Then, α has not to be confused with the angle α in the Clebsch representation of the magnetic field.

2.2.2 Code discretization

The spatial discretization of the gyrokinetic set of equations is done by a spectral decomposition in toroidal direction. The fluctuating quantities $(\hat{\phi}, \hat{A}_{||}, h_\sigma)$ are expanded as a Fourier series in the coordinate α. For example, the electrostatic potential is written as

$$\hat{\phi}(r,\theta,\alpha) = \sum_{\mathrm{j}=-\mathrm{N_n}+1}^{N_\mathrm{n}-1} \phi_\mathrm{n}(r,\theta)\exp\left[-in\alpha\right] \quad \text{such that} \quad n = j\Delta n, \tag{2.63}$$

with N_n being the parameter `TOROIDAL_GRID` and $\Delta n \rightarrow$ `TOROIDAL_SEP`. The r– and θ–dependence of ϕ_n reflects the coupling of poloidal harmonics due to the θ–dependence of curvature and ∇B drift. The θ–periodicity condition requires that

$$\hat{\phi}(r,0,\phi+\nu(\psi,0)) = \hat{\phi}(r,2\pi,\phi+\nu(\psi,2\pi)). \tag{2.64}$$

Thus, although the physical field, $\hat{\phi}$, is 2π–periodic in θ, the Fourier representation has the implication that the coefficients, ϕ_n, are nonperiodic, and satisfy the phase condition

$$\phi_\mathrm{n}(r,0) = \exp(2\pi i n q(r))\phi_\mathrm{n}(r,2\pi). \tag{2.65}$$

Then, the spectral form defined in Eq. (2.63) is $(2\pi/\Delta n)$–periodic in both α and ϕ at fixed (r,θ). The poloidal wavenumber is defined as a proper flux–surface function by $k_\theta = nq(r)/r$. As it will be shown below, it is also interesting to consider a periodic toroidal representation in the Fourier space. It is emphasized that GYRO does not make use of this.

The gyrokinetic operators are discretized via finite–difference methods for the derivatives. Gyro–orbit integral operators are derived using banded pseudo–spectral methods. The parallel motion is discretized on an orbit–time grid. The reason for this approach is the fact that the gyrokinetic Eq. (2.25) is subject to short–wavelength instabilities in regions where the variation of $v_{\|,\sigma}(\theta)$ is sufficiently strong. This well– known property leads to the requirement that time–explicit schemes must normally include dissipative smoothing in case of a solution to be found on an equally–spaced θ–grid. Moreover, at bounce points θ_b, where $v_\|(\theta_\mathrm{b}) = 0$, the distribution function might develop cusps, such that the accuracy of finite difference schemes on such a grid is questionable. In order to overcome those, GYRO introduces a normalized orbit time grid with

$$\begin{aligned}
\tau_0(\lambda,\theta) &\equiv \int_{-\theta_\mathrm{b}}^{\theta} \frac{G_\theta(\theta)d\theta'}{\sqrt{1-\lambda\hat{B}(\theta')}} \quad \text{if} \quad \lambda \le \frac{1}{\hat{B}(\pi)} \ \text{ trapped} \\
\tau_0(\lambda,\theta) &\equiv \int_{-\pi}^{\theta} \frac{G_\theta(\theta)d\theta'}{\sqrt{1-\lambda\hat{B}(\theta')}} \quad \text{if} \quad \lambda > \frac{1}{\hat{B}(\pi)} \ \text{ passing},
\end{aligned} \tag{2.66}$$

where $\hat{B} \equiv B(r,\theta)/B_\mathrm{unit}(r)$ and $\lambda = v_\perp^2/(v^2\hat{B})$ is the pitch angle parameter. Then, a normalized orbit time τ, which runs from 0 to 2 for a given λ and covers both signs of parallel velocity, is introduced by

$$\begin{aligned}
\tau(\lambda,\theta) &\equiv \tau_0(\lambda,\theta)/\hat{\tau} \quad \text{for} \quad 0 \le \tau \le 1 (\varsigma = 1) \\
\tau(\lambda,\theta) &\equiv 2 - \tau_0(\lambda,\theta)/\hat{\tau} \quad \text{for} \quad 1 < \tau \le 2 (\varsigma = -1),
\end{aligned} \tag{2.67}$$

where $\hat{\tau} = \tau_0(\lambda, \theta_\mathrm{b})$ for trapped particles, and $\hat{\tau} = \tau_0(\lambda, \pi)$ for passing particles. The important result of this is that the trapped distribution will be not only continuous, but also smooth across bounce points as a function of τ. The physical interpretation of the location of orbit time grid–points is that they are equally spaced in time, not space, along an orbit. In GYRO, the default settings are 20 points for passing and trapped particles each. The Poisson–bracket nonlinearities are decomposed with a spectral method, and the discrete forms of the derivatives are used. The fields are expanded using blending functions since the distribution function $h_{\mathrm{n},\sigma}$ is computed at different θ–points for each discrete value of λ such that there is no natural way to solve the Maxwell equations using finite–difference methods on a fixed grid. The expansion coefficients are then obtained using the Galerkin method.

The velocity space discretization is performed on a energy–pitch angle grid with $\epsilon = E/T_\sigma$. This is obtained by introducing a finite number of energy and pitch–angle gridpoints. The GYRO default settings are 8 energy points and 4 pitch angle points for both passing and trapped particles. The energy integration is done introducing

$$x(\epsilon) \equiv \frac{2}{\sqrt{\pi}} \int_0^{\epsilon_\mathrm{max}} d\epsilon \exp\left[-\epsilon\right] \sqrt{\epsilon}, \tag{2.68}$$

where ϵ_max denotes the highest point in the energy grid (default 5). For numerical purposes (Gauss–Legendre integration), this integral is split into two parts, which are summed in the end. The pitch angle integration is performed using

$$x(\lambda) \equiv \frac{1}{\mathcal{J}_\mathrm{r}} \int_0^{\lambda} d\lambda' \hat{\tau}(\lambda'), \tag{2.69}$$

where $\mathcal{J}_\mathrm{r}$ is defined through Eq. (2.49) by $\mathcal{J}_\mathrm{r} = (\partial\psi/\partial r)\mathcal{J}_\psi$. The temporal discretization is done using implicit–explicit (IMEX) Runge–Kutta schemes. This is required since the gyrokinetic treatment of electrons is particularly problematic because of the emergence of numerical instabilities connected with the discretization of the electron parallel motion. In the general form of the nonlinear gyrokinetic equation, the fluctuation electrostatic potential is present in the advection term,

$$\frac{\partial h}{\partial t} + \frac{v_\parallel(\theta)}{qR} \frac{\partial}{\partial \theta}(h - \hat{\phi}) + ... = 0. \tag{2.70}$$

Physically, the parallel term leads to (pathological) high–frequency electrostatic Alfvèn waves. At $\beta_\mathrm{e} = 0$, one gets

$$\omega_\mathrm{H} = \frac{k_\parallel}{k_\mathrm{r}} \sqrt{\frac{m_\mathrm{i}}{m_\mathrm{e}}} \Omega_\mathrm{c,i}. \tag{2.71}$$

The frequency of this mode increases indefinitely as m_e decreases or k_r decreases, which means a larger radial box size. The IMEX Runge–Kutta schemes are written for equations in the canonical form

$$\dot{y} = \tilde{Y}(y) + Y(y), \tag{2.72}$$

with $\tilde{Y}$ the explicit right hand side and Y the implicit right hand side. The connection is given by

$$y = [h_\mathrm{i}, h_\mathrm{e}]^T \quad , \quad \tilde{Y} = \left[\tilde{f}_\sigma, \tilde{f}_\mathrm{e}\right]^T \quad , \quad Y = [0, f_\mathrm{e}]^T, \tag{2.73}$$

such that only the electron motion is treated partly in an implicit way. This includes the advantage of removing the constraint of explicit schemes to resolve the fastest dynamics in the system.

The boundary conditions in GYRO can be defined in two ways. The treatment on $(\phi_{\rm n}, A_{\parallel,{\rm n}}, h_{{\rm n},\sigma})$ is either periodic (usually called flux–tube, or local) or nonperiodic (global). Introducing

$$r_{\rm i} = r - \frac{L}{2} + \Delta r(i-1) \quad \text{for} \quad i = 1, ..., n_{\rm r}, \tag{2.74}$$

where $\Delta r \equiv L/n_{\rm r}$ for periodic and $\Delta r \equiv L/(n_{\rm r}-1)$ for nonperiodic boundary conditions. The central radius is denoted by r, while $n_{\rm r}$ defines the radial box size. Together with the box size in the θ direction, defined by $k_\theta = nq(r)/r$, it is clear that the simulation domain is a rectangle in (r,θ) following a field line.

Within this work, all simulations are done using periodic boundary conditions. This is computationally very efficient since for instance $\phi_{\rm n}(r_1,\theta) = \phi_{\rm n}(r_{n_{\rm r}},\theta)$, implying a periodicity in r. However, this choice is incompatible with the variation of equilibrium profiles. In order to model that, it is necessry to abandon the flux tubes and use some type of nonperiodic boundary conditions. Global gyrokinetic simulations of turbulence include physical effects that are not retained in local flux–tube simulations. Nevertheless, in the limit of sufficiently small $\rho_* = \rho_{\rm s}/a$, representing the gyroradius compared to system size, it is expected that a local simulation should agree with a global one (at the local simulation radius), since all effects that are dropped in the local simulations are expected to vanish as $\rho_* \to 0$. As it is shown for instance in [43], global simulations of a well–established test case are indeed shown to recover the flux–tube limit at each radius.

2.2.3 Ballooning reconstruction

While GYRO solves the n–th toroidal harmonic of the gyrokinetic set of equations in the space $(r,\theta,\alpha;\epsilon,\lambda)$, where θ is an angle in the poloidal plane, it is also instructive to introduce the 'ballooning' phase space. The following discussion is close to the one in [44], and restricted to a $s-\alpha$ equilibrium. The ballooning phase space is of particular importance in local flux tube simulations, since the solution of the gyrokinetic equations naturally exhibit the so called 'ballooning' symmetry, that is the symmetry transformation

$$P_{\rm ball}: \quad \theta \to \theta + 2\pi \quad , \quad \alpha \to \alpha - 2\pi q \tag{2.75}$$

leaves the solution unchanged. For illustration, one supposes to have for a single toroidal harmonic of the electrostatic potential, $\Phi_{\rm n}$, an eikonal representation given by

$$\Phi_{\rm n}(r,\theta,\phi) = \exp\left[-in\left(\phi - q(r)\theta\right)\right]\phi_{\rm n}(r,\theta), \tag{2.76}$$

The origin of this expansion is the fact that $\mathbf{b}\cdot\nabla\phi \simeq 0$. The problem, however, is that Eq. (2.76) is generally not periodic in θ, which is in contradiction to the tokamak topology. Then, expansion about the surface $r = r_0$ gives

$$\Phi_{\rm n} = \exp\left[-in\left(\phi - q_0\theta\right) + i\theta\left(r - r_0\right)/\Delta\right]\phi_{\rm n}(r,\theta), \tag{2.77}$$

with $\Delta = 1/(n\nabla q) = 1/(sk_\theta)$, s being the magnetic shear, and $q_0 = q(r_0)$. Physically, Δ is the distance between adjacent rational surfaces. The ballooning transformation, which

was firstly introduced by [45], is embodied in the non–standard Fourier expansion

$$\phi_{\rm n}(r,\theta) = \sum_{\rm b} c_{\rm b}(\theta,\theta_0)\exp\left[i\left(\theta_0+2\pi b\right)\left(r-r_0\right)/\Delta\right], \tag{2.78}$$

where θ_0 is a linear eigenmode label. This representation ensures the required periodicity, since the choice of $\theta_0 = 0$ allows for functions, which are periodic on $r - r_0 \in [0,\Delta]$, while the choice $\theta_0 = 0,\pi$ form a basis for functions periodic on $r - r_0 \in [0,2\Delta]$. Thus, adding more values of θ_0 allows progressively greater coverage on the radial direction (in this sense, θ_0 is equivalent to $n_{\rm r}$ defining the radial grid), and a general solution of the gyrokinetic equation is a linear combination of eigenmodes for different values of θ_0. From the Fourier coefficients one can define the ballooning potential

$$\Phi_{\rm B}(\theta_{\rm b},\theta_0) = c_{\rm b}(\theta,\theta_0)\exp\left[-inq_0\left(\theta_0+2\pi b\right)\right], \tag{2.79}$$

where the extended poloidal angle $\theta_{\rm b} = \theta + 2\pi b \in [-\infty,\infty]$. Then, it is also possible to rewrite Eq. (2.39) in the ballooning space,

$$\left[\frac{\partial}{\partial t} - \frac{v_\parallel}{JB}\frac{\partial}{\partial\theta} + i\mathbf{k}\cdot\mathbf{v}_{\rm d}\right] h_{\rm n}(r,\theta;t) =$$
$$\left[\frac{q}{T}F_{\rm M}\frac{\partial}{\partial t} + \frac{dF_{\rm M}}{dr}\frac{ik_\theta}{B}\right] J_0\left(k_\perp\rho_{\rm s}\right)\left[\phi_{\rm n}(r,\theta;t) - \frac{v_\parallel}{c}A_\parallel(r,\theta;t)\right], \tag{2.80}$$

where parallel magnetic field fluctuations due to $A_\perp$ are left out for simplicity. Moreover, the subscrips 'B' have been left out. This form of the gyrokinetic equation is particularly suited for modes having an interchange character, like ITG and TEM. The general solution of the linear gyrokinetic equation is then given by

$$\Phi_{\rm n}(r,\theta,\phi) = \sum_{\theta_0}\sum_{\rm b}\exp\left[-in\left(\phi - q(r)(\theta_{\rm b}-\theta_0)\right)\right]\Phi_{\rm B}(\theta_{\rm b},\theta_0). \tag{2.81}$$

Since θ_0 appears as a parameter in the gyrokinetic, it is clear that the two dimensional calculation required to compute $\phi_{\rm n}(r,\theta)$ is reduced to a series of one dimensional calculations for $\Phi_{\rm B}(\theta_{\rm b},\theta_0)$. As already stressed, GYRO does not make use of the ballooning transformation, but nonetheless local linear numerical solutions will exhibit the exact ballooning symmetry and therefore a reconstruction of the ballooning potentials is possible.

2.2.4 The challenge of nonlinear electromagnetic simulations

It has been known for a long time that the Ampère equation, Eq. (2.34), is extremely difficult to solve numerically owing to a delicate cancelation in the electron current, which occurs when $\beta_{\rm e} > m_{\rm e}/m_{\rm D}$. This condition is well satisfied for experimentally relevant values of $\beta_{\rm e}$. The origin of the cancelation problem can be seen from the Ampères equation, rewritten in the form

$$\frac{2(k_\theta\rho_{\rm s})^2}{\beta_{\rm e}}A_{\parallel,{\rm n}} \propto \int d^3v\hat{v}_{\parallel,{\rm e}}\delta f_{\rm n,e} - \int d^3v\hat{v}^2_{\parallel,{\rm e}}A_{\parallel,{\rm n}}, \tag{2.82}$$

where only the dominant electron current has been used. Assuming $k_\theta\rho_{\rm s} \sim 0.1$ and $\beta_{\rm e} \sim 1\%$, the left hand side of Eq. (2.82) is approximately $2A_{\parallel,{\rm n}}$, while the second

term on the right hand side is approximately $3600 A_{\parallel,\mathrm{n}}$ for a deuterium plasma due to the dependence on $\hat{v}_{\parallel,\mathrm{e}}^2 = (v_{\parallel,\mathrm{e}}/c_\mathrm{s})^2$. Therefore, the two velocity integrals on the right hand side have to cancel almost exactly, the difference determining the physics. However, for Eulerian codes like GYRO it has been found out that a term by term cancelation of the terms of order $m_\mathrm{D}/m_\mathrm{e}$ in the electron current can be made. This is achieved by the numerical computation of both velocity integrals on the right hand side using exactly the same discretization scheme. For codes using an explicit scheme for the time evolution, this means to increase the temporal resolution by a factor of $\sqrt{m_\mathrm{D}/m_\mathrm{e}}$ in order to resolve correctly the fast parallel electron dynamics, which carries the main part of the parallel current fluctuation causing magnetic field fluctuations. However, experience from nonlinear simulations with GYRO, which uses a implicit–explicit scheme for the time evolution of the electron dynamics, shows that an approximately ten times higher time resolution at $\beta_\mathrm{e} = 1\%$ as compared to the electrostatic case is requested. This is in agreement with the fact that the shear Alfvèn time scales have to be resolved. They scale like $v_\mathrm{A}/c_\mathrm{s} = \sqrt{2/\beta_\mathrm{e}}$, such that the temporal resolution has to be increased by $\sim \sqrt{\beta_\mathrm{e}}$.

Moreover, GYRO has the option to treat the electron dynamics in three different ways, namely in an adiabatic, driftkinetic or gyrokinetic way. The first option neglects particle trapping and electromagnetic effects and is therefore never used within this thesis. The latter two are giving very close results, since the electron FLR effects are only very small. However, in terms of computational costs, the second option is preferable to the third and is therefore the one mainly used here. Ionic species, on the other side, are always treated in a fully gyrokinetic way.

Chapter 3

Fluid model for ion temperature gradient and trapped electron modes

In this Chapter, the physics mechanisms leading to the most common microinstabilities in the core of tokamaks, namely ion temperature gradient (ITG) and trapped electron (TEM), are discussed. Special attention is paid on the impact of an electromagnetic treatment, namely considering perpendicular magnetic field fluctuations. For the physics modeling, a basic fluid model following the Weiland model [46, 47] is derived, aiming at highlighting the interplay of the two different modes.

3.1 Fluid model

3.1.1 Basic idea

Here, the case of an even further simplification compared to the gyrokinetic approach in Chapter 2, namely a fluid model, which consists of velocity moments of kinetic equations, is considered. This consists of conservation equations, where only macroscopic quantities like density, temperature and fluid drift velocities are involved. Closed equations for their evolution in space and time are presented. The derivation of the fluid model strongly follows the works of J. Weiland, H. Nordman and coauthors, in particular [46, 47], with the book *"Collective Modes in Inhomogeneous Plasma"* by J. Weiland [39]. The electromagnetic treatment follows the works of [48, 49]. It has to be mentioned that the final linearized fluid equations, which will be presented in this Chapter, can also be obtained from moments of the gyrokinetic equation.

3.1.2 Model equations

Four particle species are considered, namely main ions (hydrogen or hydrogen isotopes) with density n_{H} and temperature T_{H}, first impurity ions with density n_{p}, temperature T_{p} and charge number Z_{p}, trapped electrons with density n_{et} and temperature T_{e}, and passing (free) electrons, with density n_{ef}. For these species, the following fluid equations

are considered. The continuity equation for a species σ reads

$$\frac{\partial n_\sigma}{\partial t} + \nabla \cdot (n_\sigma \, \mathbf{v}_\sigma) = 0, \tag{3.1}$$

where $\sigma = H, p, et$. It is important to note that this equation implies the conservation of particles, and therefore holds for the full density n_σ consisting of a background density $n_{0,\sigma}$ plus a fluctuating part $\tilde{n}_\sigma$, which is assumed to be given by a harmonic variation via

$$\tilde{n}_\sigma = \delta n_\sigma \exp(i(\mathbf{k} \cdot \mathbf{r} - \omega t)) \tag{3.2}$$

(the same decomposition will also be done for parallel velocity, temperature and electromagnetic field potentials). Depending on the particle species different expressions are considered for the fluid velocity $\mathbf{v}_\sigma$. The chosen coordinate system is highlighted in figure

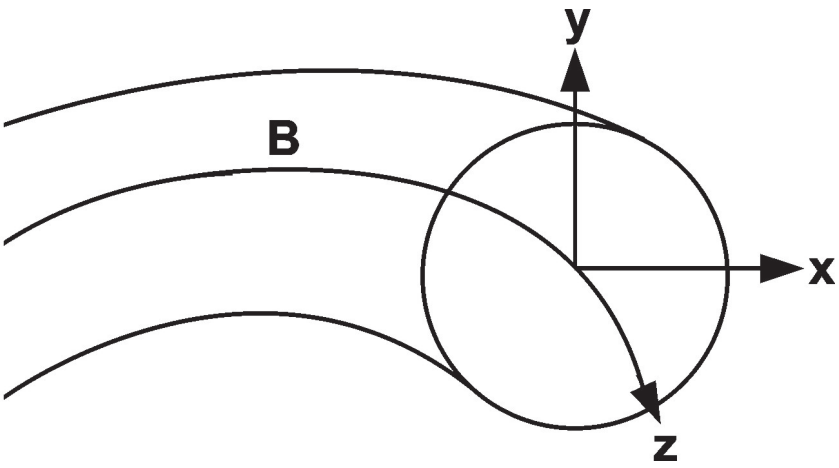

Figure 3.1: Geometry used in the fluid model.

3.1. The unit vector $\hat{\mathbf{z}} \equiv \hat{\mathbf{e}}_\parallel \equiv \mathbf{B}/B \equiv \hat{\mathbf{B}}$, the unit vector $\hat{\mathbf{x}}$ is directed in the radial direction, perpendicular to the magnetic surface, and $\hat{\mathbf{y}} \equiv \hat{\mathbf{z}} \times \hat{\mathbf{x}}$ is the binormal direction.

Firstly, the continuity equations of main ions and first impurities are considered. The fluid velocities are given by

$$\mathbf{v}_\mathrm{i} = \mathbf{v}_{\mathrm{E}\times\mathrm{B}} + \mathbf{v}_{*\mathrm{i}} + \mathbf{v}_{\mathrm{P,i}} + \mathbf{v}_{\pi,\mathrm{i}} + \hat{\mathbf{e}}_\parallel v_{\parallel,\mathrm{i}}, \tag{3.3}$$

where i stands for H,p. It is noteworthy that the included velocities are fluctuating quantities. In particular

$$\mathbf{v}_{\mathrm{E}\times\mathrm{B}} = \frac{\mathbf{E} \times \hat{\mathbf{e}}_\parallel}{B} = \frac{\hat{\mathbf{e}}_\parallel \times \nabla\phi}{B} = -i\frac{k_\mathrm{y}\delta\phi}{B}\hat{\mathbf{x}} \tag{3.4}$$

is the E cross B drift, where $\delta\phi$ is the fluctuating electrostatic potential (a equilibrium electrostatic potential is omitted, as it is explained in Chapter 2 in the derivation of the gyrokinetic equation). Also the other drifts like the diamagnetic drift

$$\mathbf{v}_{*,\mathrm{i}} = \frac{\hat{\mathbf{e}}_\parallel \times \nabla(n_\mathrm{i} T_\mathrm{i})}{Z_\mathrm{i} e n_\mathrm{i} B} = i(1 + \eta_\mathrm{i})\frac{\omega_{*\mathrm{i}}}{k_\mathrm{y}}\hat{\mathbf{y}}, \tag{3.5}$$

where $\omega_{*,\mathrm{i}} = -k_\mathrm{y} T_\mathrm{i} (Z_\mathrm{i} e B L_{\mathrm{n,i}})^{-1}$ has been used, $Z_\mathrm{i} = 1$ for hydrogen isotopes and $Z_\mathrm{i} = Z_\mathrm{p}$ for the first impurity ions, do contain fluctuations (the diamagnetic drift via n_i and T_i). It

is noteworthy that this drift (and also the following ones) are pointing in opposite direction for the electrons. Moreover, e denotes the elementary charge and

$$L_{\mathrm{ni}} \equiv -\frac{n_{\mathrm{i}}}{\hat{\mathbf{x}} \cdot \nabla n_\sigma}$$

is the radial density gradient scale length,

$$\epsilon_{\mathrm{n,i}} \equiv 2\frac{\hat{\mathbf{x}} \cdot \nabla B/B}{\hat{\mathbf{x}} \cdot \nabla n_{\mathrm{i}}/n_{\mathrm{i}}} = 2\frac{L_{\mathrm{n,i}}}{L_{\mathrm{B}}},$$

which is two times the dimensionless density gradient scale length, and

$$\eta_{\mathrm{i}} \equiv \frac{n_{\mathrm{i}}\hat{\mathbf{x}} \cdot \nabla T_{\mathrm{i}}}{T_{\mathrm{i}}\hat{\mathbf{x}} \cdot \nabla n_{\mathrm{i}}} = \frac{L_{\mathrm{n,i}}}{L_{\mathrm{T,i}}}.$$

The polarization drift is given by

$$\mathbf{v}_{\mathrm{P,i}} = \frac{d\mathbf{E}}{dt}/(B\Omega_{\mathrm{c,i}}),$$

The drift originating from the off–diagonal elements of the stress tensor π_{i} reads

$$\mathbf{v}_{\pi\mathrm{i}} = \frac{\hat{\mathbf{e}}_{\parallel} \times \nabla \cdot \pi_{\mathrm{i}}}{Z_{\mathrm{i}} e n_{\mathrm{i}} B}.$$

By inclusion of the latter two, finite Larmor radius effects (FLR) are considered in both the description of the main ion species and the first impurity species.

For the electron species, $\Omega_{\mathrm{c,e}}$ is much higher as compared to the ions and impurities. Therefore, for the trapped electrons, both FLR effects and parallel motion are neglected. Thus, for those the continuity equation reads

$$\frac{\partial n_{\mathrm{et}}}{\partial t} + \nabla \cdot (n_{\mathrm{et}}\, \mathbf{v}_{\mathrm{et}}) = 0, \tag{3.6}$$

where $\mathbf{v}_{\mathrm{et}} = \mathbf{v}_{\mathrm{E\times B}} + \mathbf{v}_{*\mathrm{e}}$. Here

$$\mathbf{v}_{*\mathrm{e}} = -\frac{\hat{\mathbf{e}}_{\parallel} \times \nabla(n_{\mathrm{e}} T_{\mathrm{e}})}{e n_{\mathrm{e}} B} = i(1+\eta_{\mathrm{e}})\frac{\omega_{*\mathrm{e}}}{k_{\mathrm{y}}}\hat{\mathbf{y}} \qquad \text{where} \qquad \omega_{*\mathrm{e}} = \frac{k_{\mathrm{y}} T_{\mathrm{e}}}{eBL_{\mathrm{ne}}}, \tag{3.7}$$

and

$$L_{\mathrm{ne}} \equiv -\frac{n_{\mathrm{e}}}{\hat{\mathbf{x}} \cdot \nabla n_{\mathrm{e}}}$$

.

The parallel motion $v_{\parallel,\sigma}$ is determined by the parallel momentum equations driven by electromagnetic forces and pressure gradient along the field lines. The electrostatic equation for the parallel motion reads

$$m_\sigma n_\sigma \frac{\partial v_{\parallel,\sigma}}{\partial t} = -eZ_\sigma n_\sigma \nabla_\parallel \phi - \nabla_\parallel (n_\sigma T_\sigma). \tag{3.8}$$

Here, it has been assumed that the electric field is solely given by the electrostatic potential ϕ. The corresponding electromagnetic parallel motion equation reads

$$m_\sigma n_\sigma \frac{\partial v_{\parallel,\sigma}}{\partial t} = -eZ_\sigma n_\sigma \left[\nabla_\parallel \phi + \frac{1}{c}\left(\frac{\partial A_\parallel}{\partial t} - (\mathbf{v}_{*,\sigma} \times \mathbf{B}_\perp) \cdot \hat{\mathbf{B}}\right)\right] - \nabla_\parallel (n_\sigma T_\sigma), \tag{3.9}$$

where both the parallel component of the vector potential $A_\parallel$ as well as the parallel projection of the $\mathbf{v} \times \mathbf{B}$ force are taken into account. The latter is given by an interplay of the (binormal) diamagnetic drift and the perpendicular component of the fluctuating magnetic field, which, in turn, includes the parallel component of the vector potential since $\mathbf{B}_\perp = \nabla \times (A_\parallel \hat{\mathbf{B}}) \approx \nabla A_\parallel \times \hat{\mathbf{B}}$. It is noted that in this treatment the compressional Alfvèn dynamics due to a fluctuating parallel magnetic field corresponding to $A_\perp$ is neglected because of its smallness in conventional tokamak plasmas.

The energy balance equation is given for all considered species by

$$\frac{3}{2} n_\sigma \left(\frac{\partial}{\partial t} + \mathbf{v}_\sigma \cdot \nabla \right) T_\sigma + n_\sigma T_\sigma \nabla \cdot \mathbf{v}_\sigma = -\nabla \cdot \mathbf{q}_\sigma, \tag{3.10}$$

where σ= H, p, et. In the energy balance equation FLR effects are neglected in the expression for $\mathbf{v}_\sigma$ for both the ion species and for the trapped electrons, while the parallel fluid velocity is not included since its contribution drops in the linearization.

The fluid closure is obtained assuming

$$\mathbf{q}_\sigma = \mathbf{q}_{*,\sigma}$$

for all the particle species, where $\mathbf{q}_{*,\sigma}$ is the diamagnetic heat flow

$$\mathbf{q}_{*,\sigma} = \frac{5}{2} \frac{n_\sigma T_\sigma}{m_\sigma \Omega_{\mathrm{c},\sigma}} (\hat{\mathbf{e}}_\parallel \times \nabla T_\sigma).$$

The gradient of this expression yields

$$\nabla \cdot \mathbf{q}_{*,\sigma} = \frac{5}{2} n_\sigma (\mathbf{v}_{*,\sigma} - \mathbf{v}_{\mathrm{D},\sigma}) \cdot \nabla T_\sigma,$$

where

$$\mathbf{v}_{\mathrm{D},\sigma} = \frac{T_\sigma}{m_\sigma \Omega_{\mathrm{c},\sigma}} \hat{\mathbf{B}} \times \left(\frac{\nabla B}{B} + \kappa \right) \tag{3.11}$$

is the drift due to $\nabla |B|$ and magnetic curvature $\kappa = \hat{\mathbf{B}} \cdot \nabla \hat{\mathbf{B}}$. They are combined in the ∇B and curvature drift frequency given by

$$\mathbf{k} \cdot \mathbf{v}_{\mathrm{D},\sigma} = \omega_{\mathrm{D},\sigma} = \frac{-2 k_\mathrm{y} T_\sigma}{Z_\sigma e B R}. \tag{3.12}$$

This leads to the useful relations $\epsilon_{\mathrm{n},\sigma} = \omega_{\mathrm{D},\sigma}/\omega_{*,\sigma}$ and $\omega_{\mathrm{D,i}}/\omega_{*,\mathrm{e}} = -T_\mathrm{i}/Z_\mathrm{i} T_\mathrm{e} \epsilon_{\mathrm{ne}}$ with $i = H, p$.

The trapped electron fraction is given by f_t with $f_\mathrm{t} = n_{\mathrm{et}}/n_\mathrm{e}$. As already mentioned, n_{et} is the density of trapped electrons and n_{ef} the density of free (circulating) electrons. Then

$$n_\mathrm{e} = n_{\mathrm{et}} + n_{\mathrm{ef}}.$$

The perturbed density $\delta n_\mathrm{e} = \delta n_{\mathrm{et}} + \delta n_{\mathrm{ef}}$ can be written

$$\frac{\delta n_\mathrm{e}}{n_\mathrm{e}} = \frac{\delta n_{\mathrm{et}}}{n_\mathrm{e}} + \frac{\delta n_{\mathrm{ef}}}{n_\mathrm{e}} = f_\mathrm{t} \frac{\delta n_{\mathrm{et}}}{n_{\mathrm{et}}} + (1 - f_\mathrm{t}) \frac{\delta n_{\mathrm{ef}}}{n_{\mathrm{ef}}}$$

Let f_Z be the fraction of impurity ions with charge Z_p relative to the electron density $f_\mathrm{Z} = n_\mathrm{p}/n_\mathrm{e}$. Quasi–neutrality gives $n_\mathrm{e} = n_\mathrm{H} + Z_\mathrm{p} n_\mathrm{p}$, where, n_H is the density of the Hydrogen isotopes and n_Z is the density of the impurity species. Then

$$\frac{\delta n_\mathrm{e}}{n_\mathrm{e}} = \frac{\delta n_\mathrm{H}}{n_\mathrm{e}} + \frac{Z \delta n_\mathrm{Z}}{n_\mathrm{e}} = (1 - Z_\mathrm{p} f_\mathrm{Z}) \frac{\delta n_\mathrm{H}}{n_\mathrm{H}} + Z_\mathrm{p} f_\mathrm{Z} \frac{\delta n_\mathrm{p}}{n_\mathrm{p}}. \tag{3.13}$$

.

3.1.3 Dispersion relation

The goal of this section is the derivation of the generalized eigenvalue problem, which in turn leads to the dispersion relation for turbulent modes. To this purpose, Eq. (3.1) is re–written in the form

$$n_\sigma \nabla \cdot \mathbf{v}_\sigma = -\frac{\partial n_\sigma}{\partial t} - \mathbf{v}_\sigma \cdot \nabla n_\sigma.$$

Therefore the continuity equation can be used to eliminate $\nabla \cdot \mathbf{v}_\sigma$ in the energy equation, Eq. (3.10). Here, when replacing $\nabla \cdot \mathbf{v}_\sigma$ from the continuity equation in the energy equation, $\mathbf{v}_\sigma = \mathbf{v}_{\mathrm{E}\times\mathrm{B}} + \mathbf{v}_{*,\sigma}$, the FLR effects from the polarization drift and the off–diagonal elements of the stress tensor have been neglected consistently with the assumption made for the energy balance equation for all particle species σ. One gets

$$n_\sigma \left(\frac{\partial}{\partial t} + \mathbf{v}_\sigma \cdot \nabla \right) T_\sigma - \frac{2}{3} T_\sigma \frac{\partial n_\sigma}{\partial t} - \frac{2}{3} T_\sigma \mathbf{v}_\sigma \cdot \nabla n_\sigma = \frac{5}{3} n_\sigma (\mathbf{v}_{*,\sigma} - \mathbf{v}_{\mathrm{D},\sigma}) \cdot \nabla T_\sigma.$$

The $\mathbf{v}_{*,\sigma}$ contributions cancel. This is because

$$n_\sigma \mathbf{v}_{*,\sigma} \cdot \nabla T_\sigma - \frac{2}{3} T_\sigma \mathbf{v}_{*,\sigma} \cdot \nabla n_\sigma - \frac{5}{3} n_\sigma \mathbf{v}_{*,\sigma} \cdot \nabla T_\sigma = -\frac{2}{3} \mathbf{v}_{*,\sigma} \cdot \nabla (n_\sigma T_\sigma) = 0,$$

since the diamagnetic drift $\mathbf{v}_{*,\sigma} = \hat{\mathbf{B}} \times \nabla (n_\sigma T_\sigma) / Z_\sigma e B n_\sigma$ is perpendicular to the gradient of the pressure $\nabla (n_\sigma T_\sigma)$. Thus, the remaining terms in the energy balance equation read

$$n_\sigma \frac{\partial T_\sigma}{\partial t} + n_\sigma \mathbf{v}_{\mathrm{E}\times\mathrm{B}} \cdot \nabla T_\sigma - \frac{2}{3} T_\sigma \frac{\partial n_\sigma}{\partial \sigma} - \frac{2}{3} T_\sigma \mathbf{v}_{\mathrm{E}\times\mathrm{B}} \cdot \nabla n_\sigma + \frac{5}{3} \mathbf{v}_{\mathrm{D},\sigma} \cdot \nabla T_\sigma = 0$$

In a curved magnetic field, as it is considered here, the divergence of the fluid velocities has to be evaluated. Following [39], it is concluded that the divergence of the diamagnetic drift flux and of the E×B flow would be zero in the absence of curvature and ∇B. Similarly, the divergence of the polarization drift and the divergence of the drift resulting from the off–diagonal part of the stress tensor are modified in the presence of a curved magnetic field. This leads to the so–called curvature relations,

$$\begin{aligned}
\nabla (n_\sigma v_{*,\sigma}) &= \mathbf{v}_{\mathrm{D},\sigma} \cdot \nabla (n_\sigma T_\sigma)/T_\sigma, \\
\nabla v_{\mathrm{E}\times\mathrm{B}} &= \frac{Z_\sigma e}{T_\sigma} \mathbf{v}_{\mathrm{D},\sigma} \cdot \nabla \delta\phi, \\
\nabla \cdot [n_\sigma (\mathbf{v}_{\mathrm{p},\sigma} + \mathbf{v}_{\pi,\sigma})] &\approx -i n_\sigma k_\mathrm{y}^2 \rho_{\mathrm{s},\sigma}^2 [\omega - \omega_{*,\sigma}(1+\eta_\sigma)] \frac{e\delta\phi}{T_\mathrm{e}}, \\
\text{where} \quad \rho_{\mathrm{s},\sigma}^2 &= \frac{T_\mathrm{e}}{m_\sigma \Omega_\sigma^2}.
\end{aligned} \tag{3.14}$$

As usual $Z_\sigma = 1$ for $\sigma = H$, $Z_\sigma = Z_\mathrm{p}$ for first impurities $\sigma = p$, and $Z_\sigma = -1$ for $\sigma = et$. Using Eq. (3.2) and the aforementioned relations in the continuity, momentum, and energy equations, Eqs. (3.1, 3.8, 3.6, 3.10), linearized equations for the perturbations are obtained. This is shown explicitly for the hydrogen species equations in order to point out the derivation of the linearized equation for the perturbed variables term by term. For simplicity the tilde for the perturbed quantities is omitted from now on.

The hydrogen continuity equation reads

$$\begin{aligned}
\frac{\partial n_\mathrm{H}}{\partial t} + n_\mathrm{H} \nabla \cdot \mathbf{v}_{\mathrm{E}\times\mathrm{B}} + \mathbf{v}_{\mathrm{E}\times\mathrm{B}} \cdot \nabla n_\mathrm{H} + \nabla \cdot (n_\mathrm{H}\, \mathbf{v}_{*,\mathrm{H}}) + \\
\nabla \cdot [n_\mathrm{H}\, (\mathbf{v}_{\mathrm{P},\mathrm{H}} + \mathbf{v}_{\pi,\mathrm{H}})] + \nabla \cdot (n_\mathrm{H}\, \hat{\mathbf{B}} v_{\parallel,\mathrm{H}}) &= 0,
\end{aligned}$$

which is transformed to

$$\begin{aligned} -\omega\frac{\delta n_{\rm H}}{n_{\rm H}}+\omega_{\rm D,H}\frac{T_{\rm e}}{T_{\rm H}}\frac{e\,\delta\phi}{T_{\rm e}}-\omega_{*,\rm H}\frac{T_{\rm e}}{T_{\rm H}}\frac{e\,\delta\phi}{T_{\rm e}}+ \\ \omega_{\rm D,H}\frac{\delta n_{\rm H}}{n_{\rm H}}+\omega_{\rm D,H}\frac{\delta T_{\rm H}}{T_{\rm H}}-k_{\rm y}^2\rho_{\rm s,H}^2(\omega-\omega_{*,\rm H}(1+\eta_{\rm i}))\frac{e\,\delta\phi}{T_{\rm e}}+k_\parallel v_{\parallel,\rm H} &= 0. \end{aligned}$$

The (electromagnetic) hydrogen parallel motion equation is given by

$$m_{\rm H}\frac{\partial v_{\parallel,\rm H}}{\partial t}+e\left[\nabla_\parallel\phi+\frac{1}{c}\left(\frac{\partial A_\parallel}{\partial t}-(\mathbf{v}_{*,\rm H}\times\mathbf{B}_\perp)\right)\cdot\hat{\mathbf{B}}\right]+\frac{1}{n_{\rm H}}\nabla_\parallel(n_{\rm H}T_{\rm H})=0,$$

which leads to

$$\begin{aligned} -\omega m_{\rm H}v_{\parallel,\rm H}+k_\parallel T_{\rm e}\frac{e\,\delta\phi}{T_{\rm e}}-T_{\rm e}\frac{\omega}{c}\frac{eA_\parallel}{T_{\rm e}}+\frac{T_{\rm e}}{c}(1+\eta_{\rm H})\omega_{*,\rm H}\frac{eA_\parallel}{T_{\rm e}}+ \\ +k_\parallel T_{\rm H}\left(\frac{\delta n_{\rm H}}{n_{\rm H}}+\frac{\delta T_{\rm H}}{T_{\rm H}}\right) &= 0. \end{aligned}$$

The hydrogen energy balance equation is given by

$$n_{\rm H}\frac{\partial T_{\rm H}}{\partial t}+\frac{5}{3}\mathbf{v}_{\rm D,H}\cdot\nabla T_{\rm H}-\frac{2}{3}T_{\rm H}\frac{\partial n_{\rm H}}{\partial t}+n_{\rm H}\mathbf{v}_{\rm E\times B}\cdot\nabla T_{\rm H}-\frac{2}{3}T_{\rm H}\mathbf{v}_{\rm E\times B}\cdot\nabla n_{\rm H}=0,$$

which is written as

$$-\omega\frac{\delta T_{\rm H}}{T_{\rm H}}+\frac{5}{3}\omega_{\rm D,H}\frac{\delta T_{\rm H}}{T_{\rm H}}+\frac{2}{3}\omega\frac{\delta n_{\rm H}}{n_{\rm H}}+\omega_{*,\rm e}\frac{\epsilon_{\rm ne}}{\epsilon_{\rm nH}}\eta_{\rm H}\frac{e\,\delta\phi}{T_{\rm e}}-\omega_{*\rm e}\frac{\epsilon_{\rm ne}}{\epsilon_{\rm nH}}\frac{2}{3}\frac{e\,\delta\phi}{T_{\rm e}}=0$$

Reordering the previous equations and producing the same operation for the other two particle species, one obtains the following set of equations. The ion continuity equation is given by

$$\begin{aligned} &(-\omega+\omega_{\rm D,i})\frac{\delta n_{\rm i}}{n_{\rm i}}+\omega_{\rm D,i}\frac{\delta T_{\rm i}}{T_{\rm i}}+ \\ &+\left\{(\omega_{\rm D,i}-\omega_{*,\rm i})\frac{T_{\rm e}}{T_{\rm i}}-k_{\rm y}^2\rho_{\rm s,i}^2\left[\omega-\omega_{*,\rm i}(1+\eta_{\rm i})\right]\right\}\frac{e\,\delta\phi}{T_{\rm e}}+k_\parallel v_{\parallel,\rm i}=0. \end{aligned} \tag{3.15}$$

The ion parallel motion equation reads

$$\begin{aligned} &-\omega m_{\rm i}v_{\parallel,\rm i}+k_\parallel T_{\rm e}\frac{e\,\delta\phi}{T_{\rm e}}-T_{\rm e}\frac{\omega}{c}\frac{eA_\parallel}{T_{\rm e}}+\frac{T_{\rm e}}{c}(1+\eta_{\rm i})\omega_{*,\rm i}\frac{eA_\parallel}{T_{\rm e}}+ \\ &+k_\parallel T_{\rm i}\left(\frac{\delta n_{\rm i}}{n_{\rm i}}+\frac{\delta T_{\rm i}}{T_{\rm i}}\right)=0. \end{aligned} \tag{3.16}$$

The ion energy balance equation is

$$\left(-\omega+\frac{5}{3}\omega_{\rm D,i}\right)\frac{\delta T_{\rm i}}{T_{\rm i}}+\frac{2}{3}\omega\frac{\delta n_{\rm i}}{n_{\rm i}}+\omega_{*,\rm e}\frac{\epsilon_{\rm n,e}}{\epsilon_{\rm n,i}}\left(\eta_{\rm i}-\frac{2}{3}\right)\frac{e\,\delta\phi}{T_{\rm e}}=0. \tag{3.17}$$

The trapped electron continuity equation is written as

$$(-\omega+\omega_{\rm D,e})\frac{\delta n_{\rm et}}{n_{\rm et}}+\omega_{\rm D,e}\frac{\delta T_{\rm e}}{T_{\rm e}}-(\omega_{\rm D,e}-\omega_{*,\rm e})\frac{e\,\delta\phi}{T_{\rm e}}=0. \tag{3.18}$$

The trapped electron parallel motion is not useful in the context of low frequency modes, since the bounce time is much lower compared to the characteristic time scales of the turbulent modes under consideration, i.e. $\omega_{\mathrm{b,et}} \gg \omega$. Therefore, the parallel motion of trapped electrons averages to zero. On the other hand, the parallel motion equation for passing electrons reads

$$\begin{aligned} &-\omega m_{\mathrm{e}} v_{\parallel,\mathrm{ef}} - k_{\parallel} T_{\mathrm{e}} \frac{e\,\delta\phi}{T_{\mathrm{e}}} + T_{\mathrm{e}} \frac{\omega}{c} \frac{eA_{\parallel}}{T_{\mathrm{e}}} \\ &-\frac{T_{\mathrm{e}}}{c}(1+\eta_{\mathrm{ef}})\omega_{*,\mathrm{ef}} \frac{eA_{\parallel}}{T_{\mathrm{e}}} + k_{\parallel} T_{\mathrm{e}} \left(\frac{\delta n_{\mathrm{ef}}}{n_{\mathrm{ef}}} + \frac{\delta T_{\mathrm{e}}}{T_{\mathrm{e}}} \right) = 0. \end{aligned} \tag{3.19}$$

From this equation an important consequence can be derived: Neglecting the first term as a consequence of the smallness of the electron mass, and assuming isothermal electrons, which in the electrostatic limit ($A_{\parallel} = 0$) means $\delta T_{\mathrm{e}} = 0$, as it will be shown below, one finds the so–called Boltzmann or adiabatic response for the electrons, namely

$$\frac{\delta n_{\mathrm{e}}}{n_0} = \frac{e\delta\phi}{T_{\mathrm{e}}}. \tag{3.20}$$

In this case there exists no phase shift between electron density fluctuations and electrostatic potential fluctuations. On the other hand, when electromagnetic effects are taken into account ($A_{\parallel}$ finite), passing electrons tend to leave the adiabatic response, and a phase shift between δn_{ef} and ϕ is obtained. This can be seen by the following reasoning. In the isothermal limit where electron inertia is ignored, the electron temperature is homogeneous along magnetic field lines, namely $\mathbf{B} \cdot \nabla T_{\mathrm{e}} = 0$. From the linearization in the perturbations of B and T_{e}, one finds for the temperature response

$$\frac{\delta T_{\mathrm{e}}}{T_{\mathrm{e}}} e = \eta_{\mathrm{e}} \frac{\omega_{*,\mathrm{e}}}{k_{\parallel} c} \frac{eA_{\parallel}}{T_{\mathrm{e}}}. \tag{3.21}$$

Combining parallel force balance for the electrons, where the inertial term is neglected, with Eq. (3.21), one gets the generalized Boltzmann relation for electromagnetic electrons,

$$\frac{\delta n_{\mathrm{e}}}{n_{\mathrm{e}}} = \frac{e\delta\phi}{T_{\mathrm{e}}} + \frac{\omega_{*,\mathrm{e}} - \omega}{k_{\parallel} c} \frac{eA_{\parallel}}{T_{\mathrm{e}}}. \tag{3.22}$$

The trapped electron energy balance equation reads

$$\left(-\omega + \frac{5}{3}\omega_{\mathrm{D,e}} \right) \frac{\delta T_{\mathrm{e}}}{T_{\mathrm{e}}} + \frac{2}{3}\omega \frac{\delta n_{\mathrm{et}}}{n_{\mathrm{et}}} + \omega_{*,\mathrm{e}} \left(\eta_{\mathrm{e}} - \frac{2}{3} \right) \frac{e\,\delta\phi}{T_{\mathrm{e}}} = 0. \tag{3.23}$$

Lastly, using Eq. (3.22), the quasi–neutrality condition is written as

$$f_{\mathrm{t}} \frac{\delta n_{\mathrm{et}}}{n_{\mathrm{et}}} + (1 - f_{\mathrm{t}}) \left(\frac{e\,\delta\phi}{T_{\mathrm{e}}} + \frac{\omega_{*,\mathrm{e}} - \omega}{k_{\parallel} c} \frac{eA_{\parallel}}{T_{\mathrm{e}}} \right) = (1 - Z f_{\mathrm{Z}}) \frac{\delta n_{\mathrm{H}}}{n_{\mathrm{H}}} + Z f_{\mathrm{Z}} \frac{\delta n_{\mathrm{p}}}{n_{\mathrm{p}}}. \tag{3.24}$$

It is clear that in the electrostatic limit Eq. (3.20) instead of Eq. (3.22) has to be used.

The present set of equations (3.15), (3.16), (3.17), (3.18), (3.23), and (3.24) can be regarded as a homogeneous set of nine equations for ten unknowns $\delta\phi$, $A_{\parallel}$, δn_{H}, δT_{H}, δn_{et}, δT_{e}, δn_{p}, δT_{p}, $v_{\parallel,\mathrm{H}}$ and $v_{\parallel,\mathrm{p}}$. These equations define the generalized eigenvalue problem, for whose solution the relation between $\delta\phi$ and $A_{\parallel}$ has to be found. This will be derived

below. The solution of the generalized eigenvalue problem provides real eigenfrequencies ω_r and growth rates γ of the unstable modes.

Before introducing the relation between $\delta\phi$ and $A_\parallel$ and discussing the physics mechanisms of the two most common microturbulence modes in tokamak plasmas at low β_e, namely the ITG and the TEM, the dimensionless form of the above equations is introduced. Using

$$\hat{\phi} \equiv \frac{e\,\delta\phi}{T_\mathrm{e}}, \quad \hat{A}_\parallel = \frac{eA_\parallel}{T_\mathrm{e}}, \quad \hat{n}_\mathrm{H} \equiv \frac{\delta n_\mathrm{H}}{n_\mathrm{H}}, \quad \hat{T}_\mathrm{H} \equiv \frac{\delta T_\mathrm{H}}{T_\mathrm{H}}, \quad \hat{v}_{\parallel,\mathrm{H}} \equiv \frac{v_{\parallel,\mathrm{H}}}{c_\mathrm{sH}}$$

$$\hat{n}_\mathrm{et} \equiv \frac{\delta n_\mathrm{et}}{n_\mathrm{et}}, \quad \hat{T}_\mathrm{e} \equiv \frac{\delta T_\mathrm{e}}{T_\mathrm{e}}, \quad \hat{n}_\mathrm{p} \equiv \frac{\delta n_\mathrm{p}}{n_\mathrm{p}}, \quad \hat{T}_\mathrm{p} \equiv \frac{\delta T_\mathrm{p}}{T_\mathrm{p}}, \quad \hat{v}_{\parallel,\mathrm{p}} \equiv \frac{v_{\parallel,\mathrm{p}}}{c_\mathrm{sp}}$$

where $c_\mathrm{s,i} \equiv \sqrt{T_\mathrm{e}/m_\mathrm{i}}$ is the ion sound speed (i = H, p). Moreover, all frequencies are normalized to the ion fluid curvature and ∇B drift frequency $\omega_\mathrm{D,i} = \mathbf{k}\cdot\mathbf{v}_\mathrm{D,i} = -2k_\mathrm{y}T_\mathrm{i}/(Z_\mathrm{i}eBR)$, such that the dimensionless frequency is introduced. For instance $\hat{\omega}$ is defined as $\hat{\omega} \equiv \omega/\omega_\mathrm{D,H}$. From now on the FLR corrections in the continuity equations of both the hydrogen and the impurity species are neglected in the following in order to keep the derivation simple. Thus, the continuity equation reads

$$-\hat{\omega}\hat{n}_\sigma + \frac{\hat{n}_\sigma + \hat{T}_\sigma}{Z_\sigma} - \left(\frac{R}{2L_{\mathrm{n},\sigma}} - 1\right)\frac{T_\mathrm{e}}{T_\sigma}\hat{\phi} + \hat{k}_{||}\hat{v}_{||} = 0. \tag{3.25}$$

In this equation, the second term on the left hand side arises from a finite value of the divergence of the diamagnetic drift, which is due to magnetic field curvature and therefore proportional to $1/Z_\sigma$. The third term includes E×B advection and compression, respectively. Both are therefore independent of the species charge. The last term on the left hand side describes compression in the parallel velocity.

The electromagnetic parallel force balance is given by

$$-\frac{A_\sigma}{A_\mathrm{i}}\hat{\omega}\hat{v}_{||} + \frac{Z_\sigma T_\mathrm{e}}{T_\sigma}\hat{k}_{||}\hat{\phi} - \frac{Z_\sigma T_\mathrm{e}}{T_\sigma}\frac{c_\mathrm{s}}{c}\left[\hat{\omega} - \frac{1}{Z_\sigma}\left(\frac{R}{2L_{\mathrm{n},\sigma}} + \frac{R}{2L_{\mathrm{T},\sigma}}\right)\right]\hat{A}_{||} + \hat{k}_{||}\left(\hat{n}_\sigma + \hat{T}_\sigma\right) = 0, \tag{3.26}$$

where we introduced $A_\mathrm{p} = m_\mathrm{p}/m_\mathrm{H}$ and assumed $T_\mathrm{i} = T_\mathrm{p}$ and $Z_\mathrm{i} = 1$. The factor in front of $\hat{A}_{||}$ is composed of terms proportional to the logarithmic gradients of density and temperature, arising from the diamagnetic drift velocity and therefore charge dependent, and a term proportional to the complex eigenfrequency due to the time derivative $\partial_\mathrm{t}A_\parallel$. The last term on the left hand side of Eq. (3.26) represents the influence of a parallel pressure gradient.

Lastly, the energy balance equation is written as

$$\left(-\hat{\omega} + \frac{5}{3Z_\sigma}\right)\hat{T}_\sigma + \frac{2}{3}\hat{\omega}\hat{n}_\sigma - \left(\frac{R}{2L_{\mathrm{T},\sigma}} - \frac{R}{3L_{\mathrm{n},\sigma}}\right)\frac{T_\mathrm{e}}{T_\sigma}\hat{\phi} = 0. \tag{3.27}$$

The first term on the left hand side includes the diamagnetic heat flow and therefore a dependence on Z_σ, the second term stems from the divergence of the fluid velocity using the continuity Eq. (3.25), and the third term includes temperature and density advection due to the E×B flow, respectively.

The resulting equation system can be computed analytically in simplified cases, as well as by numerical routines solving the generalized eigenvalue problem of the kind

$$A \cdot \mathbf{x} = \omega\, B \cdot \mathbf{x}, \tag{3.28}$$

where A and B are given matrices and $\mathbf{x}$ is a vector of unknown variables. In the case of an electrostatic description the dimension of $\mathbf{x}$ is 8, which provides a dispersion relation of order 8, since e. g. the trapped electron density can be eliminated using the quasi–neutrality condition Eq. (3.24) in the electrostatic limit, where the $\hat{A}_{||}$–term is absent. Thus, its elements are the unknowns $\hat{\phi}$, $\hat{n}_{\mathrm{H}}$, $\hat{T}_{\mathrm{H}}$, $\hat{T}_{\mathrm{e}}$, $\hat{n}_{\mathrm{p}}$, $\hat{T}_{\mathrm{p}}$, $\hat{v}_{\parallel,\mathrm{H}}$, $\hat{v}_{\parallel,\mathrm{p}}$ defined above.

3.1.4 Relationship between fluctuating potentials $\hat{\phi}$ and $\hat{A}_{||}$

In order to perform an electromagnetic treatment (finite $\hat{A}_{||}$), the set of equations to be considered are Eqn. (3.15), (3.16), (3.17), (3.18), (3.23), and (3.24). They can be regarded as a homogeneous set of nine equations for ten unknowns $\hat{\phi}$, $\hat{A}_{||}$, $\hat{n}_{\mathrm{H}}$, $\hat{T}_{\mathrm{H}}$, $\hat{n}_{\mathrm{et}}$, $\hat{T}_{\mathrm{e}}$, $\hat{n}_{\mathrm{p}}$, $\hat{T}_{\mathrm{p}}$, $\hat{v}_{\parallel,\mathrm{H}}$ and $\hat{v}_{\parallel,\mathrm{p}}$. It is clear that a relation of the fluctuating potentials $\hat{\phi}$ and $\hat{A}_{||}$ is necessary in order to solve the generalized eigenvalue problem, Eq. (3.28). Following [48, 49], and combining passing electron continuity equation and parallel force balance with the Ampère's law, the relationship between the fluctuating electrostatic potential $\hat{\phi}$ and magnetic vector potential $\hat{A}_{||}$ is derived. This will be explained in more detail in the following.

Considering the continuity equation for passing electrons, Eq. (3.1), the relation between the potentials $\hat{\phi}$ and $\hat{A}_{||}$ is found. The parallel velocity is related to the magnetic vector potential through Ampère's law by using the approximation that the total parallel current, $j_{\parallel}$, is equal to the parallel electron current, $j_{\parallel} = -c/(4\pi)\Delta A_{\parallel}$. Using again Eq. (3.21), the density response is written as

$$\begin{aligned} \hat{n}_{\mathrm{e}} &= \frac{\omega_{*,\mathrm{e}} - \omega_{\mathrm{D,e}}}{\omega - \omega_{\mathrm{D,e}}}\hat{\phi} \\ &\quad + \left(\eta_{\mathrm{e}} \frac{\omega_{\mathrm{D,e}}\omega_{*,\mathrm{e}}}{\omega - \omega_{\mathrm{D,e}}} - k_{\perp}^2 \rho_{\mathrm{s}}^2 \frac{k_{\parallel}^2 v_{\mathrm{A}}^2}{\omega - \omega_{\mathrm{D,e}}} \right) \frac{\hat{A}_{||}}{k_{\parallel} c}. \end{aligned} \tag{3.29}$$

Finally, the combination of Eqn. (3.22) and (3.29) leads to

$$\begin{aligned} &\hat{A}_{||} = \hat{k}_{||} \frac{c}{c_{\mathrm{s}}} \left\{ \frac{-T_{\mathrm{e}}}{T_{\mathrm{i}}} \frac{R}{2L_{\mathrm{ne}}} - \hat{\omega} \right\} \times \\ &\left\{ \hat{\omega} \left(\frac{T_{\mathrm{e}}}{T_{\mathrm{i}}} \frac{R}{2L_{\mathrm{ne}}} - \hat{\omega} \right) - \frac{T_{\mathrm{e}}}{T_{\mathrm{i}}} \left[\hat{\omega} - (1+\eta_{\mathrm{e}}) \frac{T_{\mathrm{e}}}{T_{\mathrm{i}}} \frac{R}{2L_{\mathrm{ne}}} \right] + k_{\perp}^2 \rho_{\mathrm{i}}^2 k_{\parallel}^2 \frac{v_{\mathrm{A}}^2}{c_{\mathrm{s}}^2} \right\}^{-1} \hat{\phi}. \end{aligned} \tag{3.30}$$

In a more compact form, this can be written as

$$\hat{A}_{||} = \hat{k}_{||} \hat{\Omega}(\hat{\omega})\, \hat{\phi}. \tag{3.31}$$

The Alfvén velocity is given by $v_{\mathrm{A}}^2 = B^2/(4\pi n_{\mathrm{e}} m_{\mathrm{i}})$. In order to identify the explicit occurrence of electromagnetic terms in Eq. (3.30), a re–arrangement of the third term in

the denominator is made. This one is the leading contribution in the limit of small β_e. Assuming $n_e = n_i$, one finds $v_A^2/c_s^2 = 2\beta_e(T_i/T_e)$ with $\beta_i = T_e/T_i\ \beta_e$. The definition of $k_{||} = (qR)^{-1}$ in the simple model leads to the normalized parallel wave vector $\hat{k}_{||}^2 = (4q^2k_y^2\rho_i^2)^{-1}$. Therefore the last term is $k_\perp^2\rho_i^2k_{||}^2v_A^2/c_s^2 = k_\perp^2/(2q^2k_y^2\beta_i)$. Since usually $\hat{\omega} = \mathcal{O}(1)$ and, in the limit of small β_i, $k_\perp^2/(2q^2k_y^2\beta_i) = \mathcal{O}(10)$ to $\mathcal{O}(100)$ (assuming $k_\perp \approx k_y$), we identify the leading terms in $\hat{\Omega}(\hat{\omega})$, Eq. (3.31) via

$$\hat{\Omega}(\hat{\omega}) = -2\frac{c}{c_s}\beta_e q^2 \frac{k_\perp^2}{k_y^2}\left(\frac{R}{2L_{ne}} + \frac{T_i}{T_e}\hat{\omega}\right). \tag{3.32}$$

It is important to note that according to this Eq. (3.32) electromagnetic effects (due to a finite $A_\parallel$) scale like $\beta_e q^2$ [50]. This will become important in Chapter 6.

3.2 Ion temperature gradient mode

3.2.1 Historical overview

The first investigations on the ion temperature gradient (ITG) mode have been performed at the beginning of the 1960s by Rudakov and Sagdeev [51]. They solved the local dispersion relation in a slab geometry with a straight and constant magnetic field. The slab counterpart of the toroidal ITG is the so–called slab ITG, where an ion acoustic wave is driven unstable by the ion temperature gradient, and is due to parallel dynamics. The effect of a twist in the magnetic field lines was included by Coppi, et al. [52] in a sheared slab geometry. The development of the ballooning representation by Connor, Hastie and Taylor [45, 53] provided an important contribution to linear investigations in full toroidal geometry. In the local treatment, each Fourier harmonic is assumed to be independent by neglecting the harmonic coupling resulting from physical inhomogeneities. Harmonic coupling, for instance, leads to the fact that the poloidal variation of curvature and ∇B drifts in a tokamak introduces a coupling of different poloidal harmonics and makes the problem two–dimensional. The ballooning formalism reduces the toroidal gyrokinetic problem to a one dimensional one by exploiting the scale separation in the perpendicular direction between fast varying fluctuations and the equilibrium. This formalism was originally developed for MHD instabilities, but revealed its power also in the framework of drift waves [17], which led to the identification of the toroidal ITG mode. The work of Horton and co–workers [17] also identified the presence of a critical value $\eta_i = L_{n,i}/L_{T,i}$ above which the toroidal ITG is unstable, for the first time. In following works, the inclusion of kinetic effects of drift resonances in the ballooning formalism or in the local limit determined the critical threshold to $\eta_{i,crit} \simeq 1$, as it was reported in [54, 55]. The influence of a finite β on the ITG growth rate has been identified in [56, 57], where a stabilizing influence of the toroidal ITG was reported. Also, using fully toroidal calculations, a strong dependence of the ITG growth rate on the magnetic shear has been reported [58]. It is noted that the ballooning theory is able to model finite magnetic shear effects in the case of an evaluation of the radial mode structure.

3.2.2 Physics mechanism

The physics mechanism leading to an ITG mode is presented. An initial periodical temperature perturbation on a flux surface is considered. This implies the existence of regions

with higher temperature and thus thermal velocities. Since curvature and ∇B drift depend on particle energy, an initial temperature perturbation produces a density perturbation. As a consequence of quasi–neutrality and the higher parallel mobility of electrons compared to the ions, they compensate the charge accumulations produced by the density fluctuation. This is due to parallel motion, and leads to a modified condition of parallel force balance, Eq. (3.19), which involves a fluctuating electric field. In the electrostatic limit, passing electrons are adiabatic (see discussion in Chapter 3.1.2), such that they instantaneously follow the perturbed electric field. As already noted above, their density fluctuation is equal to the (normalized) electrostatic potential fluctuation, given by Eq. (3.20). Trapped electrons are excluded in this simple picture, since their parallel motion is zero due to bounce–averaging. The fluctuating electric field due to electrons streaming in parallel direction is the origin of an E×B drift. This, in turn, leads to a plasma flow from the high temperature side into the hot spots of the initial perturbation in the presence of a background temperature gradient. Fig. 3.2 shows the steps that lead to a destabilization of the initial temperature perturbation in the 'bad curvature region', i.e. the outer side of the torus, where the magnetic field is lower (the magnetic field in a circular large aspect ratio tokamak is given by $\mathbf{B} = B_0 R_0/R(\mathbf{e}_\phi + r\mathbf{e}_\theta/(qR_0))$, where R_0 is the tokamak major radius). In the 'good curvature region' on the inner side of the torus, the curvature and ∇B drift is still in the same direction, but the pressure gradient is reversed, leading to an E×B convection of hot plasma into cold spots of the initial temperature perturbation. Thus, on the high field side of the torus, initial perturbations are effectively damped. In the electromagnetic case with a finite β, perpendicular magnetic field fluctuations set in, leading to a lower parallel mobility of passing electrons due to radial displacements. As a consequence of their low inertia, electrons, which are responsible to establish plasma neutrality, are particularly susceptible to this kind of non–adiabatic response, leading to a phase shift and a smaller amplitude of the fluctuating electrostatic potential. The latter is the main reason for the electromagnetic stabilization of the ITG mode.

3.2.3 Critical temperature gradient

A complete description of the toroidal ITG mode requires to solve the gyrokinetic equation. However, the simple fluid model described above is able to describe the basic mechanism and the dynamics in a more transparent way. To this purpose, the hydrogen ion fluid equations (3.15) and (3.17) are taken into account. They allow for a coupling of density and temperature fluctuations. For simplicity, the parallel motion is neglected in the continuity equation (3.15). This approach is motivated by the fact that ion inertia is very high compared to the electron inertia. The coupling to the electrostatic potential is given by the parallel electron force balance, Eq. (3.19), where electromagnetic effects are included in contrast to usual simple derivations. Using the relation between $\hat{\phi}$ and $\hat{A}_{||}$, Eq. (3.30), the electromagnetic passing electron response, Eq. (3.22) can be written as

$$\frac{\delta n_\mathrm{i}}{n_\mathrm{i}} = \left[1 + \beta_\mathrm{e}^{\#}(\hat{\omega})\right] \frac{e\phi}{T_\mathrm{e}}, \tag{3.33}$$

with $\beta_\mathrm{e}^{\#}(\hat{\omega}) = 2\beta_\mathrm{e} q^2 \left[R/(2L_{\mathrm{n,e}}) + \hat{\omega}\right] \left[\hat{\omega} + (1+\eta_\mathrm{i})\hat{\omega}_{*,\mathrm{i}}\right] (k_\perp^2/k_\mathrm{y}^2)$. For simplicity, in the following analytical calculation of the ITG dispersion relation, a large ion temperature gradient is assumed such that $\beta_\mathrm{e}^{\#}$ can be written as $\beta_\mathrm{e}^{\#} = \beta_\mathrm{e} q^2 (R/L_{\mathrm{T,i}})(\omega_{*,\mathrm{i}} k_\perp^2/k_\mathrm{y}^2)$ is a positive number independent of $\hat{\omega}$. Then, Eq. (3.33) basically means that with a finite $\beta_\mathrm{e}^{\#}$ density

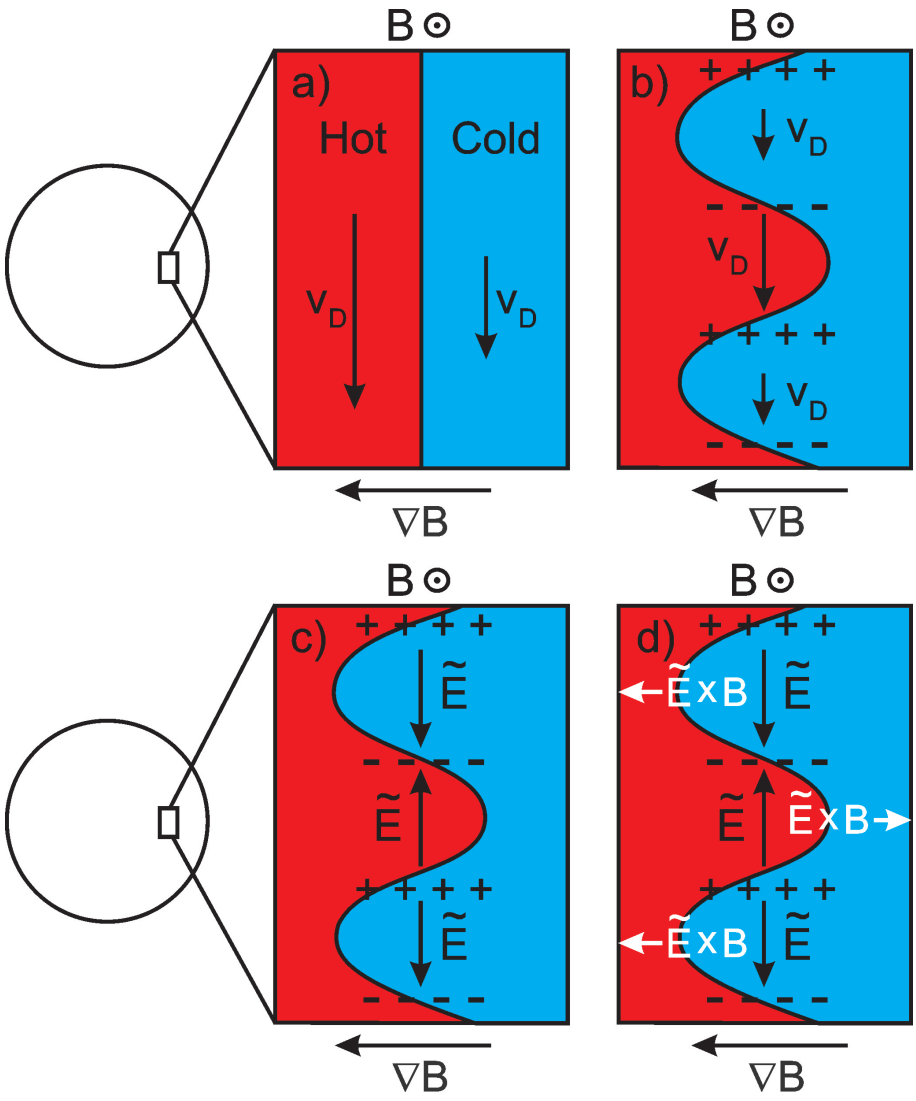

Figure 3.2: Main steps in the formation of an ion temperature gradient (ITG) mode. The initially unperturbed temperature profile leads to different curvature and ∇B drift velocities in the hot and cold region, respectively (a). A temperature perturbation causes a density perturbation (b), which is neutralized by the passing electrons producing a fluctuating electric field (c), leading to an E×B drift that destabilizes the initial temperature perturbation on the low field side (d).

fluctuations are able to only produce potential fluctuations of lower amplitude as compared to the electrostatic case, where $\beta_e^{\#} = 0$. Using Eqs. (3.15) without FLR effects, Eq. (3.17) and Eq. (3.33), and noting that $\omega_{*,e}\epsilon_{n,e}/\epsilon_{n,i} = -\omega_{*,i}$ for $Z_i = 1$ and equal ion and electron temperatures, the dispersion relation is given by

$$\begin{aligned} &(-\hat{\omega}+1)\left(-\hat{\omega}+\frac{5}{3}\right)\left(1+\beta_e^{\#}\right)- \\ \frac{2}{3}\hat{\omega}\left(1+\beta_e^{\#}\right)+\hat{\omega}_{*,i}&\left(\eta_i-\frac{2}{3}\right)+(1-\hat{\omega}_{*,i})\left(-\hat{\omega}+\frac{5}{3}\right) \;=\; 0. \end{aligned} \tag{3.34}$$

This equation has the two following roots in the flat density limit, $L_{\mathrm{n,i}} \to \infty$,

$$\omega \approx \frac{1}{6+6\beta_{\mathrm{e}}^{\#}}\left[\omega_{\mathrm{D,i}}\left(13+10\beta_{\mathrm{e}}^{\#}\right) \pm \sqrt{\omega_{\mathrm{D,i}}^2\left(49+80\beta_{\mathrm{e}}^{\#}\right) - 36\omega_{\mathrm{D,i}}\omega_{*,\mathrm{i}}\eta_{\mathrm{i}}\left(1+\beta_{\mathrm{e}}^{\#}\right)}\right], \tag{3.35}$$

where terms proportional to $(\beta_{\mathrm{e}}^{\#})^2$ are omitted due to their smallness. This expression shows the basic properties of the ITG mode. Firstly, in order to get an unstable mode, that is an imaginary part in ω, the last term in Eq. (3.35) has to overcome the first one. This is the typical situation of a threshold behavior, and it depends critically on the ion temperature gradient scale length $L_{\mathrm{T,i}}$, which is directly included in η_{i} (also indirectly in $\beta_{\mathrm{e}}^{\#}$). When $R/L_{\mathrm{T,i}}$ is large enough, ITG modes grow exponentially in time, proportional to $\exp(\gamma t)$ with a growth rate γ, arising from an imaginary part of the eigenfrequency $\omega = \omega_{\mathrm{r}} + i\gamma$. The crucial role of the perturbed E×B and magnetic curvature drifts is apparent through the dependence of the growth rate on $\omega_{*,\mathrm{i}}$ and $\omega_{\mathrm{D,i}}$. Secondly, according to the definitions of $\omega_{\mathrm{D,i}}$ and $\omega_{*,\mathrm{i}}$, Eqs. (3.5) and (3.11), the necessary requirement $\omega_{\mathrm{D,i}}\omega_{*,\mathrm{i}} > 0$ can be achieved only when $\nabla(n_{\mathrm{i}}T_{\mathrm{i}})$ and ∇B point in the same direction, otherwise the mode is stable. The requirement for an unstable mode is fulfilled at the low field side of the tokamak, whereas at the high field side $\omega_{\mathrm{D,i}}$ and $\omega_{*,\mathrm{i}}$ point in opposite directions, leading to a stabilization. Thirdly, the inclusion of electromagnetic effects, which is done here in a very crude simplification, stabilizes the ITG mode, at large $\eta_{\mathrm{i}} \gtrsim 2$ mainly due to the denominator dependence of Eq. (3.35). At small η_{i}, however, the stabilization is mainly due to a shift of the critical η_{i} towards higher η_{i} (in this simple model a change of $\beta_{\mathrm{e}}^{\#}$ from 0 to 0.05 with $\omega_{\mathrm{D,i}} = \omega_{*,\mathrm{i}} = 0.3c_{\mathrm{s}}/R$ caused an increase of the critical η_{i} from approximately 1.35 to 1.4). Lastly, as already mentioned, the toroidal ITG mode is primarily driven due to curvature and ∇B drift, which is reflected by the occurrence of $\omega_{\mathrm{D,i}}$ in Eq. (3.35). Moreover, the magnitude of ω is approximately the same as $\omega_{\mathrm{D,i}}$, typical for drift modes like the ITG, and the drift direction is the ion curvature and ∇B direction, such that $\hat{\omega}_r = \omega_{\mathrm{r}}/\omega_{\mathrm{D,i}} > 0$.

It is also instructive to discuss the additional effect of the phase shift between density and potential fluctuations due to the imaginary part of $\beta_{\mathrm{e}}^{\#}$ in Eq. (3.33). In the simplest picture of a drift wave, which is connected to the ITG mode, E×B convection is caused by density fluctuations,

$$\frac{\partial n_{\mathrm{i}}}{\partial t} + v_{\mathrm{E\times B,x}}\frac{\partial n_{\mathrm{i}}}{\partial x} = 0. \tag{3.36}$$

The electron density response is given by

$$\hat{n}_{\mathrm{e}} = \hat{\phi}(1 + i\bar{\beta}_{\mathrm{e}}^{\#}), \tag{3.37}$$

where $\bar{\beta}_{\mathrm{e}}^{\#} > 0$ is due to the electromagnetic correction from parallel dynamics. Using quasi–neutrality and with $v_{\mathrm{E\times B,x}} = -1/B\ \partial_{\mathrm{y}}\phi$, the dispersion relation

$$\omega = \frac{k_{\mathrm{y}}v_*}{1 + i\bar{\beta}_{\mathrm{e}}^{\#}} \tag{3.38}$$

from this simple model consisting of Eq. (3.36) and (3.37) can be found. For $\bar{\beta}_{\mathrm{e}}^{\#}$ small, but positive, the latter expression can be simplified to $\omega \approx k_{\mathrm{y}}v_*(1 - i\bar{\beta}_{\mathrm{e}}^{\#})$. Thus, the linear ITG growth rate $\gamma = -k_{\mathrm{y}}v_*\bar{\beta}_{\mathrm{e}}^{\#}$ is negative, which corresponds to a stable mode. Then, it

is clear that for the electromagnetic ITG mode the nonadiabatic response of electrons to density fluctuations implies a phase shift for the potential fluctuations. This phase shift acts against the mode drive and leads to a stabilization.

The simple fluid model does not contain FLR corrections or parallel dynamics of the ions. Moreover, a complete description requires the solution of the appropriate kinetic equation. The behavior of real eigenfrequencies and growth rates is shown in figure 3.3, for a typical ITG case, namely the GA-standard case with $R/L_T = 9$, $R/L_n = 3$, $q = 2$ and $s = 1$ as a function of the normalized binormal wave number $k_y\rho_s$ using the gyrokinetic code GYRO [19]. The typical ITG binormal scale length is above the ion gyroradius and

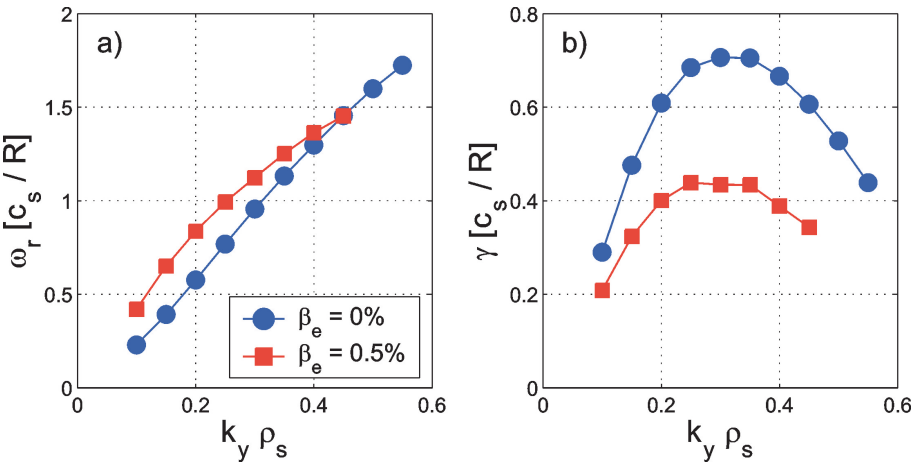

Figure 3.3: Binormal wavenumber spectrum of real eigenfrequency ω_r and linear growth rate γ for an ITG case, namely the GA standard case (parameters see text).

reaches its maximum, identified by the maximal growth rate, near $k_y\rho_s = 0.3$, see Fig. 3.3. For scales much larger than this value the instability is stabilized by parallel dynamics, for smaller scales it is stabilized by finite Larmor radius effects. Moreover, a clear stabilization of the ITG growth rate is visible in the comparison of the electrostatic case with $\beta_e = 0\%$ with the electromagnetic case at $\beta_e = 0.5\%$.

3.3 Trapped electron mode

3.3.1 Historical overview

Trapped particle modes have been described in a general review article on the subject by Kadomtsev, et al. [59]. More specific, the trapped ion mode was considered in the absence of an ion temperature gradient. It has been reported that under those conditions ion collisions are destabilizing. In a later publication the effects of a finite η_i were investigated [60]. It was found that for $\eta_i > 4/3$ ion collisions become destabilizing by tapping the free energy source of the ion pressure gradient. For the trapped electron mode (TEM), which was firstly reported in 1974 [61], an analytical threshold has been derived by Manheimer in 1976 [62]. First numerical investigations of TEM have been performed by Rewoldt and co–workers [63], which led to a more complete picture of TEMs and other small scale instabilities. The coupling between TEMs and toroidal ITG modes was shown by Weiland, Nordman and co–workers, and Romanelli and Briguglio, in 1990 [47, 64]. Below the ITG

critical threshold, the TEM can be unstable, depending on $\eta_e = L_{n,e}/L_{T,e}$ and on the electron collisionality.

3.3.2 Physics mechanism

The usual TEM is driven by $R/L_{T,e}$ and a similar picture of the mechanism can be drawn as for the ITG (for TEM, the difference in parallel dynamics between passing and trapped particles is the cause for the instability instead of the different mobility of ions and electrons in the ITG case). Here the basic picture for the formation of a TEM instability driven by a density gradient is explained. Thus, both ion and electrons are involved. Again, the focus is put on low frequency modes with typical frequencies much lower than the bounce frequency of trapped electrons. The density fluctuation causes a charge separation due to the opposite direction of curvature drifts for ions and trapped electrons. The low parallel mobility of trapped electrons is due to their very low bounce averaged parallel velocity, while for the ions inertia causes a low parallel mobility. Thus, ions and trapped electrons can be considered in the same way neglecting parallel motion. In this context it is noteworthy to point out that since trapped electrons spend most of their time on the low field side of the torus, the curvature drift has a preferred direction, whereas passing particles experience both the good and bad curvature regions and average this effect out. As in the ITG case, passing electrons neutralize the charge separation and introduce a fluctuating electrostatic potential. In the presence of a background density gradient, the resulting E×B flow enhances the density perturbation, such that the instability grows. This mechanism is shown in Fig. 3.4.

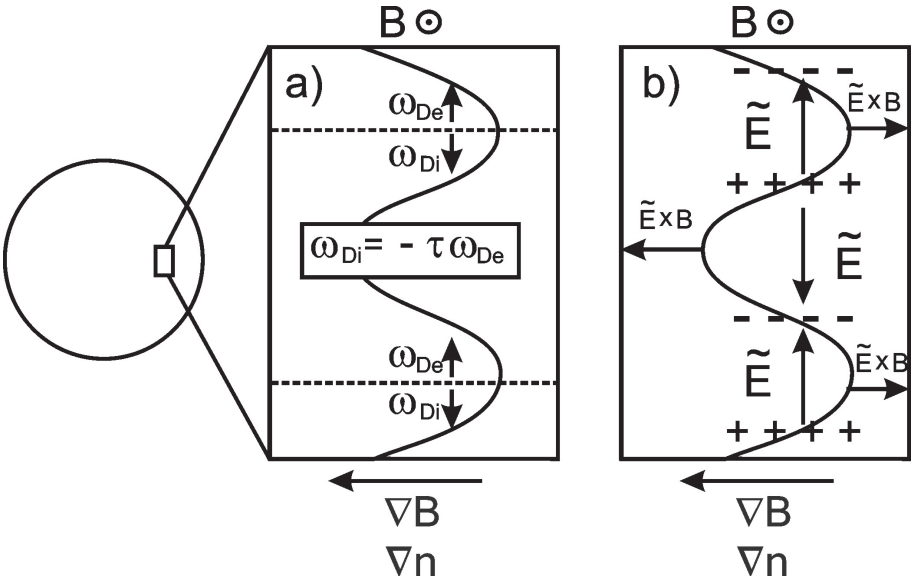

Figure 3.4: Physics mechanism leading to the formation of a trapped electron mode (TEM). A density fluctuation in connection with the different direction of ion and electron curvature drift (a) cause a charge separation. The resulting fluctuating electric field originating from passing electrons leads to an E×B flow, which enhances the initial perturbation (b).

3.3.3 Critical density gradient

Similar to the ITG case, the basic fluid model is considered in order to derive a critical density gradient for the TEM instability. In the most simple attempt, the ion and trapped electron continuity equations (3.15) and (3.18) can be written (in ion curvature and ∇B normalization) as

$$\left(-\hat{\omega}+1\right)\hat{n}_{\mathrm{i}}-\frac{1}{\tau}\left(\frac{R}{2L_{\mathrm{n}}}-1\right)\hat{\phi}=0 \tag{3.39}$$

and

$$\left(-\hat{\omega}-\frac{1}{\tau}\right)\hat{n}_{\mathrm{et}}-\frac{1}{\tau}\left(\frac{R}{2L_{\mathrm{n}}}-1\right)\hat{\phi}=0 \tag{3.40}$$

where temperature fluctuations are neglected for simplicity, and $\tau = T_{\mathrm{i}}/T_{\mathrm{e}}$ has been introduced. The quasi–neutrality condition is written as

$$\hat{n}_{\mathrm{i}} = f_{\mathrm{t}}\hat{n}_{\mathrm{et}} + (1-f_{\mathrm{t}})(1+\beta_{\mathrm{e}}^{\#})\hat{\phi}, \tag{3.41}$$

where the electrostatic potential has been modified in the same way as in the discussion of the electromagnetic ITG mode. Then, Eqn. (3.39),(3.40) and (3.41) define the dispersion relation. It shows that, in contrast to the ITG mode, the TEM drift direction is opposite to the ion curvature and ∇B direction, such that $\hat{\omega}_r = \omega_{\mathrm{r}}/\omega_{\mathrm{D,i}} < 0$. From the solution of the dispersion relation, the condition for a critical density gradient above which the TEM is unstable, can be derived. In the electrostatic limit, the expression reads

$$\frac{R}{L_{\mathrm{n}}} > 2\frac{2+\tau(1+f_{\mathrm{t}})-2(1+\tau)\sqrt{f_{\mathrm{t}}}}{1-f_{\mathrm{t}}}. \tag{3.42}$$

It is apparent that the threshold depends critically on both the trapped particle fraction f_{t} and the ion to electron temperature ratio τ. Figure 3.5 shows the dependence on these two parameters. Thus, for typical trapped particle fractions of tokamak plasmas at mid–radius, $f_{\mathrm{t}} \approx 0.5$, and equal ion to electron temperature, the threshold $R/L_{\mathrm{n,crit}}$ is below 3. A finite value of β_{e} does not change the TEM significantly, as it can be seen in figure (3.6) for the real eigenfrequency and the linear growth rate for a modified GA standard case with $R/L_{\mathrm{Ti}} = 3$ instead of $R/L_{\mathrm{Ti}} = 9$, while the other ones were kept fixed, leading to a dominant TEM instability. The TEM is much less affected by a finite value of β. This can be understood from figure 3.7. The ITG case is the GA-std case, while the TEM case is the modified GA-std case defined above (GA-std-TEM). At $k_{\mathrm{y}}\rho_{\mathrm{s}} = 0.3$, both show a similar electrostatic growth rate of $\sim 0.65[c_{\mathrm{s}}/R]$, such that a direct comparison is meaningful in terms of the ratio of perpendicular magnetic field fluctuations to electrostatic potential fluctuations. As a function of β_{e}, this ratio increases for both modes, but the absolute value is approximately one order of magnitude lower in the TEM case suggesting a much more electrostatic–like drive as compared to the ITG case. The physics picture of this difference is that for TEM the driving species, i.e. trapped electrons, experience density fluctuation, which cannot couple to parallel velocity due to the fast bounce averaging ($\langle v_{||}\rangle_{\mathrm{bounce}} = 0$), and therefore are not susceptible to $A_{||}$. ITG modes, on the other side, are driven by temperature fluctuations which couple to density fluctuations and due to Eq. (3.25) also to parallel velocity fluctuations. Therefore, they are stronger influenced by a fluctuating perpendicular magnetic field.

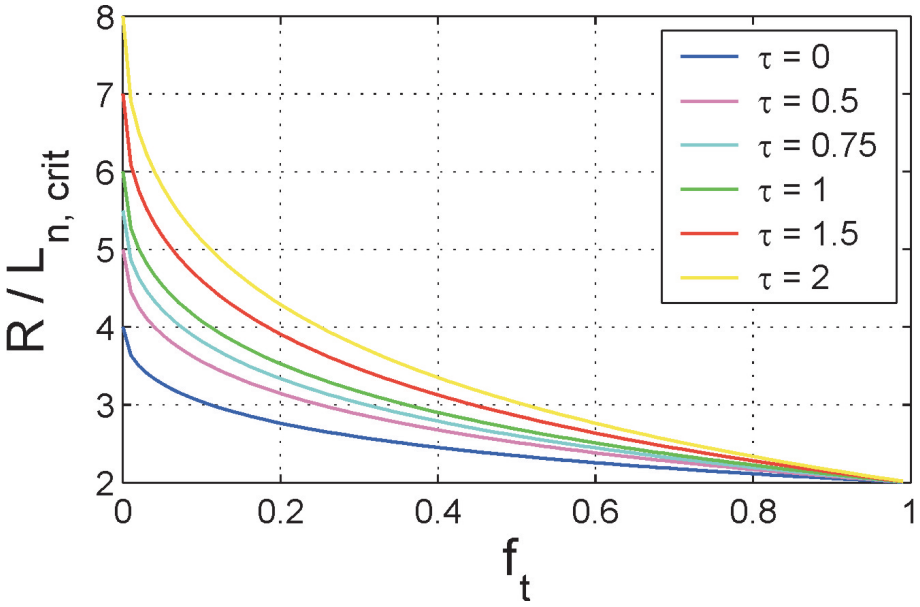

Figure 3.5: Threshold behavior of an electron temperature gradient mode (TEM) as a function of trapped particle fraction f_t and the ion to electron temperature ratio τ.

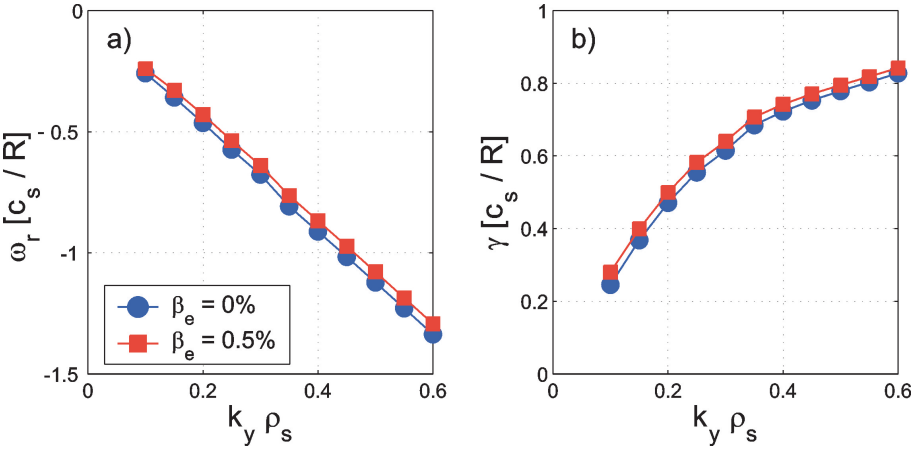

Figure 3.6: Binormal wavenumber spectrum of real eigenfrequency ω_r and linear growth rate γ for an TEM case (parameters see text).

Another important feature of TEMs is the fact that they are stabilized by electron–ion collisions, in contrast to ITG modes, which are practically unaffected. Collisions lead to trapping and de–trapping processes, and have a strong influence particularly on trapped electrons. They produce Coulomb diffusion in velocity space pushing the distribution function towards a Maxwellian. In the following it is shown how a finite electron to ion collision frequency ν_ei affects the growth rate of a TEM. To this purpose, the dissipative TEM is considered, which is driven by the combined effects of the trapped electron collisions and an electron temperature gradient. The discussion follows the work of Nilsson

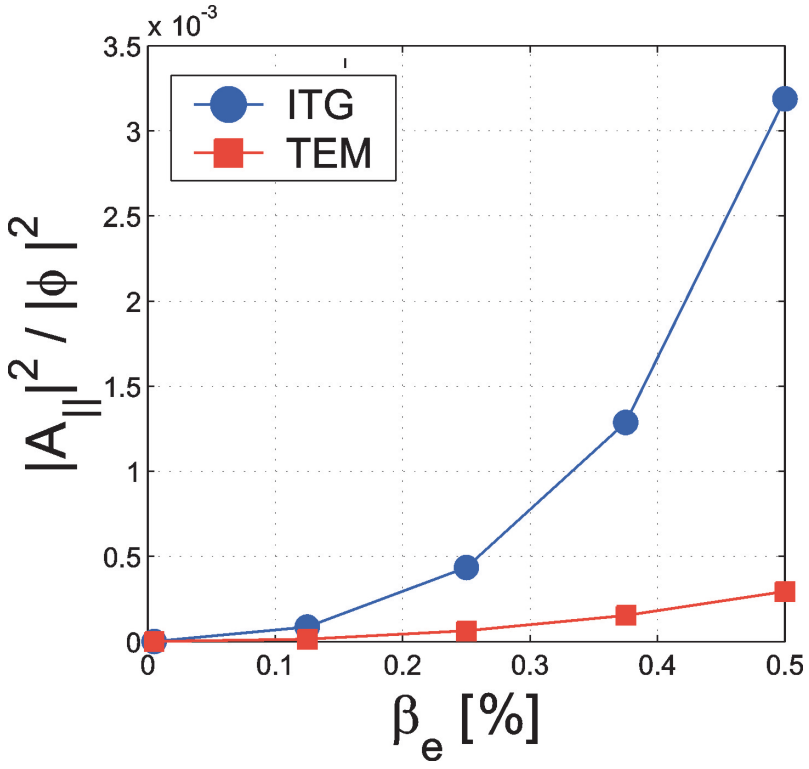

Figure 3.7: Ratio of perpendicular magnetic field fluctuations to electrostatic potential fluctuations as a function of β_e for an ITG (GA-std) and a TEM (GA-std-TEM) case (parameters see text).

and Weiland [65]. The trapped electron continuity equation is written as

$$\frac{\partial n_\mathrm{et}}{\partial t} + \nabla \cdot (n_\mathrm{et}\, \mathbf{v}_\mathrm{et}) = -\nu_\mathrm{th} \left[\delta n_\mathrm{et} - \Gamma n e\phi/T_\mathrm{e}\right], \tag{3.43}$$

with the collision frequency $\nu_\mathrm{th} = \nu_\mathrm{ei} R/r$ and $\Gamma = 1 + \eta_\mathrm{e}\omega_{*,\mathrm{e}} \left(\omega - \omega_{\mathrm{D,e}} + i\nu_\mathrm{th}\right)^{-1}$, obtained from a kinetic treatment. The latter kind of derivation is necessary since the collision frequency depends on the velocity. The purpose of the present calculation is to obtain fluid equations that do not contain velocity space integrals or plasma dispersion functions. Therefore, an approximate method is used where the velocity dependence of ν is firstly ignored. Owing to the inverse velocity dependence of ν, this method overestimates large velocities in the distribution function. Thus, the second part of the right hand side of Eq. (3.43) compensates this overestimation (details see [65]). Then, for the collision dominated TEM, one may approximate $\Gamma = 1 - i\eta_\mathrm{e}\omega_{*,\mathrm{e}}/\nu_\mathrm{th}$. Taking $\mathbf{v}_\mathrm{et} = \mathbf{v}_{\mathrm{E\times B}}$, the continuity Eq. (3.43) can be written as

$$\hat{n}_\mathrm{et} = \frac{\omega_{*,\mathrm{e}} + i\nu_\mathrm{th}\left(1 - i\eta_\mathrm{e}\omega_{*,\mathrm{e}}/\nu_\mathrm{th}\right)}{\omega + i\nu_\mathrm{th}}\hat{\phi}. \tag{3.44}$$

Using Eq. (3.20) and (3.13) with $\hat{n}_\mathrm{i} = \omega_{*,\mathrm{e}}/\omega\hat{\phi}$, and taking the limit $\nu_\mathrm{th} \gg \omega$, the dispersion relation reads

$$\omega = \omega_{*,\mathrm{e}} + i f_\mathrm{t} \eta_\mathrm{e} \omega \omega_{*,\mathrm{e}}/\nu_\mathrm{th}. \tag{3.45}$$

Since with the previously introduced limits $\nu_{\mathrm{th}} \gg \omega_{*,\mathrm{e}}$, it is $\omega \approx \omega_{*,\mathrm{e}}$, and the growth rate is

$$\gamma \simeq f_{\mathrm{t}} \eta_{\mathrm{e}} \omega_{*,\mathrm{e}}^2 / \nu_{\mathrm{th}}. \tag{3.46}$$

This relation shows the stabilization of the TEM with increasing collisionality.

3.4 Interplay of ITG and TEM

3.4.1 Eigenvalue problem

The aim of this Section is the discussion of the interplay between ITG and TEM microinstabilities. As it was explained in the previous sections, the inclusion of electromagnetic effects ($A_\parallel$ finite) does almost not change the thresholds of the unstable modes. Therefore, the electrostatic limit is assumed in the following. From the discussion in the last sections it can also be concluded that under realistic tokamak plasma conditions with mid–radius logarithmic temperature gradients of $R/L_{\mathrm{T}} = 6 - 9$ and logarithmic density gradients of $R/L_{\mathrm{n}} = 2 - 4$, both ITG and TEM may be unstable at the same time. This is underlined by the fact that the physics mechanism leading to both unstable modes are similar, and they occur at similar spacial scales. The fluid equations derived above are well suited for the study of the interplay of both modes. Impurities are present in tokamak plasmas only with a (very) low charge concentration (typically less than 5%). Therefore they are neglected for simplicity. Consequently, the five Eqn. (3.15), (3.17), (3.18), (3.23) and (3.24) in the electrostatic limit ($A_\parallel = 0$) with $f_{\mathrm{Z}} = 0$ are considered. As explained above, this set of equations is sufficient in order to cover the physics mechanisms responsible for both microturbulent modes. They lead to a generalized eigenvalue problem, which provides a dispersion relation of order four. Its solution implies the distinction between ITG and TEM, which is done by the sign of the real eigenfrequency corresponding to the largest growth rate, namely it is a dominant ITG for $\hat{\omega}_r = \omega_{\mathrm{r}}/\omega_{\mathrm{D,i}} > 0$ or a dominant TEM for $\hat{\omega}_r = \omega_{\mathrm{r}}/\omega_{\mathrm{D,i}} < 0$.

3.4.2 Numerical solution

Despite the simplicity of the equation system consisting of Eqn. (3.15), (3.17), (3.18), (3.23) and (3.24) in the electrostatic limit ($A_\parallel = 0$) with $f_{\mathrm{Z}} = 0$ and its corresponding dispersion relation, an analytical solution is impossible due to the fact that the dispersion relation is of order four. Therefore, the solution of the eigenvalue problem is calculated using a `Mathematica` routine, which is documented in the Appendix. Figure 3.8 shows four cases of a stability diagram for the combined ITG–TEM eigenvalue problem. In figure 3.8a), the case of typical tokamak plasma parameters at mid–radius with $f_{\mathrm{t}} = 0.5, \tau = 1$ is presented. If not stated otherwise, the logarithmic density and temperature gradients are the same for ions and trapped electrons and labeled by R/L_{n} and R/L_{T}, respectively. For small R/L_{n} and R/L_{T} within the green area, the plasma is stable, which means that no imaginry part for $\hat{\omega}$ is found. Increasing the logarithmic temperature gradient, the plasma gets unstable for R/L_{T} approximately exceeding 2. In the violet region, one single unstable root, that is $\gamma > 0$, is found, and the corresponding real eigenfrequency is positive. This defines the parameter area of a pure ITG. For even larger $R/L_{\mathrm{T}} \gtrsim 4$, two unstable roots occur. In the parameter range defined by the yellow color, the real eigenfrequency corresponding to the larger growth rate is positive, while the smaller growth

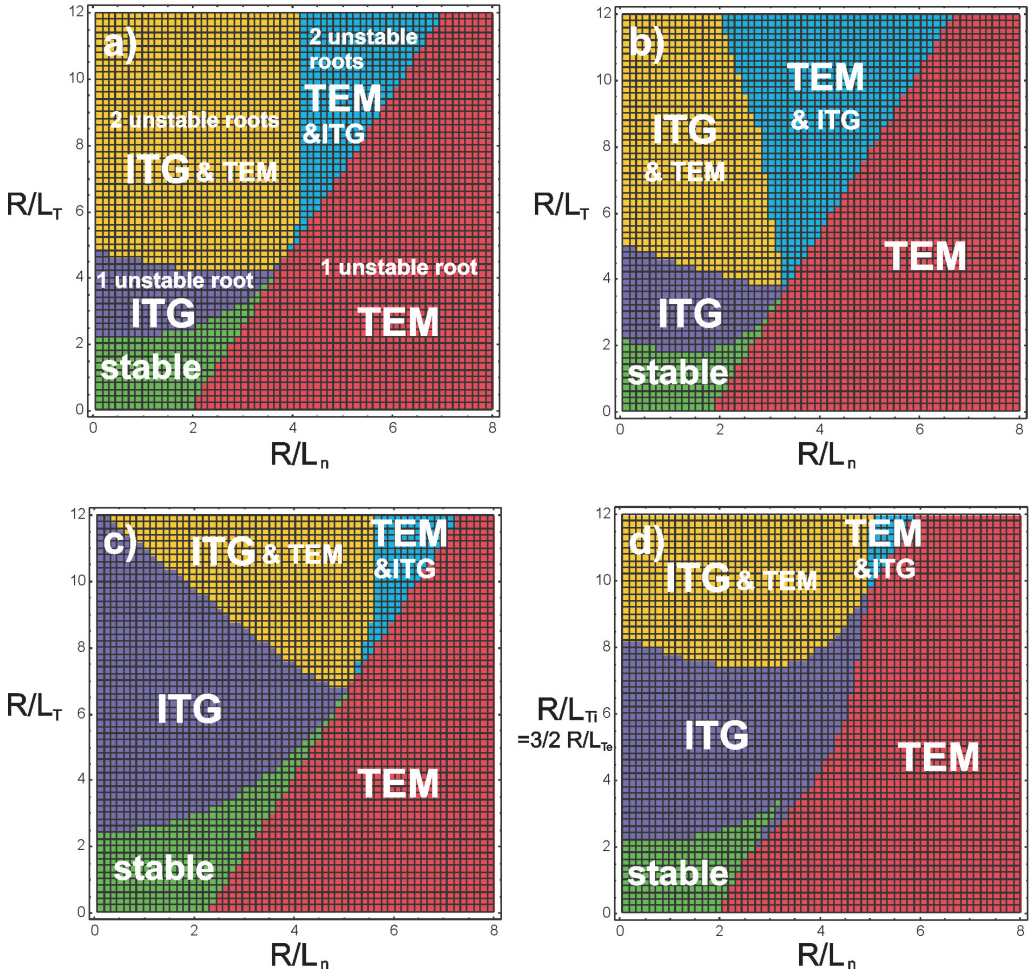

Figure 3.8: Stability diagrams for the ITG–TEM eigenvalue problem as a function of $R/L_{\mathrm{n,i}} = R/L_{\mathrm{n,e}} \equiv R/L_{\mathrm{n}}$ and $R/L_{\mathrm{T,i}} = R/L_{\mathrm{T,e}} \equiv R/L_{\mathrm{T}}$, in the case of $f_{\mathrm{t}} = 0.5, \tau = 1$ (a), $f_{\mathrm{t}} = 0.5, \tau = 0.5$ (b), $f_{\mathrm{t}} = 0.3, \tau = 1$ (c) and $f_{\mathrm{t}} = 0.5, \tau = 1$ with $R/L_{\mathrm{T,i}} = (3/2)(R/L_{\mathrm{T,e}})$ (d).

rate is connected with a negative real eigenfrequency. Therefore, the dominant instability is an ITG with a subdominant TEM. For high logarithmic temperature gradients ($R/L_{\mathrm{T}} > 6$) and logarithmic density gradients exceeding four, the situation is reversed. This leads to a dominant TEM with a subdominant ITG instability within the cyan area. For high R/L_{n} (and high R/L_{T}), only one unstable root is found. The corresponding real eigenfrequency is negative. Thus, the red area denotes the parameter range of a pure TEM.

The same color coding is used also for figures 3.8b),c) and d). In b), the same parameters as in a) have chosen, except the ion to electron temperature ratio was reduced to $\tau = 0.5$. This has the effect of slightly decreasing the TEM threshold at vanishing R/L_{T}. More pronounced and experimentally relevant is the strong shift of the boundary at which ITG and TEM have an equal growth rate, i.e. the transition from yellow to cyan, towards lower logarithmic density gradients. This means a stronger destabilization of TEMs with increasing R/L_{n} as compared to the $\tau = 1$ case in a). In figure 3.8c),

the ion to electron temperature ratio was reset to 1, but the trapped particle fraction is reduced to $f_t = 0.3$. This essentially means to move from mid–radius towards the core of the plasma. Therefore, the drive of the TEM is reduced, leading to a slightly higher threshold at vanishing temperature gradient in comparison to figure 3.8a). It also means a higher logarithmic temperature gradient threshold for subdominant TEM instabilities, since the parameter region where the ITG mode is the only unstable one, is strongly enlarged. Moreover, the transition from ITG to TEM dominated instability is shifted towards larger R/L_n. In figure 3.8d), the effect of a larger ion logarithmic temperature gradient compared to the electron one is shown. As it will be presented in the chapter on heat transport, $R/L_{T,i}$ clearly exceeds $R/L_{T,e}$ in the core of high β, low collisionality H–mode plasmas with large neutral beam or ion cyclotron resonance heating in present devices. Therefore, the assumption $R/L_{T,i} = (3/2)(R/L_{T,e})$ made here can be considered to be of relevance. Compared to figure 3.8a), this leads to a stabilization of TEMs at $R/L_{T,i} \gtrsim 4$, and to larger regions in which ITG alone or ITG and subdominant TEM are unstable. For experimentally relevant parameters of $R/L_{T,i} = 6 - 8$ and $R/L_n = 2 - 4$, the ITG is clearly the most unstable mode under those conditions.

Chapter 4

Investigations of electromagnetic effects on electron particle transport

4.1 Formulation of the problem

The increasing interest in high β_N scenarios, like the hybrid scenario with β_N up to 3 [66, 67, 68], for the operation of future fusion experiments like ITER motivates the study of the impact of β on the electron particle transport in tokamak plasmas. Particle transport determines the peaking of the density profile, which directly impacts the fusion power, since this is proportional to the density squared. The interplay between these parameters is underlined by recent studies pointing out that the cost of fusion electricity will be proportional to $\beta_N^{-0.4}(n/n_G)^{-0.3}$ [69], where n_G is the Greenwald density limit [70]. Thus, operational scenarios combining both high β_N and high densities are required to reach the goal of an economically viable energy source.

As it can be already concluded from Chapter 3, particle transport in the core of tokamaks is produced by microturbulence, mainly due to ion temperature gradient (ITG) and trapped electron modes (TEM), see [71] and references therein. This has been underlined by large amount of studies performed during the last decade from both the experimental and the theoretical standpoint. However, only a rather limited amount of experimental studies have been performed so far specifically on the dependence of electron particle transport and density peaking on β. This might be a consequence of the fact that from the experimental side, statistical analysis over large data sets have found weak effects of β on the density peaking in general [72, 73, 74]. Interestingly, however, an increase of β in all these studies has been found to be correlated with a reduction, albeit weak, of the density peaking. From the theoretical standpoint, electromagnetic effects on particle transport have been investigated with both fluid [49] and gyrokinetic [75] approaches. In [49], a quasi–linear study has revealed the existence of a convective contribution due to electromagnetic induction which is directed outward in the case of ITG modes, and which can reverse direction and become a pinch in the case of TEM. This result is consistent with the nonlinear gyrokinetic results presented in [75], where in an ITG turbulence simulation the increase of β_e is found to strongly affect the particle flux, and to reverse its direction from inward, in the electrostatic case, to outward when β_e exceeds the experimentally rel-

evant value of 0.5%. In both these previous works, the magnetic equilibrium parameters were not varied consistently with increasing β_e. Those theoretical results indicate a rather strong impact of electromagnetic effects on particle transport, which might be interpreted as being in quantitative disagreement with the experimental observations obtained so far, although qualitatively consistent with the theoretical prediction of a reduction of density peaking with increasing β.

In the framework of this thesis, specifically the effect of β on particle transport considering both the electromagnetic effect due to the inclusion in the turbulent fields of the magnetic field fluctuations given by the solution of the Ampére's law, and the geometrical (electrostatic) effect produced by an increase of β in the magnetic equilibrium, which affects the vertical drift, is studied. The investigation of both these two effects allows us to perform simulations in which the problem of the β dependence of density peaking in experimental conditions can be addressed in a realistic way. In fact, these two effects are unavoidably combined in an experiment, while they can be separated in theoretical studies, which are appropriate and interesting for specific analysis. In the following Sections, results from linear and nonlinear gyrokinetic simulations are presented, and the underlying physics is explained by means of an analytical derivation in which both the $E \times B$ and the magnetic flutter transport are computed starting from a formal analytical solution of the gyrokinetic equation. Magnetic flutter is caused by the fluctuating magnetic field in the direction perpendicular to that of the equilibrium field [76, 77, 78]. A quasi–linear approach is applied, justified by present knowledge of turbulent transport in the core of tokamak plasmas, which reveals that most of the main features obtained in nonlinear simulations are well captured by quasi–linear models [79, 80, 81]. In addition, comparisons among different assumptions for the wave number spectrum in quasi–linear calculations and nonlinear results, which require very high computational effort particularly for electromagnetic cases so far, show the critical role played by this ingredient in the quasi–linear models for the prediction of the logarithmic density gradients at the null of the flux. This quantity turns out to be a particularly well suited figure of merit for models of the wave number spectrum assumed in quasi–linear transport calculations.

Following the discussions in [82], the problem of the effects of β on electron particle transport is studied as follows. In the next Section, an analytical calculation is presented by which expressions of the electromagnetic effects on particle fluxes are derived and directly compared with the numerical results, which allows the identification of the main physical mechanisms at play. Then, a set of quasi–linear calculations with GYRO show the impact of β_e on the logarithmic density gradient at the null of the particle flux, considering separately both the effect due to magnetic field fluctuations and the effect due to the geometrical modification of the curvature drift produced by the compression of the magnetic flux surfaces with increasing β. Both collisionless and collisional simulations are performed, given the important role played by collisionality on particle transport [83]. Afterwards, a realistic case with typical parameters of a high confinement (H–) mode at mid–radius is considered and the effect of β on the logarithmic density gradient at the null of the particle flux is computed with both linear and nonlinear gyrokinetic calculations including a detailed comparison between quasi–linear and nonlinear spectra and addressing the problem of the comparison of the theoretical results with the experiment. In the end the main conclusions of this study are presented.

4.2 Analytical investigations

A detailed analytical description of particle transport is presented, in which electromagnetic effects provided by Ampère's law with a finite value of β_{e} are included. In the main part of this Section it will be shown that the most significant effect is on passing particles, consistently with a previous fluid calculation [49]. The passing particle flux is finite due to the loss of adiabaticity induced by the additional $(v_{||}/c)A_{||}$ term in the gyrokinetic equation of motion. The loss of adiabaticity of passing electrons was also pointed out in [84], and has a strong influence in ITG dominated microturbulence. A set of subsections has been included with the aim of discussing the separation of electromagnetic fluxes into their E×B and flutter components, the impact of shear and the pressure gradient parameter α, the role of collisions and the behavior in TEM dominated microturbulence. The parameter $\alpha = \alpha_{\mathrm{MHD}}$ encapsulates the pressure gradient contribution to the curvature drift in the $s-\alpha$ geometry model of circular flux surfaces in the large aspect ratio limit.

Following the discussion of Chapter 2, the linear gyrokinetic equation for a particle species σ is given by an evolution equation for the non-adiabatic component of the perturbed distribution function δf_σ, i.e. h_σ. The gyrokinetic equation for the perturbed distribution function h_{k} at the wave number k_{y}, binormal to the unperturbed magnetic field, is obtained from the ballooning representation in Eq. (2.80) and reads

$$\begin{aligned}&\left[\omega_{\mathrm{r,k}} + i\left(\gamma_{\mathrm{k}} + \nu_{\mathrm{k}}\right) - k_{||}v_{||} - \omega_{\mathrm{d,k}}/Z_\sigma\right] h_{\mathrm{k},\sigma} = \\ &\left\{\omega_{\mathrm{r,k}} + i\gamma_{\mathrm{k}} - \frac{\omega_{\mathrm{D,k}}}{Z_\sigma}\left[\frac{R}{L_{\mathrm{n},\sigma}} + \left(\frac{E}{T_\sigma} - \frac{3}{2}\right)\frac{R}{L_{\mathrm{T},\sigma}}\right]\right\}\frac{Z_\sigma e}{T_\sigma} F_{\mathrm{M}} J_{0,\sigma} U_{\mathrm{k}}\end{aligned} \tag{4.1}$$

where ω_{r} and γ are respectively the real part and the growth rate in the complex eigenfrequency ω. The subscript $||$ denotes the direction parallel to the unperturbed background magnetic field, and E is the kinetic energy of a particle. Here, the operator describing the spatial derivative along the field line is formally replaced by a parallel wave number $k_{||}$ and treated as a numerical factor proportional to $1/(qR)$. Similarly, a Krook collision operator is included, with a generic collision frequency $\nu(E,\lambda)$ with the energy E and the pitch angle parameter λ. The generalized potential $U_{\mathrm{k}} \equiv \phi_{\mathrm{k}} - (v_{||}/c)A_{||,\mathrm{k}}$ consists of the fluctuating electrostatic potential ϕ_{k} and the parallel component of the fluctuating vector potential $A_{||,\mathrm{k}}$. The effect of the compressional Alfvén dynamics due to $\delta B_{||}$ has been computed for typical tokamak parameters used in this study and turns out to impact the results in a negligible way (less than 2% for the highest β_{e} values considered here). Therefore it is neglected. However, it is worth noting that parallel magnetic field fluctuations can have an important influence at the very high values of β_{e} obtained in spherical tokamaks, as it has been shown in [85]. Here, the simplified $s-\alpha$ geometry model is used.

The radial electron particle flux, comprising both E×B and magnetic flutter, is given by

$$\Gamma_\sigma = \Re\sum_{\mathrm{k}}\langle\int d^3v\ \ J_{0,\sigma}h_{\mathrm{k}}^*\left(\frac{c}{B}\mathbf{e}_{||}\times\nabla\tilde{U}_{\mathrm{k}}\right)\nabla r\rangle_{\mathrm{FS}} = \Re\sum_{\mathrm{k}}\langle\int d^3v\ \ J_{0,\sigma}h_{\mathrm{k}}^*\left(ik_{\mathrm{y}}\rho_{\mathrm{s}}c_{\mathrm{s}}\hat{U}_{\mathrm{k}}\right)\rangle_{\mathrm{FS}}. \tag{4.2}$$

Here, the normalization $\hat{U}_{\mathrm{k}} = eU_{\mathrm{k}}/T_{\mathrm{e}}$ has been included. The $\langle ...\rangle_{\mathrm{FS}}$ operator denotes the flux surface average and the asterisk '*' the complex conjugate. Then, Eq. (4.1) can be formally solved for $h_{\mathrm{k},\sigma}$, and the result can be used in Eq. (4.2) to find an analytical expression for the particle flux. Direct electromagnetic effects caused by $(v_{||}/c)A_{||}$ on trapped

electrons can be considered small due to the small average parallel velocity produced by the fast bouncing. Therefore, for trapped electrons, electrostatic expressions, like those derived in [86] remain applicable, and indirect electromagnetic effects on trapped particle fluxes are produced by the change of the real eigenfrequency and the linear growth rate caused by the inclusion of a finite β_e. These effects, which are similar to the leading ones identified for impurity transport [87], as it will be presented in the next Chapter, remain only a minor correction in electron particle transport, as compared with the impact of the additional terms due to $(v_{||}/c)A_{||}$ for passing particles. Thus, in the analytical derivations focus is put on the passing electron response. A formal solution of Eq. (4.1) for h_k reads

$$\begin{aligned} h_{\mathrm{k},\sigma} &= \frac{N_{\mathrm{pass,k},\sigma}}{D_{\mathrm{pass,k},\sigma}} Z_\sigma F_{\mathrm{M},\sigma} J_{0,\sigma} \hat{U}_\mathrm{k}, \\ N_{\mathrm{pass,k},\sigma} &= \left\{ \omega_{\mathrm{r,k}} + i\gamma_\mathrm{k} - \omega_{\mathrm{D,k}}/Z_\sigma \left[\frac{R}{L_\mathrm{n}} + \left(\frac{E}{T} - \frac{3}{2} \right) \frac{R}{L_\mathrm{T}} \right] \right\} \times \\ &\quad \left\{ \omega_{\mathrm{r,k}} - k_{||} v_{||} - \frac{\omega_{\mathrm{d,k}}}{Z_\sigma} - i\left(\gamma_\mathrm{k} + \nu_\mathrm{k}\right) \right\}, \\ D_{\mathrm{pass,k},\sigma} &= \left(\gamma_\mathrm{k} + \nu_\mathrm{k}\right)^2 + \left(\omega_{\mathrm{r,k}} - k_{||} v_{||} - \omega_{\mathrm{d,k}}/Z_\sigma\right)^2 . \end{aligned} \tag{4.3}$$

In order to compare the expression containing $\hat{A}_{||}$ through $\hat{U}$ with the electrostatic one in former works [71, 86, 88], it is instructive to reformulate the phase correlation between fluctuating density and the generalized potential $\hat{U}$ used for the electromagnetic radial electron flux. Thus, Eq. (4.2) is rewritten in a form containing only ϕ such that the electromagnetic effects caused by $A_{||}$ are explicitly included in the phase shift. This in turn allows us to underline the actual electromagnetic ingredients in the physics. To this purpose, a relation between $\hat{A}_{||}$ and $\hat{\phi}$ is required. This can be obtained using the Fourier transformed Ampère's law for the parallel component of the vector potential, given by

$$k_\perp^2 A_{||,\mathrm{k}} = -\frac{4\pi e}{c} \sum_\sigma \int d^3 v v_{||} Z_\sigma \delta f_{\sigma,\mathrm{k}} J_{0,\sigma}. \tag{4.4}$$

Keeping in mind that only the non-adiabatic part of $\delta f_{\sigma,\mathrm{k}}$, namely $h_{\sigma,\mathrm{k}}$, produces a net current, and taking Eq. (4.3) for the passing particles, the relation between $\hat{A}_{||,\mathrm{k}}$ and $\hat{\phi}_\mathrm{k}$ reads $\hat{A}_{||,\mathrm{k}} = (c/c_\mathrm{s})\hat{\Omega}_\mathrm{k}\hat{\phi}_\mathrm{k} = (c/c_\mathrm{s})\left(\hat{\Omega}_{\mathrm{r,k}} + i\hat{\Omega}_{\mathrm{i,k}}\right)\hat{\phi}_\mathrm{k}$, with

$$\hat{\Omega}_\mathrm{k} = \frac{\beta_\mathrm{e} \sum_\sigma \int d^3 v v_{||}/c_\mathrm{s} \left(-Z_\sigma N_{\mathrm{pass,k},\sigma}/D_{\mathrm{pass,k},\sigma}\right) F_{\mathrm{M,v}} J_{0,\sigma}}{2\left(k_\perp \rho_\mathrm{s}\right)^2 + \beta_\mathrm{e} \sum_\sigma \int d^3 v v_{||}^2/c_\mathrm{s}^2 \left(-Z_\sigma N_{\mathrm{pass,k},\sigma}/D_{\mathrm{pass,k},\sigma}\right) F_{\mathrm{M,v}} J_{0,\sigma}}, \tag{4.5}$$

where $F_{\mathrm{M,v}} = F_\mathrm{M}/n_0$. From this description it is apparent that β_e is the parameter implying perpendicular magnetic field fluctuations. In present day tokamaks this parameter can reach relatively large values, typically from 0.6 % to 1.3 % in hybrid scenario operation, like in the experiments presented in [89]. Thus, the absolute value of $\hat{\Omega}_\mathrm{k}$ is of the order of a few percent. At this point it is also important to discuss the symmetry properties of the additional terms originating from fluctuations in $\hat{A}_{||}$ and contributing to Eq. (4.2) with respect to the ballooning angle θ_b, because the expression of the particle flux contains the integration over θ_b in the flux surface average. Since $\hat{\phi}_\mathrm{k}$ is symmetric in θ_b and $\hat{A}_{||,\mathrm{k}}$ is antisymmetric, $\hat{\Omega}_\mathrm{k}$ must be antisymmetric as well.

Introducing the trapped particle fraction $f_{\rm t}$, the expression for the radial particle flux caused by passing electrons reads

$$\Gamma_{\rm pass} = (1-f_{\rm t}) \sum_{\rm k} \langle k_{\rm y}\rho_{\rm s} c_{\rm s} \int d^3v \left[1 - 2\hat{v}_{||}\hat{\Omega}_{\rm r,k} + \hat{v}_{||}^2\left(\hat{\Omega}_{\rm r,k}^2 + \hat{\Omega}_{\rm i,k}^2\right)\right] F_0 J_{0,\rm e}^2 |\hat{\phi}_{\rm k}|^2 \times$$
$$\frac{\left(\hat{\gamma}_{\rm k} + \hat{\nu}_{\rm k}\right) k_{\rm y}\rho_{\rm s}\left[R/L_{\rm n} + \left(E/T_{\rm e} - 3/2\right) R/L_{\rm Te}\right] - \left[\hat{\gamma}_{\rm k}\left(\hat{k}_{||}\hat{v}_{||} + \hat{\omega}_{\rm d,k}\right) - \hat{\omega}_{\rm r,k}\hat{\nu}_{\rm k}\right]}{\left(\hat{\omega}_{\rm r,k} + \hat{k}_{||}\hat{v}_{||} + \hat{\omega}_{\rm d,k}\right)^2 + \left(\hat{\gamma}_{\rm k} + \hat{\nu}_{\rm k}\right)^2} \rangle_{\rm FS}. \tag{4.6}$$

Note that here all the frequencies have been normalized to $c_{\rm s}/R$ and velocities to $c_{\rm s}$. This has not to be confused with the frequency normalization used in the fluid model, where a hat identified the normalization to $\omega_{\rm D,i}$. The sign convention is such that a positive value of $\hat{\omega}_{\rm r}$ denotes a mode propagating in the ion diamagnetic direction, that is an ITG. Compared to former works [71], the new terms in the expression of the flux are those proportional to $\hat{\Omega}_{\rm r,k}$ and $\hat{\Omega}_{\rm i,k}$.

The calculation of $|U_{\rm k}|^2$ yields the three terms in the first square bracket at the right hand side of Eq. (4.6), where the electrostatic component, and the two electromagnetic components, at the first and the second power of $v_{||}$, and given respectively by $-2Re(\phi_{\rm k}^*\ A_{||,\rm k})v_{||}/c$, and by $|A_{||,\rm k}|^2(v_{||}/c)^2$, can be easily identified. It is important to note that the radial particle flux is not linear in the logarithmic gradients of density and temperature due to the implicit dependence of $\hat{\omega}_{\rm r}$ and $\hat{\gamma}$ on the gradients. In addition $\hat{\Omega}$ contains $R/L_{\rm n}$ and $R/L_{\rm T}$ as well, providing a new source of nonlinearity. However, Eq. (4.6) can be still decomposed, and allows the identification of diffusive, thermodiffusive and convective parts due to the explicit occurrence of terms proportional $R/L_{\rm n}$ and $R/L_{\rm T}$ or terms not explicitly proportional to any gradient, originating from the right hand side of the gyrokinetic Eq. (4.1).

In order to check the relative importance of electromagnetic effects on passing and trapped electrons, a standard case of ITG dominated microturbulence for a plasma of deuterons and electrons is defined. That case is used throughout this Section unless specified otherwise. The local parameters are the inverse aspect ratio $r/R = 0.17$, the safety factor $q = 1.4$ with a magnetic shear of $s = (r/q)\partial_{\rm r} q = 0.8$, the normalized logarithmic temperature gradients for deuterons and electrons $R/L_{\rm Ti} = R/L_{\rm Te} = 9 \equiv R/L_{\rm T}$ and the deuterium to electron temperature ratio $T_{\rm i}/T_{\rm e} = 1$.

Fig. 4.1 shows the fluxes computed in GYRO linear simulations at a single $k_{\rm y}\rho_{\rm s} = 0.1$ (where the maximum of the linear wave number spectrum of $\gamma/ < k_\perp^2 >$ is located), with different values of $R/L_{\rm n}$ in circular geometry neglecting the effects of pressure gradients on the magnetic equilibrium ($\alpha = 0$), as a function of the pitch angle parameter λ. The normalization has been taken in such a way that the total flux is given by the integral over λ, i.e. $\Gamma = \int_0^{\lambda_{\rm max}} \Gamma(\lambda) d\lambda$. The transition from passing to trapped particles is denoted by the black vertical line. From the $\beta_{\rm e} = 0$ curves it is apparent that the passing particles do not produce a significant flux since they are nearly adiabatic. Thus, the total flux is mainly given by the trapped particles, and it is inward for low $R/L_{\rm n}$, Fig. 4.1(a, b), while it points outward for large $R/L_{\rm n}$, Fig. 4.1c. At low logarithmic density gradients, the thermodiffusive and convective trapped electron fluxes are directed inwards and dominate, while at higher $R/L_{\rm n}$ the increasing contribution of the outward directed diffusive term reverses the direction of the electron flux. The reversal of the direction is qualitatively the

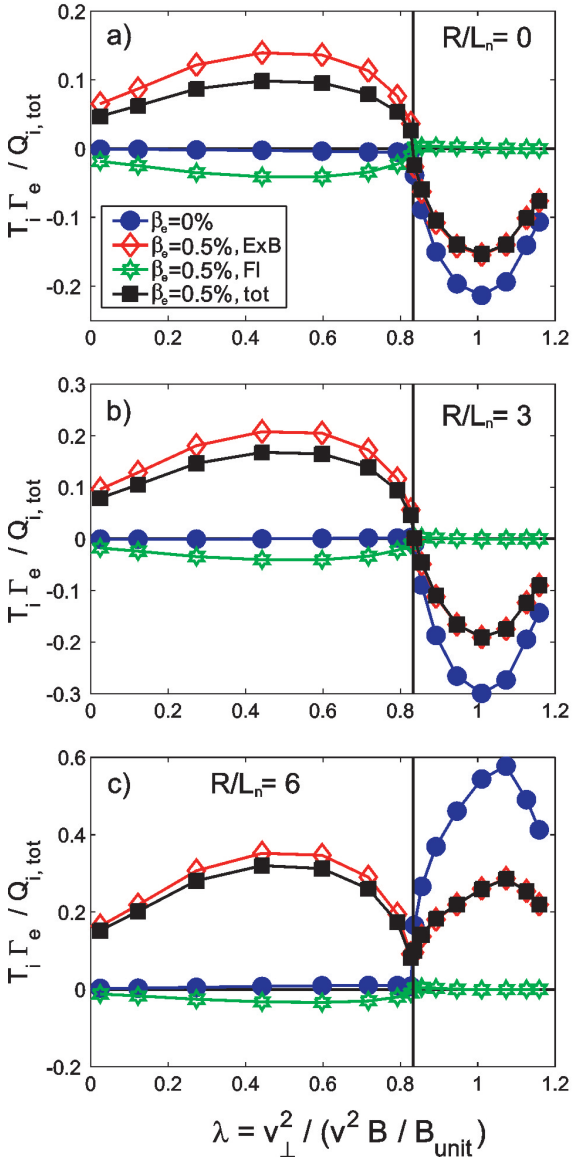

Figure 4.1: Normalized electrostatic ($\beta_e = 0$) and electromagnetic ($\beta_e = 0.5\%$) linear electron flux as a function of the pitch angle parameter λ for the logarithmic density gradient $R/L_n = 0$ (a), $R/L_n = 3$ (b) and $R/L_n = 6$ (c). A single poloidal wavenumber $k_y\rho_s = 0.1$ in circular geometry has been chosen. The electron fluxes are normalized to the full velocity space integrated ion heat flux $Q_{i,tot}$. Symbols over the curves identify the grid points in λ used in the GYRO calculations.

same also for trapped electrons at finite β_e, see the total electromagnetic flux in Fig. 4.1. The latter is calculated as the sum of the E×B and the magnetic flutter contribution (Fl), which is usually very small for the trapped particle fraction. The differences with respect to the trapped electrostatic fluxes are, as mentioned previously, due to an increase of $\hat{\omega}_{r,k}$ in the ion diamagnetic direction and a decrease of $\hat{\gamma}_k$ with increasing β_e.

The physics behind the strong push of the electron flux in the outward direction by

including electromagnetic effects is the loss of adiabaticity of the passing particle fraction as compared to the electrostatic cases. This can be seen in Fig. 4.1. Electromagnetic passing particle fluxes are directed outwards as much as the trapped fluxes are directed inwards. Thus, the resultant total flux is strongly reduced in the inward direction or even reversed at finite $\beta_{\rm e}$, as it will be shown in Section III. This behavior can be explained within the analytical description. To this end, Eq. (4.6) is rewritten in a more explicit and simple form for passing electrons which have $\lambda = 0$ already providing the full qualitative information. It reads

$$\begin{aligned}
&\Gamma_{\rm pass} = (1-f_{\rm t}) \sum_{\rm k} \langle k_{\rm y} \rho_{\rm s} c_{\rm s} n_0 \sum_{\varsigma=\pm 1} \frac{1}{\sqrt{\pi}} \int_0^\infty d\epsilon \sqrt{\epsilon} \exp(-\epsilon) \times \\
&\times \left[1 - 2\varsigma \sqrt{2\epsilon\hat{\mu}} \hat{\Omega}_{\rm r,k} + 4\epsilon\hat{\mu} \left(\hat{\Omega}_{\rm r,k}^2 + \hat{\Omega}_{\rm i,k}^2 \right) \right] \times \\
&\times \frac{\left(\hat{\gamma}_{\rm k} + \hat{\nu}_{\rm k}\right) k_{\rm y} \rho_{\rm s} \left[R/L_{\rm n} + (\epsilon - 3/2)\, R/L_{\rm T} \right] - \left[\hat{\gamma}_{\rm k} \left(\varsigma \sqrt{2\epsilon\hat{\mu}}/q + \hat{\omega}_{\rm d,k} \right) - \hat{\omega}_{\rm r,k} \hat{\nu}_{\rm k} \right]}{\left(\hat{\omega}_{\rm r,k} + \varsigma \sqrt{2\epsilon\hat{\mu}}/q + \hat{\omega}_{\rm d,k} \right)^2 + \left(\hat{\gamma}_{\rm k} + \hat{\nu}_{\rm k} \right)^2} |\hat{\phi}_{\rm k}|^2 \rangle_{\rm FS}.
\end{aligned} \tag{4.7}$$

The sign of the velocity in the parallel direction is included using $\varsigma = v_\parallel / |v_\parallel| = \pm 1$. Here, $J_0(k_\perp v_\perp / \Omega_{\rm c,e})$ is approximated to unity due to the smallness of $k_\perp v_\perp / \Omega_{\rm c,e}$. Here and in the following derivations, the parallel wave number is put to $k_\parallel = 1/(Rq)$. The high value of the deuterium to electron mass ratio is given by $\hat{\mu} = m_{\rm D}/m_{\rm e}$, and has not to be confused with the magnetic moment.

Electromagnetic contributions in Eq. (4.7) coming from $A_{\parallel,\rm k}$ can still be identified in the second and third term in the first square bracket at the right hand side. In order to identify the dominant electromagnetic contributions to the particle flux, it can be deduced that the product $\epsilon\hat{\mu}$, occurring both at the numerator and at the denominator in Eq. (4.7), is usually much larger than unity, unless particles with energies much smaller than the thermal energy are considered. However the relative magnitude of the electromagnetic terms for those particles in Eq. (4.7) remains small due to the smallness of $\beta_{\rm e}$, and the contribution to the total particle flux of particles at very low energy has small weight over the energy integral. Therefore, passing particles whose energy is of the order of the thermal energy, and for which $\epsilon\hat{\mu}$ is large, are considered.

Inserting Eq. (4.5) in Eq. (4.7), it is found that most of the contributions to the total flux are very small due to the deuterium to electron mass ratio in the denominator. In particular, it is clear that the electrostatic passing electron flux, which is determined by Eq. (4.7) imposing $\hat{\Omega}_{\rm r,k} = \hat{\Omega}_{\rm i,k} = 0$, is close to the null due to the fact that the large slab term in the denominator ($\propto \epsilon\hat{\mu}$) is not balanced in the numerator, where the strongest contribution is $\propto \sqrt{\epsilon\hat{\mu}}$. This provides an almost adiabatic response and agrees with the simulation results of Fig. 4.1.

In the case of a finite $\beta_{\rm e}$, the situation changes. The reason for this is that the dominant term in the mass ratio $\hat{\mu}$ at the denominator can be balanced by finite $\beta_{\rm e}$ terms in the numerator. In particular, it is found that the term proportional to $(\hat{\Omega}_{\rm r,k}^2 + \hat{\Omega}_{\rm i,k}^2)$ is linear in $\epsilon\hat{\mu}$ and therefore of the same order as the denominator. However, at the same time this term is of order $\beta_{\rm e}^2$, and does not give the major contribution to the flux, even when multiplied by the $\sqrt{\epsilon\hat{\mu}}$ term, coming from the $v_\parallel k_\parallel$ at the left hand side of the gyrokinetic equation, Eq. (4.1), in the last square bracket of the numerator in Eq. (4.7). The dominant electromagnetic contribution to the particle flux comes from the second term $2\varsigma\sqrt{2\epsilon\hat{\mu}}\hat{\Omega}_{\rm r,k}$

in the first square bracket in the right hand side, when it multiplies the $\hat{k}_{||}\hat{v}_{||}$ term, that is $\hat{\gamma}_{\rm k}\varsigma\sqrt{2\epsilon\hat{\mu}}/q$ in the last square bracket at the right hand side of Eq. (4.7), resulting in a term of order $\mathcal{O}(\beta_{\rm e}\epsilon\hat{\mu})$, that is of the same order in $\hat{\mu}$ as the leading term at the denominator, and yields an outward directed contribution proportional to $\beta_{\rm e}$. Thus, the dominant electromagnetic contribution to the particle flux is of pure convective type, since not provided by any term directly proportional to a density or temperature gradient, and it is produced by the phase shift between electrostatic potential and electromagnetic potential fluctuations, due to the non–adiabatic motion of passing electrons, in combination with the parallel streaming of the passing electrons described by the slab term $\hat{k}_{||}\hat{v}_{||}$. Moreover it is not caused specifically by the resonance in the denominator of Eq. (4.7), but it is present over the full velocity space of the passing electrons. A deeper demonstration of this last point is shown in subsection 4.2.5, also with the help of linear gyrokinetic calculations with GYRO. Here, on the basis of the derivation performed so far, it is interesting to discuss the following further points.

4.2.1 Separation of particle fluxes into E×B and magnetic flutter

It is instructive to separate electromagnetic fluxes into their E×B and magnetic flutter (Fl) components in an analytical way. Generally, a particle flux is given by the real part of the phase relation between density and velocity fluctuations. For the E×B component of the flux, the corresponding fluctuating velocity is $v_{\rm E\times B}$, as the name suggests. The velocity which corresponds to the flutter motion, on the other side, is the the parallel velocity which is tilted to the direction perpendicular to the equilibrium magnetic field due to $\tilde{B}_\perp$ for a short time, such that $v_{\rm Fl} = (\tilde{B}_\perp/B)v_{||}$. This means that by taking Eq. (4.2), the phase correlation of the non-adiabatic part of $h_{\rm k}$ with the electrostatic potential $\phi_{\rm k}$ and with the parallel component of the vector-potential $A_{||,{\rm k}}$ gives the E×B and flutter contributions, respectively. Therefore, using

$$\hat{U}_{\rm k} = \left[1 - \frac{v_{||}}{c_{\rm s}}\left(\hat{\Omega}_{\rm r,k} + i\hat{\Omega}_{\rm i,k}\right)\right]\left[\hat{\phi}_{\rm r,k} + i\hat{\phi}_{\rm i,k}\right], \tag{4.8}$$

and keeping only the leading order terms in the deuterium to electron mass ratio, Eq. (4.7) is rewritten as follows,

$$\Gamma_{\rm pass,E\times B} = (1-f_{\rm t})\sum_{\rm k}\langle k_{\rm y}\rho_{\rm s}c_{\rm s}n_0\left[2q\left(k_{\rm y}\rho_{\rm s}\hat{\Omega}_{\rm i,k}R/L_{\rm n} + \hat{\gamma}_{\rm k}\hat{\Omega}_{\rm r,k} + \hat{\omega}_{\rm r,k}\hat{\Omega}_{\rm i,k}\right)\right]|\hat{\phi}_{\rm k}|^2\rangle_{\rm FS} \tag{4.9}$$

and

$$\Gamma_{\rm pass,Fl} = (1-f_{\rm t})\sum_{\rm k}\langle k_{\rm y}\rho_{\rm s}c_{\rm s}n_0\left[2q\left(-k_{\rm y}\rho_{\rm s}\hat{\Omega}_{\rm i,k}R/L_{\rm n} + \hat{\gamma}_{\rm k}\hat{\Omega}_{\rm r,k} - \hat{\omega}_{\rm r,k}\hat{\Omega}_{\rm i,k}\right)\right]|\hat{\phi}_{\rm k}|^2\rangle_{\rm FS}. \tag{4.10}$$

Here, a term proportional to the temperature gradient does not contribute after the integration over energy and is therefore left out in both expressions. From Eq. (4.9) and Eq. (4.10) one realizes that the total passing flux, i.e. the sum of both contributions, recovers the result of Eq. (4.7) in the same limit of large $\epsilon\hat{\mu}$, since the terms proportional to $\hat{\Omega}_{\rm i}$ in the two equations balance exactly. Therefore, the total electromagnetic passing particle flux, i.e. the sum of the E×B and the flutter contribution, has no explicit dependence

on the logarithmic gradients of density and temperature in leading order of $\hat{\mu}$, and therefore it is of pure convective type, as already concluded, while both the E×B and flutter contributions separately exhibit a direct dependence on the logarithmic density gradient.

At this point it is instructive to simplify the relation between $\hat{A}_{||}$ and $\hat{\phi}$, Eq. (4.5). It is of interest to have a closer look on how the two potentials influence the calculation of the fluxes. It is clear that $\phi \propto \sum_\sigma Z_\sigma \int d^3v \delta f_\sigma$ from the Poisson equation, as it can be seen from Eq. (2.33), and $i\tilde{B}_\mathrm{x} \propto -A_{||} \propto \sum_\sigma Z_\sigma \int d^3v v_{||,\sigma} h_\sigma$ from Ampére's law, see Eq. (2.34). Therefore,

$$\Gamma_{\mathrm{E\times B,e}} \propto \Re\langle i \int d^3v \int d^3v \delta f_\mathrm{e} (\delta f_\mathrm{i} - \delta f_\mathrm{e})^* \rangle_\mathrm{FS} = \Re\langle i \int d^3v \int d^3v \delta f_\mathrm{e} \delta f_\mathrm{i}^* \rangle_\mathrm{FS}, \tag{4.11}$$

since $\Re\langle i \int d^3v \int d^3v \delta f_\mathrm{e} \delta f_\mathrm{e}^* \rangle_\mathrm{FS}$ is identically zero due to $\delta f_\mathrm{e} \delta f_\mathrm{e}^* = |\delta f_\mathrm{e}|^2$. For the flutter, one gets similarly

$$\Gamma_{\mathrm{Fl,e}} \propto \Re\langle i \int d^3v \int d^3v v_{\|,\mathrm{e}} h_\mathrm{e} v_{\|,\mathrm{i}} h_\mathrm{i}^* \rangle_\mathrm{FS}, \tag{4.12}$$

where the first part, $v_{\|,\mathrm{e}} h_\mathrm{e}$, comes from the density fluctuation of the transported electron species, and the second part, $v_{\|,\mathrm{i}} h_\mathrm{i}^*$, from perpendicular magnetic field fluctuations, expressed through the parallel current. From Eqn. (4.11) and (4.12) it is clear that for the E×B component of the electron particle flux, the full parallel current in the computation of the relationship between $\hat{A}_{||}$ and $\hat{\phi}$ should be taken into account. On the other hand, for the flutter component only the ion current gives a contribution through $\hat{\Omega}$.

However, for the E×B component of the flux, only the electron current is considered here while the ion current is neglected for simplicity. This approximation is valid since the electron current gives the dominant contribution to Ampére's law, especially in the cases of large real eigenfrequencies and growth rates (for $\hat{\omega}_\mathrm{r}$, $\hat{\gamma}$ of the order of one, the electron current contribution is typically one order of magnitude larger than the ion current contribution). Moreover, only the leading order terms proportional to $\epsilon\hat{\mu}_\mathrm{e}$ are taken into account. Then, as explained in more detail in the Appendix, the dominant part of the relation between $\hat{A}_{||,\mathrm{k}}$ and $\hat{\phi}_\mathrm{k}$ can be written as

$$\hat{\Omega}_\mathrm{k} = \frac{q\beta_\mathrm{e} \left(k_\mathrm{y}\rho_\mathrm{s} R/L_\mathrm{n} + \hat{\omega}_\mathrm{r} + i\hat{\gamma}\right)}{\left(k_\perp \rho_\mathrm{s}\right)^2}. \tag{4.13}$$

The real part of Eq. (4.13), $\hat{\Omega}_\mathrm{r}$, is proportional to $\hat{\omega}_\mathrm{r}$ and therefore a positive number for ITG modes, while it can become negative for TEM modes. The imaginary part $\hat{\Omega}_\mathrm{i}$ is always a positive number independent of the sign of the real frequency. This expression shows a strong similarity compared to the one obtained from the fluid model, Eq. (3.30). The latter, which is normalized in $\omega_{\mathrm{D,i}}$ units, see Eq. (3.12), can easily be rewritten to

$$\hat{A}_{||} = 2\frac{k_\perp^4 \rho_\mathrm{s}^2}{k_\mathrm{y}^2} \frac{c}{c_\mathrm{s}} \beta_\mathrm{e} \frac{q}{(k_\perp \rho_\mathrm{s})^2} \left[k_\mathrm{y}\rho_\mathrm{s} \frac{R}{L_\mathrm{n,e}} + \hat{\omega} \right] \hat{\phi}, \tag{4.14}$$

where $\tau = 1$ and $\hat{k}_{||} = k_\| c_\mathrm{s}/\omega_{\mathrm{D,i}}$ has been used. The hat in Eq. (4.14) now means the normalization to c_s/R. It is clear that Eq. (4.13) and Eq. (4.14) show the same parametric dependence. The additional factor $2k_\perp^4\rho_\mathrm{s}^2/k_\mathrm{y}^2$ is usually of order unity.

For the flutter component, it can be directly calculated that combining Eq. (4.10) with Eq. (4.13) the flux vanishes identically. Thus, only the ion current contribution in

Ampére's law has to be considered, as already mentioned. Then, in the denominator of Eq. (4.5), the integral proportional to $\hat{v}_{||}^2$ is small compared to $2\left(k_\perp \rho_\mathrm{s}\right)^2$ and is therefore neglected, such that Eq. (4.5) can be written as

$$\begin{aligned}\hat{\Omega}_\mathrm{k} \approx & -\frac{\beta_\mathrm{e}}{\left(2k_\perp\rho_\mathrm{s}\right)^2}\int d^3v F_{0,\mathrm{v}}\hat{v}_{||}\left\{\hat{\gamma}(\hat{\gamma}+\hat{\nu})+\left(\hat{\omega}_\mathrm{r}-\hat{\omega}_*\right)\left(\hat{\omega}_\mathrm{r}-\hat{k}_{||}\hat{v}_{||}-\hat{\omega}_\mathrm{d}\right)\right. \\ & \left.+i\left[\hat{\gamma}(\hat{\omega}_\mathrm{r}-\hat{k}_{||}\hat{v}_{||}-\hat{\omega}_\mathrm{d})-\left(\hat{\gamma}+\hat{\nu}\right)\left(\hat{\omega}_\mathrm{r}-\hat{\omega}_*\right)\right]\right\}\left\{\left(\hat{\omega}_\mathrm{r}-\hat{k}_{||}\hat{v}_{||}-\hat{\omega}_\mathrm{d}\right)^2+\left(\hat{\gamma}+\hat{\nu}\right)^2\right\}^{-1},\end{aligned} \tag{4.15}$$

where $\hat{\omega}_* = k_\mathrm{y}\rho_\mathrm{s}\left[R/L_\mathrm{n}+\left(\epsilon-3/2\right)R/L_\mathrm{T}\right]$. For this expression it can be shown that the real part of $\hat{\Omega}$ is proportional to $-\hat{\omega}_\mathrm{r}$ while the imaginary part is a positive number (proportional to $1/\hat{\gamma}$).

By comparing the expressions of the E×B, Eq. (4.9) together with Eq. (4.13), and the flutter components, Eq. (4.10) together with Eq. (4.15), of the passing particle flux, it has to be noted that the flutter component is approximately one order of magnitude smaller compared to the E×B. As explained above, this is due to the fact that the electron current provides the dominant contribution in Ampére's law. The direction of E×B and flutter fluxes, inward or outward, depends on the interplay among the signs of $\hat{\omega}_\mathrm{r}$ and $\hat{\Omega}_\mathrm{r}$, which can change depending on the type of instability, and the relative magnitude of the various terms (we remind that $\hat{\Omega}_\mathrm{i}$ is always positive). In particular, for ITG modes $\hat{\omega}_\mathrm{r} > 0$, $\hat{\Omega}_\mathrm{r} > 0$ and $\hat{\Omega}_\mathrm{i} > 0$, the three components of the E×B passing particle flux in Eq. (4.9) are all directed outward, acting in the same direction. Instead, the three magnetic flutter components are in opposite directions and partly balance each other. The inward directed terms $\propto \hat{\Omega}_\mathrm{i}$ are larger than that $\propto \hat{\Omega}_\mathrm{r}$, directed outward, and the flutter flux is slightly inward. In contrast, for sufficiently large TEM real frequencies in absolute value, $\hat{\Omega}_\mathrm{r}$ becomes negative, and E×B passing electron flux can be directed inward, when the terms $\hat{\gamma}\hat{\Omega}_\mathrm{r}+\hat{\omega}_\mathrm{r}\hat{\Omega}_\mathrm{i}$ exceed $k_\mathrm{y}\rho_\mathrm{s}\hat{\Omega}_\mathrm{i}R/L_\mathrm{n}$ in Eq. (4.9). The flutter component is directed outwards since the term $-k_\mathrm{y}\rho_\mathrm{s}\hat{\Omega}_\mathrm{i}R/L_\mathrm{n}$ in the flutter expression Eq. (4.10) is usually smaller than the other two. For very large density gradients in TEM turbulence, however, the situation is reversed and the E×B passing electron flux is directed outwards while the flutter is directed inwards, in agreement with simulation results.

In conclusion, for ITG modes the E×B passing flux is always outward and significant, while the magnetic flutter is inward and usually smaller in size. For TEMs with large real frequencies in absolute value, the situation is reversed, and the E×B passing flux can become directed inward, while the magnetic flutter part becomes directed outward. The reversal of the convective part of the E×B flux for modes propagating in the electron drift direction with respect to the ion drift direction has also been found in the fluid description of [49]. Differently from ITG modes, the electromagnetic contribution of passing electrons to the particle flux in the case of TEMs is usually small as compared to the one produced by trapped electrons. This will be shown below.

4.2.2 Impact of shear and α

The understanding of the role of parallel dynamics in the electromagnetic description of particle fluxes is deepened by studying the separate impact of the parameter s and α in the $s-\alpha$ model. Fig. 4.2 shows the GYRO computations of real eigenfrequency ω_r (a),

linear growth rate γ (b), normalized particle $T_\mathrm{i}\Gamma_\mathrm{e}/Q_\mathrm{i}$ (c) and normalized electron to ion heat flux $Q_\mathrm{e}/Q_\mathrm{i}$ (d) as a function of $(s-\alpha)$ for the logarithmic density gradient $R/L_\mathrm{n} = 3$ and a single poloidal wave number $k_\mathrm{y}\rho_\mathrm{s} = 0.1$. Both electrostatic and electromagnetic

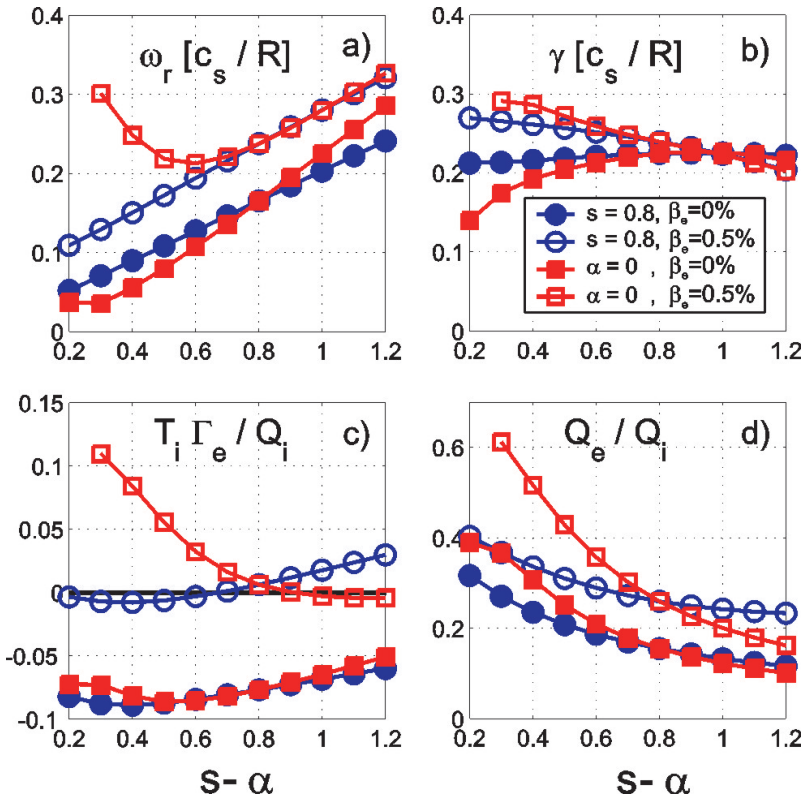

Figure 4.2: Electrostatic ($\beta_\mathrm{e} = 0$) and electromagnetic ($\beta_\mathrm{e} = 0.5\%$) dependence of real eigenfrequency ω_r (a), linear growth rate γ (b), normalized particle flux $T_\mathrm{i}\Gamma_\mathrm{e}/Q_\mathrm{i}$ (c) and normalized electron to ion heat flux $Q_\mathrm{e}/Q_\mathrm{i}$ (d) as a function of $s-\alpha$ for the logarithmic density $R/L_\mathrm{n} = 3$ and a single poloidal wave number $k_\mathrm{y}\rho_\mathrm{s} = 0.1$ in circular geometry.

dependence have been evaluated changing α while keeping the shear constant ($s = 0.8$, circles) or vice versa, i.e. scanning shear at $\alpha = 0$ (squares), respectively. For $(s-\alpha)$ values larger than ≈ 0.6, ω_r as well as γ show almost the same values regardless of the parameter which was changed, see Fig. 4.2(a, b). At $(s-\alpha) < 0.6$ and varying shear, stronger deviations to the behavior obtained with changing α can be found. The electrostatic $(s-\alpha)$ dependence of the electron flux, Fig. 4.2c, is in both cases (fixed shear or fixed α) nearly the same, while the electromagnetic dependence shows strong differences. A similar conclusion for the heat flux dependence can be drawn, Fig. 4.2d. This can be understood from the analytical derivation. Since the relation between $A_{||}$ and ϕ is given by the Ampère's law, Eq. (4.4), the perpendicular wave number $k_\perp$ plays an essential role to determine the magnitude of $\hat{\Omega}$, see Eq. (4.5). Within the $s-\alpha$ model, shear and pressure gradient enter in different ways in the expression for $k_\perp$, since the shear is multiplied by the extended ballooning angle θ and α by $\sin\theta$ (an expression of $k_\perp$ is given in Eq. (4.16)). Thus, there is a substantial difference in $k_\perp$ by either varying shear or α when the eigenfunctions become extended in θ, that is along the field line, as it is generally

the case at finite β_e, due to the non–adiabatic passing electron dynamics.

4.2.3 Effect of finite collisionality

From the physical point of view, electromagnetic effects imply radial magnetic field fluctuations which effectively decrease the otherwise fast parallel velocity of passing electrons by rapid radial displacements of their positions. A finite collisionality acts in the same way and therefore also leads to non–adiabaticity. But unlike a finite β_e, the latter enters through diffusive and thermodiffusive effects, which gives an inward contribution at small R/L_n. For the convective part, an additional flux is generated via finite collisionality being directed outwards with ITG as the most unstable mode, as shown in [71, 86, 90]. The same considerations are true for the trapped particle fraction.

4.2.4 Trapped electron modes

Linear gyrokinetic simulations for microturbulence in the TEM domain are performed. To this purpose, an electron logarithmic temperature gradient $R/L_{T,e} = 9$ is chosen, while the other gradients are $R/L_{T,i} = R/L_n = 3$ and other parameters remain as in the ITG standard case. Figure 4.3 shows the electrostatic and electromagnetic components of the passing and trapped particle fluxes. The most important difference compared to the ITG case is the fact that the trapped particle flux in the case of TEM becomes much larger than the passing particle flux, in both electrostatic and electromagnetic cases. Thus, the

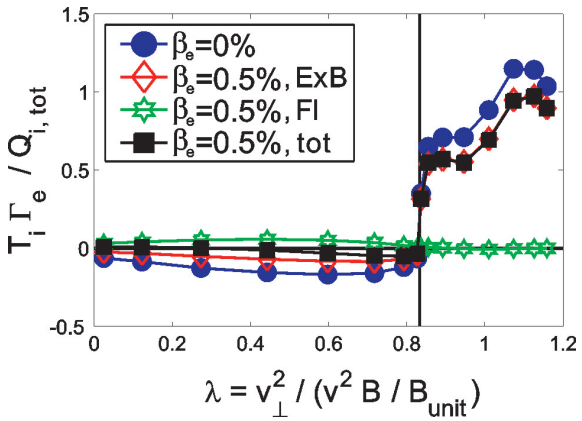

Figure 4.3: Normalized electrostatic ($\beta_e = 0$) and electromagnetic ($\beta_e = 0.5\%$) linear electron flux as a function of the pitch angle parameter λ for a trapped electron mode (TEM) case (see text). A single poloidal wavenumber $k_y\rho_s = 0.1$ in circular geometry has been chosen. The electron fluxes are normalized to the full velocity space integrated ion heat flux $Q_{i,tot}$. Symbols over the curves identify the grid points in λ used in the GYRO calculations.

impact on the particle flux due to a finite value of β_e can be expected to remain small in the case of TEMs. Moreover, it is apparent that already at $\beta_e = 0$ the passing flux is finite. The reason for this behavior is the fact that the mode real eigenfrequency is negative and thus the slab resonance in the denominator of Eq. (4.7) is obtained at higher particle energy which in turn leads to more particles encountering non–adiabaticity. The electromagnetic E×B component is still slightly positive but rather small due to the fact

that $\hat{\Omega}_r$ changes sign which leads to counteracting terms in Eq. (4.9). However, due to the stronger non–adiabaticity of low energetic passing particles the total E×B flux remains slightly inwards. The total electromagnetic passing flux contribution is almost at the null since the outward flutter component balances the E×B one. Trapped particles are directed more inwards with increasing β_e due to changes in the real eigenfrequency and growth rate. These considerations are in agreement with the previous discussions based on the analytical results.

4.2.5 Loss of adiabaticity in the full energy range

In order to show the loss of adiabaticity of passing electrons in response to electromagnetic fluctuations over the full energy range, the energy dependences of quasi–linear electrostatic ($\beta_e = 0$) and electromagnetic ($\beta_e = 0.5\%$) electron fluxes are shown in Fig. 4.4. Three different values of λ in the passing range have been chosen, and an ITG case with $R/L_n = R/L_{Te} = 0.1$ and all other parameters equal to the standard ITG case introduced in this Chapter is considered. This choice of parameters allows us to focus on the convective part of the electron particle flux. The normalization is taken in such a way that the resulting quasi–linear fluxes are plotted divided by the function of energy $\sqrt{\epsilon}\exp(-\epsilon)$, which includes the dependence on energy of both the Maxwellian and the Jacobian. This procedure allows the identification of the physics differences between an electrostatic and an electromagnetic description of electron fluxes by focusing on the resonant term in Eq. (4.6). Figure 4.4a shows the quasi–linear electrostatic fluxes for $\lambda = 0.02$, $\lambda = 0.44$ and $\lambda = 0.79$. Particles at very low energy experience the resonance, see Eq. (4.6), and therefore give a contribution to the particle flux. However, the comparison with the quasi–linear electromagnetic E×B flux, Fig. 4.4b, reveals that the electrostatic flux is very low since the electrons are almost adiabatic. The electromagnetic E×B and flutter contributions do not have a strong resonance behavior at low energy, as shown in Fig. 4.4(b, c). Instead they exhibit finite contributions in the full energy range. These numerical results are consistent with the analytical derivations obtained in Section II.

4.2.6 Conclusive remarks

In conclusion, the dominant term providing an outward push of the electron particle flux in ITG turbulence in which electromagnetic effects are included, i.e. Ampère's law due to finite β_e, has been identified. This is given by the phase shift between electrostatic potential fluctuation and magnetic vector fluctuations produced by the non–adiabatic dynamics of passing electrons, in combination with the compression of their parallel streaming. As such, this dominant transport mechanism is of pure convective type, that is, it is not directly proportional to a logarithmic density or temperature gradient. It is significant over the entire energy range, and is mainly carried by E×B transport, while magnetic flutter transport provides a smaller, inward directed, contribution. For TEM with large real frequencies in absolute value, the situation can be reversed, with the E×B transport being directed inward, while the magnetic flutter part is directed outward. However, electromagnetic passing particle fluxes in case of TEM instabilities remain small as compared to the mainly electrostatic trapped electron fluxes. These can be indirectly affected by changes of the real frequency and the growth rate produced by finite β_e.

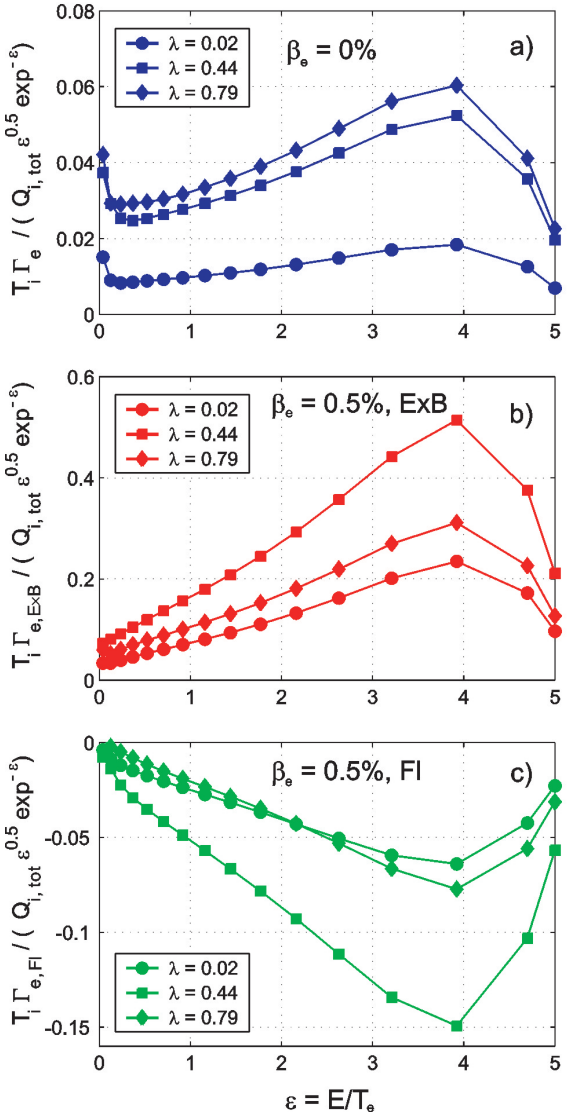

Figure 4.4: Normalized electrostatic ($\beta_e = 0$, a) and electromagnetic ($\beta_e = 0.5\%$, b, c) quasi–linear electron fluxes as a function of the normalized energy $\epsilon = E/T_e$ for an ITG case with all parameters like the standard ITG case of this Chapter. A single poloidal wavenumber $k_y\rho_s = 0.1$ in circular geometry has been chosen. The electron fluxes are normalized to the full velocity space integrated ion heat flux $Q_{i,tot}$, and divided by the Jacobian and the Maxwellian. Symbols over the curves identify the grid points in ϵ used in the GYRO calculations.

4.3 Numerical investigations

When both particle sources and neoclassical transport are negligible, the condition of turbulent particle flux at the null can be applied to compute the stationary logarithmic density gradient as a function of β, keeping fixed all the other local plasma parameters.

The stationary normalized logarithmic density gradient $R/L_{n,stat}$ is defined as the value of $R/L_n = -(R/n)\partial_r n$ where the turbulent particle flux $\Gamma_e = 0$. As anticipated

in the analytical Section, a variation of β is considered having two effects. One is the electromagnetic effect connected with the fluctuations of the magnetic field, which are given by the solution of the Ampère's law, and in which β_e appears directly as scaling parameter for the strength of the magnetic field fluctuations. The second effect is purely geometrical (electrostatic) and it is related to the role of the radial derivative of the total plasma pressure $\partial_r p$ in the magnetic equilibrium and consequently in the expression of the curvature drift. For given logarithmic gradients of the temperature and density profiles and given ion to electron temperature ratio, this term is proportional to the total plasma β.

4.3.1 Density gradient dependence of fluxes

The quasi–linear calculations in this Section are performed using the same standard ITG case in $s-\alpha$ geometry as before. With the linear version of the gyrokinetic code GYRO particle fluxes as a function of R/L_n are computed. In all the quasi–linear calculations the particle flux Γ is normalized to the ion heat flux Q_i. Fig. 4.5 shows the electromagnetic gyrokinetic numerical calculations of the quasi–linear electron particle fluxes as a function of the logarithmic density gradient R/L_n for both $\beta_e = 0$, as well as for $\beta_e = 0.5\%$. The resultant fluxes consist of the sum of E×B and magnetic flutter contributions. Two different models for the wave number spectrum of the saturation amplitude of the electrostatic potential are used. Following the works of [88, 92], either the fully computed poloidal wave number spectrum (12 points from $k_y\rho_s = 0.05$ to $k_y\rho_s = 1.5$ in logarithmic spacing) with weighting due to $\gamma/\langle k_\perp^2\rangle$, see Fig. 4.5a, or the model proposed in [91] is chosen, which assumes an exponential decrease of the saturation amplitude of the potential at $k_y\rho_s$ smaller or larger than the k_y value at which $\gamma/\langle k_\perp^2\rangle$ is at the maximum, see Fig. 4.5b. This exponential shape of the saturation amplitude is motivated by measurements of the density fluctuations at high wave numbers [93]. In the $s-\alpha$ model, the perpendicular wave number is defined as $k_\perp = \sqrt{k_x^2 + k_y^2\left[1 + (s\theta - \alpha\sin\theta)^2\right]}$ such that $\langle k_\perp^2\rangle$ is given by

$$\langle k_\perp^2\rangle = k_x^2 + k_y^2\left[1 + \langle (s\theta - \alpha\sin\theta)^2\rangle\right], \tag{4.16}$$

where

$$\langle (s\theta - \alpha\sin\theta)^2\rangle = \frac{\int (s\theta - \alpha\sin\theta)^2\,|\tilde{\phi}_k(\theta)|^2 d\theta}{\int |\tilde{\phi}_k(\theta)|^2 d\theta} \tag{4.17}$$

with θ being the extended ballooning angle and $\tilde{\phi}$ the fluctuating electrostatic potential. It is found that $\gamma/\langle k_\perp^2\rangle$ has its maximum around $k_y\rho_s \approx 0.1$ (slightly shifted towards higher values for low R/L_n and towards lower values at high R/L_n and β_e), and strongly decreases with increasing poloidal wave number such that the ratio of the maximum value of $\gamma/\langle k_\perp^2\rangle$ to the value at $k_y\rho_s = 0.5$ is of order 100, as also found in [88].

4.3.2 Stationary density gradient for increasing β

The gyrokinetic calculations in Fig. 4.5 show that with a finite β_e the fluxes are pushed in the outward direction for $R/L_n < 3$ while they are only weakly affected at high R/L_n, as already pointed out in the analytical Section. Such a behavior leads to a reduction of the logarithmic density gradient at which the flux is zero. This effect is larger in the

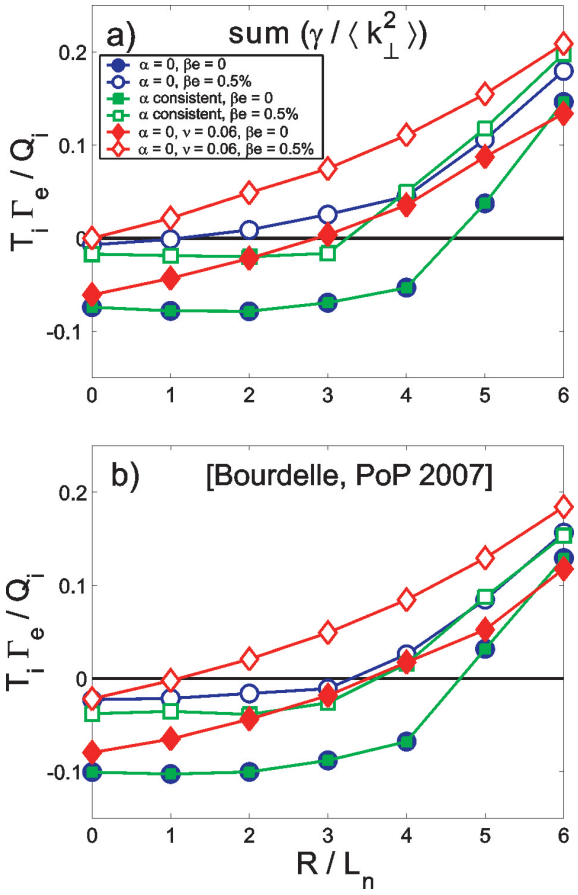

Figure 4.5: Normalized electrostatic ($\beta_e = 0$, full symbols) and electromagnetic ($\beta_e = 0.5\%$, open symbols) quasi–linear electron particle flux $T_i\Gamma_e/Q_i$ as a function of the logarithmic density gradient R/L_n with $\alpha = 0$ and collisionless (circles), with α varied consistently with β and collisionless (squares), and with $\alpha = 0$ and collisional (diamonds). Wave number spectra proportional to $\gamma/\langle k_\perp^2\rangle_{FS}$ (a) or as proposed in [91] (b) have been assumed for the fluxes.

case where $\alpha = 0$ (open circles) compared to the case in which it is included consistently with the value of $\beta_e = 0.5\%$ (open squares). A finite experimentally relevant collisionality, here $(R/c_s)\nu_{ei} = 0.06$, has also the effect of pushing the fluxes in the outward direction, see diamond symbols in Fig. 4.5. This is consistent with the discussion in the Section containing the analytical calculations. From the collisional curve with $\beta_e = 0.5\%$ it is concluded that the wave number model proportional to $\gamma/\langle k_\perp^2\rangle$ predicts a value of R/L_n close to zero.

Using these R/L_n scans, the value of the logarithmic density gradient at the null of the fluxes can be identified, and computed for increasing values of β. The influence of a finite β_e on the logarithmic density gradient at zero electron particle flux is presented in Fig. 4.6 for the two different models for the saturation amplitude of the wave number spectrum. The cases with concentric circles (a), with a self-consistent value of α(b) and with finite collisionality of $(R/c_s)\nu_{ei} = 0.06$ using concentric circles for the magnetic equilibrium (c) are considered. It can be seen that in the first case the decrease of the stationary

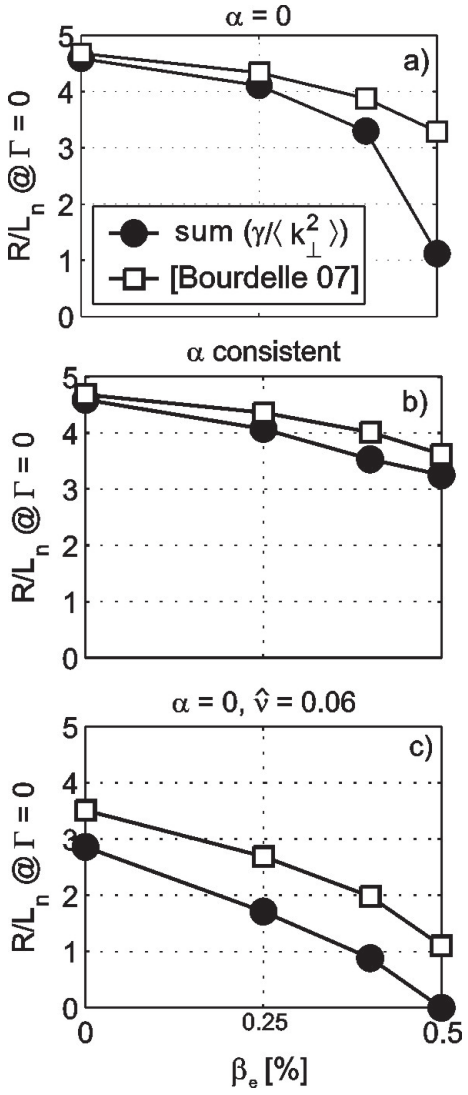

Figure 4.6: Electromagnetic dependence of logarithmic density gradient R/L_{n} at the null of the quasi–linear electron flux as a function of β_{e}. A circular case (a), a case with values of α consistent with β (b), and a circular case with finite collisionality of $(R/c_{\mathrm{s}})\nu_{\mathrm{ei}} = 0.06$ (c) with two models for the wave number spectrum of the linear fluxes are considered.

logarithmic density gradient with increasing β_{e} is weak at low values of β_{e} while it becomes strong for β_{e} approaching 0.5%. The inclusion of a consistent value of α reduces this effect. Also in the collisional case, the drop of $R/L_{\mathrm{n,stat}}$ is more linear. It is interesting to note that the model proposed in [91] predicts generally larger $R/L_{\mathrm{n,stat}}$ than the $\gamma/\langle k_{\perp}^2 \rangle$ model at high values of β_{e}, while at low β_{e} both models show similar values in the collisionless cases. The reason for this behavior is the fact that fluxes at high $k_{\mathrm{y}}\rho_{\mathrm{s}}$, which are directed inwards have a larger weight in the model of [91]. Moreover, for increasing β_{e} the high k_{y} contributions become larger in the inward direction while they are quite small at $\beta_{\mathrm{e}} = 0$. It is also of interest to note that, using a corresponding circular Miller geometry [41] at the place of the $s - \alpha$ model geometry, the predicted stationary density gradient decreases

by about 10%. These results motivate further investigations of the poloidal spectrum of particle fluxes and a detailed comparison of linear with nonlinear gyrokinetic calculations in realistic geometry. This point is adressed below for parameters close to those measured in ASDEX Upgrade.

4.4 Comparison of quasi–linear and nonlinear fluxes

In the last Section it has been pointed out that the logarithmic density gradient R/L_n, at which the particle flux is at the null, decreases with increasing β_e in Ampère's equation. However, it was shown that different choices of the wave number spectra of the fluxes provide different $R/L_\mathrm{n,stat}$. The main goal of this Section is the calculation of finite β effects on the peaking of the density profile containing both electromagnetic and geometrical implications on a realistic case. In addition, the stationary logarithmic density gradients is computed using nonlinear simulations. The comparison with linear calculations helps to identify a quasi–linear model which predicts $R/L_\mathrm{n,stat}$ in good agreement with nonlinear results.

To this purpose, calculations of electron transport including electromagnetic effects are performed for H–mode parameters around mid-radius using the Miller geometry model for the magnetic equilibrium. The choice of dimensionless parameters which are applied in the gyrokinetic simulations are typical of an ASDEX Upgrade plasma and therefore should be considered more realistic than the reference cases discussed previously. The equilibrium parameters are given by $r/a = 0.56$, $R/a = 3.53$, $q = 1.33$, $s = 1.12$, Shafranov shift $\Delta = -0.11$, elongation $\kappa = 1.38$ with elongation shear $s_\kappa = (r/\kappa)\partial_\mathrm{r}\kappa = 0.11$, and triangularity $\delta = 0.032$ with triangularity shear $s_\delta = r\partial_\mathrm{r}\delta = 0.055$. The local parameters for the two species plasma consisting of deuterons and electrons are $R/L_\mathrm{Ti} = 6.13$, $R/L_\mathrm{Te} = 6.13$, $T_\mathrm{i}/T_\mathrm{e} = 1$, $\beta_\mathrm{e} = 0.65\%$. The collisionality is $(R/c_\mathrm{s})\nu_\mathrm{ei} = 0.067$, and $Z_\mathrm{eff} = 2$. The value of β_e is scanned while the magnetic equilibrium was held constant.

In linear simulations, the dominant micro-instability under these conditions is an ITG mode for $k_\mathrm{y}\rho_\mathrm{s} \lesssim 0.7$. Beyond that value a TEM mode is found. A spectrum from $k_\mathrm{y}\rho_\mathrm{s} = 0.05$ to $k_\mathrm{y}\rho_\mathrm{s} = 1.5$ is chosen with 12 points logarithmically spaced. A sufficiently high number of radial simulation points is taken in order to keep the radial resolution $dx/\rho_\mathrm{s} \lesssim 0.5$. For nonlinear flux tube simulations, a spectrum from $k_\mathrm{y}\rho_\mathrm{s} = 0.04$ to $k_\mathrm{y}\rho_\mathrm{s} = 2.68$ using 64 toroidal modes is taken. The simulation box is chosen to be $L_\mathrm{x}/\rho_\mathrm{s} = 82$ and $L_\mathrm{y}/\rho_\mathrm{s} = 148$. Using 216 radial points, a radial resolution of $dx/\rho_\mathrm{s} = 0.38$ is obtained. Moreover, a grid of 256 points in the velocity space (8 energies, 8 passing and 8 trapped pitch angles and two signs of velocity) is used.

Figure 4.7 shows the nonlinear spectrum of electrostatic and electromagnetic particle fluxes at $R/L_\mathrm{n} = 2$, normalized to the GyroBohm diffusion $\chi_\mathrm{GB} = \rho_\mathrm{s}^2 c_\mathrm{s}/a$. It is found that while the position of the peak for both the electrostatic flux and the electromagnetic E×B flux component remains at $k_\mathrm{y}\rho_\mathrm{s} \approx 0.2$, the former is directed less strong in the outward direction compared to the latter. The peak of the electromagnetic flutter component is at slightly higher $k_\mathrm{y}\rho_\mathrm{s}$ and the flux is negative over the full range of the wave number spectrum.

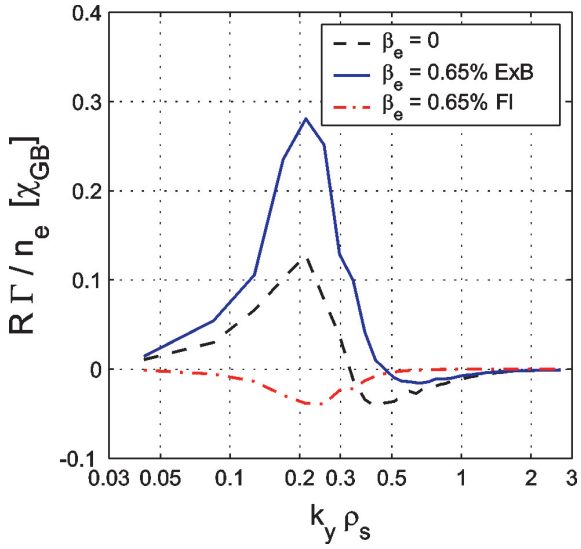

Figure 4.7: Nonlinear gyro-Bohm normalized electron particle flux spectra for plasma parameters similar to ASDEX Upgrade hybrid discharges (see text). The electrostatic as well as the electromagnetic E×B and magnetic flutter contributions are shown.

4.4.1 Stationary density gradient for increasing βe

Figure 4.8 shows the results for the stationary logarithmic density gradient using linear and nonlinear simulations at increasing β_e in Ampère's equation. Electromagnetic fluxes consist of the sum of E×B and magnetic flutter components. For the quasi–linear fluxes, different wave number spectra have been used for comparative purposes, i.e. fluxes according to the maximum of $\gamma/\langle k_\perp^2 \rangle$ and to the maximum of γ (in the ITG branch), wave number spectra according to $(\gamma/\langle k_\perp^2 \rangle)$ and $(\gamma/\langle k_\perp^2 \rangle)^{0.7}$ as well as the wave number spectrum proposed in [91].

In linear simulations, the logarithmic density gradient decreases with increasing β_e regardless of the wave number spectrum, which is consistent with the results from the parameter study in the last Section and with the analytical results. However, there are big differences in the predicted values at which the electron flux vanishes. Using the wave number spectral weight due to the maximum in $\gamma/\langle k_\perp^2 \rangle$, which peaks at $k_y \rho_s \approx 0.18$, or due to the spectral average using $(\gamma/\langle k_\perp^2 \rangle)^2$ results in a very low positive (or even negative) density gradient, while the wave number due to the maximum in γ or the spectrum due to $\gamma/\langle k_\perp^2 \rangle$ allows for moderate values of R/L_n at vanishing electron flux. Larger stationary gradients are obtained using the wave number spectrum proposed in [91].

Taking the nonlinear simulation results it is found that the decrease of R/L_n is quite substantial and rather linear with increasing β_e. The comparison to quasi–linear results reveals that the wave number spectrum proposed in [91] and $(\gamma/\langle k_\perp^2 \rangle)^z$ with $z = 0.7$ works best for these cases, while the other ones do not deliver satisfactory agreements. At β_e approaching 1% the former turn out to give higher stationary density gradients compared to the nonlinear results. However, it was impossible to obtain meaningful fluxes for $\beta_e > 1\%$ in linear simulations since the smallness of linear growth rates and subsequently the reduction of turbulence due to electromagnetic stabilization led to strong spectral variations of the fluxes such that a adequate comparison of quasi–linear and nonlinear stationary

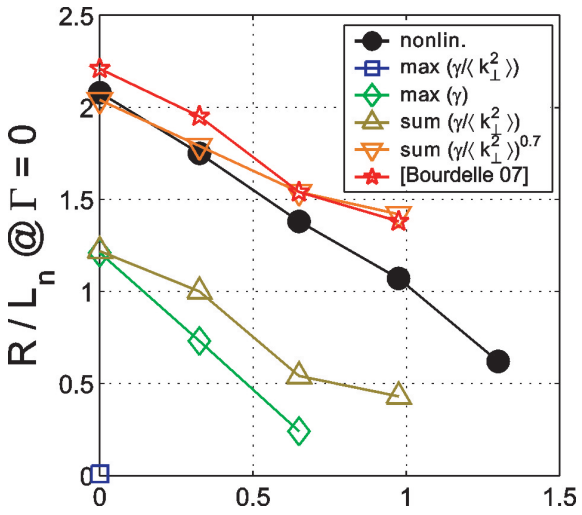

Figure 4.8: Stationary logarithmic density gradient using nonlinear simulations and quasi–linear calculations with different assumptions for the poloidal wave number spectrum of electron particle fluxes as a function of β_e.

density gradients cannot be made. In order to check the impact of a realistic description of the geometry, the value of $R/L_{n,stat}$ at $\beta_e = 0.65\%$ has been computed with a corresponding $s - \alpha$ geometry. It is found that in $s - \alpha$ the value of $R/L_{n,stat}$ is reduced by 30%.

4.4.2 Stationary density gradient for increasing βe and β'

A more appropriate and realistic description of the experimental conditions considers not only the effect of β_e in the Ampére's equation, but also the impact of $\beta' = 8\pi\,\partial_r p/B_{unit}$ in the curvature drift. To this purpose, Fig. 4.9 compares quasi–linear with nonlinear simulation results. The experimental stationary logarithmic density gradient at $\beta_e = 0.65\%$ remains unchanged, but in the cases with quasi–linear calculations including averages over the wave number spectrum (open triangles and stars), the consistent inclusion of finite β in both the Ampère's law and the magnetic equilibrium shows a much weaker dependence of $R/L_{n,stat}$ on β_e compared to the case in which only Ampère's equation is considered. This is consistent with the results in the last Section, Fig. 4.6. In nonlinear simulations, it is found that the reduction of $R/L_{n,stat}$ with increasing β_e, while changing consistently also β' in the magnetic equilibrium parameters in input (open circles), is much closer to the result obtained with increasing β_e only and keeping β' fixed (full circles), with respect to the result from quasi–linear simulations. Moreover, it is apparent that the same quasi–linear rules for the wave number spectrum, which reproduced the nonlinear results when only β_e is changed in a fairly good way, do not agree with the nonlinear results. The reason for these differences has been investigated and is shown in Fig. 4.10, for simulations with $R/L_{ne} = 2$. In Fig. 4.10a, a comparison of $|\tilde{\phi}_k|^2$ between the linear (black, full line for $(\gamma/\langle k_\perp^2\rangle)^{0.7}$ and dashed line for spectrum proposed in [91]) and nonlinear wave number spectra (color, circle for $\beta_e = \beta' = 0$, square for $\beta_e = 0$ with β' consistent to a value if β_e was 0.65%, and diamond for $\beta_e = 0.65\%$ with a β' consistent with $\beta_e = 0.65\%$) are shown for $R/L_n = 2$. The normalization is done in such a way that the integral over all binor-

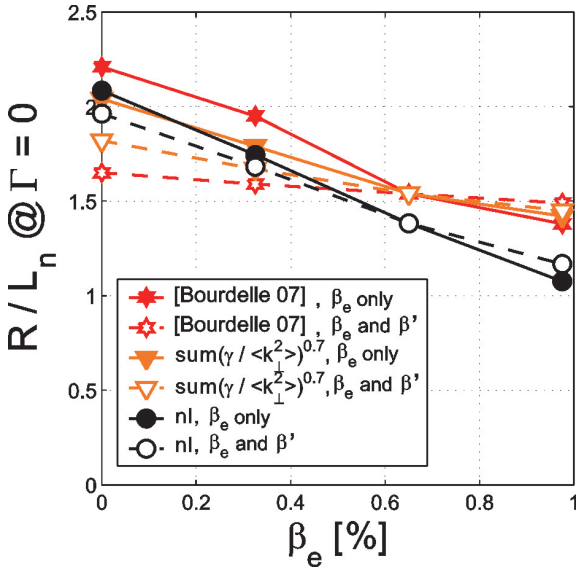

Figure 4.9: The influence of finite β exclusively in Ampère's equation ('β_e only') as well as in both Ampère's equation and the consistent magnetic equilibrium (β_e and β') on the stationary electron particle flux are shown using quasi–linear and nonlinear calculations. The chosen plasma parameters are similar to ASDEX Upgrade hybrid discharges

mal wave numbers k_y gives one. The main difference between the linear choices and the nonlinear simulation results is the fact that in linear calculations large k_y values play an important role while in nonlinear simulations the $k_y\rho_s$ values around 0.2-0.3 have a much stronger impact. Moreover it is interesting to note that for this case the linear choices for $|\tilde{\phi}_k|^2$ do not change in the three cases (maximum of $\gamma/\langle k_\perp^2\rangle$ remains at $k_y\rho_s = 0.18$) while for the nonlinear cases shifts of the maximum are obtained, namely large scales reveal non–negligible differences in the three cases while the small scale behavior ($k_y\rho_s > 0.4$) can be described by the power law $|\tilde{\phi}_k|^2 \propto k_y^{-5}$ ($|\tilde{\phi}_{k_y<1}|^2 \propto k_y^{-4.8}$ and $|\tilde{\phi}_{k_y>1}|^2 \propto k_y^{-5.2}$), which is slightly steeper than the $k_y^{-4.3}$ result for density fluctuations found in [94].

Such large differences between the spectra of $|\tilde{\phi}_k|^2$ applied in the quasi–linear calculations, and the actual ones obtained in the nonlinear simulations might lead to the conclusion that the total quasi–linear particle fluxes are always significantly far from the nonlinear ones. However this is not always the case. The reason for this is shown in Fig. 4.10b, where the quasi–linear weights $\Im(\tilde{n}_k\tilde{\phi}_k^*)/|\tilde{\phi}_k|^2$ are directly compared with those extracted from the actual nonlinear saturated state. Full symbols show the linear results, whereas open symbols show the results from nonlinear simulations. In the comparison, it is found that a clear difference appears in the high $k_y\rho_s$ part of the spectrum, where linear results are more strongly directed outwards, and cross the zero line at larger values of $k_y\rho_s$, as compared with the nonlinear spectra. Moreover, from the comparison between $\beta_e = \beta' = 0$ (circles) with $\beta_e = 0$, $\beta'(\beta_e = 0.65\%)$ (squares) and $\beta_e = 0.65\%$, $\beta'(\beta_e = 0.65\%)$ (diamonds) of the linear simulations, the cause of the larger discrepancy between nonlinear and quasi–linear stationary logarithmic density gradients in the case a consistent variation of β' is included in the simulations, shown in Fig. 4.9, can be identified. At $k_y\rho_s > 0.7$, the $\beta_e = \beta' = 0$ values are shifted in the outward direction compared

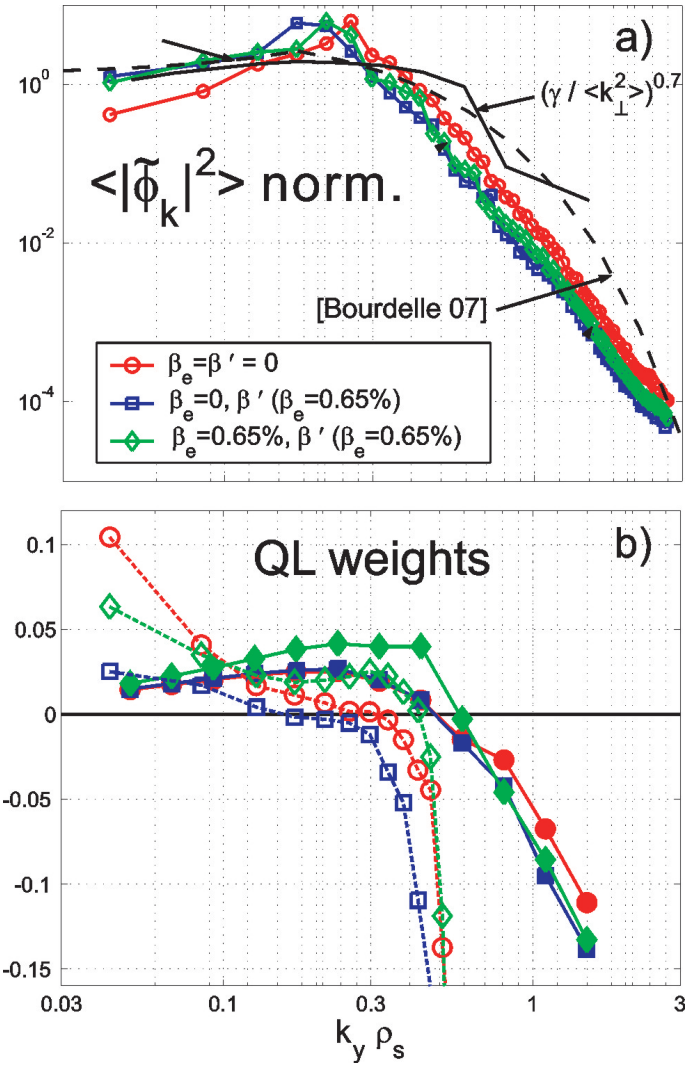

Figure 4.10: Potential fluctuation spectra $|\tilde{\phi}_k|^2$ from nonlinear gyrokinetic simulations (a). Circles denote the case of $\beta_e = \beta' = 0$, squares represent $\beta_e = 0$ with β' consistent to a value if β_e was 0.65%, and diamonds for $\beta_e = 0.65\%$ with a β' consistent with a β_e of 0.65%. Also the quasi–linear rules are shown. The normalization is $\int dk_y |\tilde{\phi}_{k_y}|^2 = 1$. Quasi–linear weights $\Im(\tilde{n}_k \tilde{\phi}_k^*)/|\tilde{\phi}_k|^2$ obtained from linear (continuous lines) and nonlinear (dashed lines) simulations (b). The chosen plasma parameters are similar to ASDEX Upgrade hybrid discharges with $R/L_n = 2$.

to the cases with fixed β', thus lowering the stationary density gradient, particularly in the case of a wave number spectrum giving a large impact to small scales, like the one proposed in [91].

From the detailed comparisons presented in Fig. 4.10 it can be concluded that, particularly when the particle flux is close to the null, the inward contribution from the relatively small scales is usually weaker in linear calculations compared to nonlinear simulations, a feature which was already observed in Ref. [90]. Thereby, in these cases, the use of the actual nonlinear spectrum for $|\tilde{\phi}_k|^2$ in quasi–linear models does not necessarily provide the

most accurate quasi–linear evaluation of the total nonlinear particle flux. A compensation should take place for a more accurate matching of the total flux, where quasi–linear weights, which are too small in size at small scales, have their contribution enhanced in a quasi–linear model in which the corresponding values of the $|\tilde{\phi}_k|^2$ spectrum at those scales are relatively larger with respect to the actual nonlinear ones. These considerations can be of particular importance for quasi–linear models of particle transport, since in this transport channel quasi–linear weights usually change their sign from outward to inward with increasing wave number, as a consequence of the different impact of collisionality at the different scales [90]. Finally, it has to be noted that in the present comparison, linear results consider only one mode at each wave number, that is the most unstable one, whereas a more appropriate approach, like for instance that undertaken in [91], should take into account the entire spectrum of unstable (or perhaps even stable) modes at each wave number. This indeed can play a role in the establishment of the quasi–linear weights in the nonlinear simulations. In addition, it is reasonable to assume that a strong component in the differences between linear and nonlinear results comes from the impact of wave number (toroidal mode) coupling, which takes place in the nonlinear simulations, but which is not included in the quasi–linear models.

4.4.3 Effect of a particle source due to NBI heating

The decrease with increasing β of the predicted value of $R/L_{n,stat}$ obtained by the nonlinear simulations with consistent variation of β', presented in Fig. 4.9, remains rather strong, and does not appear to be qualitatively consistent with the weak effect documented so far in non–dedicated experimental studies [72, 73, 74]. In order to address this problem within a more realistic approach, also the impact of a particle source like the one provided by neutral beam injection (NBI) fueling on the theoretically predicted dependence of $R/L_{n,stat}$ on β is considered. This can be done by looking for the value of R/L_n at which a given predicted ratio $\Gamma_e T/Q_{tot}$ matches the corresponding ratio of the volume integral of the particle source to the volume integral of the heat source, instead of more simply the condition $\Gamma_e = 0$, which assumes no particle source. A rough estimate of the ratio of the volume integral of the particle source density delivered by the beams, Γ_{NBI}, to the volume integral of the NBI heat power density Q_{NBI} is given by $\Gamma_{NBI}/Q_{NBI} = 1/E_{NBI}$, where E_{NBI} is an effective (averaged) beam ion injection energy. Therefore, in the presence of beam fueling, and in stationary conditions, with negligible neoclassical transport, the value of $R/L_{n,stat}$ can be expected to be given by the following condition $\Gamma_e T/Q_{tot} \simeq \Gamma_{NBI} T/Q_{NBI}\,(Q_{NBI}/Q_{tot}) \simeq (T/E_{NBI})\,(Q_{NBI}/Q_{tot})$. At constant plasma density, $\beta \propto T$ and by this it is found that with increasing β, the value of $\Gamma_e T/Q_{tot}$ at which $R/L_{n,stat}$ can be identified, increases as well. Considering that most of the present experiments are heated with intense neutral beam injection, it is of interest to check whether, on the basis of our nonlinear simulations of a realistic ASDEX Upgrade case, this source effect is significant in determining an "apparent" β dependence (or β independence) of the density peaking. For this reason typical parameters of the ASDEX Upgrade neutral beam injection system are taken, and an effective beam energy $E_{NBI} = 70$ keV is considered, which yields, with a toroidal magnetic field of 2.4 T and a fixed density of $6 \times 10^{-19} m^{-3}$, the following scaling $T/E_{NBI} = 3.41\beta_e$. Figure 4.11 shows the results of this exercise, in which three different fractions of Q_{NBI}/Q_{tot}, that is 0, 50% and 100%, are considered. On the basis of the nonlinear simulations presented in this Chapter, it is found that the effect is significant

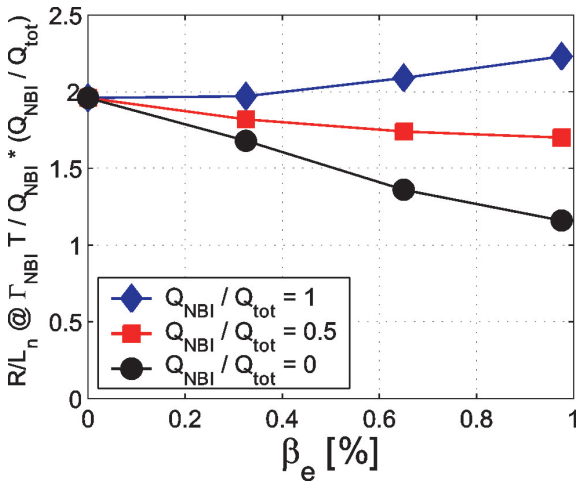

Figure 4.11: Stationary logarithmic density gradient from nonlinear simulations changing both β_e and β' consistently for three different assumptions of the fraction of neutral beam injection heating to the total heating mix for plasma parameters similar to ASDEX Upgrade hybrid discharges.

and suggests that plasma discharges in which a large fraction of the heating power is not delivered by NBI systems should observe a stronger decrease of the density peaking with increasing β with respect to experiments in which the plasma is heated almost exclusively by beams. In the latter case, a β independence or even a moderate increase of the peaking with increasing β is predicted.

4.5 Summary and conclusions

Finite β effects on electron transport in tokamak plasmas due to both Ampère's law and changes in the magnetic equilibrium have been investigated using linear and nonlinear gyrokinetic flux tube simulations. The logarithmic density gradient at the null of the turbulent particle flux $R/L_{\mathrm{n,stat}}$ has been calculated as a function of β_e. In ITG turbulence, the electromagnetic effect due to the inclusion of fluctuations of the magnetic field in the perpendicular direction implies a non–adiabatic response of the passing electrons, as it was pointed out also in [84]. This produces an outward directed convection and strongly reduces the value of $R/L_{\mathrm{n,stat}}$ with increasing β_e. In TEM turbulence the effect is found to be weaker. The physics of the electromagnetic effects on the particle flux has been investigated by means of an analytical derivation, starting from a formal solution of the gyrokinetic equation, and the analytical results have been shown to be fully consistent with the numerical simulations. The contribution due to magnetic flutter transport has been investigated, and has been found to be directed inward in ITG turbulence and non–negligible at the highest values of β_e. In this context, the present gyrokinetic study agrees and extends a previous analysis based on a fluid model [49], and confirms the reversal of the particle flux from inward to outward with increasing β_e previously found in nonlinear gyrokinetic simulations of ITG turbulence [75].

Within a more realistic description of the impact of β on the density peaking, simulation results have been presented in which also the effect of the total plasma pressure

gradient in the curvature drift, due to the modification of the magnetic equilibrium, is included consistently. The two effects are of course strongly combined in experiments, while they can be separated in the theoretical calculations. The present study shows that once both effects are included consistently in a realistic case, the predicted decrease of density peaking with increasing β becomes weaker. A significant difference has been found in these cases between quasi–linear results and nonlinear simulations, since in the latter the inclusion of a consistently varying plasma pressure gradient has a more limited impact. In fact, in quasi–linear calculations, the predicted value of the logarithmic density gradient at the null of the particle flux $R/L_{\mathrm{n,stat}}$ is found to be strongly affected by the assumptions made on the binormal wave number spectrum of the fluctuating potential. It has been shown that contributions to the particle flux at different wave numbers can be directed inward or outward, and therefore require an appropriate weighting rule in quasi–linear models in order to reproduce the total nonlinear flux. A detailed comparison between the quasi–linear and the nonlinear spectra shows that linear calculation based on the most unstable linear mode at each wave number produce contributions to the particle flux at small scales which are significantly more outward or less inward directed with respect to the corresponding nonlinear results. In this context, the predicted value of $R/L_{\mathrm{n,stat}}$ is an appropriate and experimentally relevant parameter over which the adequacy of the assumptions on the wave number spectrum made in the quasi–linear models can be tested against the nonlinear results.

In order to address at a qualitative level of the comparison with the experimental observations, the effect of core fueling by neutral beams has been included in the estimate of the predicted stationary value of the logarithmic density gradient $R/L_{\mathrm{n,stat}}$. In conditions of neutral beam injection heating only, at constant plasma density, the impact of the beam fueling on $R/L_{\mathrm{n,stat}}$ increases with increasing β. On the basis of the nonlinear gyrokinetic simulations presented here, for typical ASDEX Upgrade parameters, this is found to have non–negligible consequences on the dependence of the predicted $R/L_{\mathrm{n,stat}}$ on β. In conditions of dominant neutral beam injection heating and constant density, $R/L_{\mathrm{n,stat}}$ is found to become almost independent of β, in contrast with the prediction of a rather strong decrease of $R/L_{\mathrm{n,stat}}$ with increasing β when core fueling by neutral beams is absent. These theoretical results should motivate further dedicated experimental research on this important aspect for the performance of high β tokamak scenarios.

The present results are also relevant in other fields of plasma physics. Due to the importance of the parallel velocity for the behavior of electromagnetic particle fluxes it is emphasized that an electromagnetic kinetic treatment and in particular the consideration of magnetic flutter transport is crucial for small scale turbulence in slab-like astrophysical plasmas, since in particular the value of β in interstellar ($\beta \sim 1$, see e. g. [95]) or intergalactic media ($\beta \sim 10 - 100$, see e. g. [96]) as well as in jet-formation regions at the black hole magnetosphere ($\beta \sim 1 - 100$, see e. g. [97]), is significantly higher than in tokamak plasmas.

Chapter 5

Investigations of electromagnetic effects on trace impurity transport

5.1 Formulation of the problem

While the presence of impurities in the edge and divertor regions of a tokamak has beneficial effects like the reduction of heat loads on the first wall elements and a cold gas target around the divertor, in the central region it might imply serious limitations of performance and operation in a fusion reactor. Thus, the possibility of reaching plasma conditions with reduced inward convection or even outward convection of impurities in the core is extremely attractive for reactor operation. This is of particular importance in the presence of highly charged plasma facing components, like tungsten.

In this framework, the increasing interest in high β_{N} scenarios, like the hybrid scenario [66, 67, 68] for ITER operation, motivates the study of the impact of electromagnetic effects at finite β on the transport of impurities from the theoretical standpoint. The impact of finite β effects on light impurity transport has received some consideration from the experimental side [98, 99]. A decrease of the helium diffusivity with increasing β has been observed in DIII–D [98], and, consistently, a decrease of trace T diffusivity with increasing β has been documented in the Joint European Torus (JET) [99]. The consistency between these experimental observations provides an important test for theory validation in the prediction of the effect of increasing β on the transport of impurities. This is of particular relevance for nuclear fusion applications, since a decrease of helium diffusivity with increasing β might have negative consequences on the central helium ash concentration due to the effect of the central helium ash particle source in a burning plasma. This problem is considered in the present Chapter, and, by this, aimed at complementing recent theoretical works dedicated to impurity turbulent transport in the electrostatic limit [100, 101, 102, 103, 91, 104, 105, 106, 107, 108, 109].

Both light and heavy impurities are considered. It is shown that for experimentally achievable values of β, electromagnetic effects can be significant in some conditions. By means of an approach already applied in electrostatic calculations [104], diffusive and convective contributions to the impurity transport are identified, and both the $\mathrm{E}\times\mathrm{B}$ as well as the magnetic flutter transport are computed. The decomposition of the fluxes in diffusive and convective contributions allows the direct comparison with the experimental results. Experimental measurements, usually obtained by means of the analysis of transients pro-

duced by gas puff or laser ablation of impurities, yield separately the values of the diffusion coefficient and of the total convective velocity.

In order to reach the purpose of the desired investigations, and to consider a large range of impurity charges in different turbulence conditions, an extensive set of numerical calculations is required exploring different domains of plasma parameters. For this reason, the present study is mainly limited to the calculation of quasi–linear transport, while nonlinear electromagnetic simulations of impurity transport, which are highly demanding in computer time, are shown in only one example. Plasma parameters providing both ITG and TEM as most unstable microinstabilities in the background have been considered. Analytical derivations, starting from a simple fluid model, are performed in order to shed light on the physics processes which are responsible of the numerical gyrokinetic results. Reference cases providing strongly unstable ITG and TEM modes are used first to study the impurity transport in the two limits. Then, a more realistic case with typical plasma parameters of an H–mode plasma, like those expected in the ITER standard scenario, is considered, in order to investigate the impurity transport in the more experimentally relevant condition of an ITG mode with similar electron and ion logarithmic temperature gradients, closer to the threshold.

This Chapter is organized as follows. The next Section introduces the ITG and TEM reference cases and shows the numerical results, investigating the effects of β on impurity transport as a function of the impurity charge (Z_p) and mass ($A_\mathrm{p} = m_\mathrm{p}/m_\mathrm{H}$). Then, a simple fluid model based on the derivations in Chapter 3.1 is discussed allowing for the analytical calculation of the electromagnetic effects on impurity transport. It is used for the interpretation of the numerical results. Afterwards, the specific case of typical realistic parameters of an H–mode plasma at mid–radius are considered. The results are compared qualitatively with the experimental observations documented in the literature and discussed in projection to the operation of future fusion devices like ITER. Finally, the last section draws the main conclusions.

5.2 Gyrokinetic calculations of electromagnetic effects on trace impurity transport

In this section, results of gyrokinetic calculations are reported, in which a third particle species, namely an impurity, is included in very small charge concentration. As it can be seen from the discussion in Chapter 4, the gyrokinetic equation for a particle species σ is linear in the normalized logarithmic temperature and density gradients, respectively $R/L_{\mathrm{T},\sigma} = -R\nabla_\mathrm{r} T_\sigma/T_\sigma$ and $R/L_{\mathrm{n},\sigma} = -R\nabla_\mathrm{r} n_\sigma/n_\sigma$, see Eq. (4.1). Therefore, in a local description, a formal expression for the linear response of the perturbed distribution function δf_σ to an electromagnetic potential fluctuation U, which is the generalized potential as it was defined in 4.2, is provided by the following linear combination of these gradients,

$$\delta f_\sigma = \left(A_\sigma \frac{R}{L_{\mathrm{n},\sigma}} + B_\sigma \frac{R}{L_{\mathrm{T},\sigma}} + C_\sigma \right) U, \tag{5.1}$$

where the coefficients A_σ, B_σ and C_σ do not depend on the logarithmic gradients themselves, but are complicated functions in the phase space.

The particle flux Γ_σ in the radial direction is given by Eq. (4.2). As a direct consequence, the linearity in the gradients is formally preserved, leading to an expression for

the particle flux which is usually written as

$$\frac{R\Gamma_\sigma}{n_\sigma} = D_\sigma \frac{R}{L_{\mathrm{n},\sigma}} + D_{\mathrm{T},\sigma} \frac{R}{L_{\mathrm{T},\sigma}} + RV_{\mathrm{P},\sigma}, \tag{5.2}$$

where D_σ denotes the diagonal diffusion coefficient, $D_{\mathrm{T},\sigma}$ the thermodiffusion coefficient and $V_{\mathrm{P},\sigma}$ is the pure convection velocity. Recently it has been noted that in the presence of a radial gradient of the toroidal rotation velocity profile an additional term is present in the decomposition, which is proportional to the gradient of the toroidal velocity and can be labeled as roto–diffusion [110]. This term is not considered in this study. While Eq. (5.2) provides a useful physical decomposition, it cannot be considered as a real linear relationship for bulk plasma species, since the transport coefficients depend on the logarithmic gradients. However, for an impurity species p with a charge concentration $n_\mathrm{p} Z_\mathrm{p}/n_\mathrm{e}$ small enough to be negligible in the Poisson and Ampère's equations, the coefficients D_p, $D_{\mathrm{T,p}}$ and $V_{\mathrm{P,p}}$ become independent of the logarithmic density and temperature gradients of that species and the impurity behaves like a trace. The flux of this trace species is a linear function of the logarithmic gradients. In particular, $V_{\mathrm{P,p}}$ provides the residual flux in the absence of gradients of the impurity, that is when $R/L_{\mathrm{n,p}} = 0$ and $R/L_{\mathrm{T,p}} = 0$.

As a consequence of such a linear relationship, the three coefficients D_σ, $D_{\mathrm{T},\sigma}$ and $V_{\mathrm{P},\sigma}$ can be easily computed with a gyrokinetic code using an appropriate set of linear gyrokinetic simulations. Recasting Eq. (5.2) in the form,

$$\frac{R\Gamma_\mathrm{p}}{n_\mathrm{p}} = D_\mathrm{p} \left(\frac{R}{L_\mathrm{np}} + C_\mathrm{T} \frac{R}{L_\mathrm{Tp}} + C_\mathrm{P} \right), \tag{5.3}$$

the coefficients $C_\mathrm{T} = D_\mathrm{Tp}/D_\mathrm{p}$ and $C_\mathrm{P} = RV_\mathrm{Pp}/D_\mathrm{p}$ can be identified from the slope of the particle flux as a function of the logarithmic temperature and density gradients, as well as from the residual flux at zero gradients. In stationary conditions, in the absence of a source and for negligible neoclassical transport, the turbulent flux is at the null, namely $\Gamma_\mathrm{p} = 0$, and the coefficients C_T and C_P provide the stationary logarithmic density gradient, through the relationship $R/L_\mathrm{np} = -C_\mathrm{T}\, R/L_\mathrm{Tp} - C_\mathrm{P}$. It is worth mentioning that first comparisons between linear and nonlinear gyrokinetic calculations of these parameters in the electrostatic limit have shown a satisfactorily good agreement [108].

Here, such an approach is applied in order to compute the electromagnetic effects on the transport of an impurity. An impurity species with a charge concentration of $1/1000$ in a plasma of deuterons and electrons is included. In order to investigate the different role of ITG and TEM microinstabilities, reference cases are chosen, namely $r/R = 0.17$, $q = 1.4$, $s = 0.8$ and $R/L_\mathrm{n} = 3$ as common parameters, $R/L_{\mathrm{T,i}} = 9$ and $R/L_{\mathrm{T,e}} = 3$ for ITG and $R/L_{\mathrm{T,i}} = 3$ and $R/L_{\mathrm{T,e}} = 9$ for the TEM case, respectively. A s–α geometry [42] is assumed, and ion, impurity and electron temperatures have been chosen to be equal. Collisions are excluded.

The linear dependence of the impurity flux on the logarithmic gradients have been verified in both linear and nonlinear electrostatic simulations [101, 104, 108]. Figure 4.1 shows for the ITG case that a linear dependence is also given in calculations at a finite β_e of 1% for both the E×B (a, c) and the magnetic flutter component from fluctuations of $A_{||}$ (b,d) of the flux as functions of $R/L_{\mathrm{n,p}}$ and $R/L_{\mathrm{T,p}}$, respectively, where β_e takes electromagnetic effects into account. Here, a single value of $k_\mathrm{y}\rho_\mathrm{s} = 0.3$ in the spectrum has been selected. The contributions are calculated consistently in such a way that the sums

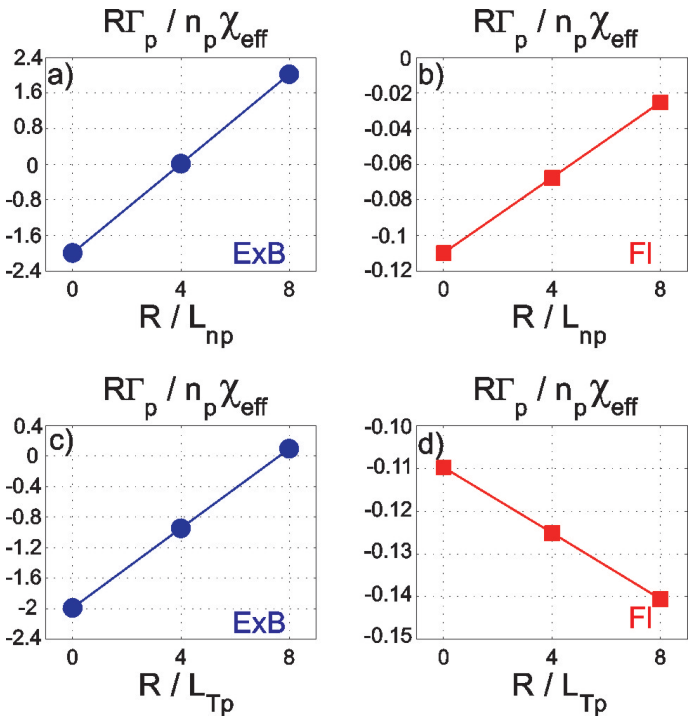

Figure 5.1: Electromagnetic ($\beta_e = 1\%$) gyrokinetic calculations of particle fluxes $R\Gamma_p/n_p$ for trace impurity helium (charge concentration $n_p Z_p/n_e = 1/1000$) as a function of the normalized logarithmic gradients R/L_{np} (a, b) and R/L_{Tp} (c, d) using GYRO. The background fluctuations in the electron–deuteron plasma have been chosen to be ITG dominated according to the ITG reference case.

of the E×B and the magnetic flutter components give the total flux. The dimensionless transport coefficients C_T and C_P become independent of the saturation amplitude of the fluctuating electrostatic and magnetic potentials, which makes them particularly suited for linear calculations.

Such a normalization cannot be applied directly to the dimensional impurity diffusion coefficient. However, an appropriate and experimentally relevant normalization can be easily identified. The average effective heat conductivity χ_{eff} of the plasma is defined such that

$$\frac{Q_{tot}}{2nT} = \frac{Q_i}{2nT} + \frac{Q_e}{2nT} = \chi_{eff}\frac{\nabla T}{T}, \tag{5.4}$$

where Q_{tot}, Q_i and Q_e are the total, ion and electron heat fluxes, respectively, $T = (T_i + T_e)/2$ and $\nabla T/T = \nabla(T_i + T_e)/(T_i + T_e)$. Using the definitions in Eq. (5.4), it can be directly derived that

$$\chi_{eff} = \frac{\chi_i \cdot \nabla T_i/T_i \cdot T_i/T + \chi_e \cdot \nabla T_e/T_e \cdot T_e/T}{\nabla T_i/T_i \cdot T_i/T + \nabla T_e/T_e \cdot T_e/T}, \tag{5.5}$$

and therefore with $T_i = T_e$ and $\nabla T_i = \nabla T_e$, $\chi_{eff} = (\chi_i + \chi_e)/2$, where χ_i and χ_e are the ion and electron effective heat conductivities, respectively. These can be computed within

the quasilinear gyrokinetic model by $\chi_{\mathrm{i,e}}(r) = -Q_{\mathrm{i,e}}(r)/n_{\mathrm{i,e}}\partial T_{\mathrm{i,e}}/\partial r$ with

$$Q_{\mathrm{i,e}}(r) = \langle \int d^3v \frac{m_{\mathrm{i,e}}v^2}{2} \delta f_{\mathrm{i,e}} \left(\mathbf{B} \times \nabla U/B^2\right) |_{\mathrm{r}} \rangle. \tag{5.6}$$

These coefficients correspond to the power balance heat conductivities determined in experiments, which easily allows direct comparisons between our quasi–linear results and the experimental observations.

The E×B and magnetic flutter transport coefficients are separated using the following definitions

$$C_{\mathrm{T}} = (C_{\mathrm{T}})_{\mathrm{E\times B}} + (C_{\mathrm{T}})_{\mathrm{Fl}} = \frac{D_{\mathrm{E}}}{D_{\mathrm{tot}}} C_{\mathrm{TE}} + \frac{D_{\mathrm{F}}}{D_{\mathrm{tot}}} C_{\mathrm{TF}} \tag{5.7}$$

and

$$C_{\mathrm{P}} = (C_{\mathrm{P}})_{\mathrm{E\times B}} + (C_{\mathrm{P}})_{\mathrm{Fl}} = \frac{D_{\mathrm{E}}}{D_{\mathrm{tot}}} C_{\mathrm{PE}} + \frac{D_{\mathrm{F}}}{D_{\mathrm{tot}}} C_{\mathrm{PF}}, \tag{5.8}$$

where D_{E} and D_{F} are the diagonal diffusion coefficients with $D_{\mathrm{tot}} = D_{\mathrm{E}} + D_{\mathrm{F}}$, $C_{\mathrm{TE}} = D_{\mathrm{TE}}/D_{\mathrm{E}}$, $C_{\mathrm{TF}} = D_{\mathrm{TF}}/D_{\mathrm{F}}$, $C_{\mathrm{PE}} = RV_{\mathrm{PE}}/D_{\mathrm{E}}$ and $C_{\mathrm{PF}} = RV_{\mathrm{PF}}/D_{\mathrm{F}}$. The quantities D_{TE} and D_{TF} are the thermodiffusion coefficients and V_{PE} and V_{PF} are the pure convective velocities due to E×B (E) and magnetic flutter (F) transport, respectively.

Figure 5.2 shows the poloidal spectrum of the linear eigenfrequency ω_{r} (a) and growth rate γ (b) in $[c_{\mathrm{s}}/R]$ units using $c_{\mathrm{s}}^2 = T_{\mathrm{i}}/m_{\mathrm{D}}$, as well as the E×B and magnetic flutter (Fl) components of the transport coefficients $D_{\mathrm{p,E\times B}}/\chi_{\mathrm{eff}}$ (c+d), $(C_{\mathrm{T}})_{\mathrm{E\times B}}$ (e+f) and $(C_{\mathrm{P}})_{\mathrm{E\times B}}$ (g+h) for the ITG and TEM cases, with helium as impurity species. The value of $\beta_{\mathrm{e}} = 0.5\%$ has been chosen. The spectrum of γ has its maximum at $k_{\mathrm{y}}\rho_{\mathrm{s}} \approx 0.3$ in the ITG case, whereas for TEM a continuous increase up to high poloidal wave numbers is found, since also electron temperature gradient (ETG) modes are unstable for this case, because the reference case was chosen with $T_{\mathrm{e}} = T_{\mathrm{i}}$.

The magnetic flutter transport reveals a significant dependence on the poloidal wave number, and is strongly reduced at large values of $k_{\mathrm{y}}\rho_{\mathrm{s}}$. However, it remains small with respect to the total transport, with a contribution which is of the order of 1% (or 10% for C_{P}) of the E×B transport. The latter, instead, does not exhibit strong variations as a function of the poloidal wave number. For this reason, for the qualitative purposes of the present study and considering also the large number of calculations required to explore the dependence of impurity species with various charge and mass in different turbulence conditions, most of the calculations presented in the followings are limited to the single representative value of $k_{\mathrm{y}}\rho_{\mathrm{s}} = 0.3$, where the maximum growth rate in the ITG case occurs. This choice is preferred to that of considering a single $k_{\mathrm{y}}\rho_{\mathrm{s}}$ value at which $\gamma/\langle k_\perp^2 \rangle$ is maximum. As already shown in Chapter 4.4, the latter choice provides results which are in larger disagreement with nonlinear results of electron particle transport. A comparison between results based on a single wave number at this binormal scale and those obtained applying an appropriate average over the wave number spectrum, is provided in [87] for the case of helium transport. The difference is reported to be rather small, especially for the E×B component, while for the flutter larger deviations are present. This can be expected from Fig. (5.2). Thus, the choice on the binormal spectrum only considering a single value at $k_{\mathrm{y}}\rho_{\mathrm{s}} = 0.3$, can be considered to be realistic.

In Figs. 5.3a and 5.3b the electromagnetic dependence of the normalized eigenfrequency and linear growth rate are shown for helium as impurity species. The values of ω_{r}, being positive for modes in the ion diamagnetic direction and negative in the electron

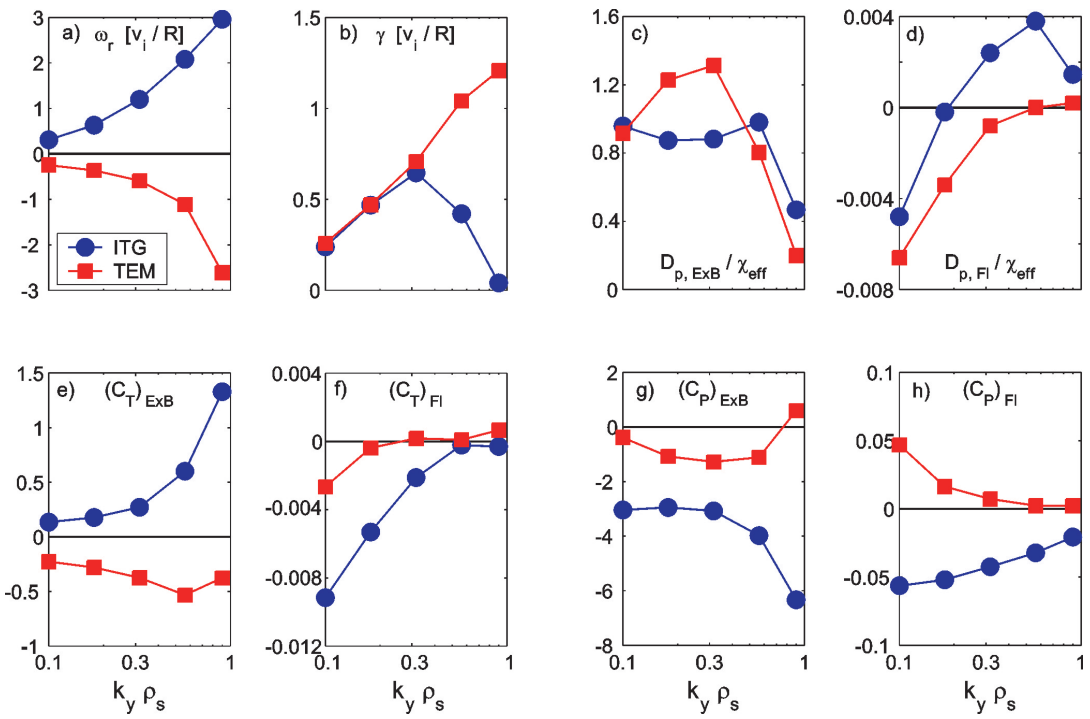

Figure 5.2: Linear gyrokinetic calculations of eigenfrequencies ω_r (a), growth rates γ (b), and of the $E \times B$ coefficients $D_{p,E\times B}/\chi_{eff}$ (c), $(C_T)_{E\times B}$ (e) and $(C_p)_{E\times B}$ (g), as well as of the corresponding magnetic flutter (Fl) components (d, f, h), as a function of $k_y\rho_s$ for trace impurity helium at $\beta_e = 0.5\%$.

diamagnetic direction, remain almost unchanged with increasing β_e in both cases. In contrast, the linear growth rate γ shows different behaviors in the ITG and TEM cases, it decreases with increasing β in the ITG reference case, while it remains almost unaffected in the TEM case [111, 75]. As it will be shown in the next Section, this difference in the behavior of the growth rate is responsible for the differences found in the dependence of impurity transport on β in the ITG and TEM cases.

Figure 5.3 shows also the behavior of the coefficients D_p/χ_{eff} (c,d), C_T (e,f) and C_P (g,h) as a function of β_e in linear gyrokinetic simulations, both for E×B and magnetic flutter (Fl) transport, respectively. First, transport due to E×B motion plays the major role. It is interesting to note that the dominant contribution of the magnetic flutter transport has the nature of a pure convection and can be up to 10% in the ITG case at high β_e. On the contrary, the diagonal diffusion and thermodiffusion contributions provided by magnetic flutter are $\approx 1\%$ in the ITG case, or even smaller for the TEM case. Second, $D_{p,E\times B}/\chi_{eff}$ decreases with β_e in the ITG case, while in the TEM case it is slightly increasing. As it will be shown, the reduction of $D_{p,E\times B}/\chi_{eff}$ in the ITG case is connected with the reduction of γ, where $D_{p,E\times B}$ decreases stronger that χ_{eff}. As usual, in both cases positive values of $D_{p,E\times B}/\chi_{eff}$ are obtained, that is outward diagonal diffusion. This is in contrast to the magnetic flutter component. Moreover, for all the flutter components of the transport coefficients, the directions exhibit a change going from ITG to TEM. Third, both the thermodiffusion and the pure convection are directed inwards in the TEM case, as indicated by the negative value of the coefficients $(C_T)_{E\times B}$ and $(C_P)_{E\times B}$. For ITG modes,

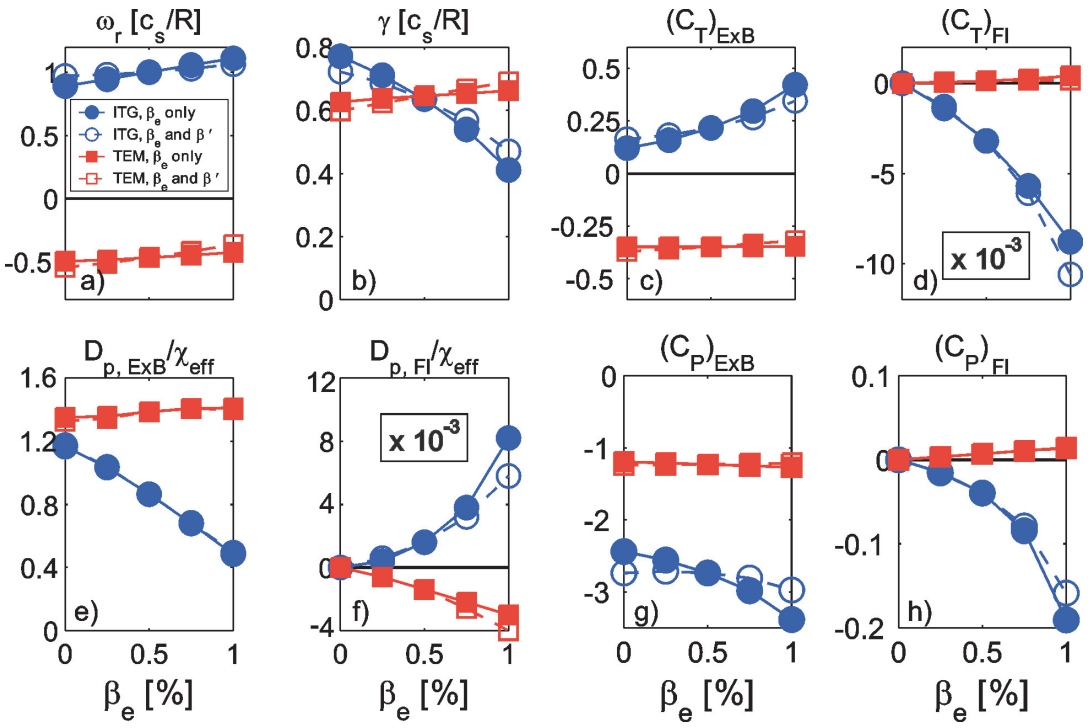

Figure 5.3: Gyrokinetic calculations of eigenfrequencies ω_r (a), growth rates γ (b), and of the $E \times B$ coefficients $(C_\mathrm{T})_{\mathrm{E\times B}}$ (c) $D_{\mathrm{p,E\times B}}/\chi_\mathrm{eff}$ (e) and $(C_\mathrm{p})_{\mathrm{E\times B}}$ (g), as well as of the corresponding magnetic flutter components (d, f , h), as a function of β_e for trace impurity helium at $k_\mathrm{y}\rho_\mathrm{s} = 0.3$. The full symbols represent simulations with only changing β_e in Ampère's law, while open symbols indicate cases in which both β_e and β' are changed consistently.

the thermodiffusion is directed outwards. The present results agree with previous results in the electrostatic limit [112, 113, 101, 103, 91]. In the case of TEM, electromagnetic effects are weak, while they play a strong role in the ITG case. In particular, the increase of the thermodiffusion factor $(C_\mathrm{T})_{\mathrm{E\times B}}$ in the outward direction can dominate over the increase of the pure convection term $(C_\mathrm{P})_{\mathrm{E\times B}}$ in the inward direction (we remind that in the calculation of the total impurity flux Γ_p the coefficient $(C_\mathrm{T})_{\mathrm{E\times B}}$ has to be multiplied by $R/L_{\mathrm{T,p}}$, which is ≥ 5 for typical parameters at mid-radius). In Fig. 5.3, the transport coefficients are calculated not only by changing β_e in Ampère's law, but also including the consistent change of β' through a consistent β'. By this the impact on the He behavior can be compared with that on electron transport presented in Chapter 4.4. This leads to only small deviations from the cases in which only β_e was varied. The largest difference in the E×B coefficients is obtained for the convection, which shows a smaller increase of the pinch with increasing β_e and β'. Considering the total flux, this smaller dependence is balanced by an also smaller dependence of the outward thermodiffusion. Moreover, flutter coefficients exhibits only small differences. For these reasons, and for the fact that nonlinear simulations for electron transport have shown only small differences (see Chapter 4), in the following only β_e with a fixed equilibrium is considered.

At this point, it is of interest to investigate the behavior of trace transport coefficients

due to changes in the impurity charge (Z_p) and mass (A_p). Figure 5.4 shows the co-

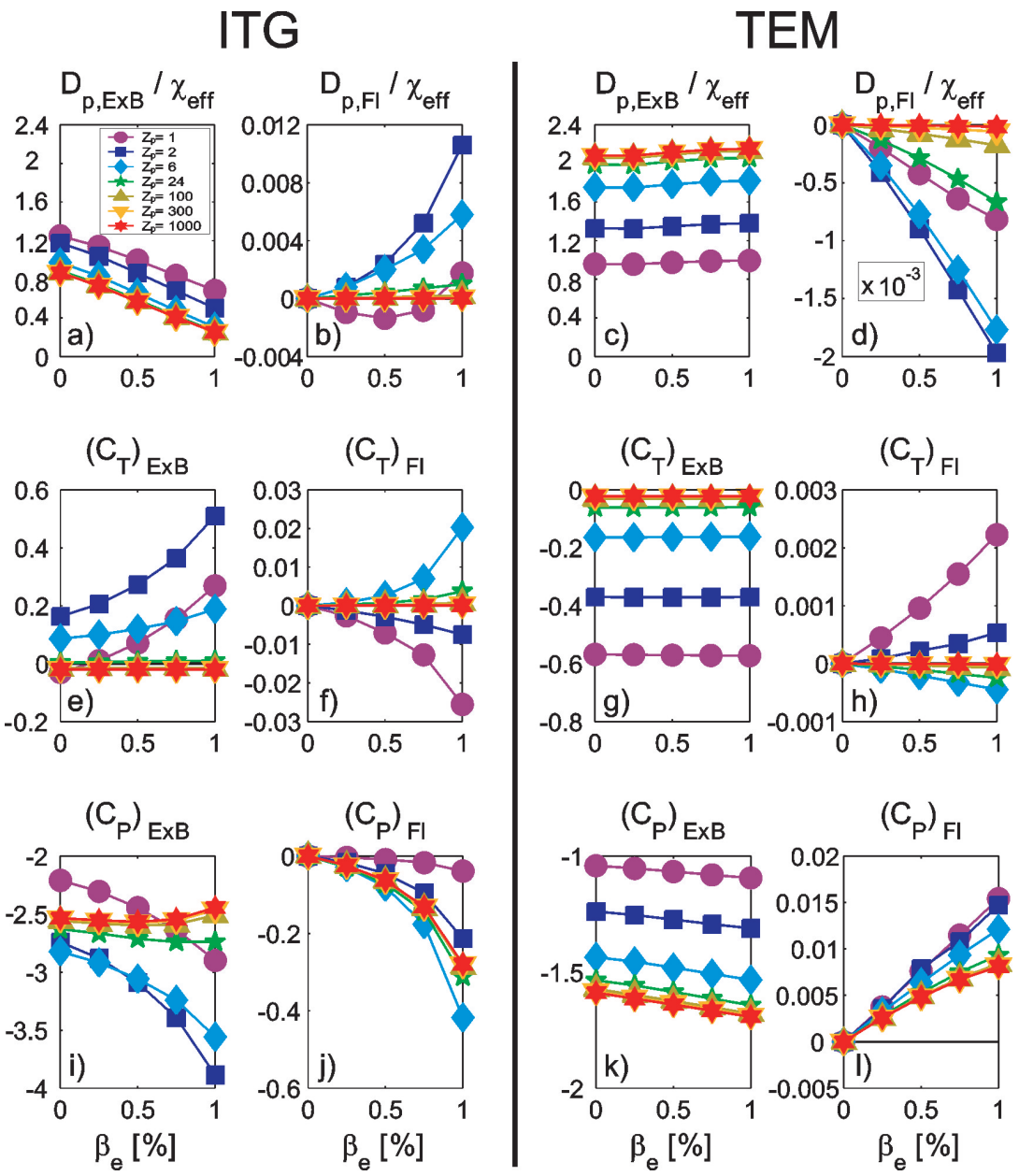

Figure 5.4: Electromagnetic dependence of the trace impurity $E \times B$ and magnetic flutter (Fl) transport coefficients $D_\mathrm{p}/\chi_\mathrm{eff}$ (a-d), C_T (e-h) and C_P (i-l) for increasing impurity charge Z_p with impurity mass $A_\mathrm{p} = 2Z_\mathrm{p}$. Left column plots show results for the ITG reference case, while right column plots show results for the TEM reference case.

efficients $D_\mathrm{p}/\chi_\mathrm{eff}$ (a-d), C_T (e-h) and C_P (i-l) for the ITG (left panel) and TEM (right panel) cases with increasing $Z_\mathrm{p} = A_\mathrm{p}/2$. Contributions from E×B and magnetic flutter (Fl) have been separated, and one observes again that E×B transport exceeds the latter by at least a factor of 10 in the ITG case and more than a factor 100 in the TEM case for small $Z_\mathrm{p} = A_\mathrm{p}/2$. With increasing impurity charge, the flutter contribution be-

comes completely negligible for diagonal diffusion and thermodiffusion at all β_e, while it reaches a finite asymptotic value for pure convection at large Z_p. The charge dependence of $D_{p,E\times B}/\chi_{eff}$ for different impurity species is not strongly affected by electromagnetic effects because all the curves at different charge are almost parallel. In contrast, $(C_T)_{E\times B}$ and $(C_P)_{E\times B}$ exhibit different dependences on β depending on the impurity charge, in particular, dependences are stronger for light impurities.

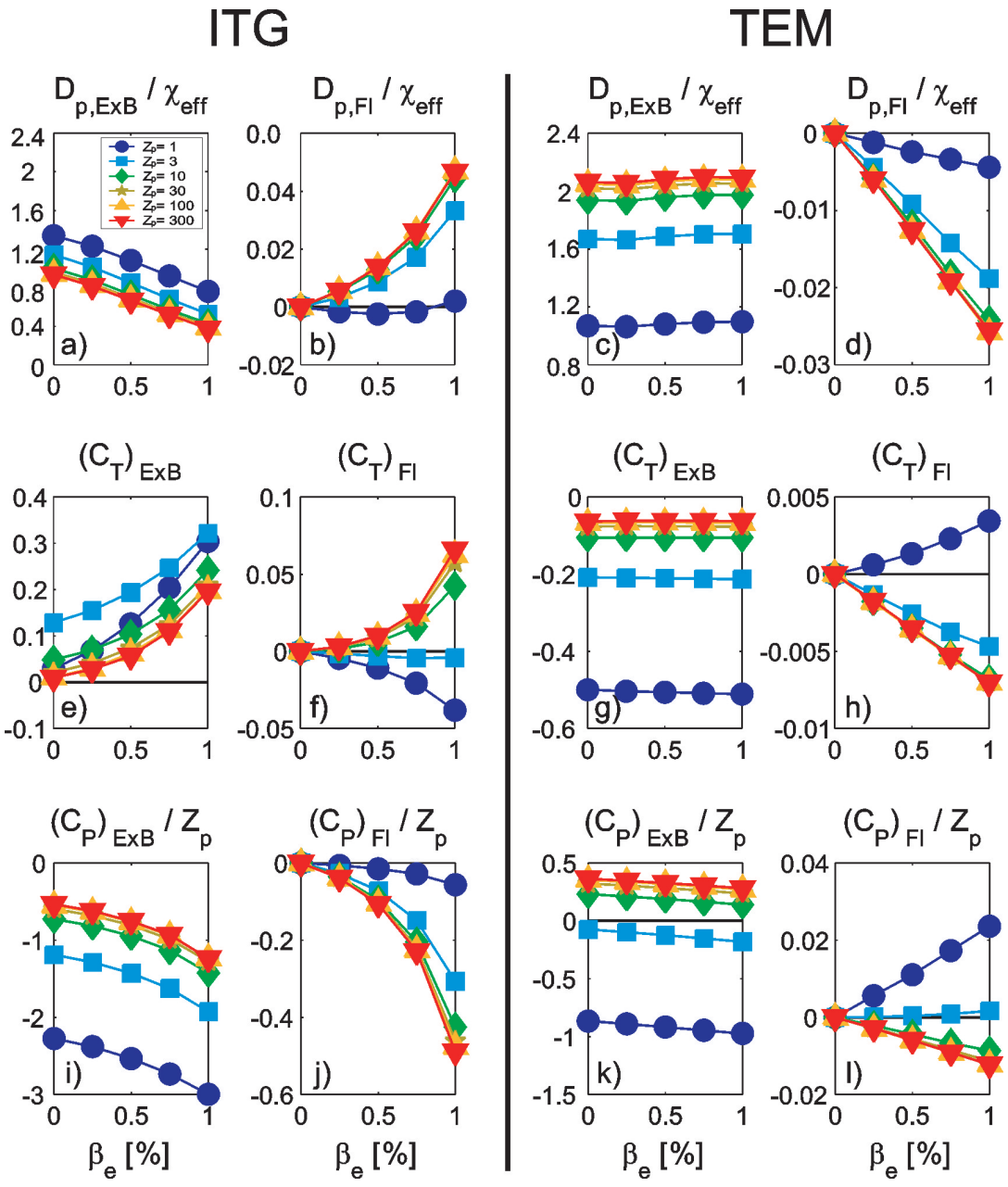

Figure 5.5: Electromagnetic dependence of the trace impurity $E \times B$ and magnetic flutter transport coefficients D_p/χ_{eff} (a-d), C_T (e-h) and C_P (i-l) for increasing impurity charge Z_p, while keeping the impurity mass fixed ($A_p = 1$). Left column plots show results for the ITG reference case, while right column plots show results for the TEM reference case.

In order to separate the effects of impurity charge and mass on the transport coefficients, also a scan of Z_p at fixed $A_\mathrm{p} = 1$ has been performed. They are presented in Fig. 5.5. For $D_{\mathrm{p,E\times B}}/\chi_\mathrm{eff}$ the behavior for both ITG and TEM is recovered. Therefore, the impurity charge is the quantity dominating diagonal diffusion coefficients. The mass A_p weakly lowers the values of $D_{\mathrm{p,E\times B}}/\chi_\mathrm{eff}$, see Figs. 5.4c and 5.5c (for instance for $Z_\mathrm{p} = 1$). The coefficients $D_\mathrm{p}/\chi_\mathrm{eff}$ and C_T show an asymptotic behavior with increasing Z_p, while C_P grows linearly at high values of Z_p, as expected from previous results [101]. Compared to Fig. 5.4, this shows that the impurity mass counteracts the effect of charge at finite values of β_e for both E×B and flutter diagonal and thermodiffusion, and prevents the linear increase of the pure convection. Obviously, the relative magnitude between E×B and magnetic flutter transport cannot be considered realistic for these cases with fixed mass.

In the next section, the simplified fluid model of Chapter 3 is used in order to shed light on the main physical processes which are responsible of the dependence of the impurity transport on β_e and of the results found in the numerical calculations.

5.3 Analytical fluid model

In order to understand the physics mechanisms which are responsible of the numerical results for the transport coefficients D_p, C_T and C_P including electromagnetic effects, the fluid model derived in Chapter 3 is considered. As already noted, the definition of the transport coefficients like in the previous section, Eqn. (5.3) and (5.4), implies that no saturation amplitude is required, making a linear model well suited. For a more direct comparison with previous analytical fluid a analysis, Eqn. (3.25), (3.26), (3.27) and (3.30) (or with (3.32) for small–β_i approximation) are used allowing for an analytical derivation of the trace impurity particle transport coefficients D_p, C_T and C_P.

5.3.1 E×B transport coefficients

The impact of electromagnetic effects on the E×B transport is studied. As already pointed out in the last section, electromagnetic effects can occur in two ways. The first way is through the modification of the phase shift between impurity density fluctuations and electrostatic potential fluctuations in the electrostatic limit produced by changes of the eigenfrequencies in response to an increase of β in the background plasma. The second way is by means of additional terms in the impurity flux introduced directly by fluctuations in the parallel vector potential. From the discussion in Chapter 4.2 it can be concluded that the first way is the one which produces the dominant effects. This is because the fluctuating vector potential $A_{||}$ is always connected with a parallel velocity. As it was shown, the latter scales with $\sqrt{\hat{\mu}}$, and is therefore small for impurities as compared to the electrons. This results in the fact that additional electromagnetic terms due to $A_{||}$ are very small, and implies that changes of ω_r and γ play the major role in understanding the electromagnetic behavior of the transport coefficients. Moreover, already electrostatic passing impurity fluxes are nonzero, in contrast to the electron species, as it can be seen from Fig. (5.6) for the diffusive part of trace helium.

Therefore, the impact of ω_r and γ is discussed firstly by focussing on the ratio of the impurity diffusivity to the total effective heat conductivity $D_{\mathrm{p,E\times B}}/\chi_\mathrm{eff}$. The effect of

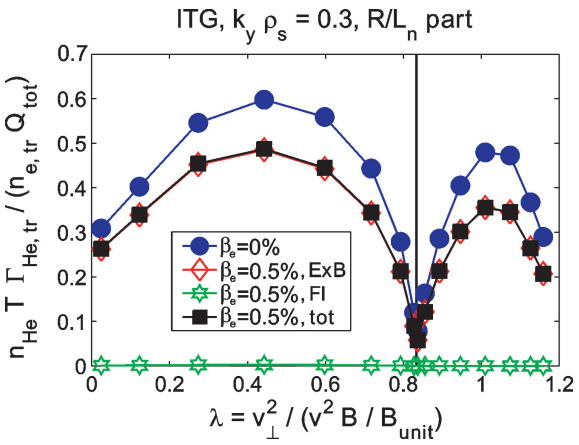

Figure 5.6: Electromagnetic dependence of the trace impurity $E \times B$ and magnetic flutter transport coefficients $D_\mathrm{p}/\chi_\mathrm{eff}$ (a-d), C_T (e-h) and C_P (i-l) for increasing impurity charge Z_p, while keeping the impurity mass fixed ($A_\mathrm{p} = 1$). Left column plots show results for the ITG reference case, while right column plots show results for the TEM reference case.

changing β_e on impurity diagonal diffusivity and total effective heat conductivity is calculated adopting the fluid model consisting of the continuity equation, the energy balance equation and the parallel motion equation of the trace species. According to Fig. 5.3b, the linear growth rate remains almost constant with increasing β_e for the TEM case while it strongly decreases in the ITG case. Thus, in the latter case, where χ_eff is mainly determined by the ion heat conductivity, the ratio $D_\mathrm{p,E\times B}/\chi_\mathrm{eff}$ due to this model is given by the coefficients

$$
\begin{aligned}
&D_\mathrm{p,E\times B} = 2\frac{\gamma\hat{\gamma}^2}{k_\mathrm{x}^2}\left\{|\hat{\omega}|^2\left(\frac{1}{2}|\hat{\omega}|^2 - \frac{7}{3Z_\mathrm{p}}\hat{\omega}_r + \frac{55}{18Z_\mathrm{p}^2}\right)\right.\\
&\left.+\hat{k}_{||}^2\frac{A_\mathrm{i}}{A_\mathrm{p}}\left[\frac{1}{6}\left(7\hat{\gamma}^2 - \hat{\omega}_r^2\right) + \frac{5}{9}\left(\hat{k}_{||}^2\frac{A_\mathrm{i}}{A_\mathrm{p}} + \frac{\hat{\omega}_r}{Z_\mathrm{p}}\right) + \frac{25}{18Z_\mathrm{p}^2}\right]\right\}\cdot\\
&\left\{\frac{1}{9A_\mathrm{i}^2Z_\mathrm{p}^4}\left\{A_\mathrm{p}^2|\hat{\omega}|^2\left[9Z_\mathrm{p}^4\left(|\hat{\omega}|^2\right)^2 + 10Z_\mathrm{p}^2\left(13\hat{\omega}_r^2 + 7\hat{\gamma}^2\right) + 25 - 100Z_\mathrm{p}\hat{\omega}_r - 60Z_\mathrm{p}^3\hat{\omega}_r|\hat{\omega}|^2\right] +\right.\right.\\
&10\hat{k}_{||}^2A_\mathrm{i}A_\mathrm{p}\left[5Z_\mathrm{p}\hat{\omega}_r - 15Z_\mathrm{p}^2\hat{\omega}_r^2 + 13Z_\mathrm{p}^3\hat{\omega}_r^3 - 3Z_\mathrm{p}^4\hat{\omega}_r^4 + 3Z_\mathrm{p}^4\hat{\gamma}^4 + Z_\mathrm{p}^2\hat{\gamma}^2\left(5 + Z_\mathrm{p}\hat{\omega}_r\right)\right] +\\
&\left.\left.25\hat{k}_{||}^4A_\mathrm{p}^2Z_\mathrm{p}^2\left[Z_\mathrm{p}^2\hat{\gamma}^2 + \left(Z_\mathrm{p}\hat{\omega}_r - 1\right)^2\right]\right\}\right\}^{-1}
\end{aligned}
\tag{5.9}
$$

and

$$\chi_{\mathrm{i}} = 2\frac{\gamma\hat{\gamma}^2}{k_{\mathrm{x}}^2}\left\{|\hat{\omega}|^2\left(\frac{1}{2}|\hat{\omega}|^2 - \hat{\omega}_r + \frac{5}{6}\right) + \frac{\hat{k}_{||}^2}{3}\left(4\hat{\gamma}^2 - 2\hat{\omega}_r^2 + 5\hat{\omega}_r\right) + \frac{5}{6}\hat{k}_{||}^4 + \right.$$
$$\frac{L_{\mathrm{Ti}}}{L_{\mathrm{ni}}}\left[|\hat{\omega}|^2\left(\frac{2}{3}\hat{\omega}_r - \frac{10}{9}\right) + \frac{\hat{k}_{||}^2}{3}\left(3\hat{\omega}_r^2 - \hat{\gamma}^2 - \frac{20}{3}\hat{\omega}_r\right) - \frac{5}{9}\hat{k}_{||}^4\right] +$$
$$\left.\frac{L_{\mathrm{Ti}}}{R}\left[|\hat{\omega}|^2\left(-\frac{2}{3}|\hat{\omega}|^2 - \frac{4}{3}\hat{k}_{||}^2\hat{\omega}_r + \frac{10}{9}(1+\hat{k}_{||}^2)\right) + \frac{20}{9}\hat{k}_{||}^2\hat{\omega}_r + \frac{10}{9}\hat{k}_{||}^4\right]\right\}\cdot$$
$$\left\{\frac{1}{9}\left\{|\hat{\omega}|^2\left[9\left(|\hat{\omega}|^2\right)^2 + 10\left(13\hat{\omega}_r^2 + 7\hat{\gamma}^2\right) + 25 - 100\hat{\omega}_r - 60\hat{\omega}_r|\hat{\omega}|^2\right] + \right.\right.$$
$$10\hat{k}_{||}^2\left[5\hat{\omega}_r - 15\hat{\omega}_r^2 + 13\hat{\omega}_r^3 - 3\hat{\omega}_r^4 + 3\hat{\gamma}^4 + \hat{\gamma}^2\left(5 + \hat{\omega}_r\right)\right] +$$
$$\left.\left.25\hat{k}_{||}^4\left[\hat{\gamma}^2 + (\hat{\omega}_r - 1)^2\right]\right\}\right\}^{-1}, \tag{5.10}$$

where $\hat{\omega} = \hat{\omega}_r + i\hat{\gamma}$ in the fluid equations such that $|\hat{\omega}|^2 = \hat{\omega}_r^2 + \hat{\gamma}^2$. For both, the usual mixing length estimate applied in Ref. [46] has been used, where the saturation level is assumed to be provided by the balance between linear growth rate and the dominant E×B convective nonlinearity. It is noteworthy that the saturation amplitude cancels identically when the ratio of the two quantities is performed and a single wave number is considered.

In order to explain the behavior of the ratio $D_{\mathrm{p,E\times B}}/\chi_{\mathrm{eff}}$, it turns out that parallel motion, which has been included in the lengthy calculation of Eq. (5.9) and Eq. (5.10), is important, because in this way the diagonal diffusion coefficient decreases in the ITG case with increasing β_{e} due to its strong dependence on $\hat{\gamma}$, while χ_{eff} only weakly decreases with increasing β_{e}. This leads to a ratio $D_{\mathrm{p,E\times B}}/\chi_{\mathrm{eff}}$, which decreases with decreasing $\hat{\gamma}$, in agreement with the gyrokinetic results. For impurities with high $Z_{\mathrm{p}} = A_{\mathrm{p}}/2$, the decrease of $D_{\mathrm{p,E\times B}}$ with raising β_{e} becomes stronger, but also the ratio of the respective denominators increases. This implies that the decrease of $D_{\mathrm{p,E\times B}}/\chi_{\mathrm{eff}}$ is not strongly affected by increasing impurity charge, as also found in the gyrokinetic results, Figs. 5.4 and 5.5. The ratio $D_{\mathrm{p,E\times B}}/\chi_{\mathrm{eff}}$ is mainly determined by the dependence of $D_{\mathrm{p,E\times B}}$ with increasing β_{e}. It is underlined that, like often performed in experimental comparisons between particle diffusion and heat conduction, the coefficient $D_{\mathrm{p,E\times B}}$ is the diagonal impurity diffusivity, while χ_{eff} is the total power balance (effective) heat conductivity. Therefore, only a part of the phase shift between $\hat{n}$ and $\hat{\phi}$ is considered in the former case, while in the latter one the total phase shift between $\hat{T}$ and $\hat{\phi}$ is taken into account. In the TEM case, the linear growth rate is changing very weakly with increasing β_{e}, and therefore neither $D_{\mathrm{p,E\times B}}$ nor χ_{eff} show a significant change, which explains why $D_{\mathrm{p,E\times B}}/\chi_{\mathrm{eff}}$ remains almost constant in gyrokinetic simulations.

Now, we turn to the effect caused by the variation of linear growth rates with increasing β on the coefficients C_{T} and C_{P} produced by electrostatic fluctuations is discussed. This can be readily discussed using the expressions in [101]. It is recalled that, neglecting parallel velocity fluctuations, the electrostatic E×B thermodiffusion coefficient for the impurities reads,

$$(C_{\mathrm{T}})_{\mathrm{ES,T}} = \frac{2}{Z_{\mathrm{p}}}\frac{\hat{\omega}_r - 5/(3Z_{\mathrm{p}})}{|\hat{\omega}|^2 - 14\hat{\omega}_r/(3Z_{\mathrm{p}}) + 55/(9Z_{\mathrm{p}}^2)}, \tag{5.11}$$

where again $|\hat{\omega}|^2 = \hat{\omega}_r^2 + \hat{\gamma}^2$. Therefore, it can be observed that a decrease of $\hat{\gamma}$ with increasing β leads to a decrease of the denominator and therefore an increase of the coefficient C_{T}, as found in the gyrokinetic results for the ITG reference case. On the contrary, in the TEM case the linear growth rates are only weakly affected with consequent small changes of the impurity thermodiffusive coefficient.

The same considerations can be made for the pure convection coefficient C_{P}. Neglecting again parallel velocity fluctuations, $(C_{\mathrm{P}})_{\mathrm{ES,T}} = -2\,(1 + 2\,(C_{\mathrm{T}})_{\mathrm{ES,T}}/3)$, which consistently provides an increase in size of C_{P} in the inward direction due to an increase of C_{T} in the case of the ITG mode, while it remains almost constant in the TEM case. The consistency with the gyrokinetic results indicates that the main mechanism through which an increase of β affects the transport of impurities derives from the coupling between density and temperature fluctuations produced by the ∇B and curvature drift.

It is certainly of interest for the physical understanding to investigate also the dependence of thermodiffusion and pure convection on the impurity charge and mass by means of the fluid model. In addition, this allows to more directly separate transport processes due to perpendicular drifts from those arizing from parallel dynamics. To this end, the full electrostatic fluid model is considered, including also the electrostatic part of the parallel motion equation, and noting that in the limit of very large impurity charge, that is $Z_{\mathrm{p}} \gg 1$, the coupling between density fluctuations and parallel velocity fluctuations is the only one which does not vanish. In the thermodiffusion coefficient, parallel dynamics introduces additional terms with respect to Eq. (5.11), yielding the following more complete expression

$$
\begin{aligned}
(C_{\mathrm{T}})_{\mathrm{ES}} \;=\; & \left\{ \frac{|\hat{\omega}|^2}{Z_{\mathrm{p}}} \left(\hat{\omega}_r - \frac{5}{3Z_{\mathrm{p}}} \right) + \frac{1}{2} \hat{k}_{||}^2 \frac{A_{\mathrm{i}}}{A_{\mathrm{p}}} \left(3\hat{\omega}_r^2 - \hat{\gamma}^2 - \frac{5}{3} \hat{k}_{||}^2 \frac{A_{\mathrm{i}}}{A_{\mathrm{p}}} \right) - \frac{10}{3Z_{\mathrm{p}}} \hat{k}_{||}^2 \frac{A_{\mathrm{i}}}{A_{\mathrm{p}}} \hat{\omega}_r \right\} \cdot \\
& \left\{ |\hat{\omega}|^2 \left(\frac{1}{2} |\hat{\omega}|^2 - \frac{7}{3Z_{\mathrm{p}}} \hat{\omega}_r + \frac{55}{18 Z_{\mathrm{p}}^2} \right) \right. \\
& \left. + \hat{k}_{||}^2 \frac{A_{\mathrm{i}}}{A_{\mathrm{p}}} \left[\frac{1}{6} \left(7\hat{\gamma}^2 - \hat{\omega}_r^2 \right) + \frac{5}{9} \left(\hat{k}_{||}^2 \frac{A_{\mathrm{i}}}{A_{\mathrm{p}}} + \frac{\hat{\omega}_r}{Z_{\mathrm{p}}} \right) + \frac{25}{18 Z_{\mathrm{p}}^2} \right] \right\}^{-1} ,
\end{aligned}
\tag{5.12}
$$

which reduces to Eq. (5.11) in the limit of $\hat{k}_{||}^2 = 0$. From this expression, it is evident that at high Z_{p} and high mass $A_{\mathrm{p}} = 2Z_{\mathrm{p}}$ the thermodiffusion coefficient vanishes. The role of parallel dynamics can be put in evidence by studying the behavior in the ideal limit of large Z_{p} with fixed impurity mass $A_{\mathrm{p}} = 1$, as it was already done in the numerical gyrokinetic results presented in Fig. 5.5. With $Z_{\mathrm{p}} \gg 1$ and $A_{\mathrm{p}} = 1$ the thermodiffusion coefficient $(C_{\mathrm{T}})_{\mathrm{ES}}$ does not vanish in the limit $\beta_{\mathrm{e}} = 0$ for both ITG and TEM instabilities, which means positive or negative values of $\hat{\omega}_r$, but decreases to finite small values. In addition, in the ITG case, the coefficient $(C_{\mathrm{T}})_{\mathrm{ES}}$ is found to increase in the limit $Z_{\mathrm{p}} \gg 1$ with increasing β_{e} and therefore with decreasing of $\hat{\gamma}$, due to the concurrent increase of the numerator and the decrease of the denominator, consistently with the gyrokinetic results shown in Fig. 5.5. In contrast, no strong dependence on β_{e} is obtained in the TEM case, where the eigenfrequencies are found to very weakly depend on β_{e}.

Then, the effect of parallel dynamics on the pure convection coefficient is considered. Neglecting temperature fluctuations this is directly given by the results in [101],

$$
(C_{\mathrm{P}})_{\mathrm{ES}\,||} = - \frac{2|\hat{\omega}|^2 + 4\hat{\omega}_r \hat{k}_{||}^2 Z_{\mathrm{p}} A_{\mathrm{i}}/A_{\mathrm{p}}}{|\hat{\omega}|^2 + \hat{k}_{||}^2 A_{\mathrm{i}}/A_{\mathrm{p}}} .
\tag{5.13}
$$

This yields an inward contribution, increasing in size with increasing Z_p for the ITG case (positive $\hat{\omega}_r$). In contrast, in the TEM case it is directed inward for small impurity charge, but reverses direction with increasing charge due to the outward contribution of the second term at the numerator (negative $\hat{\omega}_r$). These behaviors are also found in the numerical gyrokinetic results presented in Fig. 5.4, in the limit of $\beta_\mathrm{e} = 0$. The dependence on β_e found in the ITG case can be also explained by the simple fluid model, observing that with increasing β_e and therefore decreasing $\hat{\gamma}$, the second term $-4\hat{\omega}_r \hat{k}_{||}^2 Z_\mathrm{p} A_\mathrm{i}/A_\mathrm{p}/(|\hat{\omega}|^2 + \hat{k}_{||}^2 A_\mathrm{i}/A_\mathrm{p})$ in Eq. (5.13) increases in size, in the inward direction.

All these considerations based on the simple fluid model, and the consistency found with the more complete numerical gyrokinetic results, allow us to explain the dependence on β_e and impurity charge and mass found in the gyrokinetic calculations and to identify the main physical processes which are responsible for these. The main dependence arise from electrostatic type of transport processes, mainly connected with the perpendicular dynamics. An increase of β_e affects the electrostatic impurity transport through the dependence on β_e of the eigenfrequencies, and in particular the growth rate, of the background instabilities.

As mentioned above, in addition to the influence of the variation of the linear growth rates on the electrostatic part of the impurity flux, electromagnetic effects on the E×B transport are produced also by additional contributions due to the presence of electromagnetic fluctuations in $A_{||}$, which imply additional terms proportional to β itself. Despite the fact that these play only a minor role in the relatively low β limit of typical tokamak plasmas, it is interesting to explore their specific dependence on the mode frequency with the analytical model. In order to single out the electromagnetic contribution proportional to β, and adopt equations simple enough to perform analytical calculations, only the electromagnetic part in the parallel motion equation is kept,

$$\hat{v}_{||\,p} = \frac{A_\mathrm{i}}{A_\mathrm{p}} \cdot \frac{1}{\hat{\omega}} \left\{ Z_\mathrm{p} \frac{T_\mathrm{e}}{T_\mathrm{p}} \frac{c_\mathrm{s}}{c} \left[\frac{1}{Z_\mathrm{p}} \left(\frac{R}{2L_\mathrm{np}} + \frac{R}{2L_\mathrm{Tp}} \right) - \hat{\omega} \right] \right\} \hat{A}_{||}. \tag{5.14}$$

In addition, temperature fluctuations, i.e. the $\hat{T}_p$ term in the continuity equation, whose main effect has been considered in the previous discussion, are neglected, and, by this, the coupling with the energy balance is removed, which reduces the order of the algebraic system. As already underlined, the coupling between continuity and parallel motion equation is actually the only one remaining in the limit of large Z_p.

Including the relationship between the fluctuating potentials $\hat{\phi}$ and $\hat{A}_{||}$ given by Eq. (3.30), one finds

$$\hat{n}_p = \left(-\hat{\omega}^2 + \frac{\hat{\omega}}{Z_\mathrm{p}} \right)^{-1} \cdot \left\{ \left(\frac{R}{2L_\mathrm{np}} - 1 \right) \frac{T_\mathrm{e}}{T_\mathrm{p}} \hat{\omega} + \hat{K} \left[\hat{\omega} - \frac{1}{Z_\mathrm{p}} \left(\frac{R}{2L_\mathrm{np}} + \frac{R}{2L_\mathrm{Tp}} \right) \right] \hat{\phi} \right\}, \tag{5.15}$$

where

$$\hat{K} = \hat{k}_{||}^2 Z_\mathrm{p} \frac{A_\mathrm{i}}{A_\mathrm{p}} \frac{T_\mathrm{e}}{T_\mathrm{p}} \frac{c_\mathrm{s}}{c} \hat{\Omega}(\hat{\omega}). \tag{5.16}$$

By expanding the complex quantities as follows, $\hat{\omega} = \hat{\omega}_r + i\hat{\gamma}$, $\hat{K} = \hat{K}_\mathrm{r} + i\hat{K}_\mathrm{i}$, the results for the transport coefficients are

$$D_{\mathrm{p,E\times B}} = \frac{\gamma}{k_\mathrm{x}^2} \frac{\hat{\gamma}}{|\hat{N}|^2} \left\{ \hat{\gamma} |\hat{\omega}|^2 + \frac{T_\mathrm{p}}{Z_\mathrm{p} T_\mathrm{e}} \left[\hat{K}_\mathrm{r} \left(\frac{\hat{\gamma}}{Z_\mathrm{p}} - 2\hat{\gamma}\hat{\omega}_r \right) - \hat{K}_\mathrm{i} \left(\hat{\gamma}^2 + \frac{\hat{\omega}_r}{Z_\mathrm{p}} - \hat{\omega}_r^2 \right) \right] \right\}, \tag{5.17}$$

$$D_{\mathrm{p,E\times B}}\cdot(C_{\mathrm{T}})_{\mathrm{E\times B}}=\frac{\gamma}{k_{\mathrm{x}}^2}\frac{\hat{\gamma}}{|\hat{N}|^2}\frac{T_{\mathrm{p}}}{Z_{\mathrm{p}}T_{\mathrm{e}}}\left\{\hat{K}_{\mathrm{r}}\left(\frac{\hat{\gamma}}{Z_{\mathrm{p}}}-2\hat{\gamma}\hat{\omega}_r\right)-\hat{K}_{\mathrm{i}}\left(\hat{\gamma}^2+\frac{\hat{\omega}_r}{Z_{\mathrm{p}}}-\hat{\omega}_r^2\right)\right\},\quad(5.18)$$

$$D_{\mathrm{p,E\times B}}\cdot(C_{\mathrm{P}})_{\mathrm{E\times B}}=\frac{2\gamma}{k_{\mathrm{x}}^2}\frac{\hat{\gamma}}{|\hat{N}|^2}\frac{T_{\mathrm{p}}}{T_{\mathrm{e}}}|\hat{\omega}|^2\left\{-\frac{T_{\mathrm{e}}}{T_{\mathrm{p}}}\hat{\gamma}+\hat{K}_{\mathrm{r}}\hat{\gamma}+\hat{K}_{\mathrm{i}}\left(\frac{1}{Z_{\mathrm{p}}}-\hat{\omega}_r\right)\right\},\quad(5.19)$$

$$|\hat{N}|^2=|\hat{\omega}|^2\left(|\hat{\omega}|^2-\frac{2\hat{\omega}_r}{Z_{\mathrm{p}}}+\frac{1}{Z_{\mathrm{p}}^2}\right).\quad(5.20)$$

The terms proportional to $\hat{K}_{\mathrm{r}}$ or $\hat{K}_{\mathrm{i}}$ identify explicitly electromagnetic contributions through their dependence on β_{i}. The first term in $D_{\mathrm{p,E\times B}}$ is the usual term due to E×B advection, while the second and the third include the additional term due to $\hat{A}_{||}$ proportional to the density gradient in the Lorentz force, which has its origin in the diamagnetic drift. Within these, the contributions proportional to $(1/Z_{\mathrm{p}})$ enter due to the divergence of the diamagnetic heat flow, which is in fact a curvature effect. In $D_{\mathrm{p,E\times B}}(C_{\mathrm{T}})_{\mathrm{E\times B}}$ the same terms as the last two in $D_{\mathrm{p,E\times B}}$ appear due to the additional term proportional to the temperature gradient. The electrostatic part in $D_{\mathrm{p,E\times B}}(C_{\mathrm{P}})_{\mathrm{E\times B}}$ occurs from E×B compression, and the last two arise again from electromagnetic additions proportional to $\hat{\omega}$ in the Lorentz force (coming from the $\partial_{\mathrm{t}}A_{||}$ term), where contributions proportional to $(1/Z_{\mathrm{p}})$ are again due to curvature effects.

In order to simplify these results, $D_{\mathrm{p,E\times B}}$ as well as the dimensionless quantities $(C_{\mathrm{T}})_{\mathrm{E\times B}}$ and $(C_{\mathrm{P}})_{\mathrm{E\times B}}$ are calculated in the limit of small β_{e}, i.e. using Eq. (3.32). After this reduction, $\hat{K}_{\mathrm{r}}$ includes a term $\propto R/L_{\mathrm{ne}}$ arising from the E×B advection term in the electron continuity equation used to relate $\hat{A}_{||}$ to $\hat{\phi}$, and a term $\propto\hat{\omega}_r$, while $\hat{K}_{\mathrm{i}}$ is proportional to $\hat{\gamma}$ only. The latter two are due to the time derivative of the fluctuating electron density. Then, the additional contributions proportional to β in the transport coefficients are,

$$D_{\mathrm{p,E\times B}}=\frac{\gamma}{k_{\mathrm{x}}^2}\frac{\hat{\gamma}^2}{|\hat{N}|^2}\left\{\frac{1}{2}\frac{A_{\mathrm{i}}}{A_{\mathrm{p}}}\frac{T_{\mathrm{i}}}{T_{\mathrm{e}}}\frac{\beta_{\mathrm{e}}}{k_\perp^2\rho_{\mathrm{i}}^2}\left[\frac{T_{\mathrm{e}}}{T_{\mathrm{p}}}\frac{R}{2L_{\mathrm{ne}}}\left(2\hat{\omega}_r-\frac{1}{Z_{\mathrm{p}}}\right)+|\hat{\omega}|^2\right]\right\},\quad(5.21)$$

$$(C_{\mathrm{T}})_{\mathrm{E\times B}}=\frac{1}{2}\frac{A_{\mathrm{i}}}{A_{\mathrm{p}}}\frac{T_{\mathrm{i}}}{T_{\mathrm{e}}}\frac{\beta_{\mathrm{e}}}{k_\perp^2\rho_{\mathrm{i}}^2}\left[\frac{1}{|\hat{\omega}|^2}\frac{T_{\mathrm{e}}}{T_{\mathrm{i}}}\frac{R}{2L_{\mathrm{ne}}}\left(2\hat{\omega}_r-\frac{1}{Z_{\mathrm{p}}}\right)+1\right],\quad(5.22)$$

and

$$(C_{\mathrm{P}})_{\mathrm{E\times B}}=-Z_{\mathrm{p}}\frac{A_{\mathrm{i}}}{A_{\mathrm{p}}}\frac{T_{\mathrm{i}}}{T_{\mathrm{e}}}\frac{\beta_{\mathrm{e}}}{k_\perp^2\rho_{\mathrm{i}}^2}\left(\frac{T_{\mathrm{e}}}{T_{\mathrm{i}}}\frac{R}{2L_{\mathrm{ne}}}+\frac{1}{Z_{\mathrm{p}}}\right).\quad(5.23)$$

Here, only the leading order electromagnetic terms $\mathcal{O}(\beta_{\mathrm{i}}^1)$ have been taken into account. The first and second terms in $D_{\mathrm{p,E\times B}}$ and $(C_{\mathrm{T}})_{\mathrm{E\times B}}$ have the same origin, namely E×B advection and time derivative of the fluctuating electron density, respectively. The coefficient $(C_{\mathrm{P}})_{\mathrm{E\times B}}$ is given by E×B advection and a curvature term. Eqn. (5.21), (5.22) and (5.23) provide small additions on the charge and mass dependence of trace impurity coefficients $D_{\mathrm{p,E\times B}}$, $(C_{\mathrm{T}})_{\mathrm{E\times B}}$ and $(C_{\mathrm{P}})_{\mathrm{E\times B}}$ in electromagnetic simulations.

It can be concluded that these contributions proportional to β are such that in the case of diffusion and thermodiffusion the coefficients $D_{\mathrm{p,E\times B}}$ and $(C_{\mathrm{T}})_{\mathrm{E\times B}}$ depend on the real frequency of the mode, and consist of terms which are all in the outward direction for

the case of a ITG mode ($\hat{\omega}_r > 0$), while they can balance in the case of TEM ($\hat{\omega}_r < 0$). In the thermodiffusion coefficient, this part proportional to β enhances the effect previously described in the electrostatic part of the flux by the reduction of the growth rate of the instability with increasing β. On the contrary, the part of the coefficient $(C_\mathrm{P})_{\mathrm{E}\times\mathrm{B}}$ proportional to β given by Eq. (5.23), increases in size in the inward direction with increasing β_e for both the ITG and the TEM case.

5.3.2 Magnetic flutter transport coefficients

Although the magnetic flutter contribution to the total transport is small in the low β_e limit, the gyrokinetic results exhibit the interesting feature that magnetic flutter transport components can reverse their direction from the ITG to the TEM instabilities. This is particularly the case for the dominant term of the magnetic flutter transport, that is the pure convective flux. In order to investigate the main physical reason behind the numerical results, the same fluid model is applied also to the analytical calculation of the magnetic flutter flux $\Gamma_\mathrm{Fl}/n_\mathrm{p} = -k_\mathrm{y}\langle\tilde{v}_{||,\mathrm{p}}A_{||}/B\rangle$, and compared with the gyrokinetic results. The complete analytical calculation of the complex phase relationship between parallel velocity fluctuations $\tilde{v}_{||,\mathrm{p}}$ and parallel magnetic vector potential fluctuations $\hat{A}_{||}$ is as lengthy as that for the E×B transport, which instead implies the calculation of the complex phase relationship between density and electrostatic potential fluctuations. However, a rather strong simplification can be obtained keeping only first order terms in β in the expression for the flux and focusing on the calculation of the term in the pure convective contribution which survives in the limit of highly charged impurities. This shall allow us to provide an example of the dependence of the direction of the magnetic flutter transport on the sign of the real frequency of the unstable mode. Firstly, since $\hat{A}_{||} \propto \beta_\mathrm{e}$, terms directly proportional to $\hat{A}_{||}$ in the expression of $\tilde{v}_{||\,\mathrm{p}}$ given by Eq. (3.26), which stem from the electromagnetic part of the Lorentz force in the parallel motion equation, yield contributions which are proportional to β^2 in the final expression of the flux and therefore can be neglected. Moreover, is is noted that in Eq. (3.26), the effect of the parallel pressure gradient term vanishes with increasing impurity inertia, while the parallel gradient of the electrostatic potential fluctuations produces a residual effect at high charge, due to the presence of the charge in the Lorentz force. Of course, through the parallel pressure gradient, contributions to the parallel velocty fluctuations which are proportional to the radial logarithmic gradients of the equilibrium impurity density and temperature $R/L_{\mathrm{n,p}}$ and $R/L_{\mathrm{T,p}}$ occur, and these will not be included in our analytical calculation. By focusing only on the leading term for highly charged impurities, our calculation will deliver a pure convective term only. For such a term, the calculation of the phase relationship between $\hat{\phi}$ and $\hat{A}_{||}$, which is first order in β, is required. Eq. (3.31) in the small β limit is used. Recalling the discussion about the calculation of flutter fluxes in Chapter 4, and especially Eq. (4.12), whose dominant part for impurities changes to

$$\Gamma_{\mathrm{Fl,p}} \propto \Re\langle i \int d^3v \int d^3v v_{\parallel,\mathrm{p}} h_\mathrm{p} v_{\parallel,\mathrm{e}} h_\mathrm{e}^* \rangle_{\mathrm{FS}}, \tag{5.24}$$

it is clear that the approximation of only considering the electron current in Ampère's law is a meaningful simplification.

It is underlined that in Eq. (3.31) the quantity $\hat{\Omega}$ depends critically on the eigenfrequency of the instability, which occurs here due to the reactive passing electron response

given by the continuity equation in the presence of magnetic fluctuations. The analytical expression of the magnetic flutter pure convection coefficient in this limit is,

$$(C_{\mathrm{P}})_{\mathrm{Fl}} = -\frac{4\gamma\hat{\gamma}^2}{k_{\mathrm{x}}^2|\hat{N}|^2 D_{\mathrm{p,\,tot}}}\beta_{\mathrm{e}}\hat{k}_{||}^2\frac{k_{\perp}^2}{k_{\mathrm{y}}^2}\frac{A_{\mathrm{i}}}{A_{\mathrm{p}}}Z_{\mathrm{p}}\frac{T_{\mathrm{i}}}{T_{\mathrm{p}}}\left|\hat{\omega}+\frac{R}{2L_{\mathrm{ne}}}\frac{T_{\mathrm{e}}}{T_{\mathrm{i}}}\right|^2\left(2\frac{T_{\mathrm{i}}}{T_{\mathrm{e}}}\hat{\omega}_r+\frac{R}{2L_{\mathrm{ne}}}\right), \tag{5.25}$$

with

$$|\hat{N}|^2 = |\hat{\omega}|^2\left(|\hat{\omega}|^2-\frac{30}{9Z_{\mathrm{p}}}\hat{\omega}_r+\frac{25}{9Z_{\mathrm{p}}^2}\right)\cdot\left[|\hat{\omega}|^2+\frac{R}{L_{\mathrm{ne}}}\frac{T_{\mathrm{e}}}{T_{\mathrm{i}}}+\left(\frac{R}{2L_{\mathrm{ne}}}\frac{T_{\mathrm{e}}}{T_{\mathrm{i}}}\right)^2\right] \tag{5.26}$$

where the prevailing contribution in $D_{\mathrm{p,\,tot}}$ is given by the E×B diffusion and therefore is positive. The saturation level has been estimated as before, applying the relationship between $\hat{A}_{||}$ and $\hat{\phi}$, see Eq. (3.31) in the small β limit. The analytical expression can be compared with the gyrokinetic results. It is found that $(C_{\mathrm{P}})_{\mathrm{Fl}}$ in Eq. (5.25) is negative for ITG modes, that is, it describes an inward directed convection. In addition, it can reverse sign in case of TEM instabilities with sufficiently large absolute values of $\hat{\omega}_r$. This behavior agrees with the numerical results of our ITG and TEM reference cases presented in Figs. 5.3, 5.4 and 5.5, where a reversal of the sign of the coefficient is obtained in the two cases. It is also interesting to note that while in the TEM case the dependence of $(C_{\mathrm{P}})_{\mathrm{Fl}}$ on β is linear, since the eigenfrequencies of the instability are weakly affected by an increase of β itself, in the ITG case, the dependence on β is stronger, since the decrease of the growth rate of the instability with increasing β implies a reduction of the denominator in Eq. (5.25), which leads to a more parabolic type of dependence.

In a similar way, the occurrence of the mode eigenfrequency in the relationship between $\hat{\phi}$ and $\hat{A}_{||}$ impacts also the behavior of the magnetic flutter components of the diagonal diffusion and the thermodiffusion. The calculation of these terms is however longer, since it requires the derivation of the relationship between parallel velocity fluctuations and electrostatic potential fluctuations occurring through the $E \times B$ advection in the impurity continuity and energy balance equations. As already mentioned, these contributions decrease with increasing impurity mass A_{p}.

5.3.3 Conclusive remarks

In conclusion, this Section allowed us to identify the main physical mechanisms through which an increase of β affects the E×B transport of impurities. It was shown that the main variations are directly connected with the electrostatic part of the flux, which is modified by to the influence of β on the growth rate of the instability in the background plasma. In particular for the off–diagonal coefficients C_{T} and C_{P}, this is related to the electrostatic coupling between density and temperature impurity fluctuations produced by the ∇B and curvature drift, and explains why β effects are strongly reduced at large values of the impurity charge and mass. At high impurity charges with a fixed impurity mass, additional terms due to parallel motion lead to finite electromagnetic contributions to the thermodiffusion and pure convection coefficients. Also the additional contributions to the E×B transport produced by the coupling with the fluctuations of the magnetic parallel vector potential $A_{||}$ in the small β limit were investigated specifically. It is found that in the case of the diffusion and thermodiffusion coefficients, these contributions depend on the sign of the real frequency of the mode, and in particular in the ITG case, can enhance

the thermodiffusion in the outward direction, which is a particularly relevant result for the transport of light impurities. In the case of the pure convection coefficient, the contribution to the transport produced by $A_{||}$ are directed inward for both ITG and TEM, since they are found to be independent of the direction of propagation of the mode. The transport coefficients of the magnetic flutter contribution are given by the phase relation between parallel velocity fluctuations and the fluctuations in the parallel component of the vector potential. The comparison of the explicitly derived pure convection coefficient with the gyrokinetic results indicates that the main physics mechnism responsible for the reversal of the magnetic flutter convection when moving from the ITG to the TEM reference case is connected with the occurence of the mode eigenfrequency in the relationship between the fluctuating electrostatic and vector potentials, due to the non–adiabatic passing electron response in the presence of magnetic flucutations.

5.4 Impurity transport for typical H–mode plasma parameters

In this section, calculations of impurity transport including electromagnetic effects are made for typical H–mode parameters around mid–radius. It is underlined that the chosen plasma parameters are also very close to those predicted for the ITER standard scenario [114], in the dimensionless form which is applied in the gyrokinetic calculations. The logarithmic gradients at mid-radius are $R/L_{\mathrm{Ti}} = 5.0$, $R/L_{\mathrm{Te}} = 5.3$ and $R/L_{\mathrm{n}} = 2.1$, the safety factor is $q = 1.1$, the magnetic shear is $s = 0.4$, the ion to electron temperature ratio is $T_{\mathrm{e}}/T_{\mathrm{i}} = 1.05$, while the geometry parameters (elongation of 1.5 and triangularity of 0.1) have been used in Miller geometry [41]. Collisions have been included. The local collisionality is $\nu_{\mathrm{ei}}\,[c_{\mathrm{s}}/R] = 0.06$. The dominant micro–instability in these conditions is a ITG mode for all presented values of β_{e}. Therefore no large difference with respect to the ITG reference case is expected. However, here the realistic situation of comparable ion and electron logarithmic temperature gradients is considered, which is more suited for at least qualitative comparisons with the experimental results available in the literature on the impact of β on the transport of impurities. Of course, for quantitative comparisons, the actual measured experimental profiles should be used as input in the gyrokinetic calculations, and, if possible, nonlinear simulations should be performed.

Linear gyrokinetic simulations for the interesting ion species tritium, helium, carbon, nickel and tungsten with a ionization stage 46+ typical of H–modes in present devices around mid–radius ($T_{\mathrm{e}} \approx 3$ keV) are shown in Fig. 5.7. Vertical lines in the figure identify the value of $\beta_{\mathrm{e}} = 1.8$ % at the ITER standard scenario parameters, and which can be also considered typical for usual H–mode operation. Results qualitatively similar to those presented in Fig. 5.4 are obtained. The results of Fig. 5.7 allow us to draw some specific conclusions which can be expected to be directly applicable to typical H–mode plasmas.

Magnetic flutter diffusion and thermodiffusion provide only small contributions for all ion species and at all experimentally relevant values of β_{e}. In contrast, more significant can be the convective part of the magnetic flutter, particularly for fully ionized heavy impurities. The magnetic flutter convection for high–Z impurities can be as large as 10 % of the corresponding pure convective E×B transport. However, for small–Z impurities like tritium or helium it is practically negligible, as it can be seen from Fig. 5.7f). Thus, for the latter the total magnetic flutter contribution to the transport is only of the order

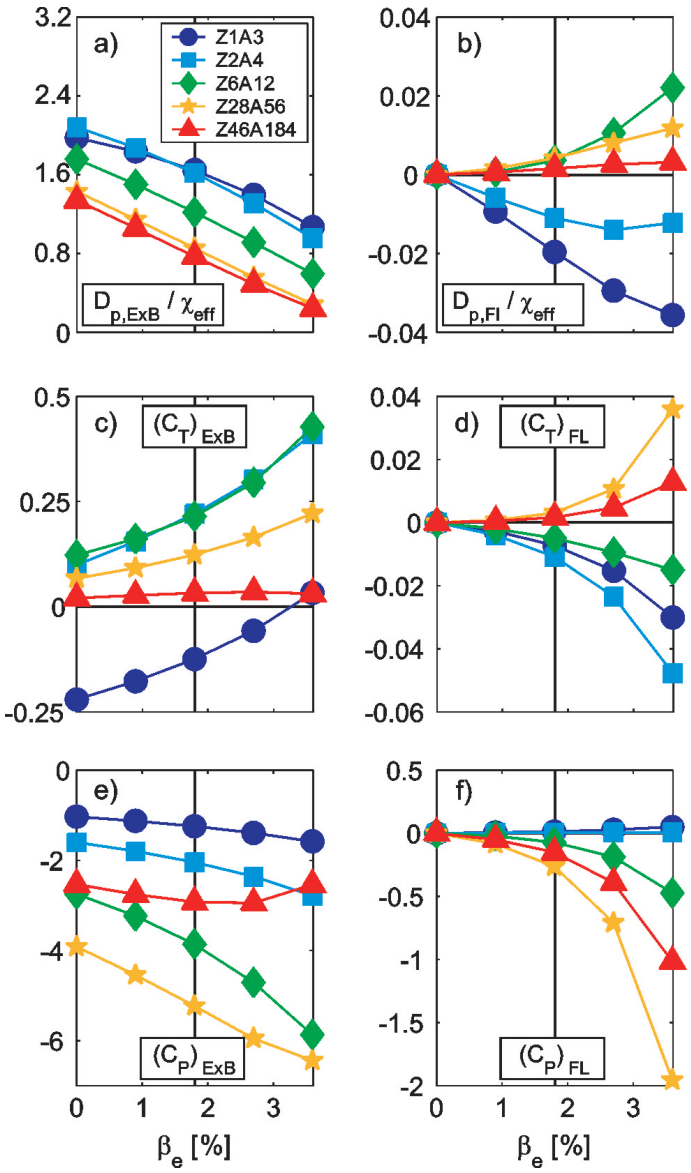

Figure 5.7: Electromagnetic dependence of $E \times B$ (left) and magnetic flutter (Fl, right) transport coefficients for the impurities tritium, helium, carbon, nickel and tungsten (at the ionization stage of 46^+) using typical H–mode profile data, as those predicted for the ITER standard scenario. The charge concentration is assumed to be $Z_\mathrm{p} n_\mathrm{p}/n_\mathrm{e} = 1/1000$.

of 1% at the highest values of β_e considered here.

The ratio of the E×B diagonal diffusion to the total effective conductivity reaches a finite asymptotic value with increasing charge and decreases with increasing β_e at all charges. As discussed in the previous Section, this is caused by the drop of the linear growth rate, which is found to affect the diagonal diffusivity much more than the total effective conductivity. The larger value of $D_{\mathrm{p,E\times B}}/\chi_\mathrm{eff}$ obtained in this case as compared to the ITG reference case can be understood as a consequence of the lower logarithmic temperature gradient applied here, and therefore in terms of proximity to linear stability,

which implies a stronger reduction in $\chi_{\rm eff}$ as compared to $D_{\rm p,E\times B}$. The theoretical result of a decrease of the light impurity diffusivity with increasing β agrees with experimental observations for helium transport in DIII-D [98] and for trace T transport in JET [99]. Since the magnitude of diagonal diffusion of helium governs the impact of the central helium source produced by fusion reactions on the helium ash concentration profile, the reduction of $D_{\rm p,E\times B}/\chi_{\rm eff}$ with $\beta_{\rm e}$ deserves consideration in the prediction of the helium ash profile in high β operational scenarios and certainly requires further theoretical and experimental investigations. It is also noted that the diffusion coefficient for helium in the electrostatic limit agrees with previous linear and nonlinear calculations [108].

At moderate values of $\beta_{\rm e}$ tritium thermodiffusion is directed inwards, while all heavier impurities move outwards. This shows an interesting difference with respect to the results for $(C_{\rm T})_{\rm E\times B}$ obtained for the ITG case shown in Fig. 5.4e. This behavior can be understood through Eq. (5.11), and shows that for sufficiently low charges the inward contribution $-5/(3Z_{\rm p})$ can prevail over the outward contribution provided by $\hat{\omega}_r$ for ITG modes. In the present case, with comparable temperature gradients and not too large value of $\hat{\omega}_r$, which is typical of reactor relevant H–mode plasmas, such a transition in the direction of thermodiffusion takes place between the charge $Z_{\rm p} = 1$ of hydrogenic species and the charge $Z_{\rm p} = 2$ of helium. In the case of TEM instabilities, thermodiffusion is always directed inwards, for any particle charge. For $(C_{\rm P})_{\rm E\times B}$, negative values are found for all impurity species, that is an inward pure convection. Its absolute value increases with increasing $Z_{\rm p}/A_{\rm p}$, while a reduction of the charge to mass ratio, like in the case of the not fully ionized W, acts to reduce the contribution.

Also the nonlinear behavior of diagonal diffusion for the considered ITER case has been calculated. Since three gyrokinetic species are required, the computational cost was reduced compared to the nonlinear runs presented in Chapter 4 by considering a spectrum of 32 toroidal modes, which leads to a coverage $k_{\rm y}\rho_{\rm s} = 0.04$ to $k_{\rm y}\rho_{\rm s} = 1.33$. This is sufficient to appropriately describe impurity transport, which takes place mainly in the range $k_{\rm y}\rho_{\rm s} < 1$. The simulation box is chosen to be $L_{\rm x}/\rho_{\rm s} = 85$ and $L_{\rm y}/\rho_{\rm s} = 146$. Using 196 radial points a resolution of $dx/\rho_{\rm s} = 0.45$ is obtained. In velocity space, 128 points are used (8 energies, 4 passing and 4 trapped pitch angles with two signs of velocity). The result is shown in Fig. (5.8). The decrease of the normalized diagonal E×B diffusion with increasing $\beta_{\rm e}$ is also present in nonlinear calculations and is therefore in qualitative agreement with experimental results. For helium, however, generally larger values of $D_{\rm p}/\chi_{\rm eff}$ are found, while for Nickel the deviation from quasi–linear results are only small. This is connected to the choice of the quasi–linear weighting, namely only considering the fluxes at $k_{\rm y}\rho_{\rm s} = 0.3$. The flutter component is again small compared to the E×B one, but stronger deviations between the nonlinear and linear results are obtained. The reason is again the spectral weighting, which is here particularly problematic due to the stronger $k_{\rm y}$ dependence of flutter fluxes as compared to their E×B counterparts, as is can be also concluded from Fig. (5.2).

Lastly, the total convection to diffusion ratios obtained in linear calculations are presented in Fig. 5.9. Here the thermodiffusion coefficient $C_{\rm T}$ has been multiplied by the actual logarithmic temperature gradient $R/L_{\rm Ti}$ and summed to $C_{\rm P}$ to obtain the ratio of the total off–diagonal flux to the diagonal diffusion. As already illustrated previously, such a ratio is equal to the value of $R/L_{\rm n}$ of the impurity in the absence of a particle source and for negligible neoclassical transport in stationary conditions. The E×B and

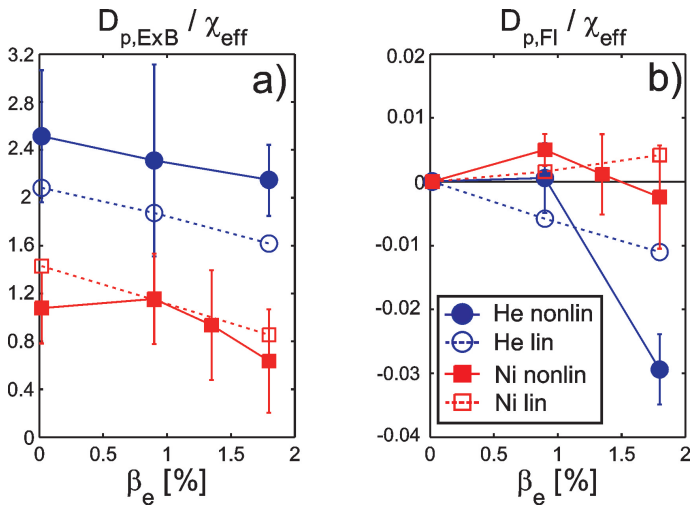

Figure 5.8: Electromagnetic dependence of trace helium and Nickel normalized diagonal diffusion coefficient for both E×B (a) and magnetic flutter (b) obtained from nonlinear (full symbols) and quasi–linear calculations (open symbols). The error bars for the nonlinear results indicate the variance of the fluctuation level.

magnetic flutter parts of the off–diagonal flux have been separated in Fig. 5.9a and Fig. 5.9b, respectively, and divided by the total diagonal diffusivity, sum of the E×B and the magnetic flutter diffusivities. Consistently with all previous results, the magnetic flutter contribution to the ratio RV/D is small for the range of standard operational scenarios ($\beta_e = 1.6\% - 1.9\%$). Nevertheless, it can reach $\approx 10\%$ of the E×B transport at the projected hybrid operation, with $\beta_e = 2.3\% - 2.6\%$. The dominant E×B part is increasing with β at small values of the impurity charge, as a consequence of the effect of thermodiffusion. This result is of particular interest for He, which turns out to have the smaller value of RV/D. On the contrary, the total convection to diffusion ratio decreases (that is, it increases in size, in the inward direction) for heavy impurities. The effect, however, remains small, and no case of real strong accumulation with increasing β is predicted to occur, which is a result favorable for nuclear fusion applications.

5.5 Summary and conclusions

Electromagnetic effects on the transport of trace impurities in tokamaks have been computed using linear gyrokinetic simulations and analytical calculations based on a simplified fluid model. The E×B and magnetic flutter components of the transport have been calculated separately, in order to investigate their relative contribution to the total impurity flux. Both components have been decomposed in their diffusive, thermodiffusive and pure convective contributions, making use of the linear dependence of the flux of trace impurities on the density and temperature logarithmic gradients. Reference cases with dominant ITG and TEM modes in the plasma background have been considered, and the dependence of the transport on charge and mass investigated.

In conditions of both ITG and TEM instabilities, the transport produced by magnetic flutter is found to be usually only of the order of 1% with respect to the E×B transport.

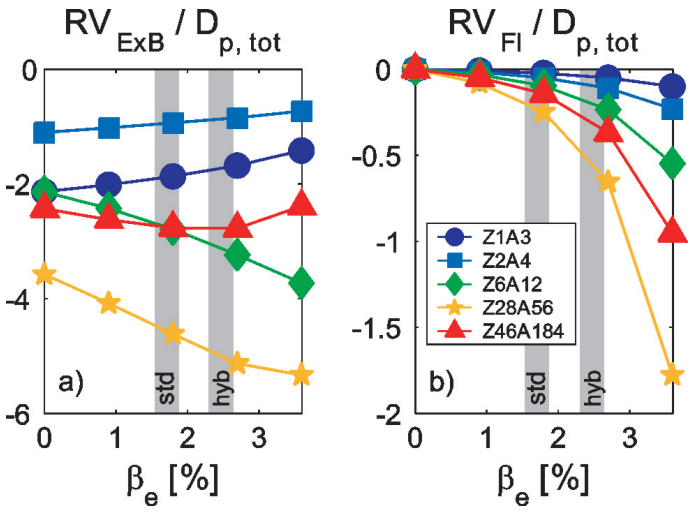

Figure 5.9: Electromagnetic dependence of the ratio of the $E \times B$ (a) and magnetic flutter (b) off–diagonal contributions (including both thermodiffusion and pure convection) to the total diagonal diffusion, $RV/D_{\mathrm{p,tot}}$, for tritium, helium, carbon, nickel and tungsten (at a ionization stage of 46^{+}), using typical H–mode profile data as those predicted for ITER. The charge concentrations are assumed to be $Z_{\mathrm{p}} n_{\mathrm{p}}/n_{\mathrm{e}} = 1/1000$. The shaded areas denote the projected β_{e} values for standard and hybrid operational scenarios.

Interestingly, the dominant part of flutter transport is of pure convective type. For ITG modes and at large values of β it can be as large as 10% as compared to the pure convection produced by E×B transport, providing a non–negligible component of the dependence of the pure convection coefficient on β. The ITG and TEM reference cases allowed us to show that changes in the background instability can strongly affect the dependence of the impurity transport coefficients on β_{e}. In the ITG case, the diagonal diffusion normalized to the effective total heat conductivity decreases with increasing β_{e}, while it remains almost constant in the TEM reference case. Thermodiffusion is found to increase in the outward direction with increasing β_{e} at all impurity charges in the ITG case. This can lead to a reversal of the thermodiffusive flux from inward to outward for very light impurities with increasing β_{e}, since, differently from heavy impurities, the thermodiffusive contribution of very light impurities can be directed inward in the electrostatic limit in the ITG case. In the TEM case, thermodiffusion is almost independent on β_{e} and directed inwards at all charges. The pure convection term is directed inwards in both cases and increases in the inward direction with increasing β_{e}. The latter effect is stronger in the ITG case, whereas in the TEM case this behavior is rather weak.

The dependence of the transport on the impurity charge is also of interest. It is found that the diagonal E×B diffusion decreases in the ITG case while it increases in the TEM case with increasing impurity charge. Impurity mass does not have a strong impact. On the other hand, as it can be easily expected from simple considerations, inertia strongly impact the properties of the magnetic flutter transport. In particular, the diagonal flutter diffusion vanishes for heavy impurities. The same is obtained for both E×B and magnetic flutter thermodiffusion. Pure convection remains finite at high $Z_{\mathrm{p}} = A_{\mathrm{p}}/2$ for both the E×B and the flutter component.

The numerical results have been interpreted by means of a reduced fluid model, consisting of the continuity, the parallel force balance including the electromagnetic Lorentz force terms and the energy balance equation for the impurity species, taken from Refs. [46, 47, 48, 39, 49]. Analytical expressions for the various impurity transport coefficients have been derived, which have been used in order to identify the main coupling mechanisms leading to electromagnetic effects on impurity transport. It is found that the main effects obtained in the gyrokinetic calculations are due to the impact on the electrostatic part of the E×B transport produced by the modification of the linear growth rate of the instability in the background plasma with increasing β_e. The main differences between ITG and TEM therefore are directly a consequence of the fact that an increase of β_e produces a reduction of the linear growth rate in ITG modes, while it affects very weakly the linear growth rate in TEM modes.

The behaviors of diagonal diffusion, thermodiffusion and pure convection have been investigated for a realistic case of typical H–mode plasma parameters, similar to those predicted for ITER. The dominant background microinstability turns out to be an ITG mode. Here, more physics effects like plasma shape and collisions are taken into account compared to the reference cases used for parametric studies. The transport coefficients show mainly the same properties as in the reference ITG case. In particular, the decrease of diagonal diffusion with increasing β_e found in the reference ITG case is confirmed by these more realistic linear and nonlinear calculations and it is in qualitative agreement with observations obtained with light impurities in DIII-D [98] and JET [99]. This result certainly requires some consideration, since too strong a reduction of diagonal diffusion of He with increasing β_e might lead to an accumulation of helium ash in the center in high β scenarios in a reactor due to an increase of the effect of the central helium source produced by fusion reactions. Our theoretical result should motivate further experimental investigations on this specific problem and direct quantitative comparisons between theoretical predictions and experimental measurements, in order to increase our predictive capability of the consequences of high β operation on helium ash accumulation in a burning plasma.

An additional interesting result is related to the behavior of the total off–diagonal transport, sum of thermodiffusion and pure convection. This is directed inwards for impurities at all charges in the realistic H–mode case. The ratio of the total off–diagonal transport to the diagonal diffusion decreases weakly in size with increasing β_e for light impurities, while it increases in size with increasing β_e for heavy impurities. Therefore, in the absence of significant central impurity sources and with small neoclassical transport, an increase of β_e is predicted to produce a small flattening of light impurity density profiles and a peaking of heavy impurity density profiles.

Chapter 6

Investigations of electromagnetic effects on parallel momentum transport

6.1 Formulation of the problem

The study of turbulent toroidal momentum transport currently receives much attention in the field of fusion plasma physics. Because of the toroidal symmetry properties of tokamaks, the toroidal angular rotation is undamped, in contrast to the poloidal component. The shear of toroidal velocity goes into both the E×B shear, which is perpendicular to the unperturbed magnetic field, and the shear of the parallel velocity. It was investigated that the latter may enhance turbulent transport due to the fact that a parallel velocity gradient adds a drive to ITG modes [115, 116, 117]. E×B shearing, on the other hand, is known to have a stabilizing influence and thus has a beneficial effect on energy confinement in fusion devices. This was reported for instance in [118] and references therein. The relative contribution of these two mechanisms is mainly determined by the ratio of poloidal to toroidal magnetic field strength. For typical values of $B_\mathrm{p}/B_\mathrm{t}$ in tokamaks, the E×B shearing effect dominates and turbulence is suppressed. Another helpful effect is the stabilization of the resistive wall mode by a sufficiently large toroidal rotation, see for example [119]. From initial studies of Mattor and Diamond a strong coupling between ion heat and momentum transport was identified, see [120] and references therein. Consequently, the diagonal transport coefficients of both channels may be of similar magnitude. This was conjectured from experiments with large external torque on the plasma provided by NBI heating, see e.g. [121]. However, even without an external torque a so–called intrinsic rotation is observed. The latter is of particular interest for plasma experiments going towards a reactor size scale since only a very small external torque will be present there. Moreover, a recent work [110] showed the impact of a finite toroidal rotation on heavy impurity transport.

Besides the mentioned fast progress made in the last years on this topic, electromagnetic effects on turbulent toroidal momentum transport have hardly been studied up to now. This might be connected with the fact that theoretical works firstly focussed on the mechanism responsible for the generation of toroidal momentum transport. Technically, flux–tube codes usually calculate the parallel momentum transport, which is very close

to the toroidal one since the poloidal component included in the first is strongly damped. Then, the transport is given by the parallel velocity moment of the perturbed distribution function, given by the gyrokinetic equation, times the fluctuating E×B velocity in radial direction. For local simulations in an up–down symmetric equilibrium geometry and without toroidal rotation, the gyrokinetic equation is symmetric under certain symmetry transformations, as is explained in [120]. Since parallel velocity fluctuations are an antisymmetric quantity, the momentum flux will be exactly zero under the aforementioned conditions. However, as it is explicitly discussed in [120], there is a finite momentum flux if the symmetry in the direction along the magnetic field line is broken. This can be caused by a finite toroidal velocity gradient $\hat{u}' = -R/c_\mathrm{s}\partial_\mathrm{r} u_\parallel$, where $u_\parallel$ is the parallel rotation of the plasma. This symmetry breaking mechanism is the origin of the diagonal part and usually expressed in terms of the Prandtl number $\chi_\phi/\chi_\mathrm{i}$ defined as the ratio of viscosity to thermal conductivity. The second mechanism originates from the toroidal rotation itself, and can be elegantly derived by transforming to the reference frame which moves with the plasma. In such a frame inertial forces, namely the Coriolis force and the centrifugal force, occur. While the latter plays only a minor role in tokamak plasmas due to the quadratic dependence on $\hat{u} = u_\parallel/c_\mathrm{s}$, which is usually less than 0.5, the former is an important contribution leading to an inward momentum flux, the so–called Coriolis pinch. As a consequence, a radial gradient of the toroidal velocity profile is generated even in the absence of an external torque [122]. There are additional leading order contributions to a finite momentum flux, namely due to the particle flux effect, E×B shearing and up–down asymmetric plasma shape, but here the focus is put on the modification of the first two due to electromagnetic effects. These can be expected to be the leading terms in the core of a low $\rho_* = \rho_\mathrm{s}/a$, fastly rotating plasma [120].

For the diagonal part, the consequence of a finite β_e has already been explored in [123] for the GA-std case, which shows an approximately 20% reduction of the Prandtl number at $\beta_\mathrm{e} = 0.5\%$ as compared to the electrostatic case. In the present study the electromagnetic influence under different physics parameters will be presented. While the main focus of this Chapter is on electromagnetic effects on the Coriolis pinch, which was never investigated up to now, also the diagonal part is studied. In this context, the influence of the self–consistent parallel mode structure, as it was explicitly reported in [124], plays a crucial role in explaining the behavior of both the pinch and the Prandtl number. There exists, however, also an additional symmetry breaking due to the inclusion of a finite β_e, but this has only a very small influence.

This Chapter is organized as follows. The next section includes gyrokinetic results of the electromagnetic effect on both the Prandtl number and the Coriolis pinch. The latter is shown to be strongly influenced by the parallel mode structure, which is inherent to the parallel wave vector $k_\parallel$. More specifically, the implication of different values of the safety factor, which in this context turns out to be the most important parameter, is discussed by use of gyrokinetic simulation results as well as by semi–analytical considerations. The obtained results are summarized in the end, and the main conclusions are drawn.

6.2 Linear simulations

As explained above, the breaking of the symmetry in the parallel direction is the cause of a finite momentum flux. The additional terms in the expression for the main contribution

to the momentum flux, which is similar to Eq. (4.7), with the additional factor $m_\mathrm{i} v_\parallel = \varsigma(2\hat{\mu}_\mathrm{i}\epsilon\hat{T}_\sigma(1-\lambda\hat{B}))^{0.5}$, suggests that additional terms proportional to $\hat{\Omega}$ being defined as the relation between $\hat{\phi}$ and $\hat{A}_{||}$, Eq. (4.5), may account for a modification of the momentum flux due to electromagnetic effects in case of $\hat{A}_{||}$ deviating from perfect antisymmetry due to a finite toroidal rotation and/or its gradient. Indeed, the parallel structure of the electrostatic potential $\hat{\phi}$ shows a breaking of symmetry when the toroidal rotation is finite, as it was reported in [124]. This is in particular visible for the imaginary part of $\hat{\phi}(\theta_\mathrm{b})$, as it is shown in Fig. 6.1a for the GA-std case defined in Chapter 4, with $\hat{u} = 0.2$ and $\hat{u}' = 0$. The imaginary part of the parallel component of the vector potential, however, does not exhibit a strong deviation from a perfect antisymmetry, see 6.1b, while the real part does. Qualitatively the same effect is also seen in cases with pure diagonal momentum transport,

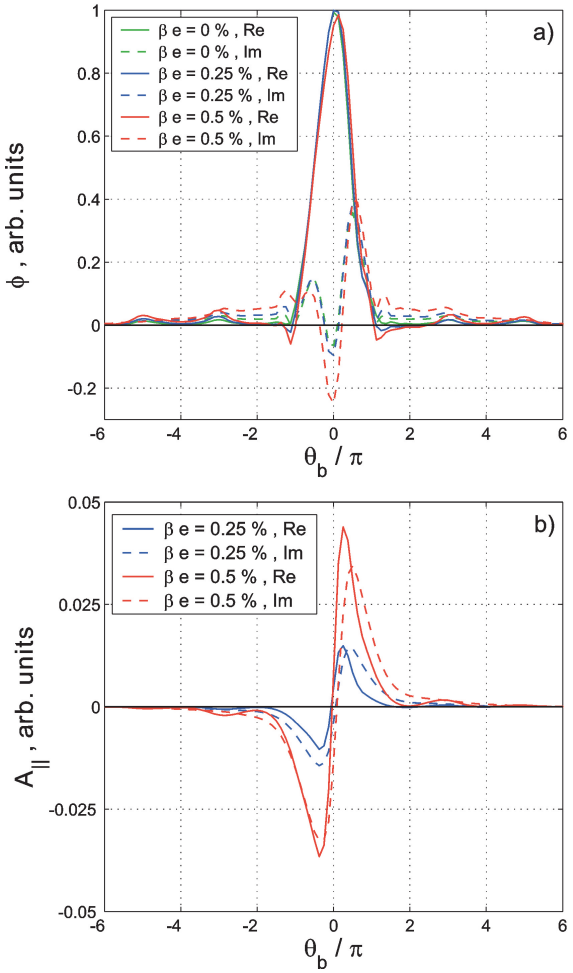

Figure 6.1: ITG mode ballooning dependence of the electrostatic potential for $\hat{u} = 0.2$ and three different values of β_e (a). Parallel component of vector potential for $\hat{u} = 0.2$ and $\beta_\mathrm{e} = 0.25, 0.5\%$ (b). The GA-std case has been used.

for example when taking $\hat{u} = 0$ and $\hat{u}' = 0.2$. As a consequence, $\hat{\Omega}$ has to compensate the symmetry breaking through the dependence on $k_\parallel$ and/or through additional terms originating from the Coriolis drift in Eq. (4.5). This implies that $\hat{\Omega}$ remains no longer

fully antisymmetric, and additional terms in the expression for the momentum flux are present.

However, as it will be explained below, these additions impact the momentum flux only by a very small amount. From the discussions in Chapter 4 it was apparent that new terms, namely the ones proportional to $\hat{\Omega}$ and therefore to β_e, play a crucial role in explaining the influence of electromagnetic effects on electron transport. The reason for their importance is the fact that parallel dynamics scales with $\sqrt{\hat{\mu}}$, which is important for electrons ($\sqrt{\hat{\mu}_\mathrm{e}} \sim 60$). For impurities, however, the additional terms imply only a very small contribution because $\hat{\mu}_\mathrm{i} \leq 1$. Since toroidal momentum transport is practically exclusively given by the ions through their higher mass as compared to the electrons (momentum transport is $\sqrt{\hat{\mu}_\mathrm{e}}$ smaller for electrons), the aforementioned additional terms do neither influence the magnitude of the 'electrostatic' symmetry breaking nor they play a strong role through the additional phase shift since they are proportional to $\sqrt{\hat{\mu}_\mathrm{i}}\beta_\mathrm{e} \sim \beta_\mathrm{e}$ and therefore very small for β_e–values being reached in tokamaks. Thus, it it expected that the influence of a finite β_e on momentum transport is an indirect, 'electrostatic–like' one, as it was the case for impurity transport. It will be shown that the modification of $k_\parallel$ due to electromagnetic effects is the leading order influence responsible for the modification of momentum transport.

6.2.1 Influence of the self consistent mode structure

While the mechanism of the symmetry breaking due to a finite toroidal rotation resulting in a Coriolis pinch is known for a while [122], the influence of the self–consistent mode structure was discussed only more recently [124]. In the latter reference, a low field side gyrofluid model was used in order to show that it is possible to formally combine the Coriolis drift with the parallel dynamics. The equations for continuity, parallel motion and energy balance read

$$\begin{aligned}
\hat{\omega}\hat{n} + 2\hat{n} + 2\hat{T} + 4\bar{u}\hat{v}_{||} &= \left[\frac{R}{L_\mathrm{n}} - 2\right]\hat{\phi}, \\
\hat{\omega}\hat{v}_{||} + 4\hat{v}_{||} + 2\bar{u}\hat{n} + 2\bar{u}\hat{T} &= \left[\hat{u}' - 2\bar{u}\right]\hat{\phi} \\
\hat{\omega}\hat{T} + \frac{4}{3}\hat{n} + \frac{14}{3}\hat{T} + \frac{8}{3}\bar{u}\hat{v}_{||} &= \left[\frac{R}{L_\mathrm{T}} - \frac{4}{3}\right]\hat{\phi}.
\end{aligned} \tag{6.1}$$

The effects from Coriolis drift and parallel mode structure are combined into one single term $\bar{u} = \hat{u} + \hat{k}_\parallel$, where $\hat{k}_\parallel = k_\parallel R/(2k_\mathrm{y}\rho_\mathrm{s})$ is the normalized parallel wave vector. This suggests that the two can actually be interchanged. There is, however, an important difference between the two. The Coriolis drift terms are entirely determined by the prescribed background rotation velocity, while the parallel wave vector has to be determined from the solution of the dispersion relation.

The following discussion is limited to the most unstable mode corresponding to a particular choice of $\hat{k}_\parallel$. This is a common assumption made in the literature. It can be shown, that for adiabatic electrons the most unstable mode satisfies $\bar{u} = 0$ or

$$\hat{u} = -\hat{k}_\parallel. \tag{6.2}$$

According to this solution, the parallel dynamics is such that it effectively eliminates the Coriolis drift from the equations. This is referred to as the 'compensation effect'

in Ref. [124]. However, the gyrofluid model, which led to this conclusion, has some limitations. It uses a single wave vector in order to describe the mode structure along the field line, while in toroidal geometry the direction along the magnetic field line is not homogeneous and various $k_{\|}$ modes would couple. This and other limitations [124] could lead to the conclusion that the simple fluid model is not able to capture the full physics effect. But in contrast, it was shown that this compensation is indeed present, and gyrokinetic simulations with adiabatic electrons give zero momentum flux. Simulations with kinetic electrons, which include kinetic electrons, reveal that the compensation is imperfect such that a finite momentum flux is obtained. This can be seen from Fig. 6.2, modified from [124], which is suited for discussing the physics mechanisms at play. The

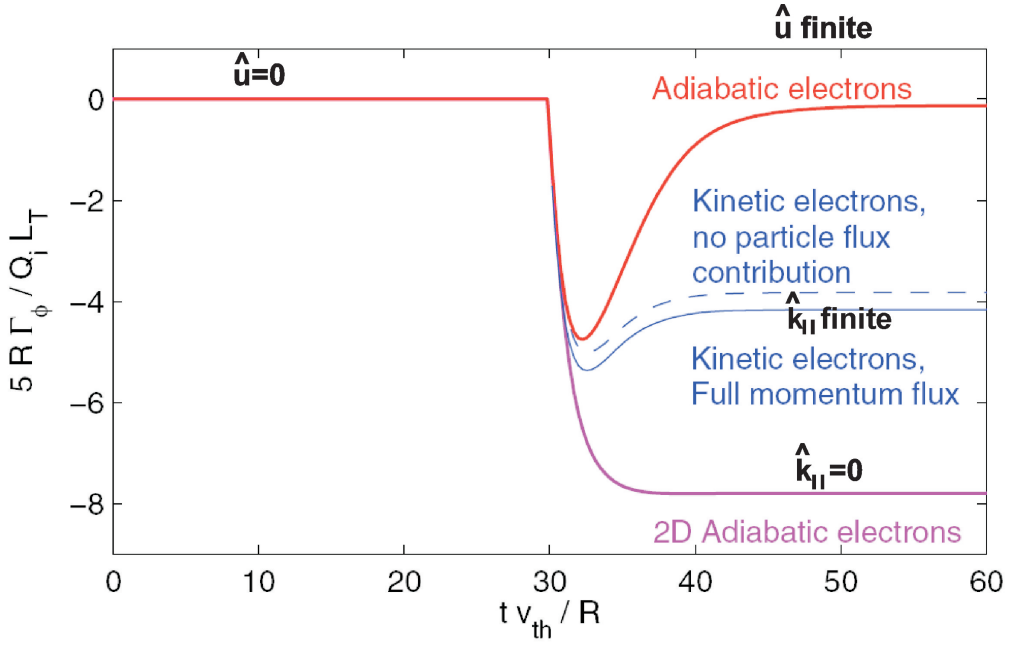

Figure 6.2: Time traces of the momentum flux for the adiabatic electron case, the kinetic electron case, and the 2D adiabatic electron case. The dashed line gives the part of the momentum flux not including the particle flux. Until the normalized time $t = 30R/v_{\mathrm{th}}$ was reached, the rotation is zero ($\hat{u} = 0, \hat{u}' = 0$). At this point, a restart using $\hat{u} = 0.2, \hat{u}' = 0$ was made (from [124]).

momentum flux is shown for different electrostatic simulations of the GA-std case in $s-\alpha$ geometry, namely a simulation with adiabatic electrons, one with kinetic electrons and one called two dimensional (2D) adiabatic electrons. The latter has $\hat{k}_{\|} = 0$ due to the fact that all parallel derivatives are set to zero. All simulations start with $\hat{u} = 0, \hat{u}' = 0$. At the normalized time $t = 30R/v_{\mathrm{th}}$, a restart using $\hat{u} = 0.2, \hat{u}' = 0$ was made. The normalization is done in such a way that the y–axis represents $RV_{\phi}/\chi_{\mathrm{i}}$ for the case of $\hat{u} = 0.2$. For the kinetic electron case, which has a finite particle flux, the dashed line gives the sum of the Coriolis pinch and the particle flux contribution. The difference to the dominant Coriolis part is small.

Without toroidal rotation, the momentum flux is at the null, as it could have been expected from the previous discussion based on the symmetry properties. The symmetric

electrostatic potential, which implies $\hat{k}_\parallel = 0$ due to the definition

$$k_\parallel \equiv \langle k_\parallel \rangle = -\frac{i}{Rq} \frac{\int d\theta_\mathrm{b} \phi^* \, \partial_{\theta_\mathrm{b}} \phi}{\int d\theta_\mathrm{b} \phi^* \phi} \tag{6.3}$$

in combination with an antisymmetric parallel velocity fluctuation leads to a zero flux. With toroidal rotation, the electrostatic potential is asymmetric, and the Coriolis drift generates an asymmetric parallel velocity perturbation [122] such that the flux is finite. In the 2D adiabatic case, the compensation is absent due to $\langle \hat{k}_\parallel \rangle = 0$ and the pinch saturates at a high negative value. For kinetic electrons, the mode structure along the field line adjusts and generates a finite $\langle \hat{k}_\parallel \rangle$ leading to a compensation effect. The latter is (almost) perfect for adiabatic electrons, as it was concluded from the simple gyrofluid model. This shows that the breaking of symmetry is a necessary but not sufficient condition for the generation of a finite momentum flux. Since electromagnetic effects modify the parallel mode structure through a decrease of the mobility of passing electrons, as it can be already seen from Fig. 6.1, it has to be expected that also the momentum pinch will change.

From Eq. (6.1) also the effect of a finite β_e on the diagonal part can be understood. The toroidal rotation gradient is removed from the parallel force balance equation if $\hat{u}' - 2\langle \hat{k}_\parallel \rangle = 0$ which implies that in this case $\langle \hat{k}_\parallel \rangle$ has to be a finite positive number for this compensation to take place, in contrast to the Coriolis pinch case. Consequently, the specific impact of a finite $\langle \langle \hat{k}_\parallel \rangle \rangle$ is discussed below in more detail using linear gyrokinetic simulations.

6.2.2 Results for Coriolis pinch and Prandtl number

Firstly, it is interesting to explore the influence of electromagnetic effects on the Coriolis pinch. The discussion is focussed on the behavior on β_e keeping fixed $\beta' = 0$. The following parameters have generally been used in order to compute the momentum flux for the Coriolis effect, namely $\hat{u} = 0.2$ with $\hat{u}' = 0$. Figure (6.3a) shows the dependence of the Coriolis pinch RV_ϕ/χ_i as a function of β_e. It is apparent that the pinch is strongly reduced with raising β_e. This result has been benchmarked with two other gyrokinetic codes, namely GKW [125] and GS2 [126, 127]. The results are very similar, especially at low β_e, where the ITG mode is the most unstable, and at high β_e, where a KBM shows the largest growth rates. For intermediate values of β_e, there are some discrepancies, especially at the transition from ITG to KBM, which may be caused by different resolutions due to the partly different discretization schemes used in the three codes. As it has been anticipated, the main reason for the decrease of the pinch is due to an increase of $\langle \hat{k}_\parallel \rangle$ in the negative direction, thus increasing the compensation of the toroidal velocity influence with raising β_e. In the electrostatic case, the normalized parallel wave vector is approximately $\langle \hat{k}_\parallel \rangle = -0.1$, which would cause a 50% reduction of the pinch since $\hat{u} = 0.2$ according to the gyrofluid model, Eq. (6.1). This can be also seen from Fig. 6.2 [124]. With increasing β_e, the value of $\langle \hat{k}_\parallel \rangle$ increases in absolute values up to approximately -0.17 for the last ITG dominated value at $\beta_\mathrm{e} = 0.6\%$, as shown in Fig. 6.3b, which leads to the conclusion that the pinch should be reduced drastically. This is clearly the case, as it is shown in Fig. 6.3a. The increase of $\langle \hat{k}_\parallel \rangle$ with β_e means a stronger symmetry breaking of the electrostatic potential $\hat{\phi}$, which can be already deduced from Fig. 6.1a. Approaching the KBM branch, the pinch can even reverse its sign from inward to outward, as a consequence of the effects

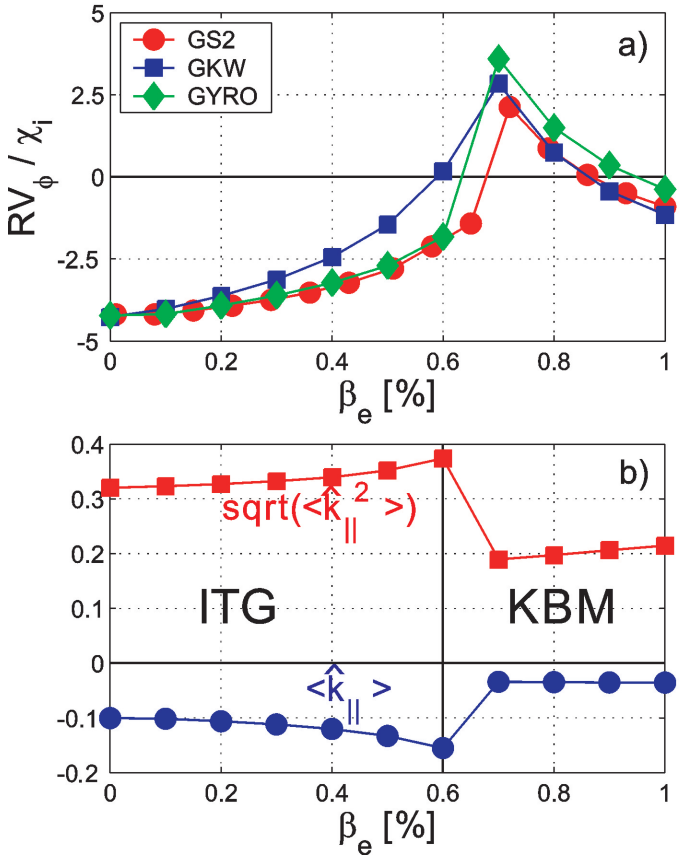

Figure 6.3: Benchmark of the electromagnetic dependence of the Coriolis pinch using GKW [125], GS2 [126, 127] and GYRO [19](a). Ballooning angle averaged parallel wavenumbers $\langle \hat{k}_{\|} \rangle$ and $\langle \hat{k}_{\|}^2 \rangle^{0.5}$ as a function of β_e, obtained with GYRO (b).

of $\langle \hat{k}_{\|} \rangle$, $\langle \hat{k}_{\|}^2 \rangle^{0.5}$ and ω_r. This behavior will be explained using the gyrokinetic formulas Eqn. (6.4) and (6.5). For KBM, $\langle \hat{k}_{\|} \rangle$ is practically zero, which can be expected because for ballooning modes $A_{\|}$ is the dominant fluctuating field. The latter is less affected by a finite toroidal rotation because the electron motion, which mainly determines $A_{\|}$ (see Chapter 4.2), is much faster than $\hat{u}$.

For illustration, a simple approximate gyrokinetic formula in $s - \alpha$ geometry with $\alpha = 0$ is derived in order to explain the electromagnetic behavior of the pinch in both the ITG and the KBM branch. It consistently allows for a finite distortion of the electrostatic potential symmetry through $\langle \hat{k}_{\|} \rangle$. An analytical expression for RV_ϕ reads

$$RV_\phi \propto \Im \left[\int d^3v \frac{\hat{v}_{||}(\hat{\omega} - \hat{\omega}_{*,0}) F_\mathrm{M} J_0}{\hat{\omega} - \langle \hat{\omega}_{\mathrm{d},0} \rangle - 2k_\mathrm{y}\rho_\mathrm{s} \langle \cos\theta_\mathrm{b} + s\theta_\mathrm{b} \sin\theta_\mathrm{b} \rangle \hat{v}_{||} \left(\langle \hat{k}_{\|} \rangle + \hat{u} \right)} \right] / \hat{u}, \tag{6.4}$$

where the θ_b dependence of ω_d has been kept, see Eq. (2.62), and $\hat{k}_{\|} = k_{\|} R / (2k_\mathrm{y}\rho_\mathrm{s}(\cos\theta_\mathrm{b} + s\theta_\mathrm{b}\sin\theta_\mathrm{b}))$. This gyrokinetic derivation includes the property that the Coriolis pinch goes to zero for $\langle \hat{k}_{\|} \rangle + \hat{u} = 0$, corresponding to the case of adiabatic electrons in Fig. 6.2 and

consistent with the gyrofluid model, Eq. (6.1). For the ion heat conductivity, a finite width of $\hat{\phi}$ in the ballooning direction through $\langle \hat{k}_{\|}^2 \rangle^{0.5}$ is used. Then, χ_i is given by

$$\chi_\mathrm{i} \propto \Im \left[\int d^3v \frac{(\hat{v}_{||}^2 + \hat{v}_{\perp}^2)(\hat{\omega} - \hat{\omega}_{*,0}) F_\mathrm{M} J_0}{2(\hat{\omega} - \langle \hat{k}_{\|}^2 \rangle^{0.5} \hat{v}_{||} - \langle \hat{\omega}_\mathrm{d} \rangle)} \right] / \frac{R}{L_\mathrm{T}}. \tag{6.5}$$

In the latter formula, the effect of the distortion of the ballooning symmetry through $\langle \hat{k}_{\|} \rangle$ is only a small correction and therefore neglected. The diagonal part is given by

$$\chi_\phi \propto \Im \left[\int d^3v \frac{\hat{v}_{||}(\hat{\omega} - \hat{\omega}_{*,0} - k_\mathrm{y} \rho_\mathrm{s} \hat{v}_{||} \hat{u}') F_\mathrm{M} J_0}{\hat{\omega} - \langle \hat{\omega}_{\mathrm{d},0} \rangle - 2 k_\mathrm{y} \rho_\mathrm{s} \langle \cos\theta_\mathrm{b} + s\theta_\mathrm{b} \sin\theta_\mathrm{b} \rangle \hat{v}_{||} \langle \hat{k}_{\|} \rangle} \right] / \hat{u}'. \tag{6.6}$$

The relation of Eq. (6.4) to Eq. (6.6) defines the Coriolis pinch and Eq. (6.6) to Eq. (6.5) the Prandtl number, where the drifts

$$\hat{\omega}_{\mathrm{d},0} = k_\mathrm{y} \rho_\mathrm{s} \left(\hat{v}_{||}^2 + \frac{1}{2} \hat{v}_{\perp}^2 \right) (\cos\theta_\mathrm{b} + s\theta_\mathrm{b} \sin\theta_\mathrm{b}) \tag{6.7}$$

and

$$\hat{\omega}_{*,0} = k_\mathrm{y} \rho_\mathrm{s} \left[\frac{R}{L_\mathrm{n}} + \left(\epsilon - \frac{3}{2} \right) \frac{R}{L_\mathrm{T}} \right] \tag{6.8}$$

have been used. It is emphasized that the decrease of the pinch in the ITG branch with raising β_e is found to be predominantly due to the increase of $\langle \hat{k}_{\|} \rangle$. Then, at $\beta_\mathrm{e} \gtrsim 0.6\%$, it appears that the pinch changes its sign due to an interplay of a smaller $\langle \hat{k}_{\|} \rangle$ in negative direction, see Fig. 6.3b, in combination with a much higher mode rotation frequency. When β_e is raised even further, the KBM growth rate increases and the real eigenfrequency decreases, leading to another sign reversal and an increase of the pinch in the negative direction. Therefore, since the influence of $\langle \hat{k}_{\|} \rangle$ is very weak in the KBM branch, the physics mechanism for a finite momentum flux has to be attributed to a symmetry breaking of parallel velocity fluctuations through a finite $\hat{u}_{\|}$, and by the changes of ω_r and γ. Inserting the parameters $\langle \hat{k}_{\|} \rangle$, $\langle \hat{k}_{\|}^2 \rangle^{0.5}$, ω_r and γ, which are obtained from GYRO, into the simple gyrokinetic model, Eqn. (6.4) and (6.5), and assuming realistic parameters for the drifts, the behavior of the pinch with increasing β_e is qualitatively recovered, as it can be seen in Fig. 6.4. However, the drastic change of the pinch in the KBM branch might not be relevant for experiments, since it is unlikely that tokamaks can operate in this regime. In the experimentally relevant ITG regime, on the other hand, the reduction of the pinch is sizeable for this case.

These results motivate further studies of electromagnetic effects on the Coriolis pinch, but also on the Prandtl number. From the previous results in Fig. 6.3 it could be conjectured that the decrease of the Coriolis pinch with increasing β_e is particularly strong in the vicinity to the onset of the KBM. From Eq. (3.32) and consistently Chapter 4.2.1 it is clear that the effect of finite perpendicular magnetic field fluctuations scales like $\beta_\mathrm{e} q^2$, as it was already reported in [50]. Thus, it is instructive to explore the behavior of both the Prandtl number and the Coriolis pinch as a function of β_e using different values of q. This is done for the GA-std case using $q = 1.1, 1.5, 2.0$ and 2.5. The results are shown in Fig. 6.5. From Fig. 6.5a it is apparent that with increasing safety factor q, the KBM becomes the most unstable mode at lower values of β_e. Therefore, both the Prandtl number, Fig.

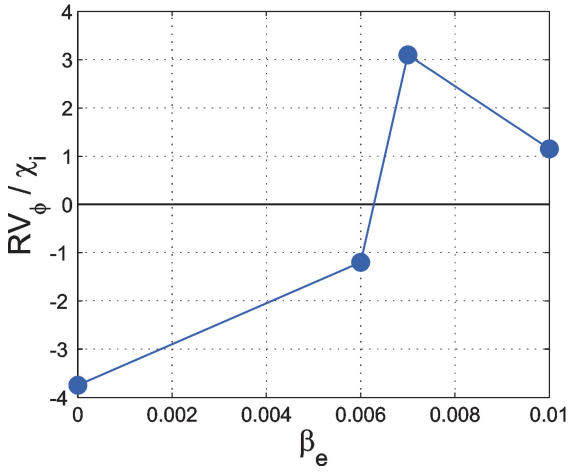

Figure 6.4: Theoretical model using the gyrokinetic formalism to compute β_e behavior of the Coriolis pich for the GA-std case. The numerical values for $\langle \hat{k}_\parallel \rangle$, $\langle \hat{k}_\parallel^2 \rangle^{0.5}$, γ and ω_r obtained by GYRO have been used.

6.5b, and the Coriolis pinch, Fig. 6.5c, are clearly reduced with increasing β_e already in the ITG domain in case of high safety factors, which in turn means a closer proximity to the KBM threshold. These results are explained by the behaviors of the parallel wavenumbers $\langle \hat{k}_\parallel \rangle$, shown in Fig. 6.5d for both the cases ($\hat{u} = 0, \hat{u}' = 0.2$, squares), used to calculate the Prandtl number, and ($\hat{u} = 0.2, \hat{u}' = 0$, circles), used to calculate the Coriolis pinch, respectively. In the case of high q, $\langle \hat{k}_\parallel \rangle$ increases in absolute values much stronger with increasing β_e in the ITG branch compared to the electrostatic value, such that according to the previous discussions both the Prandtl number, for which $\langle \hat{k}_\parallel \rangle$ is indeed positive, and the Coriolis pinch, for which $\langle \hat{k}_\parallel \rangle$ is negative, decrease. The different signs of $\langle \hat{k}_\parallel \rangle$ reflect the fact that the symmetry of the electrostatic potential in the case of a finite $\hat{u}'$ and $\hat{u} = 0$ is broken in different directions with respect to the ballooning angle as compared to a finite $\hat{u}$ and $\hat{u}' = 0$. Moreover, the β_e–behavior of the Prandtl number is also consistent with a gyrokinetic derivation, Eq. (6.6). The resulting Prandtl number behavior with respect to β_e is shown in Fig. 6.6. Again, a good qualitative agreement is obtained. Moreover, Eq. (6.6) clearly shows that it is impossible to fully balance the effect of a finite $\hat{u}'$ through $\langle \hat{k}_\parallel \rangle$.

Lastly, the magnitude of $\langle \hat{k}_\parallel \rangle$ in both cases is also in good agreement with the gyrokinetic results of Fig. 6.5. For instance, taking $\beta_e = 0.4\%$, $\langle \hat{k}_\parallel \rangle \approx -0.15$ for the Coriolis pinch case, such that the $\hat{u} = 0.2$ is practically completely balanced according to the compensation condition, Eq. (6.2). The resulting Coriolis pinch is indeed close to zero, as it can be seen in Fig. 6.5. This example shows that both the fluid model, Eqn. (6.1), and the gyrokinetic model derived within this work, Eqn. (6.4), (6.5) and (6.6) work satisfactorily well in order to explain the physics effects responsible for the electromagnetic behaviors, provided that the appropriate self–consistent $\hat{k}_\parallel$ is included.

Since the reduction of the Prandtl number and the Coriolis pinch with increasing β_e is strongly connected to the proximity to the onset of KBMs, and keeping the scaling of a finite $A_\parallel$ proportional to $\beta_e q^2$ in mind, it is also instructive to show the results of Fig. 6.5 plotted as a function of the parameter $\beta_e q^2$. This is presented in Fig. 6.7. The fact that

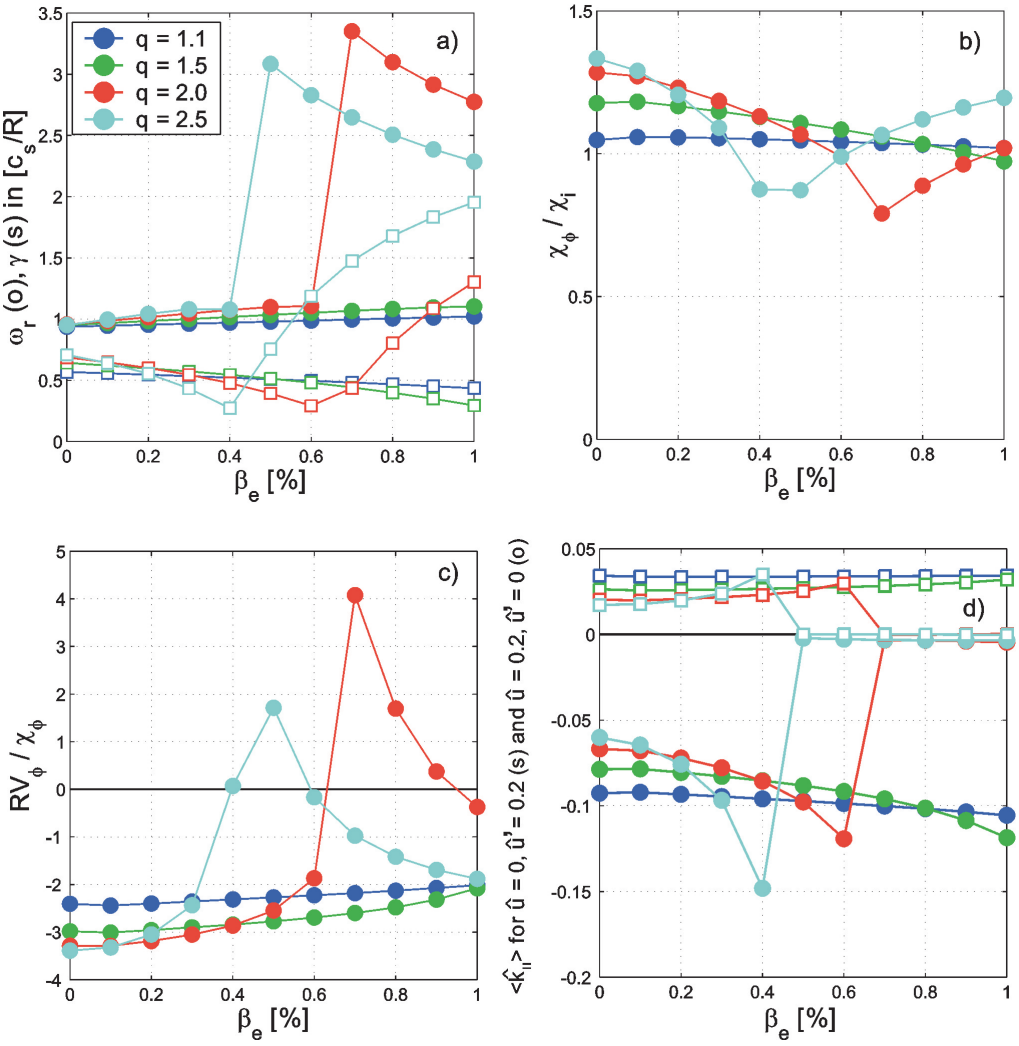

Figure 6.5: Electromagnetic behavior of γ (squares) and ω_r (circles, a), Prandtl number $\chi_\phi/\chi_\mathrm{i}$ (b), Coriolis pinch RV_ϕ/χ_ϕ (c) and parallel wavenumbers $\langle\hat{k}_\parallel\rangle$ for both ($\hat{u}=0, \hat{u}'=0.2$, squares) and ($\hat{u}=0.2, \hat{u}'=0$, circles, d) for different values of the safety factor q, respectively.

the linear growth rates and in particular the real eigenfrequencies are matching very well for the different values of q, as it can be seen in Fig. 6.7a, leads to the conclusion that the normalization used here is indeed appropriate. The electromagnetic behavior of the Prandtl number shows a decrease, which is stronger for higher values of the safety factor, Fig. 6.7b. The Coriolis pinch, which can be seen in Fig. 6.7c, decreases with increasing $\beta_\mathrm{e}q^2$ in the same way for different values of q. This, in turn, further confirms the fact that the use of the simple fluid model, Eq. (6.1), contains the main physics mechanism at play and in particular the fact that $\hat{k}_{||}$ is able to counteract both $\hat{u}$ and $\hat{u}'$, depending on the sign of $\langle\hat{k}_\parallel\rangle$, as it can be deduced from Fig. 6.7d. The electrostatic values of both the Prandtl number and the Coriolis pinch, which are generally higher for higher safety factor, further underline the crucial impact of parallel dynamics, as it can be seen in Fig.

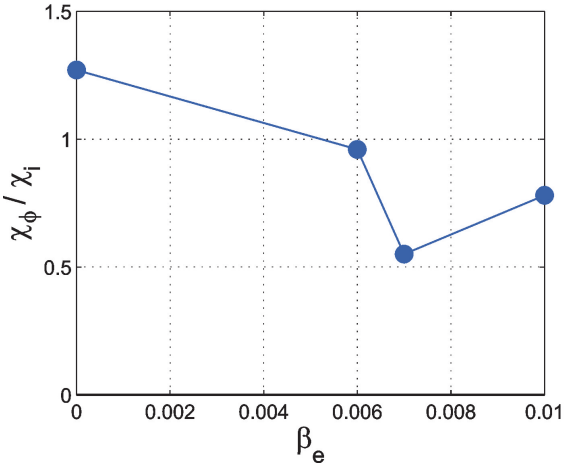

Figure 6.6: Theoretical model using the gyrokinetic formalism to compute β_e behavior of the Prandtl number for the GA-std case. The numerical values for $\langle \hat{k}_\parallel \rangle$, $\langle \hat{k}_\parallel^2 \rangle^{0.5}$, γ and ω_r obtained by GYRO have been used.

6.7b,c,d.

The difference mentioned above between the behavior of the Prandtl number and the Coriolis pinch regarding parallel dynamics is further investigated. Since the main difference of kinetic electrons to adiabatic electrons in the description of momentum flux is the existence of trapped electrons, which generate the differences observed in Fig. 6.2, it has to be expected that the momentum flux scales with the trapped particle fraction, at least for the Coriolis part [124]. Figure (6.8) shows both χ_ϕ/χ_i as well as RV_ϕ/χ_i as a function of $(r/R)^{0.5}$ being a measure for the fraction of trapped particles. The Coriolis pinch exhibits a strong reduction with decreasing $(r/R)^{0.5}$. This is obtained for all the three values of β_e. Electrostatically, the extrapolation of the GYRO results reveals that for purely passing electrons ($(r/R)^{0.5} = 0$), which are fully adiabatic due to $\beta_e = 0$, the pinch is indeed at the null, consistent with [124]. For finite β_e, however, passing electrons are no longer fully adiabatic, as it was pointed out in Chapter 4.2, such that a reduction of the pinch is obtained (or even a reversal when the trapped particle fraction is low). In this context it has to be underlined that, while the momentum flux is mainly given by the ions due to their high inertia, the electrons play a crucial role through their influence of the parallel mode structure and therefore on $\langle \hat{k}_\parallel \rangle$, which is clearly demonstrated by Fig. 6.8. The results are consistent with those obtained in Figs. (6.3) and (6.5). The Prandtl number, on the other side, does not go to zero for electrostatic fully passing electrons (the limit $(r/R)^{0.5} \to 0$), which shows that the compensation mechanism explained above is not complete for this quantity. The decrease of χ_ϕ/χ_i with increasing β_e is nevertheless visible. The (unphysical) negative values of the Prandtl number, obtained for $\beta_e = 0.5\%$ at small $(r/R)^{0.5} \lesssim 0.15$, are caused by the fact that while the trapped particle fraction is reduced because of moving towards the magnetic axis, the other parameters are held fixed. This unrealistic assumption produces negative values of χ_ϕ/χ_i. It has to be mentioned that while the electrostatic dependence of both the Prandtl number and the Coriolis pinch is almost linear (thus, linear fits are performed), especially the electromagnetic dependence of RV_ϕ/χ_i is no longer linear (thus, quadratic fits are performed for $\beta_e = 0.25, 0.5\%$).

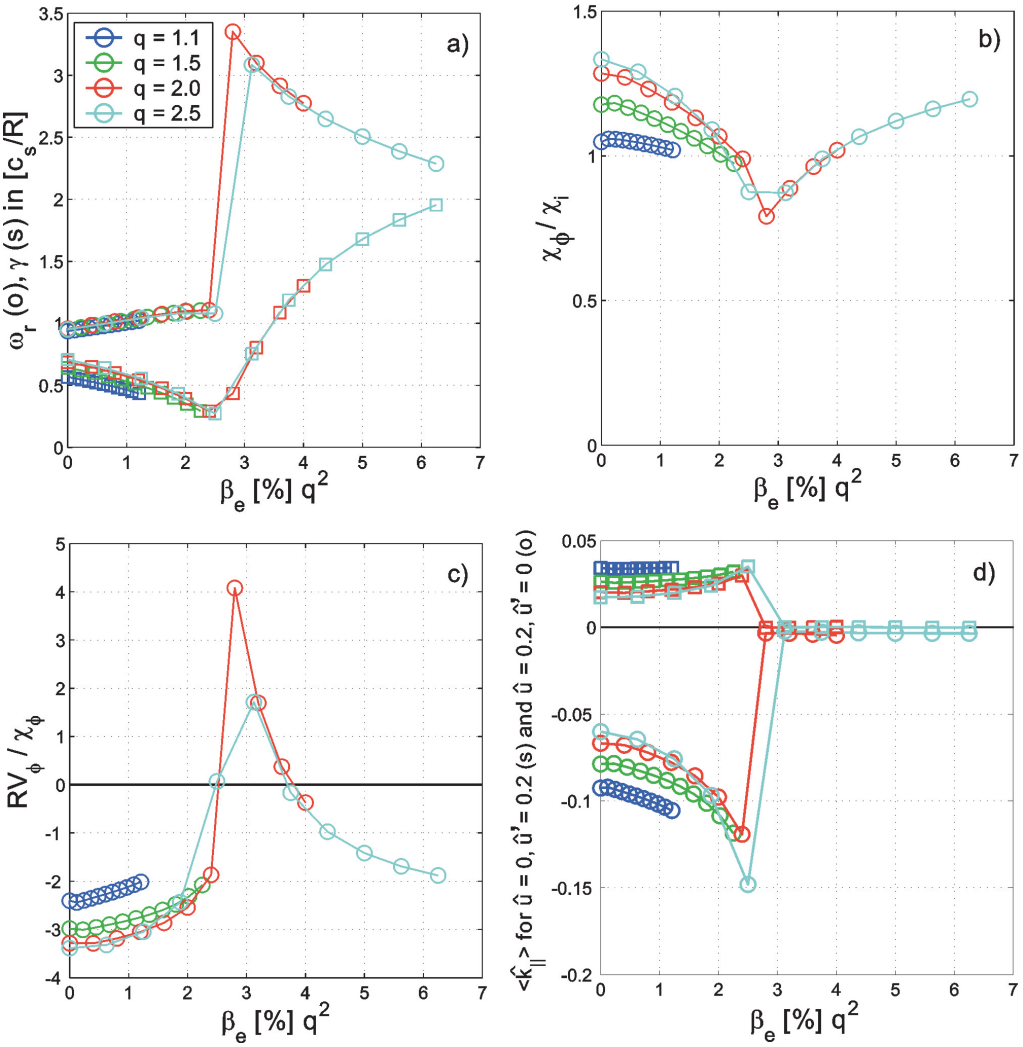

Figure 6.7: Electromagnetic behavior of γ (squares) and ω_r (circles, a), Prandtl number $\chi_\phi/\chi_\mathrm{i}$ (b), Coriolis pinch RV_ϕ/χ_ϕ (c) and parallel wavenumbers $\langle\hat{k}_\parallel\rangle$ for both ($\hat{u}=0, \hat{u}'=0.2$, squares) and ($\hat{u}=0.2, \hat{u}'=0$, circles, d) for different values of the safety factor q, respectively. The normalization to $\beta_\mathrm{e}[\%]q^2$ is used.

The electromagnetic runs on the Prandtl number show an almost linear behavior with increasing $(r/R)^{0.5}$.

Lastly, the realistic H–mode case close to parameters measured at ASDEX-Upgrade, as they were defined in Chapter 4, is considered. In order to study only the effect of a finite toroidal rotation and its gradient, a $s-\alpha$ equilibrium has been assumed. For this case, both the Prandtl number and the Coriolis pinch are calculated. The results are shown in Fig. 6.9. Due to the fact that the experimental value of β_e is 0.65% but the onset of KBMs is around $\beta_\mathrm{e}=3\%$, both the Prandtl number and the Coriolis pinch do practically not show any decrease with increasing β_e in the ITG branch. It is interesting to note that the former is higher as compared to the GA-std case considered before, which is due to the fact that the ion heat conductivity χ_i is smaller since the ion temperature gradient

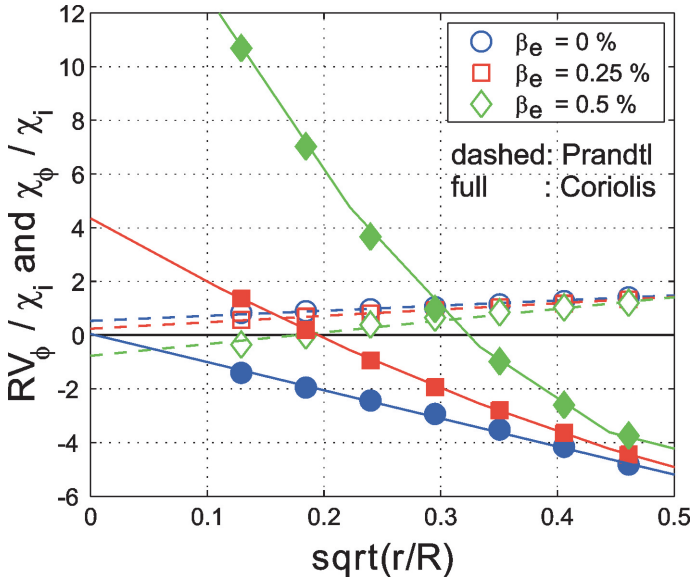

Figure 6.8: Prandtl number and Coriolis pinch as a function of $(r/R)^{0.5}$, which is a measure for the trapped particle fraction, for different values of β_e. Dashed and full lines denote linear and quadratic (see text) fits to the numerical results on the Prandtl number and the Coriolis pinch obtained with GYRO, respectively.

is lower. Additional simulations revealed that an increasing collisionality decreases the electromagnetic influence on the Prandtl number and in particular on the Coriolis pinch. An increasing value of the magnetic shear also acts to lower the finite β_e influence on RV_ϕ/χ_ϕ, as it could have been expected from the larger KBM threshold according to Fig. 1.8.

For higher values of β_e, a different kind of mode is found, namely a micro–tearing mode (MTM) between $\beta_e \sim 1.3\%$ and $\beta_e \sim 3\%$. These are characterized by the fact that magnetic field perturbations form small scale magnetic islands. The mode has a short wavelength with high poloidal mode number m. For these, the tearing parameter $\Delta' \approx -2m/r$ is negative such that the standard tearing mode theory, which is based on resistive MHD, predicts stability. There are, however, mainly two effects which can compete with Δ' and result in a growth of a magnetic perturbation to a saturated island, namely nonlinear effects, which are absent in the linear simulations considered here, and kinetic effects in a sufficiently collisional plasma. Indeed, here a finite collisionality of $(R/c_s)\nu_{ei} = 0.067$ has been used. Then, theory predicts that a necessary condition for for MTMs to occur is that the electrons satisfy $\omega/(k_\parallel v_\parallel) > 1$. Since $k_\parallel \sim m/r$, the perturbation corresponds to a narrow layer around rational surfaces for thermal velocities. This property can be seen from the elongated ballooning structure of the potentials ϕ along the field line in Fig. 6.9b. According to Eq. (2.78), a largely extended ϕ–mode in the ballooning parameter θ_b corresponds to a thin extension in the radial direction. This and the fact that the symmetry of both ϕ and $A_\parallel$ is changed compared to an ITG/TEM instability, such that the electrostatic potential becomes antisymmetric and the parallel component of the vector–potential symmetric, are clear signs of MTMs. When the latter are the most unstable ones, the Coriolis pinch changes sign, like it is the case for the

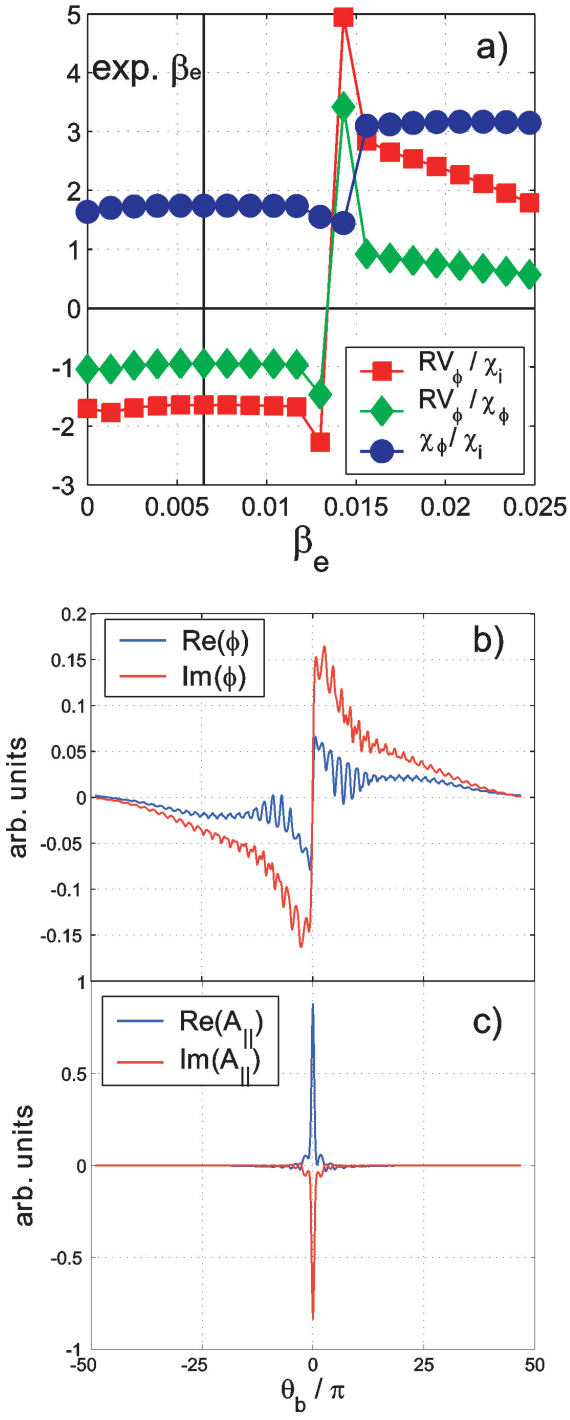

Figure 6.9: Prandtl number and Coriolis pinch as a function of β_e for the AUG similar case defined in Chapter 4(a) with a $s-\alpha$ equilibrium. The vertical line denotes the experimental value of β_e. The ballooning mode structure in ϕ and $A_\parallel$ for a micro–tearing mode (MTM) case at $\beta_e = 2.5\%$ with $\hat{u} = 0.2$ and $\hat{u}' = 0$ is shown in (b) and (c), respectively.

KBM onset. The Prandtl number is much larger than compared to the ITG domain. The behavior of the latter and of the Coriolis pinch is also consistent with Eqn. (6.4), (6.5) and (6.6). The reversal of the Coriolis pinch and the increase of the Prandtl number for $\beta_e \gtrsim 1.3\%$ is mainly due to a reversal of the sign of $\hat{\omega}_r$ in the electron drift direction and a reduction of $\hat{\omega}_{d,0}$ by $\sim 20\%$, while $\langle \hat{k}_\parallel \rangle$ and $\langle \hat{k}_\parallel^2 \rangle^{0.5}$ as well as γ are practically unchanged.

Finally, also the electromagnetic influence under TEM conditions has been investigated. It is found that both the Prandtl number as well as the Coriolis pinch are almost unaffected by a finite value of β_e. This is attributed to the fact that TEMs produce smaller fluctuations of the magnetic field lines, as it was already explained in Chapter 3.3. Consequently, the averaged parallel wave vector $\langle \hat{k}_\parallel \rangle$ remains constant with increasing β_e in the TEM branch. Moreover it can be deduced from Figs. (3.3) and (3.6) that since for TEM modes the linear growth rate remains almost constant with increasing β_e, while ITG modes are stabilized, the onset of the KBM to become the dominant mode is shifted towards higher β_e.

6.3 Summary and conclusions

Using linear gyrokinetic simulations with a fixed magnetic equilibrium, the effects of a finite β_e on the diagonal part of the momentum transport, namely the Prandtl number, as well as on a contribution of the off–diagonal components, namely the Coriolis pinch, are investigated. For dominant ITG modes, both the Prandtl number and the Coriolis pinch are reduced by a finite β_e. For the GA-std case defined in Chapter 3, the former is $Pr \sim 1.3$ and decreases to $Pr \sim 0.8$ at $\beta_e = 0.5\%$, while the latter is at $RV_\phi/\chi_\phi \sim -4$ and decreases in absolute values to $RV_\phi/\chi_\phi \sim -2.5$ at $\beta_e = 0.5\%$. At $\beta_e > 0.6\%$, the most unstable mode changes from ITG to KBM, leading to a reversal of the Coriolis pinch direction from inwards to outwards at the onset of the KBM. At $\beta_e \gtrsim 1\%$, the direction of the pinch again changes to become inward. The Prandtl number increases slightly in the KBM branch.

The physics mechanisms for the electromagnetic reduction of both the Coriolis pinch and the Prandtl number in the experimentally relevant ITG domain have been investigated. It is found that the self–consistent mode structure of the electrostatic potential is the main cause of the decrease. Finite values of β_e cause an increase of $\langle \hat{k}_\parallel \rangle$ in the negative direction for the Coriolis pinch and in the positive direction for the Prandtl number, respectively. As it has been newly shown using a gyrokinetic approach for the Coriolis pinch and the Prandtl number, the increase of $\langle \hat{k}_\parallel \rangle$ in absolute values leads to stronger balancing of the drive of the momentum flux when electromagnetic effects are taken into account. This can be also concluded from a simple gyrofluid model.

From a specific parameter analysis it is shown that the electromagnetic reduction of both the Prandtl number and the Coriolis pinch is connected with the onset of the KBM. In this context, the value of the safety factor is the most important quantity. This can be concluded from the fact that the onset of KBMs critically depends on $\beta_e q^2$. Thus, for low values of q, both the Prandtl number and the Coriolis pinch are only weakly affected by a finite β_e–values smaller than 1%, while for higher q the onset of KBM is localized at smaller β_e, causing strong electromagnetic effects. Using a more realistic AUG similar parameter case with a finite collisionality and a low value of q, it is found that both χ_ϕ/χ_i and RV_ϕ/χ_i are practically unaffected by the small experimental value of $\beta_e = 0.65\%$. By

increasing both collisionality and magnetic shear, the electromagnetic influence is reduced. The results reveal that finite–β_e effects become significant close to the KBM threshold. Hybrid scenarios at high β can be close to that limit, as it will be shown in the next Chapter, such that the decrease of the Prandtl number and the Coriolis pinch may be significant under these operational conditions.

Lastly, the reported higher values of the Prandtl number of $Pr \gtrsim 1.5$ [128] as compared to the gyrokinetic results may be attributed to the fact that the latter are usually obtained at a single $k_\mathrm{y}\rho_\mathrm{s} = 0.3$. The behavior of both the Prandtl number and the Coriolis pinch shows an increase in absolute values with raising $k_\mathrm{y}\rho_\mathrm{s}$. This result is consistent with the gyrokinetic and the gyrofluid model, which predict a decrease of $\hat{k}_\parallel = k_\parallel R/(2k_\mathrm{y}\rho_\mathrm{s})$ for increasing $k_\mathrm{y}\rho_\mathrm{s}$ (assuming $k_\parallel$ to be unchanged) and subsequently a less effective balance of the driving parallel velocity $\hat{u}$ (and also the parallel velocity gradient $\hat{u}'$) in the equations. Therefore, as it can be concluded from the discussion in Chapter 4 for the particle flux, it is important to perform an appropriate average on the wave number spectrum, possibly taking also subdominant modes or even stable modes into account (it is emphasized that for instance $\chi_\phi/\chi_\mathrm{i}$ for TEMs is significantly larger than 1), or better nonlinear simulations to obtain a more realistic estimate of momentum transport levels.

Chapter 7

Investigations of electromagnetic effects on heat transport

7.1 Formulation of the problem

The confinement properties of a plasma can be described in a global, zero dimensional description by the confinement time, as it was discussed in Chapter 1.2. The $IPB98(y,2)$ scaling [129], on which the design of a future fusion device like ITER is based, shows the main dependences of the energy confinement time on various parameters. For H–mode plasmas with edge localized modes, so–called ELMy H–modes, the main parametric dependences in terms of dimensional parameters are reported to be

$$\Omega_{\mathrm{c}}\tau_{\mathrm{E}}(IPB98(y,2)) = \rho_*^{-2.70}\beta^{-0.90}\nu_*^{-0.01}m^{0.96}q^{-3.0}(r/R)^{0.73}\kappa^{2.3}. \tag{7.1}$$

Here, Ω_{c} is the cyclotron frequency, $\rho_* = \rho_{\mathrm{s}}/a$ is the normalized Larmor radius, $\nu_* = \nu_{\mathrm{eff}}/\omega_{\mathrm{b}}$ is the normalized collision frequency (where $\nu_{\mathrm{eff}} = \nu_{\mathrm{ei}}/(r/R)$ is the effective collision frequency for particle detrapping, and $\omega_{\mathrm{b}} \approx (r/R)^{0.5}v_{\mathrm{th}}/(Rq)$ is the trapped particle averaged bounce frequency), m is the average ion mass, q is the safety factor, (r/R) is the inverse aspect ratio and κ is the elongation. This scaling includes a strong degradation of energy confinement with increasing β. However, (early) dedicated experiments on the beta–scaling of energy confinement in H–modes did not find a strong beta–dependence at all, as it is reported in [130] and references therein. On the other hand, as it is partly also reported in [130], recent experimental data from JT60U [131], AUG [132] and JET [133] support the ITER scaling by finding exponents of -0.6, -0.9 and -1.4, respectively. From the theoretical side, there have been lots of studies investigating the heat transport within tokamak plasmas dominated by ITG microturbulence. Generally, a decrease of ion heat conductivity with increasing beta is found by gyrofluid calculations, see for instance [134, 50], gyrokinetic particle–in–cell codes, see e.g. [135, 136], and gyrokinetic Vlasov codes, see for example [137, 75, 138].

Therefore, the numerical investigations of the present work are dedicated to a specific set of well diagnosed AUG and DIII-D H–mode plasmas [89] in hybrid scenario operation, which is synonymously also called the improved H–mode at AUG [139, 140]. This scenario is considered to be a very interesting operational scenario for ITER, since it combines both high confinement factors $H98(y,2) > 1$ relative to the $IPB98(y,2)$ scaling with high values of β_{N} in stationary discharges. In this context, 'stationary' means discharge timescales

longer than several energy confinement times τ_e or more than twice the current diffusion time.

Aiming at exploring heating conditions similar to those of a reactor, the hybrid scenario in AUG was obtained also using strong central ICRH. The latter was up to 50% of the total heating power, leading to a strongly reduced T_i/T_e. Central ICRH has been reported to cause a reduction of the toroidal plasma rotation in AUG NBI heated H–modes [141]. Under these conditions, the reduction is observed over the full minor radius and reaches a factor of 2 in the plasma center. It was shown that this reduction of v_{tor} is attributed to an increase in momentum diffusivity connected with the confinement degradation by the additional ICRH power flux. Also in DIII-D a degradation of energy confinement is found in experiments with reduced NBI toroidal torque, obtained by a combination of co– and counter–NB heating [142]. In both machines the reduction of E×B shearing leads to increased levels of microturbulence and transport in the confinement region, thus reducing the energy confinement.

The confinement enhancement, which outbalances the degradation, has different reasons. For instance in AUG, an improvement was found to be connected to density peaking, namely higher core densities led to higher stored energies at fixed (stiff) temperature profiles [143, 83]. The strong density peaking was connected with operation at low collisionality of roughly 1-3 times the one proposed for ITER's reference scenario at 15MA. The peaking of density, however, is limited by impurity accumulation, as it was pointed out in Chapter 5, which dilutes the burning material content and leads to increased radiation losses. The latter is of particular concern in tokamaks using high–Z metals as first walls like in AUG or as it is foreseen in ITER. Dominant neoclassical transport tends to accumulate high–Z impurities in the core. For AUG it has been shown that tungsten accumulation may be suppressed by increasing the anomalous transport in the core due to additional central electron cyclotron resonance heating (ECRH) [144].

Moreover, it has been shown that the confinement enhancement using hybrid operational scenarios was due to an improved pedestal (i.e. the steep gradient region at the plasma edge in H–mode) confinement in AUG, whereas in DIII-D it is due to a better core confinement [145]. In order to further clarify the reason of this difference in the two machines, dedicated power scans have been carried out. One of the main goals was to determine whether in hybrid discharges the pedestal pressure reaches a limit as the total input power is increased, or whether the pedestal β keeps on increasing with increasing heating power. The experimental aim was to perform power scans at constant $q_{95} \sim 4.6$ matched in both machines, constant density and fixed plasma shape. This turned out to be well suited for the comparison of pedestal heights and widths at increasing β_e in the two tokamaks. Also the different behaviors of core confinement in the two machines can be investigated in a convenient way. In this sense it has to be emphasized that the experiments were not intended to be dimensionless identity experiments in order to enable power scans in the largest possible range of β within the scenario.

Following [89], the present Chapter is organized as follows. Firstly, the main result from power scan experiments, namely the increase of confinement due to an increasing pedestal confinement in AUG and due to a better core confinement in DIII-D, respectively, is shown. In order to investigate the physics reason for the difference in core confinement, the main part of this Chapter consists of a heat transport analysis by means of gyrokinetic modeling. This is developed in three studies. Firstly, linear β_e scans are performed in order

to identify the most unstable modes. Secondly, linear R/L_{Ti} scans are used to identify the γ_{net}, which is the linear growthrate minus the E×B shearing rate. Thirdly, nonlinear scans on R/L_{Ti} are used to compare the thermal fluxes with the experimental heating power. In the end, the results are summarized and the main conclusions are drawn.

7.2 Power scans in ASDEX Upgrade and DIII-D hybrid discharges

7.2.1 ASDEX Upgrade and DIII-D hybrid discharges

Power scans carried out in AUG hybrid discharges over two experimental campaigns are considered, namely in 2005 with an approximately 70% tungsten coverage of the plasma facing components and in 2008 with a fully covered tungsten wall. In addition to the aforementioned criterion for useful hybrid discharges, namely the constancy of all main plasma parameters over at least three times the energy confinement time, only those plasmas with sufficiently good pedestal measurements have been considered. The latter is achieved by performing a slow (600ms period) sweep of the outer plasma during the stationary phase(s) of the discharge in order to increase the spatial resolution of the edge diagnostics. All discharges were carried out at a plasma current of $I_{\mathrm{P}} = 1.0$MA and with similar plasma shape, a lower single null configuration with average triangularity $\delta \sim 0.25$.

The main difference of the shots in the 2005 campaign compared to 2008 is that in the former about 1.4MW of central electron cyclotron resonance heating (ECRH) was applied in addition to the main NBI heating because of the tungsten coating of the ICRH antenna limiters, while in the latter 3MW of ICRH have been used. In 2008, hybrid operation requested $B_{\mathrm{t}} = 2.55$T due to the central ECRH in order to prevent tungsten accumulation, in contrast to the $B_{\mathrm{t}} = 2.4$T in 2005, thus changing q_{95} from approximately 4.6 to 4.8. The line averaged densities were $n_{\mathrm{e}} \sim (5-6) \times 10^{19}\mathrm{m}^{-3}$ in the 2005 shots and $n_{\mathrm{e}} \sim 8 \times 10^{19}\mathrm{m}^{-3}$ for the 2008 hybrids. Further information of the hybrid discharges in 2005 and 2008 can be found in [89].

For the hybrid discharges in DIII-D, the same selection criterion, namely the constancy of the profiles over $t > 3 \times \tau_{\mathrm{e}}$, has been used. The power scans were performed at fixed $q_{95} \sim 4.6$ with a constant density of $n_{\mathrm{e}} \sim 4 \times 10^{19}\mathrm{m}^{-3}$. One peculiarity of the DIII-D plasmas is the fact that the plasma shape was changed in order to differentiate between power and shape dependence of the pedestal pressure. The two low single null plasma shapes are shown in Fig. 7.1. The high ($\delta = 0.5$) shape is optimized for hybrid studies in DIII-D and the low ($\delta = 0.23$) 'AUG shape' was developed in order to match the reference plasma shape used in the AUG hybrids. In order to determine whether changes in the plasma stored energy of the hybrid scenario were linked to changes in the pedestal as the toroidal rotation was varied significantly, co– and counter–directed NBI was performed in the DIII-D high δ shape. With counter–NBI, the toroidal rotation was reduced to ~ 30km s^{-1} from ~ 200km s^{-1} in the co–NBI cases. Further information is found in [89].

7.2.2 Pedestal and global confinement

As it is typically found in hybrid discharges, the $H98(y,2)$ confinement factor increases with total β_{N} both in the AUG and DIII-D power scans. This is shown in Figs. (7.2a,b) for AUG and DIII-D, respectively. The DIII-D experiments indicate that at a given β_{N}

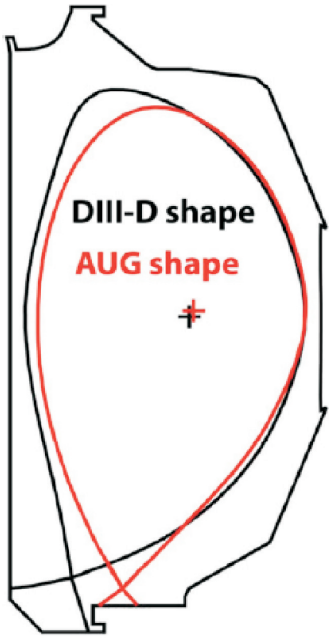

Figure 7.1: High triangularity ($\delta = 0.5$) 'DIII-D shape' and low triangularity ($\delta = 0.23$) 'AUG shape' matched at DIII-D (from [89])

the confinement factor is higher in the high δ shape. This well known experimental result for H–mode discharges is related to the improved edge stability, leading to higher pedestal pressure, as it can be seen from Fig. 7.2d. This beneficial property, in turn, leads to less input power needed to achieve a given β_N as compared to hybrid discharges run at a low δ shape. Moreover, as it can be seen from Fig. 7.2b, a low toroidal rotation causes a decrease of the confinement factor. But despite the significant decrease in the pedestal toroidal rotation, the pedestal confinement remains similar to what was obtained with high v_{tor} at the same β_N–value. It is reported that this lack of dependence of the pedestal pressure on variations of the momentum input is consistent with edge stability studies showing that the pedestal gradient stability limit is not significantly affected by toroidal rotation [146, 147]. Additionally, the gradient of the pedestal electric field, which along theoretical models is linked to supression of transport in the edge transport barrier, is generally dominated by the gradient of the pressure profile and not by the gradient of the toroidal rotation.

The analysis of the total and pedestal betas, shown in Figs. 7.2c,d, indicates a different behavior of these two parameters in the two machines. While β_N^{PED} increases linearly with β_N in AUG hybrid discharges, in DIII-D the pedestal beta increases only weakly for the low triangularity cases and seems to even decrease with raising β_N at high δ. The dependence found in DIII-D is in contrast to what is found in another study of hybrid scenarios in the same tokamak [147], where the pedestal pressure was also increasing with β_N. The latter result is reported to be due to an increase of the pedestal width. The difference in the behavior of β_N^{PED}, however, is not fully understood yet, but might be attributed to changes in the edge current density profile due to differences in the plasma shape.

The variation of the ratio of total to pedestal stored energy as a function of increasing

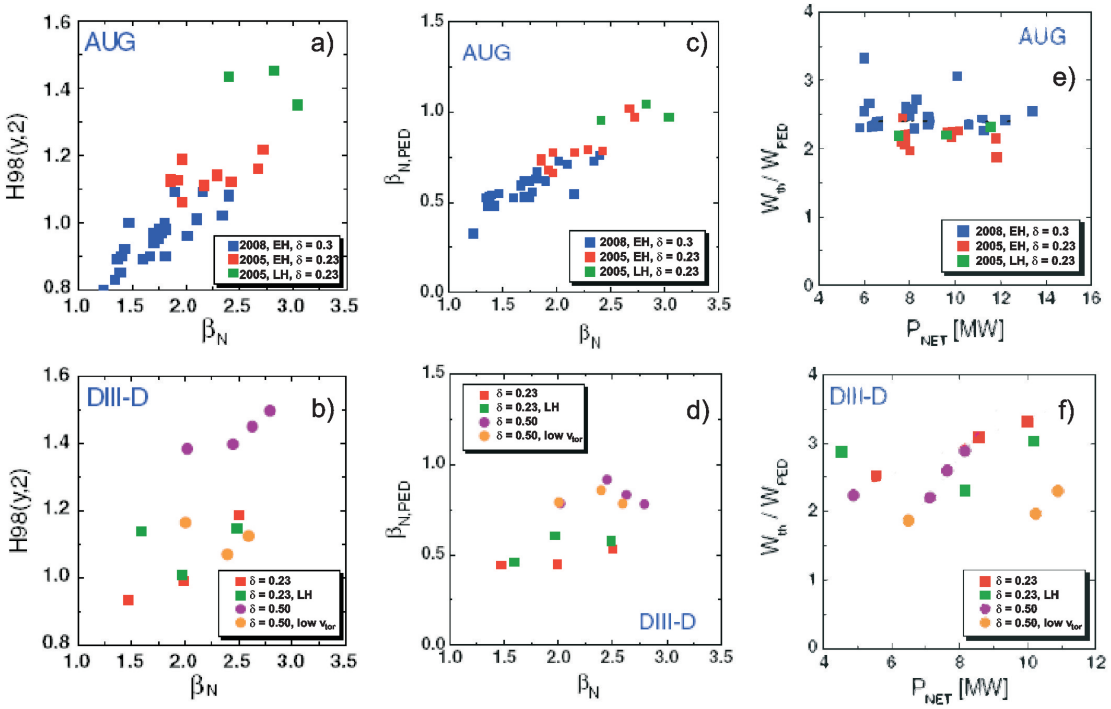

Figure 7.2: $H98(y,2)$ confinement factor versus the total normalized beta for the AUG (a) and DIII-D (b) power scans. Pedestal versus total normalized beta for the AUG (c) and the DIII-D (d) power scans. Ratio of total to pedestal stored thermal energy as a function of net input power for AUG (e) and DIII-D (f) hybrid discharges. In the legends, 'EH' and 'LH' denote early and late heating, respectively (see [89]).

net input power P_{NET} is a suited measure for the core confinement properties in the two machines. To this purpose, $W_{\mathrm{th}}/W_{\mathrm{PED}}$ is shown in Figs. 7.2e,f for AUG and DIII-D, respectively. In AUG, this ratio is found to be rather constant with increasing P_{NET}, which implies no significant improvement in core confinement with raising power. The variation of $W_{\mathrm{th}}/W_{\mathrm{PED}}$ with increasing P_{NET} in DIII-D shows a larger scatter, which is partly due to the variation of plasma shape (low and high triangularity) and momentum input (co–NB and balanced NB injection at high δ). Despite the fact that the considered set of discharges is very limited, different trends may be identified depending on the operation scenario. In the DIII-D power scans with high momentum input and early heating, i.e. the red and the violet points in Fig. 7.2f, the ratio of total to pedestal stored energy is increasing with P_{NET}, for the high triangularity case at least at high powers. This implies a increase in core confinement that is larger as the one which could have been expected from profile stiffness. On the other hand, in both cases of late heating 'LH' and low toroidal rotation velocity v_{tor} (due to counter–NBI), no (or only a small) increase of core confinement can be deduced. Thus, in conclusion with the observations from Figs. (7.2b,d), it is reasonable to assume that the reduction of global confinement at low v_{tor} is due to a reduction in core confinement, most likely to be driven by the decrease in E×B flow shear in the core, which leads to enhanced turbulence. The pedestal confinement on the other hand is practically not changed. Lastly, it is interesting to note that the power scan at low δ, the 'AUG

shape' matched in DIII-D, exhibits behaviors that are kind of intermediate between the AUG power scans and the ones in DIII-D with high triangularity. The edge stability is reduced due to lower shaping, leading to lower pedestal pressures. However, a $\sim$ 20% increase in the $H98(y,2)$ factor is observed with increasing β_{N}, mainly due to an increase in core confinement, in contrast to the hybrids in AUG with the same plasma shape.

The above observations lead to the following conclusive picture. In the DIII-D hybrid discharges with the (original) high triangularity, the increase in $H98(y,2)$ confinement factor with input power is due to an increased core confinement, independently of whether the pedestal pressure reacts on the increase in input power. Conversely, in the AUG hybrid scenario, which has a low triangularity and is predominantly run with the early heating scheme , the confinement factor enhancement with raising β_{N} is due to an increase in pedestal confinement. This different response motivates more detailed studies on both core heat transport and edge stability. The former is subject of the next Section. For specific details of the latter studies, which are not subject of the present thesis, the reader is referred to [89], Sections 5 and 6.

7.3 Turbulent core heat transport

7.3.1 Experimental profile data of the selected discharges

For a detailed study of the core transport of the discharges presented here and in order to understand similarities and differences between AUG and DIII-D hybrids with increasing β_{N}, selected discharges are analyzed. To this purpose, high quality kinetic profiles and good 'Motional Stark Effect' (MSE) data, which constrain the equilibrium reconstructions, are necessary as input for the analysis. Because the AUG 2005 hybrids were run at pedestal collisionalities closer to the ones at DIII-D as compared to the AUG 2008 shots, and MSE data as well as kinetic profiles are available only for the 2005 data set, the low and high power phases of a well analyzed AUG 2005 power scan (#20116) are taken in two corresponding time windows. For DIII-D, the representative shots are the ones at lowest and highest power in the dataset, namely (#128250) and (#128249), respectively. Both exhibit the 'normal', high triangularity DIII-D shape.

As an example for the corresponding profiles, the dependence of ion and electron temperatures in both the AUG low power ($\beta_{\mathrm{N}} = 2.0$) and high power ($\beta_{\mathrm{N}} = 2.7$) as well as the DIII-D low power ($\beta_{\mathrm{N}} = 2.0$) and high power ($\beta_{\mathrm{N}} = 2.8$) are shown in Fig. 7.3 as a function of the normalized radius ρ_{pol}, defined via the poloidal flux. For each parameter all profiles within the stationary time window selected for the analysis have been combined together. The solid lines are fits to the experimental data. There exists a clear difference in the ratio of ion and electron temperature profiles in the two machines. Despite the lower pedestal density than in the AUG hybrid discharge, $T_{\mathrm{i}}^{PED} \sim T_{\mathrm{e}}^{PED}$ in DIII-D and the ion and electron temperature profiles remain very similar further inside the confinement region as far as $\rho_{\mathrm{pol}} \sim 0.6$. In the AUG power scan $T_{\mathrm{i}}/T_{\mathrm{e}}$ increases at the plasma edge from low to high power, particularly in the region just inside the pedestal top (e.g. $T_{\mathrm{i}}/T_{\mathrm{e}}$ increases from 1.2 at low power to 1.46 at high power at $\rho_{\mathrm{pol}} = 0.8$). The comparison of the kinetic profiles at mid–radius reveals that $T_{\mathrm{i}} \sim T_{\mathrm{e}}$ at low beta both in AUG and DIII-D, with $T_{\mathrm{i}}/T_{\mathrm{e}}(\rho_{\mathrm{pol}} = 0.5) \sim 1.1$, whereas at high beta a higher ratio is obtained in AUG (with $T_{\mathrm{i}}/T_{\mathrm{e}} \sim 1.5$ at $\beta_{\mathrm{N}} = 2.7$) compared to DIII-D ($T_{\mathrm{i}}/T_{\mathrm{e}} \sim 1.2$ at $\beta_{\mathrm{N}} = 2.8$).

In AUG hybrid discharges with no external gas fueling, which is the case of the shot

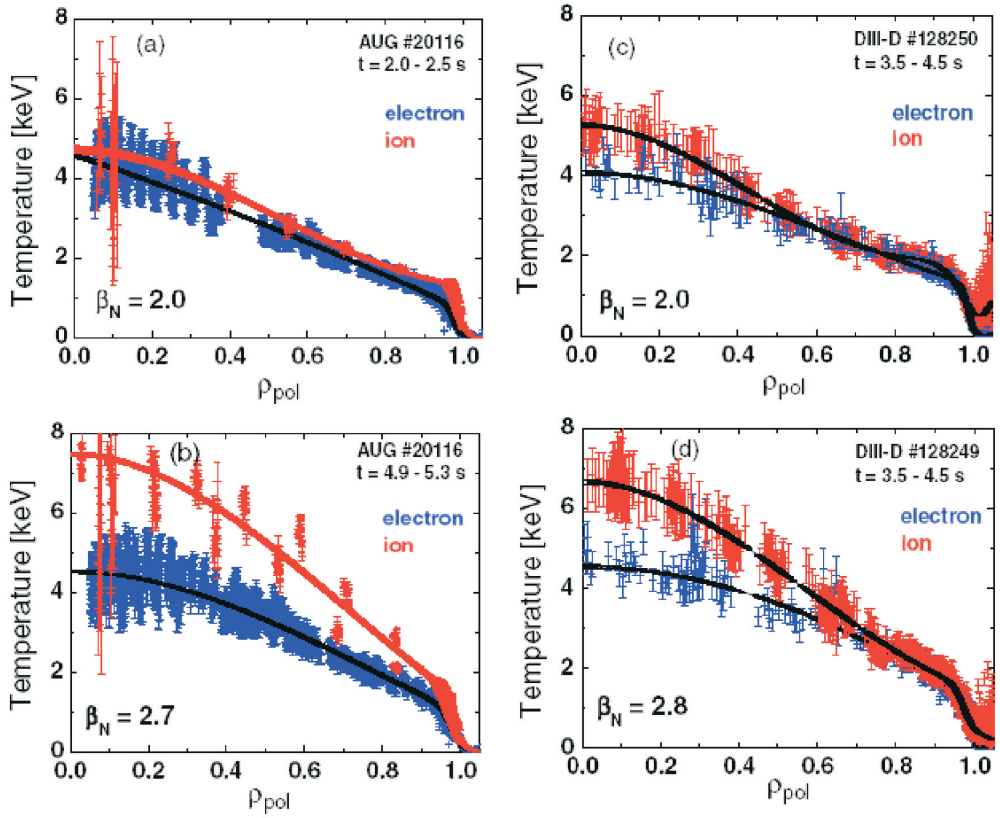

Figure 7.3: Ion and electron temperature profiles for low (a) and high (b) power cases of AUG hybrid power scan #20116, and for low (c) and high (d) power cases of the DIII-D hybrid power scan at high δ. Black solid lines are fits to the data. The density of the DIII-D data points in (c) and (d) has been reduced by a factor of 10 in order to allow for a distinction of the fitted profiles (from [89]).

analyzed, n_e typically increases with beam fueling as the total input power is increased. The increase in n_{PED} by 20% from low to high power represents the upper bound of the density variation observed in the hybrid power scans. In DIII-D, good density control during the discharge allows the hybrid power scan to be run at constant density. In the stationary phase of DIII-D hybrid discharges, the control over the particle inventory is maintained by active feedback and pumping, with the wall playing a small role in the particle balance [148]. Some of these differences between the two devices are related to the fact that the wall behavior is likely to be different in a tokamak with tungsten compared to carbon plasma facing components [149]. The increase in pedestal density with beam fueling in the AUG hybrid power scans without external D2 fueling contributes to the increase in the pedestal pressure with power in such discharges. However, the ion and electron temperature at the pedestal top increase from low to high power in the AUG hybrid power scans analyzed in this work, independently of the level of external gas fueling. Therefore, differences in the wall conditions of the two tokamaks are not likely to be the main reason for the different response to power of the AUG and DIII-D pedestals. In the DIII-D power scan the pedestal density is lower and the density profile is more peaked

than in the AUG hybrid discharge, with a peaking factor of 1.8 (defined here as the ratio of core to pedestal density) compared with 1.37 (at low power) and 1.25 (at high power) in the AUG case. However, in DIII-D the peaking factor remains constant as the NBI power is increased in the power scan, and thus density peaking is not likely to play a role in the relative increase in core confinement from low to high beta. In particular, it has to be mentioned that the logarithmic density gradient in DIII-D is more than a factor 2 higher as compared to AUG at mid–radius (see Table 7.1).

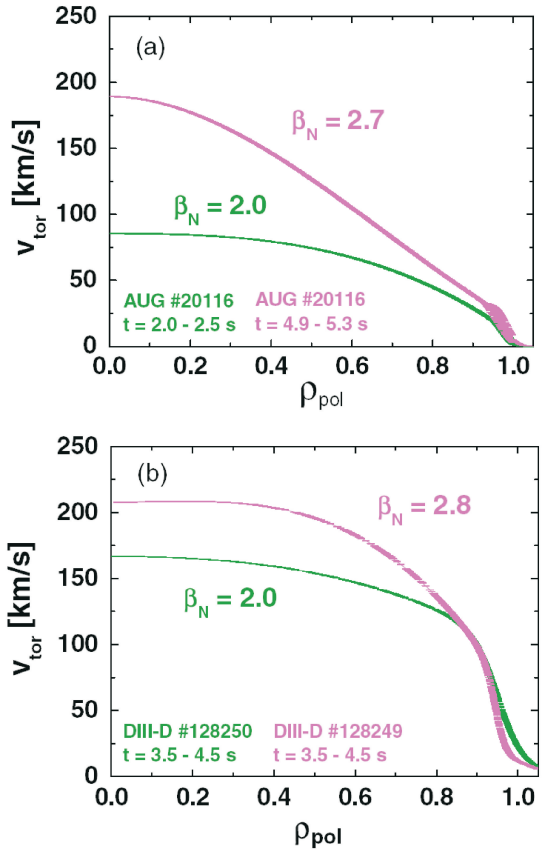

Figure 7.4: Fitted toroidal rotation profiles at low and high power for the AUG (a) and DIII-D (b) hybrid power scan (from [89]).

The rotation profiles, shown in Fig. 7.4, are quite different in the two devices, especially at outer radii, where v_{tor} is significantly higher in DIII-D than in AUG. At low β_{N}, the toroidal rotation is significantly lower in the AUG discharge. These differences may be partly related to the lower pedestal density in the DIII-D discharges (thus less NB attenuation compared with the AUG case) and the additional ICRH heating in the AUG discharge (3MW throughout the pulse to prevent tungsten accumulation, as described in section 2.1). In the core plasma the toroidal rotation shear plays a dominant role in the E×B shearing rate and thus in the core transport properties. As will be shown below, E×B shearing rate stabilization of core turbulence is significant in both machines at mid–radius at increasing input power, with $\omega_{\mathrm{E\times B}}$ being larger for DIII-D than for AUG.

The profiles of the normalized ion temperature gradient length R/L_{Ti} for AUG and

DIII-D reveal that as the total input power is increased, R/L_{Ti} at mid-radius increases from 5 to 5.7 in DIII-D, but remains constant in the AUG power scan. At larger values of ρ_{tor}, for instance at $\rho_{\mathrm{tor}} \sim 0.65$, R/L_{Ti} increases with beta in both machines. The most important parameters for the low and high power discharges of AUG and DIII-D at $\rho_{\mathrm{tor}} = 0.5$ are summarized in Table 7.1. It has to be noted that the toroidal velocity

	AUG LP	DIII-D LP	AUG HP	DIII-D HP
β_{N}	2.0	2.0	2.7	2.8
q	1.51	1.69	1.69	1.69
s	0.8	1.20	0.56	1.14
$T_{\mathrm{i}}/T_{\mathrm{e}}$	1.10	1.02	1.55	1.13
R/L_{Ti}	6.12	5.00	6.07	5.70
R/L_{Te}	5.49	3.92	5.27	3.88
R/L_{n}	1.15	2.73	0.95	2.67
v_{tor} [km/s]	74	154	126	198

Table 7.1: Main plasma parameters for the low (LP) and high power (HP) discharges from AUG and DIII-D at $\rho_{\mathrm{tor}} = 0.5$ used for the core thermal transport study.

profile was only used for calculation of the E×B shearing rate. The effect of a finite parallel velocity gradient on heat transport was not included.

7.3.2 Numerical investigations

The AUG and DIII-D power scans for the selected discharges have been analyzed performing gyrokinetic simulations with GYRO in order to identify the dominant unstable modes and the proximity to KBM or MTM regimes. The largest variation in experimental parameters important for ion heat transport is found in R/L_{Ti} and $T_{\mathrm{i}}/T_{\mathrm{e}}$, as it can be deduced from Table 7.1. The local analysis is firstly performed at $\rho_{\mathrm{tor}} = 0.5$. At this radius, the normalized ion temperature gradient length does not change to the increase in input power in the AUG power scan, whereas it increases by about 15% from low to high beta in the DIII-D power scan. The GYRO simulations show that at low β_{N} the most unstable linear mode is an ITG mode in both machines. At high power the most unstable linear mode is an ITG mode for the DIII-D case and a microtearing mode for the AUG case (compare, e.g. [111]). As already discussed in the previous Chapters, a stabilizing effect on the ITG modes of these plasmas is due to the inclusion of electromagnetic effects, namely a finite value of β_{e} (the magnetic equilibrium is kept fixed within this study), in the gyrokinetic calculations. A detailed analysis of the electromagnetic effects at mid-radius is shown in Fig. 7.5, where the variation of the growth rate of the most unstable mode with β_{e} is studied for the AUG and DIII-D discharges as the input power is increased in each power scan.

The numerical study uses the local values and gradients of the experimental profiles, as described in Table 7.1, from a given power level. As β_{e} is increased, the most unstable mode changes from ITG modes at low β_{e}, occasionally to MTMs at intermediate values of β_{e}, and finally to KBMs at high values of β_{e}. The actual ranges of β_{e} corresponding to the transition from one mode to another are listed in Table 7.2. The vertical lines in Fig. 7.5 intercept the values of β_{e} at the operational points. In the calculations at mid-radius, it is

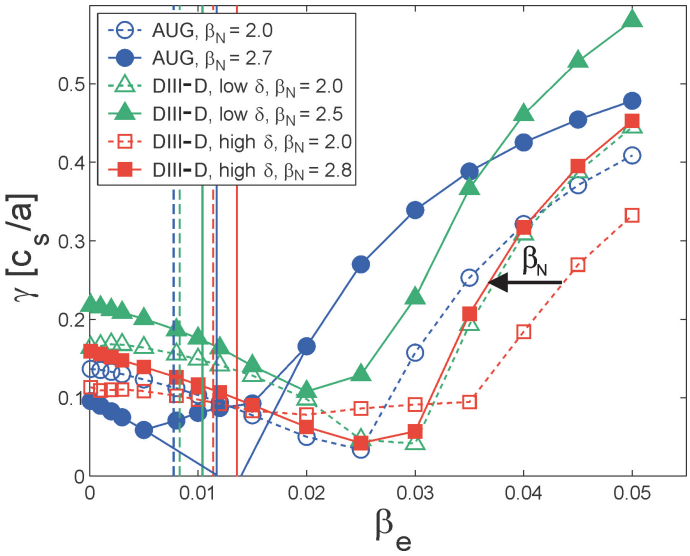

Figure 7.5: Linear growth rate of the most unstable mode at $\rho_{\mathrm{tor}} = 0.5$ versus β_{e} for AUG (blue), DIII-D high δ shape (red) and additionally DIII-D low δ shape (green). The most unstable mode changes from ITG at low values of β_{e} to MTM at intermediate β_{e} in some cases (see Table 7.2) to kinetic ballooning at high values of β_{e}. Open symbols correspond to low power and full symbols to high power in each beta scan. The vertical lines intercept the values of β_{e} at the operational points (same color convention), dashed lines corresponding to low power and solid lines to high power in each beta scan. The arrow indicates the increase in β_{N} in the experiment, from low power to high power in each scan (from right to left in the plot).

	ITG	MTM	KBM	exp. β_{e}[%]
AUG, $\beta_{\mathrm{N}} = 2.0$	$\beta_{\mathrm{e}} < 2.5$	–	$\beta_{\mathrm{e}} > 2.5$	0.77
AUG, $\beta_{\mathrm{N}} = 2.7$	$\beta_{\mathrm{e}} < 0.5$	$0.5 < \beta_{\mathrm{e}} < 1.8$	$\beta_{\mathrm{e}} > 1.8$	1.17
DIII-D, low δ, $\beta_{\mathrm{N}} = 2.0$	$\beta_{\mathrm{e}} < 2.8$	–	$\beta_{\mathrm{e}} > 2.8$	0.83
DIII-D, low δ, $\beta_{\mathrm{N}} = 2.5$	$\beta_{\mathrm{e}} < 2.0$	$2.0 < \beta_{\mathrm{e}} < 2.7$	$\beta_{\mathrm{e}} > 2.7$	1.04
DIII-D, high δ, $\beta_{\mathrm{N}} = 2.0$	$\beta_{\mathrm{e}} < 1.7$	$1.7 < \beta_{\mathrm{e}} < 3.5$	$\beta_{\mathrm{e}} > 3.5$	1.14
DIII-D, high δ, $\beta_{\mathrm{N}} = 2.8$	$\beta_{\mathrm{e}} < 2.8$	–	$\beta_{\mathrm{e}} > 2.8$	1.36

Table 7.2: Changes in the most unstable mode as β_{e} is increased in the gyrokinetic simulations illustraded in Fig. 7.5. The last column lists the experimental values of β_{e} in %.

found that in both machines the onset of kinetic ballooning modes shifts to lower values of β_{e} as the input power is increased in the experiments (see Table 7.2). However, the experimental point is much closer to the onset of kinetic ballooning modes in AUG than in DIII-D, as shown by Fig. 7.5 and Table 7.2. For example, for the AUG hybrid case at $\beta_{\mathrm{N}} = 2.7$, β_{e}(experiment) $= 1.17\%$ and the onset of kinetic ballooning modes occurs at $\beta_{\mathrm{e}} > 1.8\%$, while for the DIII-D hybrid discharge at high δ and $\beta_{\mathrm{N}} = 2.8$, β_{e}(experiment) $= 1.36\%$ compared with $\beta_{\mathrm{e}} > 2.8$ for kinetic ballooning mode onset. The specific influence of the different parameters between AUG and DIII-D, high δ, for the low and high power

cases is shown in Fig. 7.6a,b, respectively. It turns out that the safety factor profile

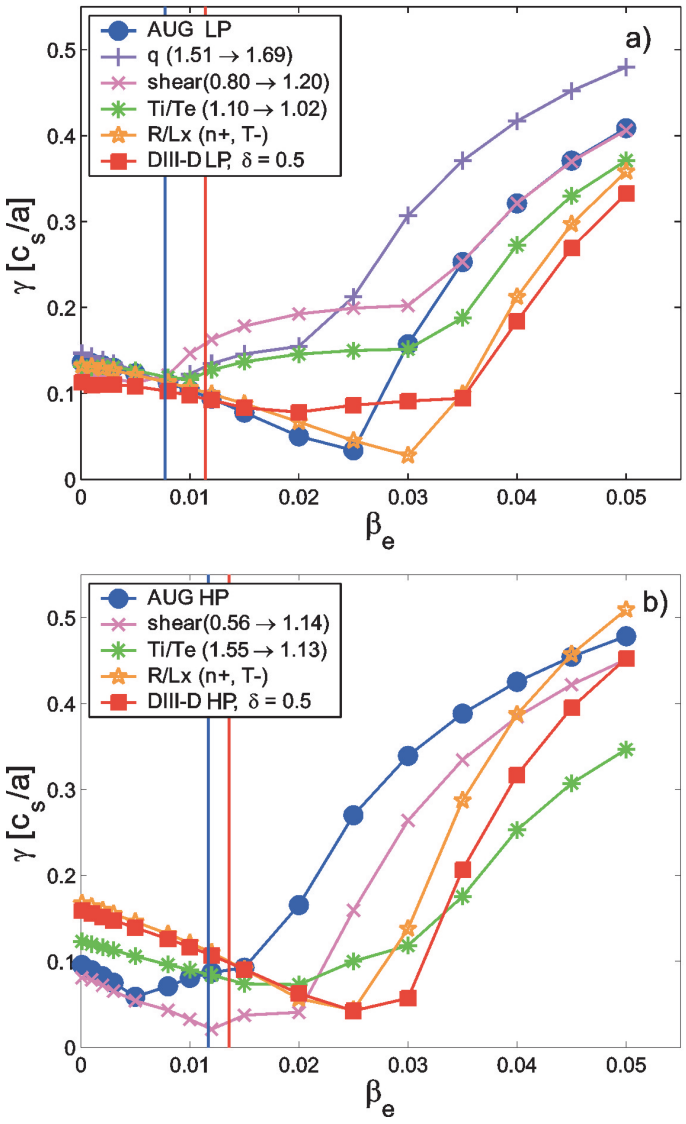

Figure 7.6: Linear growth rate of the most unstable mode at $\rho_{\mathrm{tor}} = 0.5$ versus β_{e} for AUG low power (a) and high power (b) mid–radius parameters going to the corresponding DIII-D, high δ parameters, respectively.

has a strong influence. For example, as shown in Fig. 7.6a, the increase of the safety factor from 1.51 $\rightarrow$ 1.69 has a strong influence on the onset of the KBM to be the most unstable, in such a way that it is shifted towards smaller values of β_{e}, as it was also shown in Chapter 6 by the scaling $\beta_{\mathrm{e}} q^2$, see Fig. 6.7. A higher value of magnetic shear shifts the onset of KBM towards higher β and leads to the destabilization of a wider window with MTMs. Also the ion to electron temperature ratio $T_{\mathrm{i}}/T_{\mathrm{e}}$ has a strong influence, as it is particularly visible in Fig. 7.6b. The decrease from $T_{\mathrm{i}}/T_{\mathrm{e}} = 1.55$ in AUG high power to $T_{\mathrm{i}}/T_{\mathrm{e}} = 1.13$ in DIII-D leads to a shift of KBMs towards higher β_{e}. The gradients of density and temperature as well as the geometry have only a smaller influence. Moreover,

it is clear that mainly differences in T_i/T_e are responsible for the differences of the KBM onset between low and high power discharges of the two machines. The DIII-D power scan at low δ (i.e. the AUG plasma shape matched in DIII-D) lies between the AUG case and the DIII-D case at high δ. The main reason for this is the fact that the DIII-D low δ discharges have a higher magnetic shear, namely $s = 1.19$ for the low power case and $s = 1.12$ for the high power case, as compared to the AUG shots. The onset of KBMs for the DIII-D low δ shots is at lower β_e as compared to the high δ DIII-D shots since the former exhibit higher ion temperature gradient scale length. Lastly, a similar local analysis performed at $\rho_{tor} = 0.65$ shows, that both AUG and DIII-D plasmas are far from the kinetic ballooning threshold. In fact at this radius MTMs are the most unstable modes and the kinetic ballooning threshold is found at much higher values of β_e.

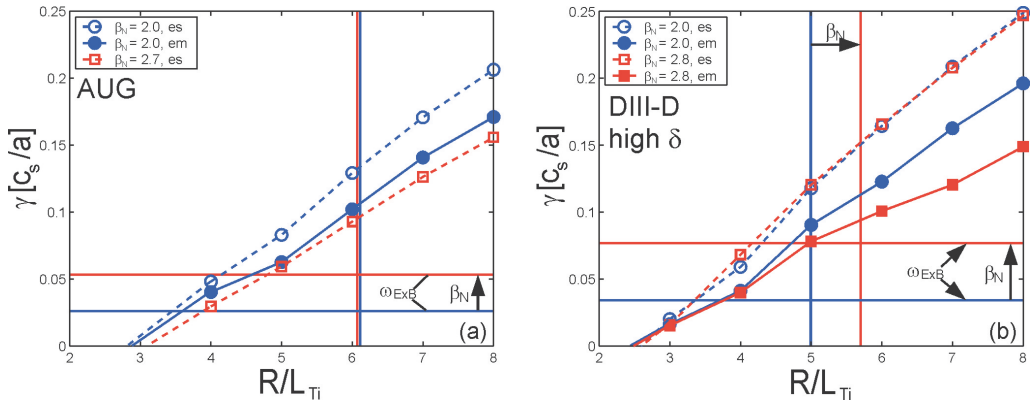

Figure 7.7: Linear growth rate of the most unstable mode (ITG mode) versus R/L_{Ti} at $\rho_{tor} = 0.5$ for the low and high power phases of (a) the AUG hybrid #20116 and (b) the DIII-D hybrid scan at high δ shape (#128250 and #128249). Open symbols correspond to the electrostatic calculations, full symbols indicate the calculations including finite β_e. Vertical lines mark the variation in R/L_{Ti} in the experiment from low power (blue line) to high power (red line). Horizontal lines denote the E×B shearing rate, calculated according to [150], for the low power (blue line) and high power (red line) cases.

Figure 7.7 shows the dependence of the linear growth rate of the ITG mode on R/L_{Ti} at mid-radius for the AUG power scan (a) and the DIII-D power scan at high δ (b) at low and high β_N. The vertical lines mark the variation in R/L_{Ti} at mid-radius in the experiment from low power (blue lines) to high power (red lines). The results of both electrostatic and electromagnetic calculations are shown by the circle and square symbols, respectively, and both calculations were again performed for the same geometry and thus the same Shafranov shift. The figures reveal the significant E×B shearing rate stabilization in both machines as beta is increased (where $\omega_{E\times B}$ is calculated as in [150] and is indicated by the horizontal lines in Figs. 7.7a,b, for the low power (blue lines) and high power (red lines) cases). In addition, the figures illustrate the non-negligible stabilizing effect of β_e on the ITG modes of these plasmas. The electromagnetic calculations for the AUG discharge at high beta are not plotted in figure Fig. 7.7a because the experimental point falls in the micro-tearing domain. In this case the ITG mode becomes subdominant mainly due to the large T_i/T_e ratio that stabilizes the ITG modes and destabilizes the micro-tearing modes. Subdominant modes are not followed in these simulations, which use the GYRO

initial value solver (and not the GYRO eigenvalue solver). The electrostatic calculations show a reduction in the linear growth rate as the power is increased in the AUG beta scan, which is due to the increase in T_i/T_e at mid–radius in the experiment (Fig. 7.3). In the DIII-D scan, for which the variation of $T_i/T_e(\rho_{tor} = 0.5)$ from low to high beta is much smaller, see Figs. (7.3c,d), such a stabilization is not found in the calculations, as shown in Fig. 7.7b. This analysis indicates that a sizeable reduction in core transport is predicted at mid–radius in both machines as β_N is raised in the experiment. The predicted increase in R/L_{Ti} with β_N is due to a significant E×B shearing rate stabilization of the ITG modes and to the inclusion of electromagnetic effects in the gyrokinetic calculations, which provide additional stabilization at β_N values achieved in the experiment. However, while in the DIII-D case the predicted increase in R/L_{Ti} is of the same order as the measured one, in the AUG case R/L_{Ti} is constant as the heating power is increased. The proximity of the AUG plasma at high β_N to the onset of kinetic ballooning modes might explain the constancy of $R/L_{Ti}(\rho_{tor} = 0.5)$ when the heating power is increased. As mentioned above, this picture changes at outer radii, where R/L_{Ti} increases with power in both machines and the AUG and DIII-D plasmas are both far from the onset of kinetic ballooning modes.

In order to further clarify this issue, the variation of the total ion heat flux as a function of R/L_{Ti} with increasing input power has been examined. Nonlinear gyrokinetic simulations with the same resolution as the ones in Chapter 5.4 are performed in flux-tube geometry using periodic boundary conditions with and without the inclusion of E×B shearing. They allow us to determine the slope of the ion heat flux Q_i as a function of the driving logarithmic gradient R/L_{Ti} . The dependence of the heat flux as a function of R/L_{Ti} is usually very close to a linear function (e.g. [137, 151]). It is often not appreciated in the behavior of core confinement in H-mode plasmas, that, as a consequence of the increase in the temperature at the pedestal top, the normalized heat flux in the core can be reduced when the auxiliary heating power is increased in a power scan. This is visible in Fig. 7.8, showing the normalized ion heat flux $Q_{i,norm}$ as a function of R/L_{Ti}. Here, Q_i is normalized using $Q_{i,norm} = RQ_i/(n_iT_i)$ expressed in gyroBohm units, where $\chi_{GB} = \rho_s^2 c_s/a$. This normalization reflects the fact that the natural scaling of diffusivity for turbulent heat transport in local simulations is proportional to $\lambda_{turb}^2\gamma$, where the growth rate $\gamma \sim c_s/a$. The gyroBohm (GB) scaling is to be expected when the turbulence length scale λ_{turb} is not affected by the system size a and is usually found under experimental conditions. From a simple random walk argument, $\lambda_{turb} = \rho_s$ and the normalization to χ_{GB} appears naturally. It is noteworthy that the GB scaling predicts the energy confinement time to be proportional to ρ_*^{-3}, which is not too different from the $IPB98(y, 2)$ scaling, see Eq. (7.1). The normalized ion heat fluxes from power balance for AUG and DIII-D low and high power cases are compared in Fig. 7.8 (horizontal lines, with solid lines for low beta case and dashed lines for high beta case) to the ion heat flux calculations from GYRO at low power (open circles) as a function of R/L_{Ti}. The comparison is performed at $\rho_{tor} = 0.5$. Power balance analysis was performed using ASTRA [152] for the AUG power scan, with FAFNER calculations [153] as input for the neutral beam sources and TORIC runs [154] providing the ICRH sources. For the DIII-D discharges power balance analysis was performed with the ONETWO transport code [155], which uses a Monte Carlo code to calculate the neutral beam deposition profiles. As β_N increases in the experiment, the reduction in heat flux in AUG is much larger than in DIII-D ($Q_{i,norm} \sim T_i^{5/2}$ and T_i/T_e increases more in AUG than in DIII-D as the input power is increased). As can be expected

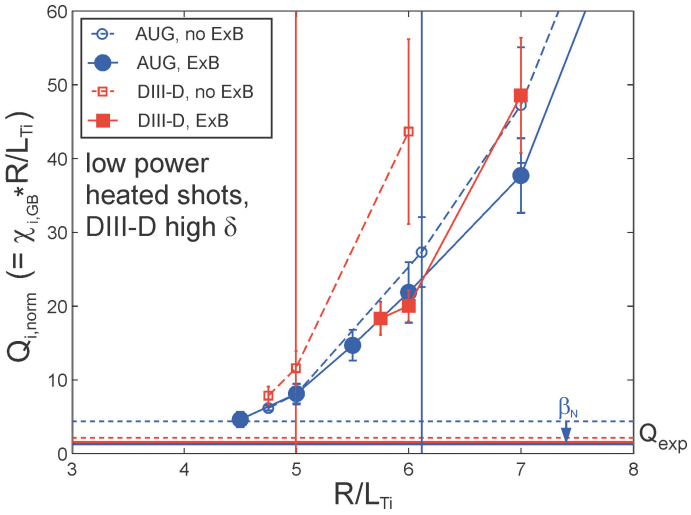

Figure 7.8: Nonlinear electromagnetic flux–tube simulations with GYRO for the normalized ion heat flux $Q_{\mathrm{i,norm}}$ at $\rho_{\mathrm{tor}} = 0.5$ for the AUG and DIII-D low beta cases, without (open symbols) and with (full symbols) E×B shearing. The error bars indicate the fluctuation levels of the calculations. Vertical lines denote the experimental R/L_{Ti} at low beta in the two machines, horizontal lines mark the values of the normalized ion heat flux from power balance (see text) at low power (solid line) and high power (dashed line). The arrows indicate the increase in β_{N} from low to high power in each experiment (blue for AUG and red for DIII-D).

from previous results [137], nonlinear simulations without E×B shearing deliver heat fluxes which are generally larger than those found in the experiments. In this analysis, however, also the runs with $\omega_{\mathrm{E\times B}}$–inclusion reveal higher fluxes as compared to the experimental ones. It is emphasized that simulations at lower values of R/L_{Ti} as the ones shown in Fig. 7.8 having the lowest heat flux, are stable, which implies no meaningful fluxes as result. Nevertheless, linear extrapolation of our nonlinear results to the lower heat fluxes allows a rough estimate for the differences in R/L_{Ti} to be expected. This is done via crossing of the simulated slopes from both cases without and with E×B shearing with the heat fluxes from power balance, respectively. As a result, a sizeable reduction in the normalized logarithmic temperature gradient of order $\Delta R/L_{\mathrm{Ti}} \sim 1$ for AUG is obtained, while the shift in R/L_{Ti} for DIII-D is practically negligible, as it can be deduced from Fig. 7.8. Thus, as the input power is increased in the AUG hybrid scan, the power balance analysis presented above predicts a decrease in R/L_{Ti} of order one. On the other hand, the linear calculations shown in Fig. 7.7 predict a gain in R/L_{Ti} of order one from low to high power in the scan, due to the combined stabilizing effects of $T_{\mathrm{i}}/T_{\mathrm{e}}$, $\omega_{\mathrm{E\times B}}$ and beta on the ITG modes. It is thus possible that these two compensating effects account for the lack of variation in R/L_{Ti} at mid-radius as the input power is increased in the AUG hybrid discharge. In the DIII-D power scan, on the other hand, the reduction in $Q_{\mathrm{i,norm}}$ is smaller (due to the smaller increase in $T_{\mathrm{i}}/T_{\mathrm{e}}$ with power) and the associated variation in R/L_{Ti} negligible, as shown in Fig. 7.8. This supports the result found with the linear simulations shown in Fig. 7.7b, namely that E×B shearing rate and beta stabilization of the ITG modes can explain the magnitude of the measured increase in R/L_{Ti} in the

plasma core of the DIII-D hybrid discharges.

From this analysis it can be concluded that the observation that in AUG hybrid discharges R/L_{Ti} is roughly constant at mid–radius as beta is increased is not explained by profile stiffness, as it may appear at first glance, but by a more complex combination of effects. Namely, $T_{\mathrm{i}}/T_{\mathrm{e}}$, $\omega_{\mathrm{E\times B}}$ and beta stabilization of ITG modes at mid–radius is compensated by a sizeable reduction in the normalized ion heat flux as the input power is increased. While these effects are analyzed in the core, they are not independent of the boundary conditions at the edge. As noted before, the increase in T_{i} in the pedestal region in AUG from low to high input power drives a reduction in the normalized ion heat flux in the core. The larger increase in $T_{\mathrm{i}}/T_{\mathrm{e}}$ at the plasma edge in AUG than in DIII-D as the auxiliary heating is increased leads to a higher $T_{\mathrm{i}}/T_{\mathrm{e}}$ ratio at mid–radius in AUG. In addition, proximity of the AUG experimental point at high β_{N} to the kinetic ballooning threshold may also play a role in keeping R/L_{Ti} constant at mid–radius as the input power is increased in AUG. It must be stressed, however, that analysis at outer radii shows that in this region both AUG and DIII-D hybrids are far from the onset of kinetic ballooning modes and although the normalized ion heat flux decreases as the input power is increased in the experiment, a strong increase in R/L_{Ti} occurs there in both machines.

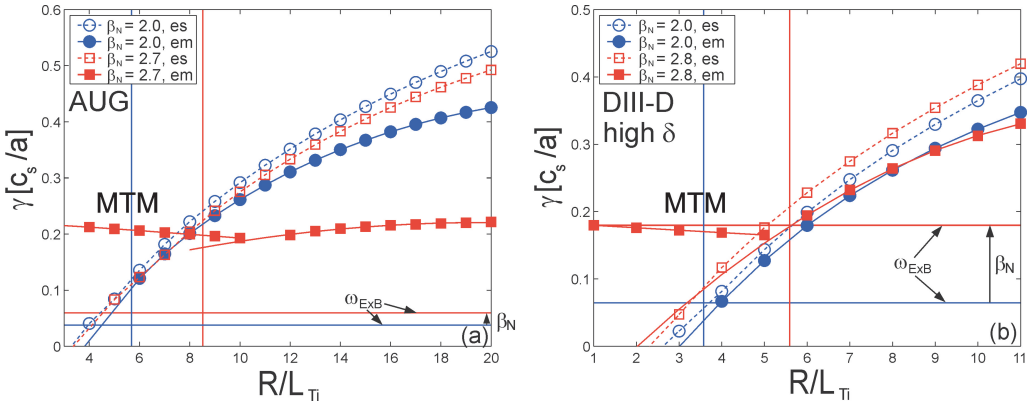

Figure 7.9: Linear growth rate of the most unstable mode versus R/L_{Ti} at $\rho_{\mathrm{tor}} = 0.65$. The same conventions as in Fig. 7.7 are used.

In Fig. 7.9, the dependences of the linear growth rate of the most unstable mode on R/L_{Ti} at $\rho_{\mathrm{tor}} = 0.65$ for the AUG power scan (a) and the DIII-D power scan at high δ (b) at low and high β_{N} are illustrated, respectively. There, a different picture as compared to the mid–radius scans emerges. The increase of R/L_{Ti} with β_{N} in both machines, denoted by the vertical lines, leads to a stronger $\gamma_{\mathrm{net}} = \gamma - \gamma_{\mathrm{E\times B}}$ in AUG, and therefore can be expected to be responsible for stronger turbulence levels, since in AUG smaller E×B shearing rates as compared to DIII-D are found, especially in the high power cases. Consequently, the DIII-D discharges are at the γ_{net} threshold, whereas the AUG shots do not show this behavior. It has to be noted that in AUG higher logarithmic ion temperature gradients are found than in DIII-D. These observations, in turn, also support the idea that in DIII-D the better overall confinement is due to a better core confinement. Moreover, it is interesting to note that for electromagnetic calculations at the high power discharges MTMs are the most unstable modes at the experimental conditions, such that their influence is increased for DIII-D as compared to the simulation results at mid–radius.

The ITG mode at high R/L_{Ti} is strongly stabilized for the AUG high power shot, which is mainly due to a higher $T_{\mathrm{i}}/T_{\mathrm{e}}$ in comparison to DIII-D.

7.4 Summary and conclusions

In this study, aspects of core and partly pedestal confinement of the hybrid scenario in ASDEX Upgrade and DIII-D with increasing auxiliary heating are illustrated. Power scans were carried out in each device at fixed q_{95} (matched in both machines), constant density and fixed plasma shape. In addition, DIII-D spanned the hybrid plasma shapes of the two devices, a low δ shape for AUG and a high δ shape for DIII-D, to separate between shape and power dependence of the pedestal pressure. Elements of similarity are found between the two tokamaks (which should be expected, given the similarity of the two devices in terms of engineering parameters), but also different responses of the plasma performance to heating power (β_{N}).

The $H98(y,2)$ confinement factor is found to increase with the total β_{N} in both tokamaks and it is higher in DIII-D with a higher δ plasma shape at a given β_{N}. This is understood in terms of improved edge stability at higher shaping, a well-known property of type I ELMy H-modes, and confirmed by MHD stability analysis of selected AUG and DIII-D hybrid discharges. Thus hybrid operation at high plasma triangularity benefits from higher pedestal pressures, since less input power is needed to achieve a given β_{N} as compared with hybrid discharges in a low triangularity shape.

As the additional NB heating power is increased, the confinement enhancement with respect to the $IPB98(y,2)$ scaling is due to an increase in pedestal confinement in the AUG hybrid scenario and to an increase in core confinement in the DIII-D hybrid scenario. Analysis of turbulence and transport in the plasma core of selected AUG and DIII-D power scans of this study shows that the largest variation in experimental parameters related to microinstabilities are found in R/L_{Ti} and $T_{\mathrm{i}}/T_{\mathrm{e}}$. At mid–radius, AUG exhibits a larger increase in $T_{\mathrm{i}}/T_{\mathrm{e}}$ with heating power than DIII-D. This is partly related to the larger $T_{\mathrm{i}}/T_{\mathrm{e}}$ ratio at the plasma edge observed in AUG as compared to DIII-D in the hybrid power scans considered, despite the lower pedestal density in DIII-D.

Linear gyrokinetic simulations of the selected power scans at mid-radius indicate that ITG modes are usually the most unstable modes in both machines (with the exception that, for AUG at high power, micro-tearing modes dominate). In both devices a sizeable reduction in core transport is predicted as the input power is increased in the experiment. The increase in R/L_{Ti} with beta at mid-radius is predicted to be due to a significant E×B shearing rate stabilization of the ITG modes in the selected power scans of both AUG and DIII-D. Both at low and high β_{N} at mid-radius $\omega_{\mathrm{E\times B}}$ is larger in DIII-D than in AUG. These results are related to differences in the toroidal velocity profiles of the AUG and DIII-D hybrid power scans. While v_{tor} increases significantly with power in both machines, it is higher in DIII-D at a given β_{N} value. Such differences in the toroidal rotation profiles may be partly related to the lower pedestal density of the DIII-D hybrid power scan and to the additional ICRH heating in the AUG hybrid power scan, which reduces v_{tor} in AUG NBI heated H-modes. Inclusion of electromagnetic effects in the gyrokinetic calculations provides additional stabilization at β_{N} values achieved in the experiment. At mid-radius, the predicted increase in R/L_{Ti} with beta is of the same order of that measured experimentally in the DIII-D power scan. In AUG, proximity to the kinetic ballooning

threshold and/or a stronger reduction in normalized ion heat flux with power (due to the larger increase in $T_\mathrm{i}/T_\mathrm{e}$ and in the pedestal top temperature) are possible explanations for the constancy of R/L_Ti at mid-radius as beta is increased. Similar analysis at outer radii shows that in this region both AUG and DIII-D hybrids are far from the onset of kinetic ballooning modes and although the normalized ion heat flux decreases as the input power is increased in the experiment, a strong increase in R/L_Ti occurs there in both machines. An additional linear analysis of growth–rates at $\rho_\mathrm{tor} = 0.65$ reveals that $\omega_{\mathrm{E}\times\mathrm{B}}$ acts strongly stabilizing in the DIII-D tokamak, while there is practically no stabilization for AUG. The results at $\rho_\mathrm{tor} = 0.5$ are in agreement with the experimental observation of a confinement improvement with increasing β_N, which is in DIII-D mainly due to a better core confinement, whereas in AUG it has to be attributed to pedestal physics.

The present study of the core heat transport is intended to give a first hint of the different physics mechanisms leading to the different response of AUG and DIII-D hybrid scenario shots investigated here for increasing levels of β_N. The difficulties in order to obtain a consistent picture from local analysis at $\rho_\mathrm{tor} = 0.5$ and $\rho_\mathrm{tor} = 0.65$ are connected to different physics behaviors. This suggests that the best framework are global electromagnetic nonlinear simulations of the chosen plasmas at $\rho_* \lesssim 1/300$ possibly with the measured heating profiles in order to capture the full interplay of the various effects listed above and possibly also others. Especially for the high power cases, ρ_* is smaller than the above value (for AUG at $T_\mathrm{i} = 5\mathrm{keV}$ one gets $\rho_* \approx 170$ while for $T_\mathrm{i} = 2\mathrm{keV}$ $\rho_* \approx 270$, such that for the latter the flux tube limit is better satisfied, as it was demonstrated for instance in [44]). Of course, global electromagnetic simulations are more consuming in terms of computer time.

Chapter 8

Conclusion

In this Chapter, the main results obtained in the framework of the present thesis are summarized, highlighting analogies and differences of the electromagnetic effects in the various transport channels. Finally, the results are put in perspective by discussing their implications to a high–β operational scenario, required for a burning plasma in a fusion reactor.

The main scope of this PhD work has been to investigate the effects of a finite β, defined as the kinetic to magnetic pressure ratio, on the various transport channels, mainly from the theoretical standpoint. This is of strong importance for fusion development towards a reactor, since economically viable tokamak operation implies a high β (of the order of a few percent), such that its influence cannot be neglected in the modeling. Moreover, the investigations of finite–β effects are interesting from the physics point of view, because they imply the presence of two fluctuating electromagnetic fields through both the fluctuating electrostatic potential and the parallel magnetic vector potential. The latter two are closely connected such that the study of the relationship between them, mainly produced by passing electron dynamics, is required. This relation is given by Ampère's law, which connects the electromagnetic potential $A_\parallel$ due to perpendicular magnetic field fluctuations with the current parallel to the equilibrium magnetic field, and depends only on the electron pressure parameter β_e. The parallel current is mainly determined by the fluctuating electrostatic potential ϕ, whose gradient points primarily in poloidal direction, as it was shown in Chapter 4.2. In the electromagnetic description, the potentials ϕ and $A_\parallel$ lead to two processes for turbulent transport, the E×B and magnetic flutter, respectively. In addition to affecting mainly electrostatic type of instabilities and turbulence, like ion temperature gradient (ITG) and trapped electron modes (TEM), which are usually the most important microturbulent modes leading to anomalous transport, a finite β can also lead to the destabilization of electromagnetic type of instabilities, like microtearing modes (MTM) and kinetic ballooning modes (KBM), whose occurrence and relevance in present and future high–β experimental scenarios has to be explored.

Due to the complex interplay of the implications connected with a finite β_e, a realistic description requires numerical calculations, but deeper physical understanding can be obtained only by concurrent analytical investigations. For this reason, numerical calculations have been always performed in concert with analytical derivations, developed within gyrokinetic and fluid models in the framework of the present thesis. These also allowed us to clarify the connection between the electromagnetic results obtained here, and their

corresponding limits in the electrostatic case, which were often already documented in the previous literature.

In conclusion, a rather broad and comprehensive theoretical investigation of electromagnetic effects on the various transport channels, in particular for electron, impurity and toroidal momentum transport, has been obtained. These effects received very limited consideration by the nuclear fusion community so far, or were practically neglected. The investigations on the different transport channels allows also the assessment of different physical mechanisms, by which a finite β can impact the transport (direct and indirect mechanisms).

8.1 General conclusions

Finite β effects on electron, trace impurity, parallel momentum and ion heat transport in tokamak plasmas have been studied in the present thesis by means of analytical calculations and numerical simulations.

The effects of a finite β_e on the different transport channels can be divided into two branches. Direct β_e effects are due to the additional terms proportional to the fluctuating $A_\parallel$ in the expression of the fluxes, whereas indirect β_e effects are caused by changes of the eigenfrequency and/or the eigenfunction of the considered mode. It has to be mentioned that both effects are always present, but one of them is usually the dominant contribution. For instance, the electromagnetic behavior of electron particle transport is mainly due to the large parallel mobility of passing electrons. This implies the loss of adiabaticity and therefore additional leading order terms proportional to β_e in the formula for the flux, Eq. (4.7), such that a finite β_e has a direct effect. In contrast, indirect effects due to the modification of the eigenfrequency of the dominant mode can be regarded as a small correction. The transport of trace impurities, parallel momentum (mainly due to ions) and ion heat shows that the indirect effects are dominant since the parallel mobility of ions is of order $(m_\mathrm{i}/m_\mathrm{e})^{0.5}$ smaller than that of electrons. This leads to the conclusion that the main electromagnetic effect in the latter channels is caused by both trapped and passing particle physics, while for electron transport it is passing particle physics alone.

Finite–β_e effects have been investigated for various transport channels under conditions of both ITG and TEM microturbulence. The latter two instabilities, which are usually the most important ones in the core of tokamak plasmas, cause different behaviors of the various transport channels with respect to an increase of β_e. It has been found that ITG turbulence is significantly affected by a finite β_e, while TEM turbulence shows only weak effects. This is due to the fact that ITG modes are connected with larger fluctuating perpendicular magnetic field due to the stronger coupling to the parallel velocity. In the theoretical modeling, the latter is always connected with $A_\parallel$ being proportional to β_e. Due to this difference, microturbulence in which ITG modes are dominant, shows a decrease of the stationary density gradients of electrons and low–Z trace impurities. Furthermore, the momentum transport flux decreases as well as the ion heat flux. These common behaviors, however, are due to very different reasons connected with the above mentioned different physics processes ongoing in the case of finite perpendicular magnetic field fluctuations.

These differences, in turn, also imply that the main role of β takes place in different components of the transport (diagonal or off–diagonal) depending on the transport channel. The finite β_e effects on electron transport lead to a non–adiabatic response of passing

electrons and are mainly of convective type. This implies that in conditions of dominant ITG modes the passing particle flux is directed outwards, and results in lower stationary density gradients. Thus, the predicted density peaking is reduced with increasing β_e, particularly in the absence of neutral beam injection (NBI) fueling, as shown in Chapter 4. For trace impurity transport, both the diagonal and off–diagonal transport coefficients are affected by an increase of β_e. The normalized diffusion coefficient decreases with increasing β_e, while the off–diagonal thermodiffusion and pure convection coefficients both increase in absolute values, the former in outward direction and the latter in inward direction. Thus, the off–diagonal finite β_e effects are partly balanced such that the convection to diffusion ratio determining the stationary trace impurity density gradient is usually only a weakly varying function of β_e. The diagonal component of turbulent parallel momentum transport shows a decrease with raising β_e. This behavior is also obtained for the Coriolis pinch, which is the off–diagonal contribution considered in the framework of the present thesis (see discussion in Chapter 6.1). Both the ratios of viscosity to heat conductivity and Coriolis pinch to viscosity decrease with increasing β_e. In high–β operational scenarios in present devices, and therefore usually in the presence of substantial NBI torque, the two effects can balance, since the first implies an increase of the toroidal rotation velocity gradient, while the second a decrease. In the absence of NBI torque, which is likely to be the case in a fusion reactor, the toroidal rotation velocity gradient will be mainly determined by the ratio between the off–diagonal contributions to the momentum flux and the diagonal viscosity, and in this case, the second effect will be dominant. This leads to the prediction of a decrease of the toroidal rotation velocity gradient in operational conditions close to the trigger of KBMs. It is therefore important to establish how close high–β scenarios can be with respect to the trigger of these modes. In Chapter 7.3.2 we have shown that the experimental condition of proximity to KBMs can occur in hybrid scenarios.

Another aspect connected with the physics differences of the finite β_e contributions for each transport channel is the relative importance of E×B and magnetic flutter. For low–Z trace impurities and ion heat it can be practically neglected. The reason for this difference is the fact that electrons are stronger affected by perpendicular magnetic field fluctuations due to their smaller inertia as compared to the ions and impurities. Generally, it is found that E×B transport is dominant, and magnetic flutter transport provides only a small addition. For instance, in the case of low–Z trace impurities and ion heat transport, magnetic flutter is usually around 1% of the E×B part at $\beta_e = 1\%$. High–Z impurities show a stronger influence of magnetic flutter fluxes (up to 10% for the highest β_e values considered in this work). For electron and parallel momentum transport, magnetic flutter plays also a weak role (around 1% of the E×B part at $\beta_e = 1\%$). However, in conditions of a very small E×B component, which is the case at the stationary density gradient determined by the requirement of the electron particle flux to be at the null (see Chapter 4.3), or at the transition from ITG to KBMs for the parallel momentum transport (see Chapter 6.2), the flutter flux is in general not vanishing, but can be as big as the E×B contribution or even dominant.

For a more realistic treatment, the inclusion of a finite β implies another aspect for the theoretical modeling of tokamak plasmas, namely the inclusion of the geometrical (electrostatic) effect produced by an increase of β in the magnetic equilibrium, which affects the vertical drift. Of course, in experiments this effect is inevitably closely connected

to a finite β_e in Ampère's law, but in theoretical investigations it can be distinguished. As it was shown in Chapters 4.4.2 and 5.2 for electron and trace impurity transport, the influence of the geometrical effect is observed to be weak. In particular, this was found from nonlinear simulations for electron transport, see Fig. 4.9. However, quasi–linear studies showed a larger effect. This underlines the importance of appropriate spectral weighting of quasi–linear fluxes in order to match the nonlinear results.

Lastly, the proximity to MHD instabilities plays an important role for the behavior of the parallel momentum transport coefficients. For ITG modes, an increasing β_e in the vicinity of the kinetic ballooning mode threshold leads to stronger decrease of the diagonal parallel momentum transport, and can even reverse the sign of the Coriolis pinch, as it was discussed in Chapter 6.2.2. Instead, the proximity to the micro–tearing mode threshold does not show large variations of the transport coefficients. For the other transport channels, in the vicinity to the KBMs similar behaviors are found, as it was also reported in [50] for the ion heat transport.

8.2 Outlook

The electromagnetic effects on the different transport channels discussed in the framework of the present thesis are relevant for future fusion experiments towards the goal of energy production. In this context, operational scenarios which combine both large confinement factors with high values of β, are of particular importance. In contrast to present day experiments, a burning plasma in a tokamak device will be mainly heated through α–particles generated from the D–T fusion reaction, with no or only weak additional heating due to neutral beam injection (NBI). As it was explained in Chapter 4.4.3, the absence of NBI heating in combination with high values of β_e is predicted to lead to a substantial decrease of the peaking of the density profile and therefore to a smaller amount of stored energy. This unfavorable result, however, might be beneficial in case impurity transport in the core is dominated by neoclassical transport. In contrast, electromagnetic effects on turbulent impurity transport do not exhibit mechanisms leading to strong accumulation, as it was shown in Chapter 5.4. These two points may be confirmed or rejected by experimental studies in present fusion experiments using a large fraction of ion/electron cyclotron resonance heating with only a small fraction of NBI.

Moreover, a burning plasma in a tokamak device will only experience a weak external torque (also because of the minimal NBI heating with respect to present devices). Then, the plasma rotation in the core will depend on Coriolis pinch and intrinsic rotation mechanisms (all of the off–diagonal terms in the expression of the momentum flux, as it was explained in Chapter 6.1). For operation at high β_e, presumably close to the trigger of MHD modes like the KBM, the Coriolis pinch will be close to the null or even reversed, as it can be concluded from the discussion in Chapter 6.2. Therefore, also the stationary toroidal velocity gradient may become small, leading to lower values of $E \times B$ shearing and thus larger turbulence levels, which, in turn, cause a decrease in the energy confinement time. Another interesting point is that one of the most important parameters to get large Coriolis pinch is the logarithmic density gradient. Since the latter is predicted to decrease significantly with increasing β_e, also the pinch in the momentum decreases, which is an indirect effect in addition to the direct reduction due to high β. Moreover, MHD modes like the resistive wall mode are less stabilized by a smaller toroidal rotation, which can

lead to a strong limitation for the parameter space in which a high–β operation is possible, especially in the case of a broad current profile.

From the previous discussions it can be concluded that electromagnetic effects cause a large diversity of operational consequences. Moreover, the interplay of the different transport channels sketched above further increases the complexity of the studies in order to get the ultimate answer to the question of the influence of electromagnetic effects on tokamak plasmas. From the theoretical standpoint, further investigations have to be made, for many reasons. Firstly, most of the results in the framework of the present thesis are obtained at mid–radius. Thus, simulations with global codes over a large radial window (ideally the full radial domain) might fortify the present result on a global scale, or might be giving new insights on the transport properties. The complexity in transport modeling due to the interplay of the different transport channels on an energy confinement time scale could be tackled by a new kind of approach like TGYRO [156] or TRINITY [157], whose aim is to manage execution of multiple instances of a global kinetic neoclassical code together with a (local) gyrokinetic code. Equilibrium profiles of density and temperature are modified by an iteration procedure until measured losses from collisions and turbulence balance experimental power and density sources.

Of course, all the results presented in the framework of this thesis may also be confirmed or rejected by further experimental studies using high β operational scenarios in present fusion devices. Especially conditions with the absence of strong NBI heating, and therefore small beam fueling and external torque, have to be investigated. This is the best method to study the full physics of the mentioned effects and their interplay, which is extremely helpful for the next steps towards a fusion reactor.

Appendix

Mathematica routine for ITG–TEM stability analysis

The following Mathematica-5.0 routine has been used for the calculation of figure 3.8.

```
(*Frequencies in \[Omega]_Di - Normalisation,
note : \[Tau] = Ti/Te;
order (\[Phi], ni, net, Ti, Tet)*)

Mat := {{(1 - 1/2*RLni)/\[Tau],-om + 1, 0, 1, 0},
{(1/2*RLTi-1/3*RLni)/\[Tau], -2/3*om, 0, om -5/3, 0}, {1/2*RLne -
1,0, 1 +\[Tau]*om, 0, 1}, {1/2*RLTe - 1/3*RLne, 0, -2/3*\[Tau]*om,
0,\[Tau]*om + 5/3}, {1 - ft, -1, ft, 0, 0}};

Mat//MatrixForm

Matdet[om_, ft_, \[Tau]_, RLni_, RLTi_, RLne_,RLTe_] = Det[Mat];

Matdets[ft_, \[Tau]_, RLni_, RLTi_, RLne_, RLTe_] :=
  Solve[Matdet[om, ft, \[Tau], RLni, RLTi, RLne, RLTe] == 0, om];

growthrate[ft_, \[Tau]_, RLni_, RLTi_, RLne_, RLTe_] :=

Module[{i,r, s, t},
t := Sort[Table[om /. Matdets[ft, \[Tau], RLni,
  RLTi, RLne, RLTe][[i]],{i,1,4}], Im[#1] > Im[#2] &];
s :=Select[
  Table[Abs[Im[om /.Matdets[ft, \[Tau], RLni, RLTi, RLne, RLTe]
  [[i]]]],{i, 1,4}], # > 0 &][[1]]; t];

Counter[ft_, \[Tau]_, RLni_, RLTi_, RLne_, RLTe_] :=
    Count[Im[growthrate[ft, \[Tau], RLni, RLTi, RLne, RLTe]],
     _?Positive];

casefunction[ft_, \[Tau]_, RLni_, RLTi_, RLne_, RLTe_] :=
    Module[{x},Switchfunction[x_] :=
        Switch[x, _Real, 0, _Complex,
        Counter[ft, \[Tau], RLni, RLTi, RLne, RLTe]*Sign[Re[x]]];
```

```
Switchfunction/@
growthrate[ft, \[Tau], RLni, RLTi, RLne, RLTe]][[1]]
```

Using the functions listed above, figure 3.8a) was plotted using

```
DensityPlot[casefunction[0.5, 1, i, j, i, j], {i, 0.05, 8},
{j,0.05,12}, PlotPoints -> 60, Frame -> True, FrameLabel ->
{"R/Ln","R/LT"}, RotateLabel -> False, FormatType -> OutputForm,
ColorFunction -> (Hue[0.35 - 0.61*#] &), ColorFunctionScaling ->
False]
```

Normalized velocity space variables and gyrokinetic derivation of $\hat{\Omega}$

The normalized velocity–space coordinates $(\epsilon, \lambda, \varsigma)$ are defined as

$$\begin{aligned} \epsilon &= \frac{m_\sigma v^2}{2T_\sigma} \\ \lambda &= \frac{v_\perp^2}{v^2 \hat{B}} \\ \varsigma &= \mathrm{sgn}(\hat{v}_{\parallel,\sigma}). \end{aligned} \tag{1}$$

Then,

$$\begin{aligned} v_\parallel^2 &= v^2(1-\lambda\hat{B}) \\ v_\perp^2 &= v^2\lambda\hat{B}. \end{aligned} \tag{2}$$

The sign of the velocity, ς, is required in order to separate two populations of trapped particles for each value of λ. With these definitions, the normalized parallel velocity becomes

$$\hat{v}_{\parallel,\sigma} = \pm\sqrt{2\hat{\mu}_\sigma \epsilon \hat{T}_\sigma (1-\lambda\hat{B})}, \tag{3}$$

where $\hat{T}_\sigma = T_\sigma/T_\mathrm{e}$. Then, the Jacobian $\mathcal{J}$ of the coordinate transformation from $(v_\perp, v_\parallel) \to (\epsilon, \lambda, \varsigma)$ is given by

$$\mathcal{J} = \varsigma \frac{T_\sigma}{m_\sigma} \frac{1}{2\sqrt{\lambda\hat{B}(\lambda\hat{B}-1)}}. \tag{4}$$

Consequently, the velocity integral over a Maxwellian is given by

$$\begin{aligned} \int d^3v F_{\mathrm{M,v}} &= \sum_\varsigma 2\pi \int_0^\infty \int_0^\infty \varsigma v_\perp F_{\mathrm{M,v}} dv_\parallel dv_\perp \\ &= \sum_\varsigma 2\pi \int_0^\infty \int_0^1 \varsigma \frac{T_\sigma}{m_\sigma} \frac{1}{2\sqrt{\lambda\hat{B}(\lambda\hat{B}-1)}} \varsigma \sqrt{2\epsilon \frac{T_\sigma}{m_\sigma} \lambda\hat{B}} \times \\ &\quad \left(\frac{m_\sigma}{2\pi T_\sigma}\right)^{3/2} \exp\left[-\epsilon\right] d(\lambda\hat{B}) d\epsilon \\ &= \sum_\varsigma \frac{1}{2\sqrt{\pi}} \int_0^\infty \int_0^1 \varsigma^2 \frac{\sqrt{\epsilon}}{1-\lambda\hat{B}} \exp\left[-\epsilon\right] d(\lambda\hat{B}) d\epsilon \\ &= 1 \end{aligned} \tag{5}$$

Using this, the relation Eq. (4.5) can be simplified in the case of only considering the electron current. This means that the $\sum_\sigma$ reduces to one term given by the electrons. Assuming $J_{0,\mathrm{e}} = 1$ and taking only the large parallel velocity terms to leading order in $\hat{\mu}_\mathrm{e}$, this gives

$$
\begin{aligned}
&\int d^3v\hat{v}_{||}\frac{N_{\mathrm{pass,k}}}{D_{\mathrm{pass,k}}}F_{\mathrm{M,v}} = \\
= &\sum_\varsigma \frac{1}{2\sqrt{\pi}}\int_0^\infty\int_0^1 \varsigma^2\frac{\sqrt{\epsilon}}{1-\lambda\hat{B}}\exp\left[-\epsilon\right]\varsigma\sqrt{2\hat{\mu}_\sigma\epsilon\hat{T}_\sigma(1-\lambda\hat{B})}\times \\
&\left\{\hat{k}_\parallel\varsigma\sqrt{2\hat{\mu}_\sigma\epsilon\hat{T}_\sigma(1-\lambda\hat{B})}\left[k_\mathrm{y}\rho_\mathrm{s}\left(\frac{R}{L_{\mathrm{n,e}}}+\frac{R}{L_{\mathrm{T,e}}}\left(\epsilon-\frac{3}{2}\right)\right)+\hat{\omega}_\mathrm{r}+i\hat{\gamma}\right]\right\}\times \\
&\left\{2\hat{k}_\parallel\varsigma^2\hat{\mu}_\mathrm{e}\epsilon\left(1-\lambda\hat{B}\right)\right\}^{-1}d(\lambda\hat{B})d\epsilon \\
= &\frac{q}{\sqrt{\pi}}\int_0^\infty\int_0^1\sqrt{\epsilon}\exp\left[-\epsilon\right]\frac{1}{\sqrt{1-\lambda\hat{B}}}\left[k_\mathrm{y}\rho_\mathrm{s}\frac{R}{L_{\mathrm{n,e}}}+\hat{\omega}_\mathrm{r}+i\hat{\gamma}\right]d(\lambda\hat{B})d\epsilon \\
= &2q\left[k_\mathrm{y}\rho_\mathrm{s}\frac{R}{L_{\mathrm{n,e}}}+\hat{\omega}_\mathrm{r}+i\hat{\gamma}\right], \qquad (6)
\end{aligned}
$$

where $\hat{k}_\parallel = 1/q$ was taken for simplicity. Note that a term proportional to the temperature gradient, namely $k_\mathrm{y}\rho_\mathrm{s}\left(\epsilon - 3/2\right)R/L_\mathrm{T}$, has been left out since it does not give a contribution after integration over energy.

The integral $\int d^3v\hat{v}_{||}^2 N_{\mathrm{pass,k}}/D_{\mathrm{pass,k}}F_{\mathrm{M,v}}$ vanishes identically under the assumptions mentioned above because of an additional ς under the sum over $\varsigma = \pm$. This leads to the expression of Eq. (4.13).

Bibliography

[1] D. H. Meadows, D. L. Meadows, J. Randers, and W. W. Behrens, *The Limits to Growth* (Universe Books, 1972).

[2] D. H. Meadows, J. Randers, and D. L. Meadows, *Limits to Growth, The 30 Year Update* (Chelsea Green Publishing, 2004).

[3] C. F. von Weizsäcker, Phys. Z., **38** (1937).

[4] H. A. Bethe, Phys. Rev., **55** (1939).

[5] S. Coda, T. P. Goodman, M. A. Henderson, F. Hofmann, Z. A. Pietrzyk, O. Sauter, S. Alberti, C. Angioni, K. Appert, R. Behn, P. Blanchard, P. Bosshard, R. Chavan, A. Degeling, B. P. Duval, D. Fasel, A. Favre, I. Furno, P. Gomez, P. Gorgerat, J.-P. Hogge, P.-F. Isoz, B. Joye, P. Lavanchy, J. B. Lister, X. Llobet, J.-C. Magnin, A. Manini, B. Marltaz, P. Marmillod, Y. Martin, A. Martynov, J.-M. Mayor, J. Mlynar, J.-M. Moret, P. Nikkola, P. J. Paris, A. Perez, Y. Peysson, R. A. Pitts, A. Pochelon, H. Reimerdes, J. H. Rommers, E. Scavino, A. Sushkov, G. Tonetti, M. Q. Tran, H. Weisen, and A. Zabolotsky, Plasma Phys. Controlled Fusion, **42**, B311 (2000).

[6] P. Politzer, A. Hyatt, T. Luce, F. Perkins, R. Prater, A. Turnbull, D. Brennan, J. Ferron, C. Greenfield, J. Jayakumar, R. L. Haye, C. Petty, and M. Wade, Nucl. Fusion, **45**, 417 (2005).

[7] J. D. Lawson, Proceedings of the Physical Society B, **70** (1957).

[8] *ITER Technical Basis* (ITER EDA Documentation Series No. 24 (IAEA, Vienna), 2002).

[9] R. D. Hazeltine and J. D. Meiss, *Plasma Confinement* (Addison-Wesley, New York, 1992).

[10] J. Hugill, Nucl. Fusion, **23**, 331 (1983).

[11] F. Wagner and U. Stroth, Plasma Phys. Controlled Fusion, **35**, 1321 (1993).

[12] F. Troyon and R. Gruber, Physics Letters A, **110**, 29 (1985).

[13] A. Hirose, L. Zhang, and M. Elia, Phys. Rev. Lett., **72**, 3993 (1994).

[14] W. M. Tang, J. W. Connor, and R. J. Hastie, Nucl. Fusion, **20**, 1439 (1980).

[15] N. Joiner and A. Hirose, Phys. Plasmas, **15**, 082107 (2008).

[16] A. Hirose and M. Elia, Phys. Plasmas, **10**, 1195 (2003).

[17] W. Horton, D. I. Choi, and W. M. Tang, Phys. Fluids, **24**, 1077 (1981).

[18] C. A. Primmerman, L. M. Lidsky, and P. A. Politzer, Phys. Rev. Lett., **33**, 957 (1974).

[19] J. Candy and R. E. Waltz, J. Comput. Phys., **186**, 545 (2003).

[20] J. Candy and R. E. Waltz, Phys. Rev. Lett., **91**, 045001 (2003).

[21] T. Northrop, *Adiabatic motion of Charged Particles* (Wiley, New York, 1963).

[22] R. J. Fonck, G. Cosby, R. D. Durst, S. F. Paul, N. Bretz, S. Scott, E. Synakowski, and G. Taylor, Phys. Rev. Lett., **70**, 3736 (1993).

[23] G. McKee, C. Petty, R. Waltz, C. Fenzi, R. Fonck, J. Kinsey, T. Luce, K. Burrell, D. Baker, E. Doyle, X. Garbet, R. Moyer, C. Rettig, T. Rhodes, D. Ross, G. Staebler, R. Sydora, and M. Wade, Nucl. Fusion, **41**, 1235 (2001).

[24] P. H. Rutherford and E. A. Frieman, Phys. Fluids, **11**, 569 (1968).

[25] J. B. Taylor and R. J. Hastie, Plasma Phys., **10**, 479 (1968).

[26] P. J. Catto, Plasma Phys., **20**, 719 (1978).

[27] T. M. Antonsen and B. Lane, Physics of Fluids, **23**, 1205 (1980).

[28] P. J. Catto, W. M. Tang, and D. E. Baldwin, Plasma Phys., **23**, 639 (1981).

[29] E. A. Frieman and L. Chen, Physics of Fluids, **25**, 502 (1982).

[30] A. H. Boozer, Phys. Fluids, **23**, 904 (1980).

[31] R. G. Littlejohn, Phys. Fluids, **24**, 1730 (1981).

[32] J. R. Cary, Physics Reports, **79**, 129 (1981).

[33] D. H. E. Dubin, J. A. Krommes, C. Oberman, and W. W. Lee, Phys. Fluids, **26**, 3524 (1983).

[34] T. S. Hahm, Phys. Fluids, **31**, 2670 (1988).

[35] A. Brizard, J. Plasma Physics, **41**, 541 (1989).

[36] A. J. Brizard and T. S. Hahm, Rev. Mod. Phys., **79**, 421 (2007).

[37] R. G. Littlejohn, J. Plasma Physics, **29**, 111 (1983).

[38] H. Sugama, Phys. Plasmas, **7**, 466 (2000).

[39] J. Weiland, *Collective Modes in Inhomogeneous Plasma - Kinetics and Advanced Fluid Theory* (Institute of Physics (IOP) Publishing, Bristol and Philadelphia, 2000).

[40] M. D. Kruskal and R. M. Kulsrud, Phys. Fluids, **1**, 265 (1958).

[41] R. L. Miller, M. S. Chu, J. M. Greene, Y. R. Lin-Liu, and R. E. Waltz, Phys. Plasmas, **5**, 973 (1998).

[42] J. W. Connor, R. J. Hastie, and J. B. Taylor, Phys. Rev. Lett., **40**, 396 (1978).

[43] J. Candy, R. E. Waltz, and W. Dorland, Phys. Plasmas, **11**, L25 (2004).

[44] J. Candy, R. E. Waltz, and M. N. Rosenbluth, Phys. Plasmas, **11**, 1879 (2004).

[45] J. W. Connor, R. J. Hastie, and J. B. Taylor, Phys. Rev. Lett., **40**, 396 (1978).

[46] J. Weiland, A. B. Jarmén, and H. Nordman, Nucl. Fusion, **34**, 1810 (1989).

[47] H. Nordman, J. Weiland, and A. Jarmén, Nucl. Fusion, **29**, 983 (1990).

[48] G. Bateman, A. H. Kritz, J. E. Kinsey, A. J. Redd, and J. Weiland, Phys. Plasmas, **5**, 1793 (1998).

[49] A. Eriksson and J. Weiland, Phys. Plasmas, **12**, 092509 (2005).

[50] B. D. Scott, Plasma Phys. Controlled Fusion, **45**, A385 (2003).

[51] L. Rudakov and R. Sagdeev, Soviet Phys. Doklady, **7**, 417 (1961).

[52] B. Coppi, M. N. Rosenbluth, and R. Z. Sagdeev, Phys. Fluids, **10**, 582 (1967).

[53] J. W. Connor, R. J. Hastie, and J. B. Taylor, Proc. R. Soc. Lond., **A365**, 1 (1979).

[54] P. N. Guzdar, L. Chen, W. M. Tang, and P. H. Rutherford, Phys. Fluids, **26**, 673 (1983).

[55] F. Romanelli, Phys. Fluids B, **1**, 1018 (1989).

[56] B. G. Hong, W. Horton, and D.-I. Choi, Plasma Phys. Controlled Fusion, **31**, 1291 (1989).

[57] J. Weiland and A. Hirose, Nucl. Fusion, **32**, 151 (1992).

[58] J. Q. Dong, W. Horton, and J. Y. Kim, Phys. Fluids B, **4**, 1867 (1992).

[59] B. B. Kadomtsev and O. P. Pogutse, Nucl. Fusion, **11**, 67 (1971).

[60] H. Biglari, P. H. Diamond, and M. N. Rosenbluth, Phys. Fluids B, **1**, 109 (1989).

[61] B. Coppi and G. Rewoldt, Phys. Rev. Lett., **33**, 1329 (1974).

[62] W. M. Manheimer, K. R. Chu, E. Ott, and J. P. Boris, Phys. Rev. Lett., **37**, 286 (1976).

[63] G. Rewoldt, W. M. Tang, and M. S. Chance, Phys. Fluids, **B1**, 109 (1982).

[64] F. Romanelli and S. Briguglio, Phys. Fluids B, **2**, 754 (1990).

[65] J. Nilsson and J. Weiland, Nucl. Fusion, **34**, 803 (1994).

[66] A. C. C. Sips, R. Arslanbekov, C. Atanasiu, W. Becker, G. Becker, K. Behler, K. Behringer, A. Bergmann, R. Bilato, D. Bolshukhin, K. Borrass, B. Braams, M. Brambilla, F. Braun, A. Buhler, G. Conway, D. Coster, R. Drube, R. Dux, S. Egorov, T. Eich, K. Engelhardt, H.-U. Fahrbach, U. Fantz, H. Faugel, M. Foley, K. B. Fournier, P. Franzen, J. C. Fuchs, J. Gafert, G. Gantenbein, O. Gehre, A. Geier, J. Gernhardt, O. Gruber, A. Gude, S. Günter, G. Haas, D. Hartmann, B. Heger, B. Heinemann, A. Herrmann, J. Hobirk, F. Hofmeister, H. Hohenöcker, L. Horton, V. Igochine, D. Jacobi, M. Jakobi, F. Jenko, A. Kallenbach, O. Kardaun, M. Kaufmann, A. Keller, A. Kendl, J.-W. Kim, K. Kirov, R. Kochergov, H. Kollotzek, W. Kraus, K. Krieger, B. Kurzan, P. T. Lang, P. Lauber, M. Laux, F. Leuterer, A. Lohs, A. Lorenz, C. Maggi, H. Maier, K. Mank, M.-E. Manso, M. Maraschek, K. F. Mast, P. McCarthy, D. Meisel, H. Meister, F. Meo, R. Merkel, D. Merkl, V. Mertens, F. Monaco, A. Mück, H. W. Müller, M. Münich, H. Murmann, Y.-S. Na, G. Neu, R. Neu, J. Neuhauser, J.-M. Noterdaeme, I. Nunes, G. Pautasso, A. G. Peeters, G. Pereverzev, S. Pinches, E. Poli, M. Proschek, R. Pugno, E. Quigley, G. Raupp, T. Ribeiro, R. Riedl, S. Riondato, V. Rohde, J. Roth, F. Ryter, S. Saarelma, W. Sandmann, S. Schade, H.-B. Schilling, W. Schneider, G. Schramm, S. Schweizer, B. Scott, U. Seidel, F. Serra, S. Sesnic, C. Sihler, A. Silva, E. Speth, A. Stäbler, K.-H. Steuer, J. Stober, B. Streibl, E. Strumberger, W. Suttrop, A. Tabasso, A. Tanga, G. Tardini, C. Tichmann, W. Treutterer, M. Troppmann, P. Varela, O. Vollmer, D. Wagner, U. Wenzel, F. Wesner, R. Wolf, E. Wolfrum, E. Würsching, Q. Yu, D. Zasche, T. Zehetbauer, H.-P. Zehrfeld, and H. Zohm, Plasma Physics and Controlled Fusion, **44**, B69 (2002).

[67] T. Luce, M. Wade, J. Ferron, A. Hyatt, A. Kellman, J. Kinsey, R. L. Haye, C. Lasnier, M. Murakami, P. Politzer, and J. Scoville, Nucl. Fusion, **43**, 321 (2003).

[68] E. Joffrin, A. Sips, J. Artaud, A. Becoulet, L. Bertalot, R. Budny, P. Buratti, P. Belo, C. Challis, F. Crisanti, M. de Baar, P. de Vries, C. Gormezano, C. Giroud, O. Gruber, G. Huysmans, F. Imbeaux, A. Isayama, X. Litaudon, P. Lomas, D. McDonald, Y. Na, S. Pinches, A. Staebler, T. Tala, A. Tuccillo, K.-D. Zastrow, and J.-E. C. to the Work Programme, Nuclear Fusion, **45**, 626 (2005).

[69] D. J. Ward, I. Cook, Y. Lechon, and R. Saez, Fusion Eng. Design, **75-79**, 1221 (2005).

[70] M. Greenwald, J. Terry, S. Wolfe, S. Ejima, M. Bell, S. Kaye, and G. Neilsen, Nucl. Fusion, **28**, 2199 (1988).

[71] C. Angioni, E. Fable, M. Greenwald, M. Maslov, A. G. Peeters, H. Takenaga, and H. Weisen, Plasma Phys. Controlled Fusion, **51**, 124017 (2009).

[72] H. Weisen, A. Zabolotsky, M. Maslov, M. Beurskens, C. Giroud, D. Mazon, and J.-E. contributors, Plasma Phys. Controlled Fusion, **48**, A457 (2006).

[73] C. Angioni, H. Weisen, O. Kardaun, M. Maslov, A. Zabolotsky, C. Fuchs, L. Garzotti, C. Giroud, B. Kurzan, P. Mantica, A. Peeters, J. Stober, and the ASDEX Upgrade Team and contributors to the EFDA-JET Workprogramme, Nucl. Fusion, **47**, 1326 (2007).

[74] M. Maslov, C. Angioni, H. Weisen, and JET-EFDA contributors, Nucl. Fusion, **49**, 075037 (2009).

[75] J. Candy, Phys. Plasmas, **12**, 072307 (2005).

[76] J. D. Callen, Phys. Rev. Lett., **39**, 1540 (1977).

[77] A. B. Rechester and M. N. Rosenbluth, Phys. Rev. Lett., **40**, 38 (1978).

[78] B. Scott, Plasma Phys. Controlled Fusion, **39**, 1635 (1997).

[79] T. Dannert and F. Jenko, Phys. Plasmas, **12**, 072309 (2005).

[80] A. Casati, C. Bourdelle, X. Garbet, F. Imbeaux, J. Candy, F. Clairet, G. Dif-Pradalier, G. Falchetto, T. Gerbaud, V. Grandgirard, Ö. Gürcan, P. Hennequin, J. Kinsey, M. Ottaviani, R. Sabot, Y. Sarazin, L. Vermare, and R. Waltz, Nucl. Fusion, **49**, 085012 (2009).

[81] R. E. Waltz, A. Casati, and G. M. Staebler, Phys. Plasmas, **16**, 072303 (2009).

[82] T. Hein, C. Angioni, E. Fable, and J. Candy, Phys. Plasmas, **17**, 102309 (2010).

[83] C. Angioni, A. G. Peeters, G. V. Pereverzev, F. Ryter, and G. Tardini, Phys. Rev. Lett., **90**, 205003 (2003).

[84] V. Naulin, A. Kendl, O. E. Garcia, A. H. Nielsen, and J. J. Rasmussen, Phys. Plasmas, **12**, 052515 (2005).

[85] C. Bourdelle, W. Dorland, X. Garbet, G. W. Hammett, M. Kotschenreuther, G. Rewoldt, and E. J. Synakowski, Phys. Plasmas, **10**, 2881 (2003).

[86] E. Fable, C. Angioni, and O. Sauter, Plasma Phys. Controlled Fusion, **52**, 015007 (2010).

[87] T. Hein and C. Angioni, Phys. Plasmas, **17**, 012307 (2010).

[88] E. Fable, C. Angioni, and O. Sauter, Plasma Phys. Controlled Fusion, **50**, 115005 (2008).

[89] C. Maggi, R. Groebner, C. Angioni, T. Hein, L. Horton, C. Konz, A. Leonard, C. Petty, A. Sips, P. Snyder, J. Candy, R. Waltz, and ASDEX Upgrade and DIII-D Teams, Nucl. Fusion, **50**, 025023 (2010).

[90] C. Angioni, J. Candy, E. Fable, M. Maslov, A. G. Peeters, R. E. Waltz, and H. Weisen, Phys. Plasmas, **16**, 060702 (2009).

[91] C. Bourdelle, X. Garbet, F. Imbeaux, A. Casati, N. Dubuit, R. Guirlet, and T. Parisot, Phys. Plasmas, **14**, 112501 (2007).

[92] F. Jenko, T. Dannert, and C. Angioni, Plasma Phys. Controlled Fusion, **47**, B195 (2005).

[93] P. Hennequin, R. Sabot, C. Honor, G. T. Hoang, X. Garbet, A. Truc, C. Fenzi, and A. Qumneur, Plasma Phys. Controlled Fusion, **46**, B121 (2004).

[94] A. Casati, T. Gerbaud, P. Hennequin, C. Bourdelle, J. Candy, F. Clairet, X. Garbet, V. Grandgirard, O. D. Gürcan, S. Heuraux, G. T. Hoang, C. Honoré, F. Imbeaux, R. Sabot, Y. Sarazin, L. Vermare, and R. E. Waltz, Phys. Rev. Lett., **102**, 165005 (2009).

[95] A. Bhattacharjee, C. S. Ng, and S. R. Spangler, The Astrophysical Journal, **494**, 409 (1998).

[96] P. P. Kronberg, Phys. Plasmas, **10**, 1985 (2003).

[97] S. Koide, D. L. Meier, K. Shibata, and T. Kudoh, The Astrophysical Journal, **536**, 668 (2000).

[98] C. C. Petty, T. C. Luce, D. C. McDonald, J. Mandrekas, M. R. Wade, J. Candy, J. G. Cordey, V. Drozdov, T. E. Evans, J. R. Ferron, R. J. Groebner, A. W. Hyatt, G. L. Jackson, R. J. L. Haye, T. H. Osborne, and R. E. Waltz, *45th Annual Meeting of the APS Division of Plasma Physics*, Albuquerque, New Mexico, USA (2004).

[99] K.-D. Zastrow, J. M. Adams, Y. Baranov, P. Belo, L. Bertalot, J. H. Brzozowski, C. D. Challis, S. Conroy, M. de Baar, P. de Vries, P. Dumortier, J. Ferreira, L. Garzotti, T. C. Hender, E. Joffrin, V. Kiptily, J. Mailloux, D. C. McDonald, R. Neu, M. O'Mullane, M. F. F. Nave, J. Ongena, S. Popovichev, M. Stamp, J. Stober, D. Stork, I. Voitsekhovitch, M. Valovic, H. Weisen, A. D. Whiteford, A. Zabolotsky, and JET EFDA Contributors, Plasma Phys. Controlled Fusion, **46**, B255 (2004).

[100] C. Estrada-Mila, J. Candy, and R. E. Waltz, Phys. Plasmas, **12**, 022305 (2005).

[101] C. Angioni and A. G. Peeters, Phys. Rev. Lett., **96**, 095003 (2006).

[102] R. Guirlet, C. Giroud, T. Parisot, M. E. Puiatti, C. Bourdelle, L. Carraro, N. Dubuit, X. Garbet, and P. R. Thomas, Plasma Phys. Controlled Fusion, **48**, B63 (2006).

[103] N. Dubuit, X. Garbet, T. Parisot, R. Guirlet, and C. Bourdelle, Phys. Plasmas, **14**, 042301 (2007).

[104] C. Angioni, R. Dux, E. Fable, A. G. Peeters, and the ASDEX Upgrade Team, Plasma Phys. Controlled Fusion, **49**, 2027 (2007).

[105] H. Nordman, T. Fülöp, J. Candy, P. Strand, and J. Weiland, Phys. Plasmas, **14**, 052303 (2007).

[106] V. Naulin, J. J. Rasmussen, C. Angioni, C. Giroud, M. Valisa, M. E. Puiatti, and L. Carraro, AIP Conference Proceedings, **1013**, 191 (2008).

[107] H. Nordman, R. Singh, T. Fülöp, L.-G. Eriksson, R. Dumont, J. Anderson, P. Kaw, P. Strand, M. Tokar, and J. Weiland, Phys. Plasmas, **15**, 042316 (2008).

[108] C. Angioni, A. Peeters, G. Pereverzev, A. Bottino, J. Candy, R. Dux, E. Fable, T. Hein, and R. Waltz, Nucl. Fusion, **49**, 055013 (2009).

[109] T. Fülöp and H. Nordman, Phys. Plasmas, **16**, 032306 (2009).

[110] Y. Camenen, A. G. Peeters, C. Angioni, F. J. Casson, W. A. Hornsby, A. P. Snodin, and D. Strintzi, Phys. Plasmas, **16**, 012503 (2009).

[111] L. Vermare, C. Angioni, A. Bottino, A. G. Peeters, and ASDEX Upgrade Team, J. Phys.: Conf. Ser., **123**, 012040 (2008).

[112] M. Frojdh, M. Liljestrom, and H. Nordman, Nucl. Fusion, **32**, 419 (1992).

[113] X. Garbet, N. Dubuit, E. Asp, Y. Sarazin, C. Bourdelle, P. Ghendrih, and G. T. Hoang, Phys. Plasmas, **12**, 082511 (2005).

[114] G. Pereverzev, C. Angioni, A. Peeters, and O. Zolotukhin, Nucl. Fusion, **45**, 221 (2005).

[115] A. G. Peeters, C. Angioni, and A. U. Team, Phys. Plasmas, **12**, 072515 (2005).

[116] J. E. Kinsey, R. E. Waltz, and J. Candy, Physics of Plasmas, **12**, 062302 (2005).

[117] C. M. Roach, I. G. Abel, R. J. Akers, W. Arter, M. Barnes, Y. Camenen, F. J. Casson, G. Colyer, J. W. Connor, S. C. Cowley, D. Dickinson, W. Dorland, A. R. Field, W. Guttenfelder, G. W. Hammett, R. J. Hastie, E. Highcock, N. F. Loureiro, A. G. Peeters, M. Reshko, S. Saarelma, A. A. Schekochihin, M. Valovic, and H. R. Wilson, Plasma Phys. Controlled Fusion, **51**, 124020 (2009).

[118] R. E. Waltz, G. D. Kerbel, and J. Milovich, Phys. Plasmas, **1**, 2229 (1994).

[119] A. Bondeson and D. J. Ward, Phys. Rev. Lett., **72**, 2709 (1994).

[120] A. G. Peeters, C. Angioni, A. Bortolon, Y. Camenen, F. J. Casson, B. Duval, L. Fiederspiel, W. A. Hornsby, Y. Idomura, N. Kluy, P. Mantica, F. I. Parra, A. P. Snodin, G. Szepesi, D. Strintzi, T. Tala, G. Tardini, P. de Vries, and J. Weiland, *IAEA contribution*, **OV/5-4** (2010).

[121] J. Rice, W. Lee, E. Marmar, P. Bonoli, R. Granetz, M. Greenwald, A. Hubbard, I. Hutchinson, J. Irby, Y. Lin, D. Mossessian, J. Snipes, S. Wolfe, and S. Wukitch, Nucl. Fusion, **44**, 379 (2004).

[122] A. G. Peeters, C. Angioni, and D. Strintzi, Phys. Rev. Lett., **98**, 265003 (2007).

[123] D. Strintzi, A. G. Peeters, and J. Weiland, Phys. Plasmas, **15**, 044502 (2008).

[124] A. G. Peeters, C. Angioni, Y. Camenen, F. J. Casson, W. A. Hornsby, A. P. Snodin, and D. Strintzi, Phys. Plasmas, **16**, 062311 (2009).

[125] A. Peeters, Y. Camenen, F. Casson, W. Hornsby, A. Snodin, D. Strintzi, and G. Szepesi, Comp. Phys. Commun., **180**, 2650 (2009).

[126] M. Kotschenreuther, G. Rewoldt, and W. M. Tang, Comput. Phys. Commun., **88**, 128 (1995).

[127] N. Kluy, C. Angioni, Y. Camenen, and A. G. Peeters, Phys. Plasmas, **16**, 122302 (2009).

[128] P. Mantica, T. Tala, J. S. Ferreira, A. G. Peeters, A. Salmi, D. Strintzi, J. Weiland, M. Brix, C. Giroud, G. Corrigan, V. Naulin, G. Tardini, K.-D. Zastrow, and JET-EFDA Contributors, Phys. Plasmas, **17**, 092505 (2010).

[129] ITER Physics Basis Editors, Nucl. Fusion, **39**, 2137 (1999).

[130] C. C. Petty, Phys. Plasmas, **15**, 080501 (2008).

[131] H. Urano, T. Takizuka, H. Takenaga, N. Oyama, Y. Miura, and Y. Kamada, Nucl. Fusion, **46**, 781 (2006).

[132] L. Vermare, F. Ryter, C. Angioni, A. Peeters, J. Stober, R. Bilato, L. Horton, B. Kurzan, C. Maggi, H. Meister, J. Schirmer, G. Tardini, and the ASDEX Upgrade Team, Nucl. Fusion, **47**, 490 (2007).

[133] D. C. McDonald, L. Laborde, J. C. DeBoo, F. Ryter, M. Brix, C. D. Challis, P. de Vries, C. Giroud, J. Hobirk, D. Howell, E. Joffrin, T. C. Luce, J. Mailloux, V. Pericoli-Ridolfini, A. C. C. Sips, K. Thomsen, and JET EFDA Contributors, Plasma Phys. Controlled Fusion, **50**, 124013 (2008).

[134] P. B. Snyder and G. W. Hammett, Phys. Plasmas, **8**, 744 (2001).

[135] S. E. Parker, Y. Chen, W. Wan, B. I. Cohen, and W. M. Nevins, Phys. Plasmas, **11**, 2594 (2004).

[136] A. Bottino, M. Borchardt, T. B. Feher, R. Hatzky, K. Kauffmann, R. Kleiber, A. Könies, A. Mishchenko, A. G. Peeters, E. Poli, and B. Scott, *IAEA contribution*, **THC/P4-02** (2010).

[137] J. Candy and R. E. Waltz, Phys. Rev. Lett., **91**, 045001 (2003).

[138] M. J. Pueschel, M. Kammerer, and F. Jenko, Phys. Plasmas, **15**, 102310 (2008).

[139] O. Gruber, R. C. Wolf, R. Dux, C. Fuchs, S. Günter, A. Kallenbach, K. Lackner, M. Maraschek, P. J. McCarthy, H. Meister, G. Pereverzev, F. Ryter, J. Schweinzer, U. Seidel, S. Sesnic, A. Stäbler, J. Stober, and the ASDEX Upgrade Team, Phys. Rev. Lett., **83**, 1787 (1999).

[140] A. Sips, G. Tardini, C. Forest, O. Gruber, P. M. Carthy, A. Gude, L. Horton, V. Igochine, O. Kardaun, C. Maggi, M. Maraschek, V. Mertens, R. Neu, A. Peeters, G. Pereverzev, A. Stbler, J. Stober, W. Suttrop, and the ASDEX Upgrade Team, Nucl. Fusion, **47**, 1485 (2007).

[141] D. Nishijima, A. Kallenbach, S. Günter, M. Kaufmann, K. Lackner, C. F. Maggi, A. G. Peeters, G. V. Pereverzev, B. Zaniol, and the ASDEX Upgrade Team, Plasma Phys. Controlled Fusion, **47**, 89 (2005).

[142] P. Politzer, C. Petty, R. Jayakumar, T. Luce, M. Wade, J. DeBoo, J. Ferron, P. Gohil, C. Holcomb, A. Hyatt, J. Kinsey, R. L. Haye, M. Makowski, and T. Petrie, Nucl. Fusion, **48**, 075001 (2008).

[143] A. Peeters, O. Gruber, S. Günter, M. Kaufmann, H. Meister, G. Pereverzev, F. Ryter, A. Sips, J. Stober, W. Suttrop, G. Tardini, R. Wolf, H. Zohm, and the ASDEX Upgrade team, Nucl. Fusion, **42**, 1376 (2002).

[144] R. Neu, R. Dux, A. Kallenbach, T. Pütterich, M. Balden, J. Fuchs, A. Herrmann, C. Maggi, M. O'Mullane, R. Pugno, I. Radivojevic, V. Rohde, A. Sips, W. Suttrop, A. Whiteford, and the ASDEX Upgrade team, Nucl. Fusion, **45**, 209 (2005).

[145] C. Maggi, R. Groebner, N. Oyama, R. Sartori, L. Horton, A. Sips, W. Suttrop, the ASDEX Upgrade Team, A. Leonard, T. Luce, M. Wade, the DIII-D Team, Y. Kamada, H. Urano, the JT-60U Team, Y. Andrew, C. Giroud, E. Joffrin, E. de la Luna, and EFDA-JET Contributors for the Pedestal and Edge Physics and the Steady State Operation Topical Groups of the ITPA, Nucl. Fusion, **47**, 535 (2007).

[146] P. Snyder, K. Burrell, H. Wilson, M. Chu, M. Fenstermacher, A. Leonard, R. Moyer, T. Osborne, M. Umansky, W. West, and X. Xu, Nucl. Fusion, **47**, 961 (2007).

[147] A. W. Leonard, R. J. Groebner, T. H. Osborne, and P. B. Snyder, Phys. Plasmas, **15**, 056114 (2008).

[148] M. Wade, T. Luce, R. Jayakumar, P. Politzer, A. Hyatt, J. Ferron, C. Greenfield, M. Murakami, C. Petty, R. Prater, J. DeBoo, R. L. Haye, P. Gohil, and T. Rhodes, Nucl. Fusion, **45**, 407 (2005).

[149] V. Rohde, M. Mayer, V. Mertens, R. Neu, K. Sugiyama, and the ASDEX Upgrade Team, Nucl. Fusion, **49**, 085031 (2009).

[150] R. E. Waltz, G. M. Staebler, W. Dorland, G. W. Hammett, M. Kotschenreuther, and J. A. Konings, Phys. Plasmas, **4**, 2482 (1997).

[151] A. M. Dimits, G. Bateman, M. A. Beer, B. I. Cohen, W. Dorland, G. W. Hammett, C. Kim, J. E. Kinsey, M. Kotschenreuther, A. H. Kritz, L. L. Lao, J. Mandrekas, W. M. Nevins, S. E. Parker, A. J. Redd, D. E. Shumaker, R. Sydora, and J. Weiland, Phys. Plasmas, **7**, 969 (2000).

[152] G. Pereverzev and P. N. Yushmanov, *IPP Report*, **5/98** (2002).

[153] G. G. Lister, *IPP Report*, **4/222** (1985).

[154] M. Brambilla, Plasma Phys. Controlled Fusion, **41**, 1 (1999).

[155] H. St. John, T. S. Taylor, Y. R. Lin-Liu, and A. D. Turnbull, editors, *Transport simulation of negative magnetic shear discharges* (15th International Conference on Plasma Physics and Controlled Nuclear Fusion Research, Seville, Spain, 26 Sep. - 1 Oct. 1994).

[156] J. Candy, C. Holland, R. E. Waltz, M. R. Fahey, and E. Belli, Phys. Plasmas, **16**, 060704 (2009).

[157] M. A. Barnes, *Trinity: A unified treatment of turbulence, transport, and heating in magnetized plasmas* (University of Maryland, College Park, 2009).

Acknowledgement

I am indebted to express my gratitude to all people, who have supported me during the last three years in many respects. First of all, I would like to thank my family for supporting me all the years up to this point. Their patronage was a great benefit for my choices all my life long. This thesis is dedicated to you!

I gratefully acknowledge the support of my supervisor Clemente Angioni, who combined his immense knowledge and great patience for helping me to master the provided subject. Among all the other helpful people at IPP, two persons deserve a particular mention. Firstly, Alberto Bottino kindly offered me the exceptional opportunity to share his office. Moreover, I express my deep gratitude for his friendly attitude and support like solving lots of computer problems. Secondly, I'd like to thank Emiliano Fable for his generous assistance and lots of very useful discussions.

Many thanks go to Jeff Candy for the provision and refinements of the gyrokinetic code GYRO, which was used for all the simulation results obtained within the present thesis. The fruitful collaboration with Costanza Maggi is gratefully acknowledged. I appreciated the valuable physics discussions with Bruce Scott and Arthur Peeters. The so–called 'Italian group' at IPP (Vittoria Belmondo, Alessandro Biancalani, Roberto Bilato, Omar Maj, Emanuele Poli, Andrea Scarabosio, Mattia Siccinio, Giovanni Tardini, Marco Wischmeier) kindly absorbed me and I am thankful for the great company, also to Norbert Kluy, Andreas Stegmeir and Christian Veth. The football sessions with the 'Platzhirsche' and the other people from the 'SV Plasmaphysik' have been very enjoyable. I'd like to thank them for the nice practice rounds, which were very useful as a physical exercise and a mental distraction.

Lastly, but indeed not least, I acknowledge the great support from the Max–Planck–Institut für Plasmaphysik, which allowed me not only to study the very interesting subject of transport in tokamak plasmas, but also provided the opportunity to participate at international conferences (EFTC in Riga 2009, TTG–TTF in Córdoba 2010) and internal meetings (Ringberg 2008 and 2010, and Sellin 2009). Many thanks go to the head of the department, Sibylle Günter.